Young-Jo Kim
Tallal Charles Mamisch
Editors

Hip Magnetic Resonance Imaging

Springer

Hip Magnetic Resonance Imaging

Young-Jo Kim • Tallal Charles Mamisch
Editors

Hip Magnetic Resonance Imaging

Springer

Editors
Young-Jo Kim
Department of Orthopedic Surgery
Boston Children's Hospital
Boston, MA
USA

Tallal Charles Mamisch
Department of Radiology
Brigham & Women's Hospital
Boston, MA
USA

ISBN 978-1-4614-1667-8 ISBN 978-1-4614-1668-5 (eBook)
DOI 10.1007/978-1-4614-1668-5
Springer New York Heidelberg Dordrecht London

Library of Congress Control Number: 2013950381

"Twenty years from now you will be more disappointed by the things that you didn't do than by the ones you did do. So throw off the bowlines. Sail away from the safe harbor. Catch the trade winds in your sails. Explore. Dream. Discover."

—Mark Twain.

When I embarked on this journey nearly 14 years ago, I did not know what I would find. Biochemical imaging was a laboratory novelty, and hip joint preservation was almost considered sham surgery. It is remarkable how things have changed. Along the way, I have had many mentors and supporters and have had the great pleasure of making key friendships that I will treasure for life. I will only mention a few.

I owe a great debt to Deborah Burstein, Martha Gray, Diego Jaramillo, and Michael Millis for their support during the initial implementation of the dGEMRIC MRI technique for the hip. Based on Deb and Martha's basic research, it appeared logical that dGEMRIC would work, and it did! It was a good thing I did not know at the time all the things that could have gone wrong.

After our initial work and publication, I was searching for a faster way to perform T1 mapping. My prayers were answered when Charles Mamisch and Christoph Zilkens literally dropped in from the sky. I still recall the day when these two German orthopedists came to the office and said they wanted to work with us on dGEMRIC, no questions asked. With the help of Tim Hughes from Siemens, we were able to make dGEMRIC a practical clinical tool.

All of us in this field of hip preservation surgery, including myself, personally owe a great deal of thanks to Reinhold Ganz. His vision and determination has made this all possible.

In addition, I am grateful for the friendship of Michael Leunig and Klaus Siebenrock. I met them when they were sharing an office in Bern—a time when we were much younger—and I look forward to many more years of friendship and collaboration. This time was and now continues to be a period of great excitement for hip preservation surgery.

Finally, I would like to thank my mother and my family. My mother, who exemplifies the definition of unconditional love, is the source of my stubborn single-mindedness. To my wife Lois, I thank her for her unconditional support and sacrifice. Without her ability to make everything else in my life work, this work would not have been possible. Lastly, I am grateful for the collaboration and friendship I have with Charles Mamisch. His genuine enthusiasm for science and his ability to get things done across cultural and national borders is truly amazing.

Young-Jo Kim M.D., Ph.D.

Preface

During the past decade, we have seen tremendous advances and enthusiasm for hip joint preservation surgery. At present, approximately 60,000 cases of hip arthroscopy are performed per year in the United States with yearly growth rates of ~15 % per year. Given the high prevalence of cam deformity in the population, it is possible that this growth will continue for the foreseeable future. Coincident with advances in our understanding of hip pathology and treatment methods are advances in hip MR imaging. Both morphologic and biochemical imaging of the hip has benefited greatly by the use of higher field magnets, improved coil design and sequences.

In many respects, both the clinical and imaging aspects of hip disorders are complementary and essential in order for further advances in each field. Biochemical imaging of cartilage has long languished in the laboratory for lack of clinical relevance. It is an ideal technique to assess the efficacy of osteoarthritis disease modifying treatment; however, to date no disease-modifying drug exists. On the clinical side, disease-modifying drug for osteoarthritis has tremendous potential; however, it has been very difficult to develop due to lack of an early marker of disease that is accepted by the regulatory agencies. It is a classic catch-22 situation.

Now with advances in hip preservation surgery, it may be possible to make progress in our understanding of how osteoarthritis develops as well as understand the role of advancing MR imaging in advancing knowledge and treatment of osteoarthritis. At this point in time, the surgical techniques of hip preservation surgery are maturing and early clinical results are promising in demonstrating efficacy in improving symptoms. Similar to the development of osteoarthritis disease modifying drugs, in order to demonstrate disease modification over a short period of time, the use of advanced imaging will be required. Fortunately, we feel imaging technologies are now available to make this possible.

This book is a current summary of both clinical and imaging knowledge relevant to understanding hip pathology. It is our hope that this book will be useful in the present, but more importantly may stimulate future advances.

Contents

List of Contributors

Sebastian Apprich, MD Department of Radiology, Centre for High-Field MR, Medical University of Vienna, Vienna, Austria

Oliver Bieri, PhD Division of Radiological Physics, Department of Radiology, University of Basel Hospital, Basel, Switzerland

Bernd Bittersohl, MD Department of Orthopedics, Heinrich-Heine University, Medical School, Düsseldorf, Germany

Sarah D. Bixby, MD Department of Radiology, Boston Children's Hospital, Boston, MA, USA

Deborah Burstein, PhD Department of Radiology, Beth Israel Deaconess Medical Center, Boston, MA, USA

Luis Perez Carro, MD Servicio de Cirugía Ortopédica y Traumatología, Hospital Clinica Mompía/Hospital Universitario Marqués de Valdecilla, Santander, Spain

Nancy A. Chauvin, MD Department of Pediatric Radiology, The Children's Hospital of Philadelphia, Perelman School of Medicine at the University of Pennsylvania, Philadelphia, PA, USA

Kathleen L. Davenport, MD Hospital for Special Surgery, New York, NY, USA

Victor de Diego, MD Servicio Cirugia Ortopédica y Traumatología, Centro Médico Lealtad y Hospital Universitario Marqués de Valdecill, Santande, Spain

Stephan Domayer, MD, PhD Department of Orthopaedics, Medical University of Vienna, Vienna, Austria

Natalia Fernandez Escajadillo, RN Servicio Cirugia Ortopédica y Traumatología, Centro Médico Lealtad y Hospital Universitario Marqués de Valdecilla, Santander, Spain

Pau Golano, MD Human Anatomy Unit Department of Pathology and Experimental Therapeutics, University of Barcelona, Barcelona, Spain

Department of Orthopaedic Surgery, University of Pittsburgh, Pittsburgh, PA, USA

Friedrich F. Hennig, MD Department of Trauma Surgery, University Hospital of Erlangen, Erlangen, Germany

Andreas Hingsammer, MD Department of Orthopedic Surgery, Boston Children's Hospital, Boston, MA, USA

Diego Jaramillo, MD, MPH Department of Pediatric Radiology, The Children's Hospital of Philadelphia, Perelman School of Medicine at the University of Pennsylvania, Philadelphia, PA, USA

Young-Jo Kim, MD, PhD Department of Orthopedic Surgery, Boston Children's Hospital, Boston, MA, USA

Bryan T. Kelly, MD Orthopedic Surgeon, Hospital for Special Surgery, New York, NY, USA

Orthopedic Surgery, Weill Cornell Medical College, Center for Hip Preservation, New York, NY, USA

Michael Leunig, MD Department of Orthopaedics, Schulthess Clinic, Zurich, Switzerland

T. Charles Mamisch, MD Department of Radiology, Brighman & Women's Hospital, Boston, MA, USA

Andreas Mauerer, MD Department of Trauma Surgery, University Hospital of Erlangen, Erlangen, Germany

Peter J. Moley, MD Department of Psychiatry, Hospital for Special Surgery, New York, NY, USA

Clinical Rehabilitation Medicine, Weill Cornell Medical College, Center for Hip Preservation, New York, NY, USA

Jeffrey J. Nepple, MD Department of Orthopaedic Surgery, Washington University School of Medicine, St. Louis, MO, USA

Luis Cerezal Pesquera, MD Servicio Radiología, Diagnóstico Medico Cantabria, Santander, Spain

Kawan S. Rakhra, MD, FRCPC Department of Medical Imaging, The Ottawa Hospital, General Campus, Ottawa, ON, Canada

Nadja Mamisch-Saupe, MD Department of Radiology/Center for Musculoskeletal Surgery, Hirslanden Clinic, Zurich, Switzerland

Courtney E. Scher, DO Musculoskeletal Radiology, Henry Ford Hospital, Detroit, MI, USA

Benjamin Schmitt, MD Department of Radiology, Centre for High-Field MR, Medical University of Vienna, Vienna, Austria

Carl Siversson, PhD Computational Radiology Laboratory, Children's Hospital Boston, Harvard Medical School, Boston, MA, USA

Department of Medical Radiation Physics, Lund University, Malmö, Sweden

Siegfried Trattnig, MD Department of Radiology, Medical University of Vienna, Vienna, Austria

Lisa M. Tibor, MD Center for Hip Preservation, Hospital for Special Surgery, New York, NY, USA

Miguel Ruperez Vallejo, MD Servicio Cirugia Ortopédica y Traumatología, Centro Médico Lealtad y Hospital Universitario Marqués de Valdecill, Santande, Spain

Goetz H. Welsch, MD Department of Trauma Surgery, University Hospital of Erlangen, Erlangen, Germany

Department of Radiology, MR Center, Medical University of Vienna, Vienna, Austria

Ira Zaltz, MD Musculoskeletal Radiology, Henry Ford Hospital, Detroit, MI, USA

Christoph Zilkens, MD Department of Orthopedics, Heinrich-Heine University, Medical School, Düsseldorf, Germany

Section I

MRI Principles

Basic MRI Physics and Artifacts

1

Carl Siversson

Magnetic resonance imaging (MRI) is a well-established imaging technique, which is available at most larger hospitals today. Since MRI is sensitive to the chemical surroundings of the atomic nuclei within the body, the images have excellent contrast between different soft-tissues. Due to the combination of this high contrast and the fact that MRI does not emit any hazardous ionizing radiation, MRI is often used for investigation of a large range of pathologies in almost all parts of the body.

A typical MRI scanner consists of a large superconducting electromagnet in which the patient is positioned. Most clinical scanners have a static magnetic field strength of either 1.5 or 3 tesla (T), although efforts are made to increase the field strength further as that would result in even higher image quality.

When the patient is placed in this strong static magnetic field, the tissue in the body becomes temporarily magnetized. By exposing the tissue to a series of radio frequency pulses and magnetic field gradients, the nuclei in the tissue start to emit radio frequency signals of their own. These signals are detected by the MRI scanner and formed into an image. In clinical MRI, signals from hydrogen nuclei are the most widely used, due to the abundance of hydrogen-rich components, such as water and fat, in the human body.

In this chapter an overview of the MRI phenomena is given. Covering the complete theoretical background of MRI within one chapter would not be feasible and is therefore not the purpose of this text. Instead, this text should be considered an introduction for the uninitiated reader who is interested in gaining an intuitive understanding of the relevant concepts. For a deeper theoretical journey through the physics of MRI, the reader is instead referred to any of the excellent textbooks dedicated to this topic [1–3].

Nuclear Spin

Protons and neutrons both have an intrinsic property called spin. In an atomic nucleus the number of protons and neutrons determines whether the nucleus will have an overall spin or not. Of primary interest in clinical MRI is the hydrogen nucleus, which possesses an overall spin since it consists of only a single proton.

In a strict sense, the spin of an individual nucleus should be described from a quantum physics perspective. That said, there are a number of spin models based on classical physics that are not fully comprehensive, but which are still valuable and provide an intuitive understanding of the phenomenon. In one such model, the spin property can be described as each nucleus rotating around its own axis (Fig. 1.1). Since the nucleus is positively

C. Siversson (✉)
Computational Radiology Laboratory,
Boston Children's Hospital, Harvard Medical School,
Boston, MA, USA

Department of Medical Radiation Physics
Lund University, Malmö, Sweden
e-mail: carl.siversson@med.lu.se

Y.-J. Kim (eds.), *Hip Magnetic Resonance Imaging*,
DOI 10.1007/978-1-4614-1668-5_1,

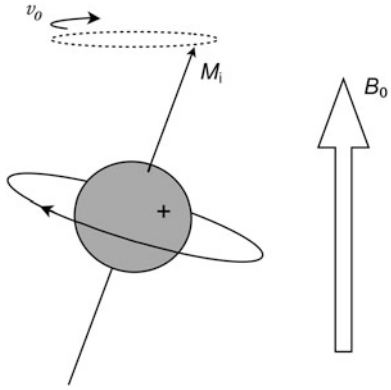

Fig. 1.1 The hydrogen nucleus spins around its own axis, generating an intrinsic magnetic vector M_i, which in turn makes the nucleus precess with the Larmor rotation frequency v_0 about the direction of the external field B_0

charged itself, the rotating charge is equivalent to a rotating current, generating a small magnetic field. Hence, each nucleus has its own intrinsic magnetic vector pointing along its axis of rotation.

Without external influences, the intrinsic magnetic vectors of nuclei in a normal tissue sample are pointing in completely random directions. Hence, from a macroscopic perspective these vectors are averaging themselves out to zero net magnetization.

When placing nuclei in an external magnetic field, B_0, the intrinsic magnetic vector of each nucleus will align along the direction of this field.[1] However, this alignment will not make the vectors become strictly parallel to the B_0 field. Instead, the nuclei will start to precess around the axis of the B_0 field, making the intrinsic magnetic vectors circle at an angle around this direction. This circling will occur with a rotational frequency called the Larmor frequency, v_0 (Fig. 1.1), which varies with the strength of the external B_0 field by

$$v_0 = \gamma \cdot B_0 \tag{1.1}$$

where γ is a nuclei-specific constant called the gyromagnetic ratio ($\gamma = 42.6$ MHz/T for the hydrogen nucleus).

[1] Strictly speaking, there are almost as many hydrogen nuclei aligned against the B_0 field, with only a small surplus of nuclei aligned as described above.

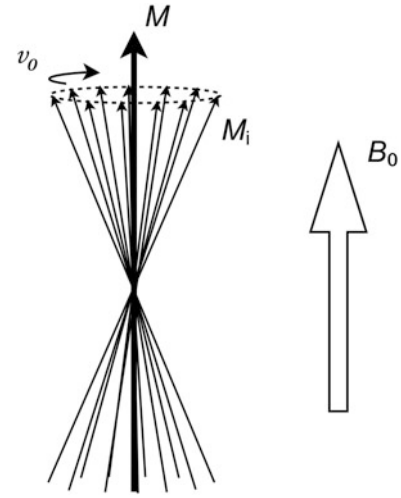

Fig. 1.2 Each individual intrinsic M_i vector has a random angular position. Thus, the sum of all M_i vectors in an isochromat is a new vector, M, pointing in the same direction as the externally applied B_0 field

In any tissue sample, even an extremely small volume contains many millions of hydrogen nuclei. For this reason, it is instructive to consider a large number of nuclei as a single unit, called an isochromat (Fig. 1.2). The intrinsic magnetic vectors of each nucleus in an isochromat are all circling around the B_0 field, but at random angular positions. Thus, adding all intrinsic vectors of the isochromat together results in a bulk magnetization vector, M, pointing in the same direction as the B_0 field.

Coils and RF Pulses

In order to interact with the precessing nuclei, radio frequency (RF) magnetic pulses are used. Such pulses are generated and received by coils, which must be placed in the vicinity of the tissue to be imaged. Coils are available in a variety of types and are usually shaped to come as close as possible to the tissue of interest. For example, for brain imaging a cylindrically shaped coil is often used, efficiently surrounding the entire head, whereas for hip imaging a flat flexible coil that can be directly strapped onto the body surface is more feasible.

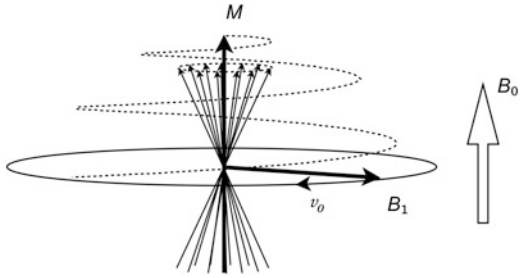

Fig. 1.3 The RF pulse can be thought of as a magnetic B_1 field rotating around the B_0 direction. The nuclei will then precess around both the B_0 and the B_1 fields, which results in the M vector spiraling away from the B_0 direction

In order for the coil to generate an RF pulse, a current oscillating with the Larmor frequency is passed through it. The oscillating magnetic field generated by this current can be divided into separate components. Of particular interest is the component that is perpendicular to the B_0 field, which can be thought of as an additional, weaker magnetic field (called the B_1 field) rotating around the B_0 direction (Fig. 1.3).

From the nuclei's perspective there are now two concurrent magnetic fields around which they will precess. Since one is a strong stationary field (B_0) and the other is a weak rotating field (B_1), the result is that the bulk magnetization vector M will spiral itself away from the B_0 direction at a relatively slow speed. This spiraling will proceed for the duration of the RF pulse. An RF pulse is characterized by the resulting angle between the magnetization vector M and the B_0 direction. This flip angle is primarily determined by the duration (typically 0.5–5 ms) and the amplitude of the pulse.

As soon as the M vector points away from the B_0 direction it will no longer be time and space invariant. Instead, it will rotate around the B_0 direction. Thus, the nuclei themselves generate an oscillating magnetic field, which will induce a signal in the conductors of the receiver coil. At this point the spinning nuclei are said to be excited and the associated RF pulse is often referred to as an excitation pulse. The signal that follows immediately after excitation is denoted free induction decay (FID). However, in clinical MRI other types of signals are more commonly used, which requires a few additional steps to generate. Such signals are referred to as echoes and are described later in this chapter.

For a 90° excitation pulse flip angle the M vector is turned perpendicular to the B_0 field and the generated signal will have its maximum amplitude.

T_1, T_2, and Proton Density

There are three primary parameters required in order to describe the spin-behavior of a set of hydrogen nuclei. These are the T_1, T_2, and proton density (PD) parameters. In most MR images the contrasts origin from the variation of these parameters between tissue types.

The proton density is the most intuitive parameter, as the number of hydrogen nuclei per unit volume is directly proportional to the amplitude of the signal generated by these nuclei. However, in clinical MRI this parameter is often not of primary interest, as it does not provide much information about the chemical composition of the tissue.

The T_1 parameter is a measure of how fast the longitudinal (parallel to B_0) magnetization recovers (Fig. 1.4). When the magnetization vector M is perturbed by an RF pulse, it will take a certain amount of time until it has recovered back to its equilibrium state (i.e., when the isochromats are fully relaxed). This recovery occurs exponentially with time and is characterized by the T_1 parameter, which can be thought of as the time it takes for the nuclei to recover 63 % of the longitudinal magnetization that was lost when the RF pulse was applied.

The T_2 parameter is a measure of how fast the transverse (perpendicular to B_0) magnetization decays (Fig. 1.4). It can be pictured by considering an isochromat immediately after an RF pulse, at which time the M vector has a large rotating transverse component, which can induce a current in an external pickup coil. After a short while, the intrinsic vectors that make up the isochromat will dephase and point in slightly different directions, resulting in a reduction of the rotating component of the M vector. After yet another while the

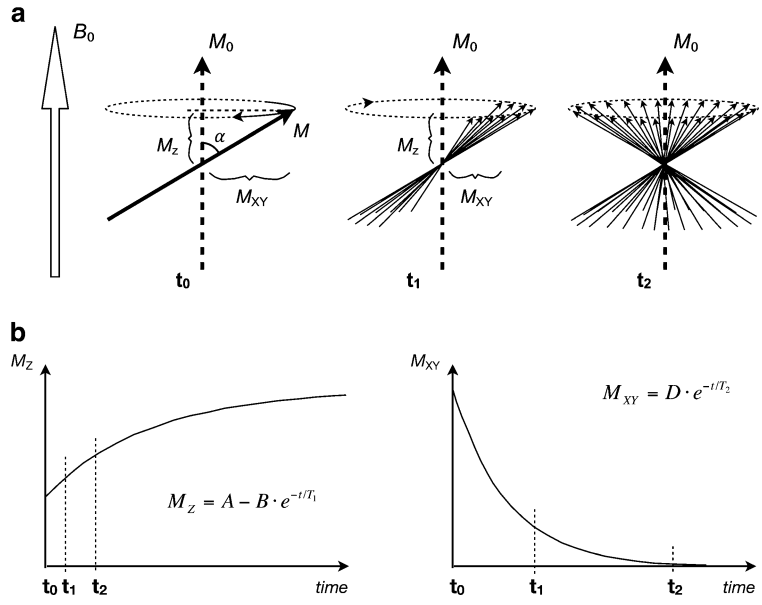

Fig. 1.4 (**a**) Immediately after an RF pulse (t_0) the magnetization vector M is perturbed from its initial M_0 direction by a flip angle α. M_z is the remaining longitudinal magnetization, which will eventually recover to back to M_0. At this point, the transverse magnetization component M_{xy} is time variant, allowing a signal to be induced in an external pickup coil. A short while later (t_1) the individual spinning nuclei that make up the M vector have dephased somewhat, resulting in a smaller time variant component M_{xy} and a decreased amplitude of the induced signal. After yet another while (t_2) the spinning nuclei have dephased totally, resulting in no time variant component at all. At this point, no signal will be induced in the external coil. The dephasing time is characterized by the T_2 parameter. (**b**) The longitudinal magnetization (*left*) recovers exponentially at a rate determined by T_1. The transverse magnetization (*right*) decays exponentially at a rate determined by T_2. The transverse magnetization always decays much faster than the longitudinal magnetization recovers. Time points t_0, t_1, and t_2 refer to illustrated states in (**a**)

intrinsic vectors are completely dephased, leaving no rotating component at all. This decline occurs exponentially with time and is characterized by the T_2 parameter, which can be thought of as the time it takes for the transverse magnetization to decline to 37 % of what it was immediately after the RF pulse.

Any individual nucleus is surrounded by millions of other nuclei. Since all nuclei possess some type of motion (Brownian motion, tumbling motion, etc.), the intrinsic magnetic vectors of all these nearby nuclei will summarize into a slightly fluctuating magnetic field that is superimposed onto the static B_0 field.

The component of this fluctuating magnetic field that is perpendicular to the B_0 field will reveal itself to the nuclei as an additional vector around which they will try to precess. Even though this vector is not strong enough to cause actual precession (as the B_0 and B_1 fields do), it is strong enough to affect the longitudinal relaxation behavior of the nuclei. Thus, this describes one of the primary effects determining the T_1 value.

The other component of the fluctuating magnetic field, parallel to the B_0 field, will add scalar to the B_0 field strength, causing a slight fluctuation of Larmor frequency between individual nuclei. This effect is one of the primary reasons for T_2 relaxation, since a variation in Larmor frequency for nuclei within an isochromat causes its compounding intrinsic magnetic vectors to dephase.

As can be understood, both the T_1 and T_2 relaxation times are determined by the combined characteristics of the fluctuating magnetic fields that are present within a sample. As such, there are no simple rules as to what the T_1 and T_2 values will be for a specific tissue. In general, the T_1 and T_2 values are dependent on what types

of bindings exist between hydrogen nuclei and their surroundings, as well as the mobility of the nuclei. For example, in very low-viscous fluids such as cerebrospinal fluid (CSF) the hydrogen mobility results in very long T_1 values (2,000–3,000 ms), whereas it is very short in fatty tissue (down to 100 ms) where the motion of the nuclei is much more restricted.

In a perfect measurement setup the signal picked up by the receiver coil would strictly follow the decay of the transverse T_2 magnetization, as is described above. However, in practice there are always local inhomogeneities in the applied B_0 field, causing additional variation in Larmor frequency between nuclei and thereby making the nuclei dephase faster than predicted by the T_2 value. These local inhomogeneities are a result of macroscopic effects, such as the technical difficulties of designing an absolutely homogenous magnet in combination with magnetic susceptibility variation between different tissue types. Compared to the mechanism governing the T_2 decay, these local inhomogeneities are static in the sense that they will not vary with time at a specific location. Thus, the dephasing caused by such local inhomogeneities can be reversed using refocusing RF pulses, which is described later in this chapter. The combination of T_2 decay and the decay caused by local inhomogeneities is usually referred to as T_2* decay.

Magnetic Field Gradients

In order to form images it is necessary to be able to differentiate between signals coming from nuclei in different parts of the subject. This is achieved using the gradient coils.

The gradient coils generate magnetic fields that are designed such that they vary in strength along their axis of operation (Fig. 1.5). When a gradient is switched on, its field will superimpose onto the static B_0 field. The total magnetic field strength will then be somewhat higher in one end of the investigated volume and somewhat lower in the other end. Hence, the Larmor frequency of the nuclei in the volume will also vary throughout

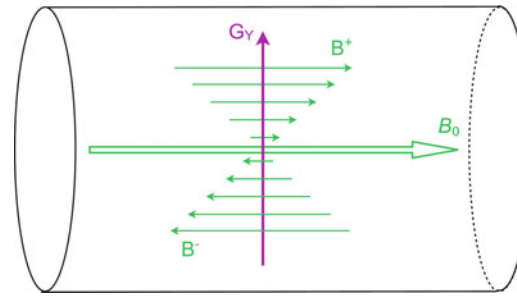

Fig. 1.5 In this figure the *y*-gradient (G_Y) is illustrated inside the MRI scanner, although the principle is the same also for the *x* and *z*-gradients. When the gradient is operated, its field (B^+ trough B^-) will add onto the static B_0 field, so that the total magnetic field is somewhat higher in the upper part of the bore and somewhat lower in the bottom part. Thus, the Larmor frequency of nuclei will vary depending on where they are located. The strength of the gradient can be arbitrarily adjusted by the MRI scanner

the different positions. This is the effect used to form images.

There are three sets of gradient coils in a clinical MRI scanner, generating magnetic field gradients in three orthogonal directions (*x*, *y* and *z* direction). The strength of each gradient can be arbitrarily adjusted by the MRI scanner. By combining these three gradient coils (i.e., running them simultaneously and at different strengths) apparent magnetic field gradients can be generated in any direction. There are typically three different ways to use the gradients for encoding spatial information:

1. Applying a narrow-band RF pulse while a magnetic field gradient is switched on will exclude all nuclei whose Larmor frequencies are outside of the RF pulse bandwidth, meaning that a specific section through the tissue can be selected for excitation. This is referred to as a spatially selective gradient. A slice-selection gradient is a commonly used spatially selective gradient.
2. Applying a gradient for a short while immediately after an RF pulse will create a difference in phase of signals emitted from nuclei at different positions. The phase can be thought of as a measure of how well the emitted signals are synchronized. This is referred to as a phase encoding gradient and the direction in which it

is applied is denoted the phase encoding direction.

3. Applying a gradient during acquisition of the signals will make nuclei at different positions emit signals with different frequencies. Such gradient is referred to as a readout gradient and the direction in which it is applied is denoted the frequency encoding direction.

Thus, by sampling the emitted signals and analyzing their phase and frequency spectrum, information about nuclei from different parts of the subject can be obtained. However, all information required to generate an image cannot be contained within just one sampled signal. Thus, the combination of gradients and RF pulses must be repeated many times, changing the phase encoding gradient slightly for each repetition, in order to obtain the information necessary to generate an image. Such combination of repeated gradients and RF pulses is denoted a pulse sequence and can be configured in a large number of ways in order to enhance the obtained image for different purposes. The execution time of a clinical pulse sequence typically ranges between 1 and 10 min.

When a pulse sequence is executed, the sampled signals together constitute a spatial frequency representation of the object, which can later be Fourier transformed into a real visible image. Such frequency representation is called a *k*-space image.

Gradient Echoes and Spin Echoes

As described earlier, nuclei that are perturbed by an external RF pulse will respond by generating an RF signal of their own (i.e., a FID). In order to use this signal for image formation it is necessary to first subject the nuclei to a series of magnetic field gradients, as signals originating from different parts of the tissue would otherwise not be distinguishable. Since these gradients have a duration in the order of a few milliseconds, the acquisition of signal is usually delayed from the RF pulse, leaving enough time for the gradients to be applied. This type of acquired signals is referred to as echoes, of which the two most commonly used types are the gradient echo and the spin echo.

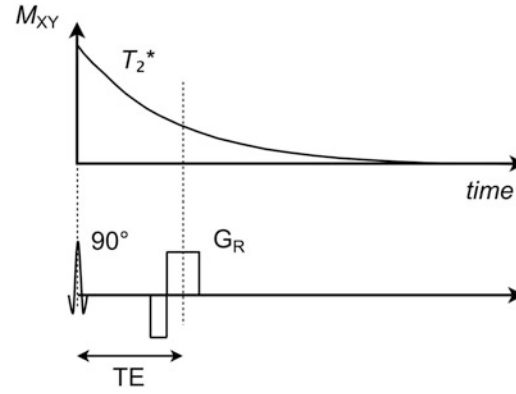

Fig. 1.6 Transverse magnetization (M_{XY}) during a gradient echo. An initial RF pulse generates a FID signal which decays according to the T_2* of the tissue. Immediately after the RF pulse a set of image-encoding gradients is applied, having a final readout gradient (G_R) during which the echo is retrieved. The echo time (TE) can be set arbitrarily and determines the amount of T_2*-weighting within the image

The gradient echo is the simplest type of echo as it basically only involves an excitation RF pulse followed by a set of gradients applied directly on the FID signal. These gradients can be configured in a variety of ways, although they are all characterized by having a final readout gradient during which the actual echo signal is retrieved (Fig. 1.6). The time that arises between the RF pulse and the echo is denoted the echo time (TE), which can be set arbitrarily with respect to the minimum time required for the gradients to apply. However, it should be noted that since the FID signal decays at the relatively fast T_2* speed, the echo time must be kept short (typically 2–20 ms) in order for the echo amplitude not to be unreasonably low. As a consequence, the echo time can be used to adjust how much impact the T_2* of the tissue will have on the echo amplitude and thereby also on the contrast within the resulting image.

A spin echo is characterized by being generated by two separate RF pulses after which an echo arises (Fig. 1.7). The first pulse perturbs the magnetization, resulting in a FID signal which will quickly decay due to T_2* dephasing effects. However, since T_2* is partially an effect of local inhomogeneities that are spatially and temporally static, its impact can be partly reversed by applying

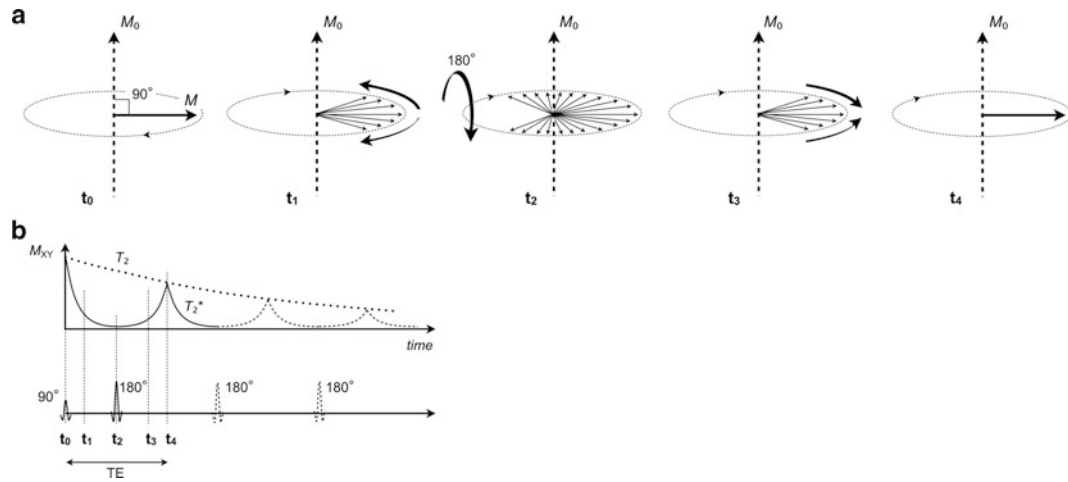

Fig. 1.7 Magnetization during a spin echo. (**a**) Shows the behavior of a set of excited nuclei while (**b**) describes the concurrent RF pulses and the echo signal. At time point t_0 a 90° RF pulse is applied, flipping the M vector perpendicular to its original direction. A FID signal is then emitted, which decays quickly due to T_2* effects (t_1). At time point t_2 a 180° refocusing RF pulse is applied, which reverses the direction by which the individual vectors move relative to each other, meaning that a rephase of the vectors will occur (t_3). At time point t_4 all individual vectors are in phase again and a spin echo occurs. After the spin echo the vectors will once again start to dephase. By adding more 180° RF pulses additional spin echoes can be induced (*dashed line* in (**b**)). The amplitude of successive spin echoes will decline according to the T_2 of the tissue (*dotted line* in (**b**)), since pure T_2 dephasing is not temporally and spatially static and will thus not be rephased

a refocusing RF pulse (typically a 180° pulse). Such a pulse will effectively flip all magnetization vectors upside down, meaning that any dephasing that has occurred due to local inhomogeneities since the first RF pulse will reverse and begin to rephase. At precisely twice the time between the two RF pulses, the magnetization will again be in phase and a spin echo will occur. Since all local inhomogeneity effects are canceled during this echo time, only the decay caused by the actual T_2 of the tissue remains. For this reason the echo time determines how much impact T_2 will have on the echo amplitude and the resulting image contrast. This is often utilized to adjust which tissues and pathologies are to be emphasized in the image.

Immediately after the spin echo, the magnetization will again start to dephase. By adding further RF pulses the magnetization can be refocused again, resulting in additional spin echoes. The amplitude of successive spin echoes will decay according to the T_2 of the tissue (Fig. 1.7b).

Compared to a gradient echo sequence, the echo time for a spin echo sequence can be much longer (since $T_2 > T_2$*) without unacceptable signal loss. As a consequence there are numerous possibilities to incorporate image-encoding gradients, which will be described more in detail later in this chapter.

As to which type of echo is preferred over the other depends on the situation and requested type of image. Spin echo sequences are much more robust and generate stronger signals than gradient echo sequences, since they do not suffer from T_2* losses and are less sensitive to disturbances in the magnetic field. On the other hand, spin echo sequences are often more time-consuming than gradient echo sequences, due to the additional refocusing pulse. For this reason, gradient echoes are usually preferred for three-dimensional high-resolution scans where acquisition time is an issue.

Image Acquisition

There are many different strategies for acquiring an MR image. An MR image can be either a two-dimensional (2D) image, which shows a slice through the subject in an arbitrary direction, or

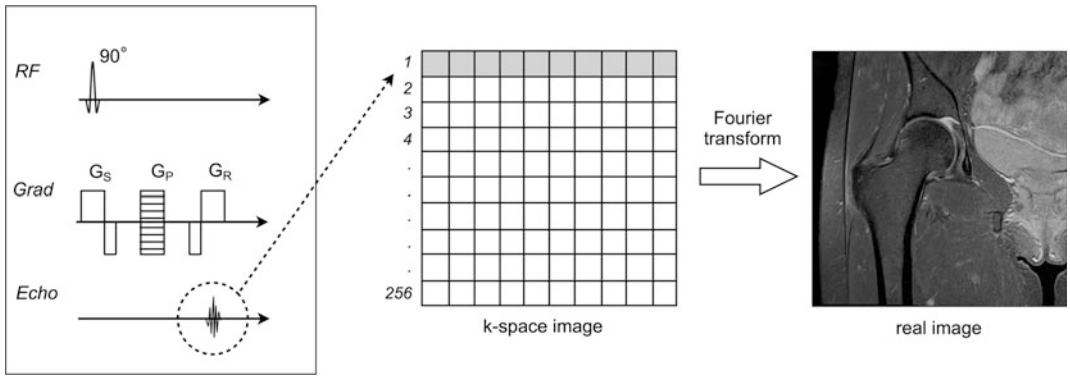

Fig. 1.8 A typical 2D pulse sequence. During the RF pulse a slice selection gradient (G_S) is turned in, which acts to make sure that only one slice of nuclei are excited by the RF pulse. Following the RF pulse a phase encoding gradient (G_P) is applied and during the echo a readout gradient (G_R) is on. The echo is sampled and stored as one line in the *k*-space image. This process is repeated, using different phase encoding, for all lines in *k*-space. When the *k*-space image is fully acquired it is Fourier transformed into a real visible image

it can be a three-dimensional (3D) image where an entire volume of image data is retrieved at once. A 3D sequence is basically constructed the same way as a 2D sequence. The main difference is that instead of just one phase encoding gradient, two such gradients are applied in different directions, in order to account for the spatial encoding of the additional dimension. An alternative to using real 3D imaging is to acquire several 2D images stacked next to each other, creating a so-called multi-slice image. This approach is common when only a few slices are required.

For both 2D and 3D images the number of repeated echoes that are required depends on the desired resolution of the final image. Most pulse sequences collect one full line of *k*-space data for each echo, often using a *k*-space image that is of the same size as the desired final image. For instance, if a 2D image of size 256 × 256 pixels is requested and each sampled echo constitutes one line in the *k*-space image, a total of 256 echoes are required to fill the entire *k*-space (Fig. 1.8). However, if instead a 3D image of size 256 × 256 × 64 is to be acquired a total of 256 × 64 = 16,384 echoes are required.

For this reason, high-resolution 3D images are best suited for use with echoes that can be generated quickly, such as gradient echoes, or the acquisition time might be unfeasibly long. Many techniques have been developed to speed up the acquisition process further, for example by generating multiple echoes following a single excitation pulse or by interleaving the acquisition of 2D slices such that several slices are acquired at once.

Image properties such as pixel size, slice thickness, and field of view can be set almost arbitrarily on an MRI scanner. Technically, these parameters are the result of gradient properties such as strength, duration and increment in combination with the RF pulse bandwidth. However, in any clinical MRI scanner the adjustment of this type of image properties is simplified such that the desired values can be directly typed on the scanner console, thereby letting the user disregard most of the technical details.

A recurring issue in MRI is that of noise in the acquired image. A common measure of noise in an image is the signal-to-noise ratio (SNR), which is high if the amount of noise in the image is low. Typically in MRI, both higher SNR and shorter acquisition time are required, which are parameters that are usually contrary to each other. Thus, the best balance between these parameters always needs to be found.

If the voxel size in an image is decreased fewer echo emitting nuclei will reside within each voxel. The image will then become noisier

and the SNR will be low. This can occur both as an effect of increasing the number of pixels or as an effect of decreasing the field of view. In case the SNR is unacceptably low this can be resolved by acquiring the same image several times, from which a mean image is calculated. This process is commonly known as averaging the image. Other ways of increasing the SNR includes using different types of RF coils or using other types of pulse sequences.

Image Contrast

In any MR image the resulting pixel intensity is a combination of T_1, T_2 (or T_2*), and proton density together with both acquisition parameters and technical parameters, including signal attenuation through the body and signal gain through coils and amplifiers. Thus, the absolute pixel intensities within an image are usually unpredictable and should not be considered when evaluating an image. Instead, it is the relative contrast between different tissues that is of interest in an MR image.

It is generally not possible to generate an MR image in which the image contrast depends on just one of the T_1, T_2, or proton density parameters (unless using a combination of different images, as is described later in this chapter). What is possible, on the other hand, is to adjust which of the parameters are of most impact. This is commonly referred to as weighting. In, for example, a T_1-weighted image, tissue with short T_1 will appear brighter than tissue with long T_1. However, in a T_2-weighted image the relation is opposite, as tissue with long T_2 will appear brighter than tissue with short T_2.

The amount of weighting is determined by the acquisition parameters in combination with the choice of pulse sequence. The two sequence parameters that are of primary interest in this context are the echo time (TE) and the repetition time (TR). As previously described, the echo time is the time between the initial excitation pulse and the generated echo. The repetition time is the time between the excitation pulses.

Table 1.1 The relations between echo time (TE), repetition time (TR), and image weighting

	Short TE	Long TE
Short TR	T_1-weighted	
Long TR	Proton density weighted	T_2 or T_2*-weighted

In a sequence where only one echo is generated per excitation pulse the repetition time is also equal to the time between successive echoes. In short, the relations between these parameters are described in Table 1.1.

The T_1 dependence is mostly determined by the repetition time. At each RF pulse some of the longitudinal magnetization is converted into an echo. The repetition time determines for how long the remaining longitudinal magnetization is allowed to recover before the next RF pulse is applied and the process is repeated. If the repetition time is very long, all longitudinal magnetization will have time to recover and the resulting echo signal will always be high, irrespective of its T_1 value. However, if the repetition time is relatively short, tissue having short T_1 will recover much more during this period than tissue with long T_1 (Fig. 1.9). This is the effect that is utilized to achieve T_1-weighting.

The T_2 dependence is mostly determined by the echo time. The longer the echo time, the larger the impact of T_2 decay (or T_2* decay for a gradient echo sequence) will be on the echo signal. For a short echo time the signal will always be high. However, if the echo time is reasonably long, tissue having short T_2 will experience more signal loss than tissue having long T_2 (Fig. 1.10). This is the effect used to achieve T_2-weighting.

By combining the behavior of the repetition time and the echo time, it is apparent that if both parameters are short there will be more T_1-weighting and less T_2-weighting. Likewise, if both parameters are long there will be more T_2-weighting and less T_1-weighting. Finally, if the repetition time is long and the echo time is short both T_1- and T_2-weighting will be minimized, leaving proton density as the primary contrast contributor.

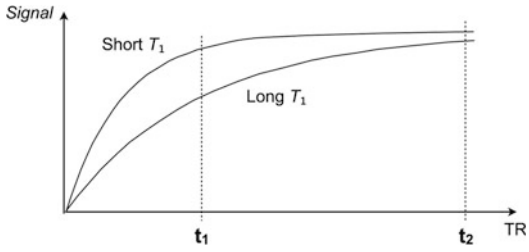

Fig. 1.9 The relation between echo signal and repetition time (TR) for tissues with two different T_1. A long TR (t_2) results in a high signal for both tissues. For a shorter TR (t_1) there is a large signal difference, which depends on the T_1 value. Note that if TR is too short there will be no signal at all

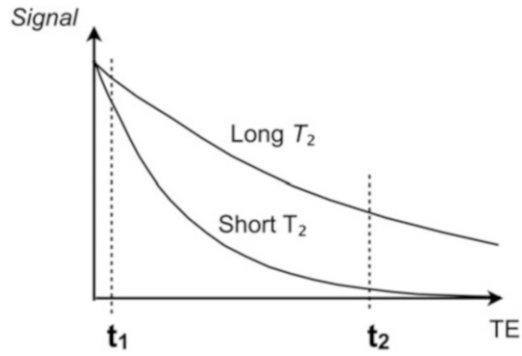

Fig. 1.10 The relation between signal and echo time (TE) for tissues with two different T_2. A short TE (t_1) results in a high signal for both tissues. For a longer TE (t_2) there is a large signal difference, which depends on the T_2 value. Note that if TE is too long all signals will have decayed to zero

Common Imaging Artifacts

An image artifact is any feature which appears in an image that is not physically present in the imaged object. Image artifacts are very common in MRI and can appear for a variety of reasons. Sometimes they are the result of improper operation of the scanner, while other times they are a consequence of natural processes or properties of the human body. It is important to be familiar with the appearance of artifacts since some artifacts can either obscure, or be mistaken for, pathology. As a result of this, image artifacts can lead to both false negative and false positive findings. A few of the most common types of image artifacts are described below.

Phase Wrap Artifacts

Phase wrap artifacts (also known as aliasing artifacts) occur when tissue that should be outside of the field of view suddenly appears within the field of view. The typical example is seen when tissue structures extend outside of the image on one side and then continues into the image again on the opposing side (Fig. 1.11). Depending on how the subject is positioned this may result in structures being imaged on top of each other. Phase wrap artifacts usually only appear in the phase encoding direction of the image.

A simplified explanation of these artifacts is given by picturing the phase encoding gradient when it is operating at a strength such that the phase of the signal is $-180°$ on one side of the field of view and $+180°$ on the other. Signal from nuclei that is positioned slightly outside of the field of view on one side will then have a phase that is slightly outside of this interval, for example $195°$. However, since $195°$ cannot be distinguished from $-165°$ (since $195°–360°=-165°$), such signal will be interpreted as if it was positioned within the field of view but close to the other side.

One solution when this type of artifact appears is to increase the field of view until no tissue extends outside it in the phase encoding direction. However, since this may not always be feasible other solutions include changing the phase encoding direction such that the problem is avoided or using saturation bands to suppress signal outside of the field of view (which is described later in this chapter).

Chemical Shift

Chemical shift misregistration artifacts appear as bright or dark outlines predominantly at the interface between fat and water. This type of artifacts appear since fat might be shifted a few pixels away from water within an MRI image. Due to different chemical surroundings of hydrogen, the Larmor frequencies are slightly different in water

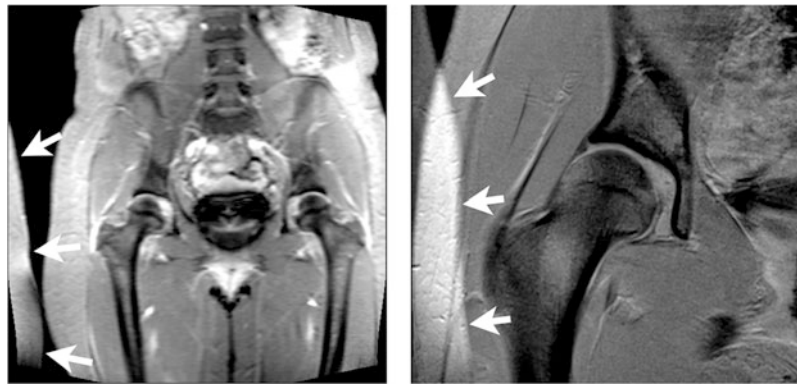

Fig. 1.11 The *white arrows* in the two images point at tissue that is physically located to the *right* of the image, but which appears within the image due to phase wrap artifacts. In the *right* image it can be seen that such artifacts may appear on top of actual structures within the image

and fat (225 Hz difference at 1.5 T). Chemical shift artifacts are an effect of this difference, since echoes having different frequencies will be interpreted as originating from different positions in the frequency encoding direction.

Thus, a dark band appears where fat and water are shifted away from each other (Fig. 1.12), whereas a bright band appears where fat and water are shifted to overlap. Once recognized, this type of artifacts can generally be disregarded when evaluating the images.

Motion Artifacts

Motion artifacts occur due to patient displacement during image acquisition and are often seen as bright noise or repeating densities in the phase encoding direction of the image (Fig. 1.13). Respiratory motion or patient movement are two common reasons for such displacement. Since an MRI scan has a typical duration in the order of minutes, a patient must remain very still in order to avoid motion artifacts. For patients in pain or disease this is sometimes very troublesome.

The artifacts can be explained by considering that many echoes are required to generate an image. Thus, motion that occurs between these echoes will distort the *k*-space information and cause errors in the final image. Motion artifacts are typically distinguished from other types of artifacts in that they extend across the entire field of view.

Flow Artifacts

Movement of body fluid in MRI can produce several types of artifacts. As the most prominent flow in the body is that of blood, image artifacts are possible whenever a large blood vessel appears within the imaging plane (Fig. 1.14).

Some of these artifacts arise from the location change that the flowing hydrogen nuclei experience during the image-encoding gradients. Since the hydrogen nuclei in the blood are moving through these gradient fields, the effect of the gradients on these nuclei will not be the same as on nuclei in stationary tissue. Thus, image encoding of signal from blood may be incorrect. Furthermore, since the pulsation of the blood flow is usually asynchronous to that of the pulse sequence repetition time, these effects may differ between *k*-space lines. The resulting image artifacts are often of similar character as motion artifacts (although more localized and not as severe).

Flow artifacts can be reduced, for example, by changing the phase encoding direction or by applying saturation bands (described later in this chapter) to suppress signal from blood vessels outside of the field of view. Specialized gradients can sometimes also be applied, designed to compensate for blood flow.

Fig. 1.12 Image of the knee joint. Within the bone marrow are large amounts of fat, which is what provides the primary signal within the bone. Thus, a chemical shift artifact can appear between the bone and the surrounding tissue, which is seen in the image as a black band between bone and cartilage on the femoral side

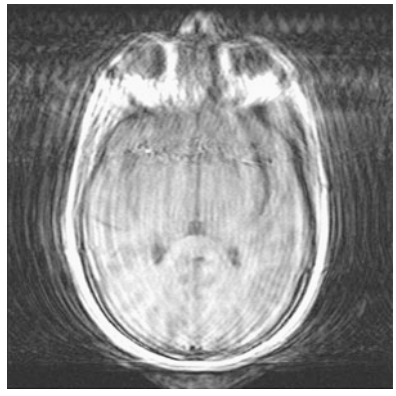

Fig. 1.13 MRI image of the brain. Severe motion artifacts are seen in the horizontal direction of the image

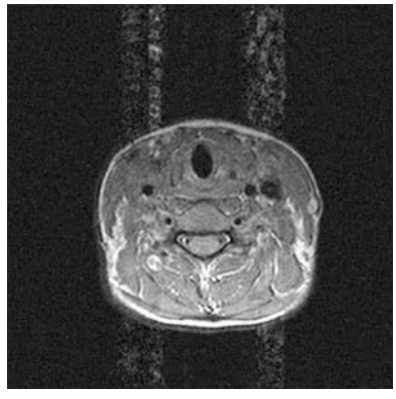

Fig. 1.14 Gradient echo image of the neck with vertical flow artifacts associated with the carotid arteries

Common Imaging Techniques

On a clinical MRI scanner there are typically dozens of different pulse sequences and imaging techniques to choose from, each of which generates images that have different characteristics in terms of acquisition time, signal-to-noise, and image contrast. Some sequences are very similar to each other, while others are more unique. Which pulse sequence should be used depends on the particular application, which is why it is important to understand the different characteristics in order to both request and interpret MRI images. In this section a few of the most frequently used pulse sequences and imaging techniques are described.

Inversion Recovery

Inversion recovery pulse sequences are often used to suppress signals, typically from fat or free fluid, based on their T_1 values. The ability of doing this is valuable in situations when a certain tissue type would otherwise be obscured due to a high fraction of fat or free water in the same local region. In this type of sequence a 180° inversion pulse is applied prior to the excitation pulse. By adjusting the inversion time (TI) between these two pulses, the T_1 values to suppress are decided (Fig. 1.15).

When the inversion pulse is applied all available longitudinal magnetization is inverted, typically from a positive to a negative value. At that time, the longitudinal magnetization will start to recover back towards its positive max value at a speed determined by its T_1 value. Since this recovery starts at a negative value and works its way towards a positive value, it must at some point pass through zero. By setting the inversion time such that the excitation pulse occurs precisely at this time point, any signal from tissue with this specific T_1 value will be effectively nulled.

Provided that a region contains two or more tissue types with different T_1 values, the inversion time can be adjusted such that the signal from one of these tissues is heavily suppressed while the signal from other tissues remains to generate an image. An inversion recovery sequence in which

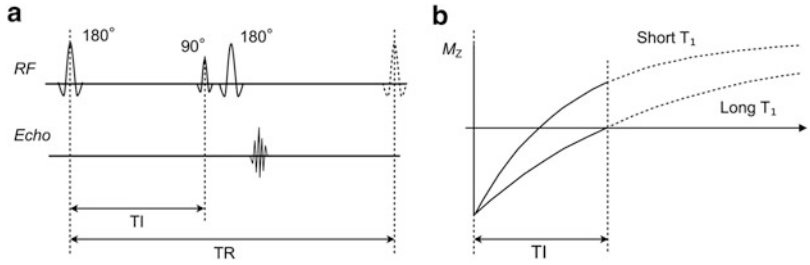

Fig. 1.15 Diagram of an inversion recovery spin echo pulse sequence. Following a 180° inversion pulse, a set of 90° and 180° pulses are applied from which a spin echo is generated (**a**). The inversion pulse and the 90° pulse are separated by an inversion time (TI) during which the longitudinal magnetization recovers (**b**). By adjusting the inversion time appropriately, this recovery can be set such that the signal of tissues having certain T_1 values is effectively nulled, whereas tissues having other T_1 will still yield a usable signal (**b**)

fat is suppressed is often referred to as a STIR sequence (short TI inversion recovery), whereas an inversion recovery sequence where free fluid is suppressed is referred to as a FLAIR sequence (fluid attenuated inversion recovery).

Multiple Spin Echo

A common technique for speeding up the acquisition of a spin echo image is to generate multiple echoes following each single 90° excitation pulse. The technique also goes by several vendor-specific labels, including turbo spin echo (TSE), fast spin echo (FSE), and rapid acquisition with refocusing echoes (RARE).

In a conventional spin echo sequence, a 90° RF pulse is followed by a 180° pulse, after which an echo is generated and encoded to one line in *k*-space. Following the echo a relatively long wait period is applied, until the next 90° pulse. In a multiple spin echo sequence, the echo is instead followed by additional 180° pulses which will refocus the magnetization into additional echoes (cf. Fig. 1.7). Each such echo is generated with a different phase encoding gradient and is assigned to its own line in *k*-space, which can result in a drastically reduced acquisition time (a 256 × 256 scan in typically 30–60 s) compared to the conventional spin echo sequence.

The length of the echo train can be set arbitrarily, although it must be understood that the signal will be decreased between subsequent echoes according to the T_2 value of the tissue. This may result in edge blurring, especially for very long echo trains. In practice, the echo train is usually set at around 5–20 echoes depending on how the image is weighted.

Fast Gradient Echo Sequences

In 3D imaging, gradient echo sequences with short repetition time and low flip angle excitation pulses are often used, as they allow fast acquisition of high-resolution images (a 256 × 256 × 100 scan in typically less than 5 min). This type of images is usually T_1-weighted. Many variations of these sequences exist, which all go by different vendor-specific labels such as fast low-angle shot (FLASH), spoiled gradient echo (SPGR), or fast field echo (FFE).

Since the excitation pulses are typically 5°–30°, only a fraction of the available longitudinal magnetization is lost at each pulse. Due to this, the repetition time can also be kept very short, since not very much magnetization needs to be recovered between pulses. While the advantage of this approach is high acquisition speed, the downside is weaker signal from the echoes and thereby noisier images.

Fast gradient echo imaging is sometimes combined with other techniques, such as a preparatory inversion pule. In such configuration certain features of the inversion recovery sequence can be inherited to the fast gradient echo sequence.

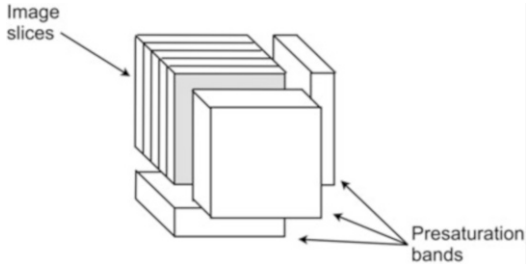

Fig. 1.16 Presaturation bands placed to the *right*, below, and in front of the imaging slices

Presaturation Bands

Presaturation is a method for removing unwanted signal from a specific location. It is particularly useful for reducing phase wrap artifacts and for minimizing artifacts from blood flowing into the image area.

The idea is that a spatially selective 90° pulse is applied which is set to only target a specific region within the body (Fig. 1.16). Immediately after the pulse, the nuclei within this region are said to be saturated since all their longitudinal magnetization is temporarily nulled. By applying such saturation pulses to specific regions immediately before an actual imaging sequence, the lack of longitudinal magnetization will result in no echo signal being generated from these regions.

In situations when it is not feasible to avoid the presence of tissue outside the image in the phase encoding direction, presaturation bands provide a possibility to generate images that are not obscured by phase wrap artifacts. Likewise, when the presence of large blood vessels within an image is unavoidable, presaturation bands can be used for saturating the blood prior to entering the image area, thereby suppressing any signal that would be emitted by the flowing blood.

Quantifying T_1

In certain types of examinations it is of interest to generate images in which each pixel represents the actual T_1 value of the corresponding tissue volume. Such images are generally referred to as T_1 maps. As mentioned previously in this chapter it is not possible to directly generate T_1 maps from an MRI pulse sequence. Instead, T_1 maps can be calculated from a set of two or more images that are acquired using slightly different parameters.

There are several image types that can be used for T_1 quantification, each of which has its own pros and cons in terms of accuracy and acquisition time. In this section two of the most commonly used T_1 quantification methods are briefly described.

2D Inversion Recovery T_1 Quantification

One of the most accurate and stable methods to generate a T_1 map is to use a set of inversion recovery images acquired using different inversion times [4]. This method is generally very stable and usually results in correct T_1 values even if not all parameters are perfectly optimized. The disadvantage is its long acquisition time, which is why this method is only suitable for 2D acquisitions. A 256 × 256 pixel T_1 map is typically acquired in about 5 min.

Commonly, a set of about six inversion recovery images are acquired using inversion times that are spread over an interval larger than the T_1 values of interest (frequently used inversion times are 50, 100, 200, 400, 800, and 1,600 ms). All other parameters, including image position, should be the same for all images.

Consider a specific pixel in each of these six images. As can be understood from Fig. 1.15b the value of this pixel will depend both on its T_1 value and on the inversion time at which it was acquired. The higher the inversion time is, the more magnetization will have had time to recover at the time of the excitation pulse.

The next step is to plot each of these six pixel values in a diagram (Fig. 1.17). As can be seen they will form the shape of a longitudinal recovery curve. Since the equation for this recovery is known, a curve-fitting algorithm can be used to find the T_1 value which generates that particular shape of the curve. Thus, the T_1 value of that specific pixel is calculated. By using computer

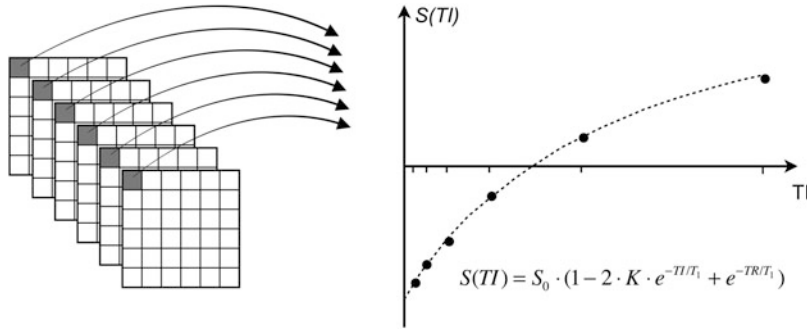

Fig. 1.17 A set of inversion recovery images is acquired using different inversion times (TI). Each same pixel at each TI is then plotted in a diagram where it can be seen that the values follow the longitudinal recovery curve. By fitting these values to the known recovery equation the T_1 value for the pixel is retrieved

software that repeats this process for each pixel, the entire T_1 map is calculated.

3D Dual Flip Angle T_1 Quantification

The dual flip angle T_1 quantification method is common in applications where acquisition of 3D T_1 maps is required. With this method T_1 is quantified using two or more successive fast gradient echo sequences applied with different excitation pulse flip angles. Consequently, 3D dual flip angle T_1 maps can be generated very rapidly using standard 3D gradient echo sequences [5]. A $256 \times 256 \times 100$ voxel T_1 map is typically acquired in less than 10 min.

In a spoiled gradient echo sequence, the longitudinal magnetization is stabilized at a level where exactly as much magnetization is recovered between pulses as is lost at each pulse. This is denoted the longitudinal steady state level and is dependent on a number of parameters, including the T_1 value. Thus, by running the same gradient echo sequence twice, with all parameters equal except the flip angles, a set of equations can be set up from which the T_1 value is solved.

For the dual flip angle method to perform optimally, the flip angles must be selected with regard to the T_1 value to measure. For any T_1 value and repetition time there will be a specific flip angle, denoted the Ernst angle, at which the signal from a gradient echo sequence has a maximum. It has been shown that the optimal flip angle combination for a dual flip angle T_1 measurement is the two flip angles for which the signal is 71 % of that at the Ernst angle (Fig. 1.18) [6]. With this flip angle combination the calculated T_1 values will be least sensitive to any acquired noise.

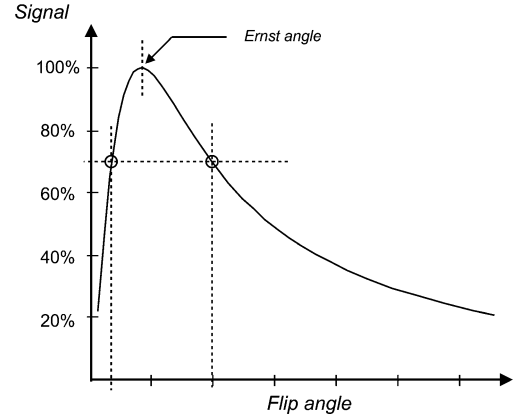

Fig. 1.18 Steady state gradient echo amplitude as a function of the excitation pulse flip angle, for some arbitrary T_1 and TR. The optimal flip angle combination for T_1 mapping is marked with *circles*

The dual flip angle method requires accurate knowledge about the flip angles of the comprised gradient echo sequences in order for the T_1 values to be correctly calculated. The most widely used way of achieving this is to simply assume that the nominal flip angles, as specified in the user interface of the scanner, are sufficiently accurate and

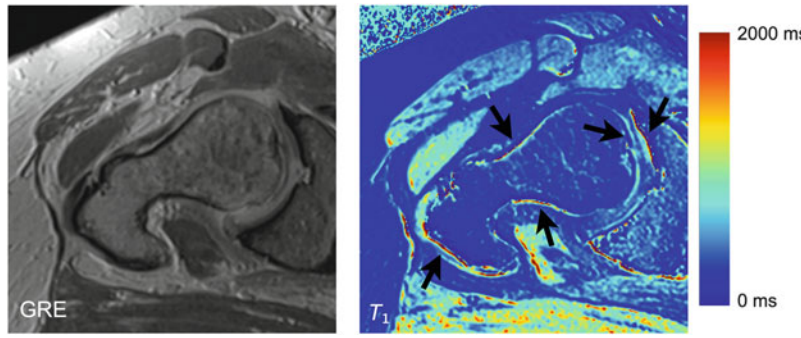

Fig. 1.19 Right image is a T_1 map covering the femoral head and neck. *Left* image is one of the gradient echo images from which the T_1 map is calculated. The *black arrows* in the *right* image point out artifacts due to patient movement, which appears as narrow bands of extremely high or extremely low T_1 values along the bone structures

use them for T_1 calculation. However, there are a number of effects that may be hard to predict which can cause the actual flip angle to deviate severely, resulting in erroneous T_1 calculations. Especially at high magnetic field strength (i.e., 3 T), these effects may cause unacceptable errors [7].

This type of errors can be corrected for if the accuracy of the flip angle is measured at different positions within the field of view. Such measurement is commonly known as a B_1 map, which can be calculated using an additional pulse sequence specifically designed for this purpose [8]. This type of additional B_1 mapping sequence typically will add a few minutes of scan time, which is usually time well spent, considering the gained T_1 mapping accuracy.

Since T_1 maps are calculated from a combination of several images, the accuracy of the T_1 calculation is highly sensitive to patient movement between the different images. This is true for all types of T_1 measurements, although it is of particular importance for dual flip angle T_1 maps since those are calculated from only two images. Errors due to patient movement are sometimes very hard to notice. For a dual flip angle T_1 map such errors are often seen as narrow bands of extremely high (>2,000 ms) or extremely low (<100 ms) T_1 values that appear along the borders of different structures (especially bone structures, Fig. 1.19). If such artifacts are seen, new T_1 maps must be generated. This can be done either by reacquisition of the images or, in some circumstances, by just recalculating the T_1 maps after registering the existing images.

References

1. Mitchell DG, Cohen MS. MRI principles. 2nd ed. Philadelphia, PA: Saunders; 2004.
2. Bernstein MA, King KF, Zhou XJ. Handbook of MRI pulse sequences. London: Academic; 2004.
3. Haacke EM, Brown RW, Thompson MR, Venkatesan R. Magnetic resonance imaging: physical principles and sequence design. New York: Wiley; 1999.
4. Gupta R, Feretti J, Becker E, Weiss G. A modified fast inversion-recovery technique for spin–lattice relaxation measurements. J Magn Reson. 1980;38:447–52.
5. Brookes JA, Redpath TW, Gilbert FJ, Murray AD, Staff RT. Accuracy of T1 measurement in dynamic contrast-enhanced breast MRI using two- and three-dimensional variable flip angle fast low-angle shot. J Magn Reson Imaging. 1999;9(2):163–71.
6. Deoni SC, Rutt BK, Peters TM. Rapid combined T1 and T2 mapping using gradient recalled acquisition in the steady state. Magn Reson Med. 2003;49(3):515–26.
7. Siversson C, Chan J, Tiderius CJ, Mamisch TC, Jellus V, Svensson J, Kim YJ. Effects of B1 inhomogeneity correction for three-dimensional variable flip angle T1 measurements in hip dGEMRIC at 3 T and 1.5 T. Magn Reson Med. 2012;67(6):1776–81.
8. Stollberger R, Wach P. Imaging of the active B1 field in vivo. Magn Reson Med. 1996;35(2):246–51.

Non-contrast Biochemical Imaging

2

Stephan Domayer, Sebastian Apprich, Benjamin Schmitt, Oliver Bieri, and Siegfried Trattnig

Introduction

Much of the difficulty in studying OA and the efficacy of interventions is due to the current limitations in the use of plain radiographs, which are currently deemed the gold standard for noninvasive assessment of clinical OA. Often, changes such as joint space narrowing or formation of osteophytes, which can be detected on radiographs, manifest at late stage [1], when disease modifying therapies including surgery and/or drug treatment may already be ineffective. Sensitive techniques that could detect early OA and reliably monitor its progression would help to identify patients who may benefit from joint preserving interventions, to reduce the number of patients requiring arthroplasty or at least delaying the need of total hip arthroplasty (THA). In addition, the identification of patients who are likely to progress rapidly would be particularly useful when designing clinical trials. Therefore, an early diagnosis of cartilage degeneration and a sensitive, noninvasive diagnostic tool are highly desirable.

In morphologic images, the signal intensity of each pixel results from a vast number of both intrinsic and extrinsic factors. The principle extrinsic factors are field strength, magnetic field homogeneity and the general hard- and software setup of the MR scan. The principle intrinsic parameters in clinical imaging are T1, T2, and proton density, which has led to the terms T1-, T2-, and proton-weighted images.

The basic principle of biochemical MR imaging is that single intrinsic parameters of the cartilage tissue are assessed by the use of dedicated sequences. This allows for a more specific description of the tissue, as distinct MR parameters directly correspond to specific properties of the cartilage tissue.

For these reasons, there is a topical interest in advancing non-contrast biochemical imaging techniques sensitive to changes at the molecular level of articular cartilage, such as T2 mapping, T2* mapping, T1 rho, diffusion-weighted Imaging (DWI), CEST, or Sodium. A number of studies showed very promising first results over the recent years for quantitative, non-contrast cartilage MR imaging for early detection of cartilage degeneration. However, owing to the availability of high-quality knee coils the majority of work was based on the knee joint cartilage. With a few exceptions, literature reporting on the feasibility of quantitative "biochemical" non-contrast MR imaging of the hip joint is lacking. As the hip joint cartilage is a relatively thin and curved structure, it makes great demands on the investigator and the available hardware and sequences for valid imaging. Existing evaluation methods suffer from insufficient spatial resolution, prolonged acquisition times, and low signal-to-noise ratio (SNR). New 3.0 T and 7.0 T magnetic

S. Trattnig (✉)
Department of Radiology, Medical University of Vienna, Währinger Gürtel 18-20, Vienna 1090, Austria
e-mail: siegfried.trattnig@meduniwien.ac.at

Y.-J. Kim (eds.), *Hip Magnetic Resonance Imaging*,
DOI 10.1007/978-1-4614-1668-5_2,

resonance scanners have decreased the scan time by a factor of 2–3, improved the SNR, the spatial resolution, and allow thinner slice thickness. With concurrent improvement in coil-technology and optimization of imaging protocol, quantitative MR imaging has a high potential for future human in vivo imaging and may overcome the present restrictions in imaging of the hip cartilage.

T2 Mapping

The spatial variation of T2 values across cartilage was first reported in 1989 [2]. In normal cartilage, T2 shows a subtle decrease from the subchondral lamina to the deep layer, and subsequently a steady increase towards the surface.

Several aspects contribute to this phenomenon. In the deep zone, the collagen fibers run anisotropically perpendicular to subchondral bone; there is a reduced mobility of water protons, and therefore reduced T2 relaxation time values. In the superficial zone, the collagen fibers are randomly oriented which leads to an increase of T2 values from the deep to superficial zone in normal hyaline cartilage.

Additionally, the dipolar coupling of collagen-associated water is minimum at 54.7° to the static magnetic field, which leads to increased T2 (magic angle effect) [3–5]. This phenomenon depends on the orientation of the cartilage to the static magnetic field, and therefore is an extrinsic factor that can substantially alter T2 measurements.

Free water leads to a prolongation of T2 in general; as a consequence, a loss of proteoglycan content and subsequently increased water is deemed to lead to increased T2 in cartilage.

Several investigators have explored the relevance of these factors for T2 of cartilage particularly with regard to the magic angle effect.

Grunder et al. [6] reported a 300 % increase of T2 when the sample was oriented at 55° to the magnetic field in an in vitro setting at 7.1 T. Mosher et al. [7] evaluated the relevance of this phenomenon for in vivo T2 measurements in the knee in a clinical setting. They found that the magic angle effect contributed less than expected to variations in T2. When oriented at 55°, T2 increased 8.6 % at a normalized distance of 0.3 from the bone 18.3 % at 0.6, and 29.1 % near the surface. However, at all orientations the zonal variation of T2 was clearly present. In conclusion, the increase of free water in the superficial zone during the absence of compression and conversely, a decrease of T2 of the superficial layer under compression was deemed to be more accountable for regional differences of T2 (especially joint loading areas versus the posterior femoral condyle) than the orientation to the magnetic field. They concluded the magic angle effect was unlikely to account for significant regional differences in clinical imaging. Nieminen et al. [3] compared polarized light microscopy and optical density of safranin O analysis with T2 in order to evaluate the morphologic parameters that determine T2 and concluded that proteoglycan content does not contribute significantly to T2, but that free water collagen content and the architecture of the collagen fibers are reflected in T2.

As a consequence, T2 mapping has found widespread application in in vivo MRI studies on osteoarthritis. Based on the hypothesis that the loss of proteoglycan will result in an increase of free water, increased T2 was expected to be a marker for osteoarthritis. However, there is data demonstrating unchanged T2 or decreased T2 in degraded cartilage in vitro and in clinical T2 images [2]. A possible explanation is the creation of collagen cleavage sites in the course of degradation that interact with free water, decreasing T2.

A moderate relationship between age and T2 of the cartilage layer has been reported [8]; however, the range of individual cartilage T2 is such that no predictive value can be deduced at this time.

In contrast, the technique has proven immensely useful for the assessment of surgical cartilage repair techniques. A basic condition for cartilage repair is that the adjacent articular cartilage is intact. Under this assumption, T2 values of repair tissue can be compared to healthy cartilage in each patient, which substantially differentiates the application of T2 in cartilage repair from monitoring OA.

A horse model study by White et al. [4] demonstrated that normal hyaline cartilage and cartilage repair tissue could be differentiated by zonal T2 mapping. Arthroscopic osteochondral autograft transplantation (OAT) and MFX were performed and evaluation of zonal T2 variation showed a characteristic distribution across the depth of the cartilage in control and OAT sites, with low T2 values near the subchondral bone and higher T2 values near the cartilage surface [4]. In contrast, no zonal variation was found within MFX repair tissue. Correlation with histology and collagen structural anisotropy as assessed by polarized light microscopy demonstrated a near perfect specificity of T2. OAT and normal hyaline cartilage sites illustrated a normal zonal collagen organization, whereas MFX showed disorganized fibrous reparative tissue [4].

Using quantitative global T2 mapping of patients at different postoperative intervals after MACT surgery, significantly higher T2 values were found in cartilage repair tissue in the early stage (3–13 months) after surgery in an intra-individual comparison with native hyaline cartilage [9]. Furthermore, a decrease in repair tissue T2 values was observed over time, with the T2 values becoming similar to native healthy cartilage. This finding was in agreement with a study by Kurkijarvi et al. [10] who reported T2 of the repair tissue and normal hyaline in the range of 60 and 50 ms at 1.5 T, respectively, in 10 patients at 10–15 months after ACI surgery. The zonal variation of repair tissue [9] has been demonstrated by the analysis of the T2 line profiles showing the variation of T2 values from the subchondral bone to cartilage surface. With increasing postoperative interval the shape of the T2 line profiles (and the calculated T2 line profile values) was found to become similar to the reference healthy cartilage sites [9]. A direct comparison of cases after MFX and after MACT in the knee has demonstrated that MFX yields repair tissue with significantly lower T2 than MACT; significant differences could be demonstrated in terms of the degree of zonal variation. Whereas there is no spatial variation of T2 in MFX repair tissue, a subtle increase was found after MACT, albeit not comparable to the native adjacent cartilage [11]. With regard to the inherently large variation of T2 among individuals, it has proven to be useful to describe the T2 properties of the repair tissue relative to the adjacent reference cartilage. The relative T2 relaxation time (rT2) is calculated from the global T2 values (rT2 = T2 of repair tissue/T2 of reference cartilage) [5].

A direct correlation of rT2 and the clinical outcome showed there was a relationship between the repair tissue T2 properties and the clinical outcome. Cases that have repair tissue with T2 properties that are equal to the reference are more likely to do well.

The technique could be transferred to the ankle, albeit with limitations. Due to the thin cartilage layers of the ankle, it was not feasible to optimize the protocol for a zonal assessment of the cartilage layers. However, it was possible to assess rT2 after MFX and after MACT of the ankle. rT2 was 1.00 ± 0.20 (0.72–1.36) in a series of 14 cases after MFX and 0.85 ± 0.21 (0.49–1.26) in a series of 8 cases after Hyalograft C, and in another series of 12 cases after MACT rT2 was 1.05 (50.1 ± 8.0 ms in the RT and 47.6 ± 9.3 ms in the reference cartilage) [12–14]. Other than in the knee, the water and collagen content was similar to the reference cartilage after both treatment modalities. It should, however, be noted that a zonal analysis was not feasible at 3 T, mainly due to the lower SNR. A subsequent study at 7 T demonstrated that other than in the knee, MFX of the ankle results in organized RT and may be particularly suited for the treatment of cartilage defects of the ankle, as there was a significant increase of T2 towards the surface in the repair tissue (OAC 7T).

Methodological Considerations

Spin echo imaging with separate acquisitions for each TE is considered the gold standard for T2 measurement, but it is not feasible in clinical routine due to acquisition time. Multislice multiecho spin echo (MESE) sequences provide faster imaging, but there are some aspects to be considered with regard to accuracy.

Multislice imaging requires slice-selective refocusing pulses that will produce transitional regions at slice boundaries. Resulting imperfect refocusing and therefore stimulated echo contribution in fast spin echo introduce mixed T1 and T2 contrast to the image. A detailed comparison of a single echo spin echo with a multiecho spin echo sequence in agarose phantoms with T2 values in the range of articular cartilage and differing T1 values at 1.5 T [15] yielded an error of 10 % that increased with longer T1 as the later echoes had increased signal due to the stimulation by the imperfect refocusing pulses. When the first echo was dropped from the curve fitting, the error decreased considerably to 0.3–5.2 %; elimination of the first pulse improved T2 accuracy because the decay rate of mixed T1/T2 was similar to pure T2. Still, a comparison in volunteers showed the error was still between −11.6 and 16.9 %. Even though the qualitative T2 pattern of cartilage was comparable with the different sequences, absolute T2 differed considerably.

Furthermore, magnetization transfer contrast created by refocusing pulses for other slices diminishes signal intensity in cartilage and can thus impair the accuracy of T2 measurement [15]. Additional factors that may affect T2 quantification are field inhomogeneities and insufficient sampling of the T2 decay curve [16].

A comparative phantom study by Pai et al. [16] at 3 T regarding sequence-dependent T2 quantification yielded the MESE sequence had the best accuracy; however, the measures in volunteers confirmed an increase in T2 measured by MESE compared to SE T2 in accordance with Maier et al.. With regard to the phantom study, the authors concluded that rather a T2 underestimation of the SE than an overestimation by the MESE was found in cartilage.

Regarding the reproducibility of T2, coefficients of variance in the range of 0.1–2.8 % in phantoms and 5.3 % in cartilage have been reported for a MESE sequence; a comparison with the other sequences showed that the average coefficient of variance was lowest in the MESE (1.3 %). In other volunteer studies, the relative precision errors for T2 are reported to range between 2.76 and 5.37 % at 1.5 T, and a further comparison of T2 mapping at 1.5 T and 3 T demonstrated comparable coefficient of variation at either field strength in the same resolutions, suggesting good discriminatory power of the technique [17, 18].

Regarding the magic angle effect, there remains considerable uncertainty regarding its influence on absolute T2. At least in cartilage repair assessment the phenomenon can be considered in the ROI analysis by comparing the repair tissue to a reference area with the same orientation to the static magnetic field.

In summary, a considerable error of absolute T2 values has to be expected when using different T2 mapping protocols. This can be aggravated by the use of different coils, and obviously, T2 values obtained at different field strengths cannot be compared. Additionally, there seems to be a large variability of T2 in healthy cartilage. It is therefore unlikely that thresholds can be defined to distinguish between normal cartilage and OA. The strength of the technique lies in the assessment of the zonal collagen network organization of cartilage and cartilage repair tissue.

T2* Mapping

Within a clinical imaging protocol, T2 mapping is still limited. The long echo trains of to the spin echo technique, needed to accurately characterize the cartilage T2 decay curve, contribute to prolonged acquisition times (TA), typically exceeding 10 min for complete coverage of full joints. The 2D-acquisition precludes reformatting the data into 3D surface maps and requires reliable positioning to achieve reproducible results. Furthermore, the inherent variability in the 180° refocusing pulses leads to errors in T2 estimates as a result of the contribution from simulated echos and magnetization transfer [19].

T2* relaxation time mapping, based on a non-contrast gradient-echo (GRE) sequence, might be an alternative biochemical marker. This technique combines the potential of short scan time

and high isotropic resolution of thin cartilage layers due to high signal-to-noise ratio and three-dimensional (3D) imaging. This is especially important concerning the complex hip joint with its curved surface and thin cartilage. In morphological MRI studies, radial evaluation of the hip cartilage in a clockwise manner from anterior to posterior and perpendicular around the femoral neck has become the gold standard for hip imaging. Isotropic 3D T2* data sets and the capability of multi-planar reconstruction allow for quantitative evaluation in the same manner [20].

In contrast to standard T2-weigted spin echo techniques, 3D-GRE-sequences lack the 180° refocusing pulse. As a consequence, time-independent inhomogeneities of the external magnetic field ($B0$) and intrinsic factors like susceptibility artifacts contribute to a faster dephasing of the spins, resulting in an overall signal decay that is faster than described by T2 (T2*).

The T2* relaxations time is related to T2 as follows: $1/T2^* = 1/T2 + \gamma \Delta B0$ where y represents the gyromagnetic ratio and $\Delta B0$ defines the difference in strength of the locally varying field. Assuming the applied static magnetic field ($B0$) is uniform and constant over the region of interest, then T2* will be influenced by both the transverse relaxation (T2) and by the local susceptibility fields. Such local fields can operate at the macroscopic level, i.e., at the bone–cartilage interface, or at the microscopic level associated with the underlying microstructure of proteoglycans and collagen fibers within the cartilage. The lack of radiofrequency refocusing pulses substantially decreases the contribution of magnetization transfer to cartilage contrast, and thus, may lead to differences in sensitivity of T2* and T2 to changes in the collagen content in cartilage.

Typical T2* mapping sequences for the cartilage use 6–8 TE's in the range of 5–50 ms to measure the T2* decay. Subsequently, T2* maps are generated ideally throughout an inline processing package, which utilizes a nonlinear least square fitting routine, to avoid time-consuming post-processing.

A further important point which should be considered within a setting of clinical studies is the placement of the T2/T2* mapping sequence at the end of the MR-protocol. Related to T2 mapping studies with unloading of the knee joint [21, 22], a recent study on T2* mapping of the hip joint has shown the effect of rehydration of the cartilage to be of crucial importance for designing an MR-protocol in patients with FAI [23].

A limitation of T2* mapping within a clinical setting is the application of this technique in the presence of metallic particles as a result of surgery due to the greater sensitivity to susceptibility-included artifacts. Another factor that must be considered, in particular when assessing the spherical shape of the hip joint cartilage, is the magic angle effect. It is characterized by an increase of T2 (and therefore T2*) values when the cartilage is orientated at ~56° to the main magnetic field and the dephasing effect of parallel-oriented dipolar interactions of protons in water molecules binding to collagen is minimized. However, the dependency of T2* on collagen fiber orientation has to be systematically evaluated in future studies on articular cartilage.

In theory, injury to the calcified cartilage zone, or changes in the cartilage microstructure could lead to changes in the magnetic susceptibility of the tissue that could be exploited using T2* mapping.

Chemical Exchange Saturation Transfer

Chemical exchange saturation transfer (CEST) is a ^{1}H MR imaging (MRI) technique that enables visualization of chemical exchange processes between protons bound to solutes and surrounding bulk water molecules [24–26]. To induce a CEST contrast, the off-resonant solute protons are labeled by a saturation radiofrequency (RF) pulse and the label is then transferred to bulk water by chemical exchange. The magnitude of the subsequent reduction of

bulk water signal depends consequently on the dynamics of chemical exchange as well as on the ratio of exchangeable solute protons to bulk water protons [27]. The rate constant of chemical exchange (k), i.e., the velocity of chemical exchange, is principally influenced by the pH value and the temperature within the exchange environment. If the latter two parameters can be assumed to be distributed homogeneously in tissue and maintained at a constant level during one experiment, the CEST effect will be a surrogate marker of the concentration of a certain solute molecule in tissue. In order for a solute molecule to be considered suitable as an endogenous CEST agent, it must carry labile protons that exchange with bulk water at exchange rates that fulfill the condition $k < \Delta\omega$; where $\Delta\omega$ is the resonance offset of the solute protons to the water protons in [s^{-1}] [27].

Glycosaminoglycan-dependent chemical exchange saturation transfer (gagCEST) imaging was introduced by Ling et al. as a CEST imaging method that produces a contrast based exclusively on the chemical exchange between endogenous solute GAG molecules and surrounding bulk water [28]. This is of interest because GAGs are major constituents of the extracellular matrix of different connective tissues, such as cartilage, intervertebral discs (IVD) and menisci, and they are responsible for the biomechanical properties of these tissues [29–31]. Since pH value and temperature are relatively stable within connective tissues, variations of gagCEST signals were shown to correlate linearly with sodium content in cartilage assessed by ^{23}Na MRI [28], which, in turn, is a reference method for assessment of GAG content in cartilage [32–35]. In order to evaluate the potential of gagCEST imaging as a noninvasive tool for monitoring of cartilage GAG content, two initial studies were conducted in patients after cartilage repair surgeries [36, 37]. Previous studies had shown that cartilage repair tissue is likely to exhibit lower GAG content than native cartilage [38–40]. This finding, in combination with a usually well-defined repair area, makes repair tissue an ideal model system for evaluation of gagCEST or other possibly GAG-sensitive imaging techniques [41–43]. Both aforementioned gagCEST studies were conducted on human 7 T MR systems and gagCEST results were compared to sodium imaging as a reference for GAG content. The first study focused on patients, which had undergone microfracturing (MFX) therapy or matrix-associated chondrocyte transplantation (MACT). Both GAG-sensitive methods showed a strong correlation between each other and indicated significantly lower GAG content in repair tissue compared to native cartilage [37]. This result was confirmed in a second study that examined the long-term outcome of patients after autologous osteochondral transplantation (AOT) [36]. In the latter study, gagCEST and sodium imaging consistently showed reduced GAG content in repair sites. In addition to cartilage assessment, gagCEST imaging was used to investigate GAG content in IVDs [44, 45] and feasibility was demonstrated in healthy volunteers at 3 T. Both IVD studies showed different gagCEST signal intensities in nucleus pulposus compared to the annulus fibrosus as a result of the different GAG concentrations in these IVD compartments.

The common method for acquisition of a CEST dataset is to acquire multiple image datasets with presaturation at different offset frequencies (S_{Sat}) around the water resonance, and one reference dataset without saturation (S_0). This is regardless of the specific agent or resonance frequency that is evaluated to generate the desired CEST contrast. The normalized signal as a function of the presaturation offset (z-spectrum) can then be used to determine and quantify CEST effects, which are asymmetric with respect to the water resonance; i.e., a CEST effect appears either up- or downfield from water and can hence be extracted from the z-spectrum via analysis of its asymmetry with respect to the water resonance. Nevertheless, in vivo z-spectra are inherently asymmetric due to conventional magnetization transfer (MT) effects arising predominantly from solid-phase macromolecules. CEST effects are also masked by concomitant direct water saturation ("RF spillover") as a result of the bandwidth of the saturation pulses. This phenomenon is further emphasized if the resonance frequencies of the investigated exchangeable protons have only small chemical shift differences to bulk water protons. The

exchangeable protons of GAG molecules that are used to generate the gagCEST contrast, namely hydroxyl and amide protons, exhibit relatively small chemic shift offsets from bulk water protons. In particular, the labile –NH protons resonate at $\Delta\omega = 3.2$ ppm offset from the water resonance and –OH protons at $\Delta\omega = 0.9$–1.9 ppm ($\triangleq \sim 114$–241 Hz at 3.0 T). Additionally, the exchange rates of the hydroxyl protons can be on the order of up to 1,000 s^{-1}. Therefore, exchange rates may be in the intermediate to fast exchange regime at a magnetic field strength of 3.0 T ($k \geq \Delta\omega$), which makes the resonance signals difficult to resolve at 3.0 T. Although the situation improves considerably when switching to a field strength of 7.0 T, it is generally necessary to use tailored CEST acquisition and saturation strategies for gagCEST investigations. This means that time-efficient and narrowband saturation of CEST resonances must be enabled in addition to rapid signal readout after saturation.

Since multiple datasets are acquired in one gagCEST examination, it is mandatory for proper analysis of *z*-spectra to compensate for patient motion between acquisitions so the datasets recorded with different presaturation offsets are correctly aligned. Furthermore, correction of inhomogeneities of the static magnetic field, which can lead to severe miscalculation of CEST effects, has to be performed before analysis of *z*-spectra.

Several acquisition strategies have been proposed for gagCEST imaging, predominantly relying on 3D gradient-echo, or single-slice slice fast spin echo and GRE approaches [28, 37, 44–46]. While 3D acquisition techniques enable a more comprehensive overview of imaging volumes than single-slice techniques, they usually require longer scan times, which can be of concern for clinical routine. Additionally, in some joints where cartilage is thin compared to knee cartilage such as in the ankle or the hip, high spatial resolution is required for proper assessment of biochemical cartilage properties. However, gagCEST effects are in the order of 1–4 % of the bulk water signal at 3.0 T, and of 3–8 % at 7.0 T in healthy knee cartilage [37, 45]. Thus, high intrinsic image SNR is required to reliably detect and quantify gagCEST effects. Image SNR in MRI can only be maintained by increasing the scan time when higher spatial resolution is desired. Consequently, the maximum achievable spatial resolution for gagCEST imaging will certainly be limited by the scan time available for an exam. The acquisition strategy proposed by Schmitt et al. [37] was based on a 3D GRE approach and sampled *z*-spectra with 13 points from $\Delta\omega = -2.6$ to 2.6 ppm with a voxel resolution of $0.6 \times 0.6 \times 3.3$ mm^3 in 11:24 min (measurement at 7.0 T, full knee coverage).

Another limitation of gagCEST imaging may be the observed intra-individual differences of absolute gagCEST values, which impairs comparability of results between individuals. The differences are attributed to the fact that gagCEST signal intensities depend strongly on the absolute water content of tissue and tissue T_2 relaxation times. Both parameters can vary considerably among individuals and will thus influence absolute CEST values unless a proper normalization is applied or correction factors are introduced.

Imaging of Cartilage Diffusion

Molecular diffusion, also known as Brownian motion (see Einstein–Smoluchowski relation [47, 48]), refers to the random movement of small particles (atoms or molecules) in a homogeneous medium by thermal energy, captured by the so-called diffusion coefficient, D, measuring of the diffusivity or mobility of the particles. In biological tissues, however, water is diffusing not only in a solvent containing macromolecules but, typically, for the time periods involved in MRI also in a complex microstructure having different biophysical and biochemical properties. In that case, the notion of an apparent diffusion coefficient (frequently termed ADC) is used. Furthermore, diffusion is generally not directionally uniform, as it would be for water in a bucket of water, but directionally sensitive, that is anisotropic. Especially in highly oriented structures, such as muscle or nerve fibers, the apparent diffusion coefficient along different directions can differ by up to a factor of 3. As a result, for the

characterization of water diffusion in tissues, the diffusion coefficient is no longer a scalar value but a three-by-three matrix (or tensor) representing the different directional sensitivities. Complete characterization of the diffusion tensor is a demanding task, and frequently diffusion effects are confined into a simple orientational averaged mean diffusivity, $\langle D \rangle$, calculated from the trace of the diffusion tensor. Typical values for the mean diffusivity of water in biological tissues are in the range of 0.7×10^{-3} mm^2/s for human brain, 1.3×10^{-3} mm^2/s for cartilage, and up to 3.0×10^{-3} mm^2/s for fluids.

In MRI, Diffusion Weighted Imaging (DWI) refers to a class of methods able to probe the diffusivity of water in biological tissues, in vivo and noninvasively. The essence to any DWI experiment is that in the presence of a magnetic gradient field diffusion causes random phase shifts in the transverse magnetization of each water molecule leading within an imaging voxel to a loss of net magnetization, as compared to the static case. Diffusion measurements were already described by Stejskal and Tanner in 1965 for NMR [49] and entered MRI in the mid-1980s [50–52]. Since then, water diffusion MRI has proven to be a highly sensitive and specific parameter, mainly for the detection of neurological disorders. As a result, contemporary DWI sequences are typically single shot techniques consisting of a diffusion-sensitizing preparation part (a spin echo or stimulated echo) followed by an echo planar imaging (EPI) signal readout. EPI sequences have the major advance that they are highly insensitive to bulk motion and are probably the fastest imaging sequences available, but application to the musculoskeletal (MSK) system is demanding: typically, T_2 of cartilage or muscle is about a factor of 2–3 shorter than the one of brain tissue, leading to a prominent signal loss, especially in combination with the high resolution and large field-of-view requirement of MSK applications. In addition, strong magnetic field inhomogeneities from bone-tissue interfaces lead to severe image distortions that may need retrospective correction. As a result, especially steady state DWI sequences have gained increased importance for MSK imaging due to their excellent spatial resolution and high diffusion sensitivity [53–55].

Diffusion sensitivity to steady state free precession (SSFP) sequences is commonly induced by large gradient crusher moments, leading to a steady state signal that is composed of many different transverse and longitudinal echo paths or modes; including also stimulated echoes. For DWI, especially the "Echo" (that is the refocused signal immediately preceding the RF pulse) turns out to be very sensitive to diffusion representing a unique alternative to common EPI-based DWI, whereas the "FID" signal (that is the signal immediately following the RF pulse) is generally not used, since its sensitivity to diffusion is quite low. Over the years, several models have been developed for the description of diffusion effects in SSFP [56–60], all of them being based on the seminal work of Kaiser, Bartholdi, and Ernst (KBE) [56]. In MRI, besides semi-empirical approaches, such as the one presented by LeBihan [57], the extension of the KBE ansatz to pulsed gradient SSFP by Wu and Buxton [59, 60] is generally well accepted and several research groups have examined the effect of a constant crusher gradient for DWI with SSFP-Echo (also known as PSIF, CE-FAST) [53–55, 61, 62].

Diffusion quantification with SSFP-Echo, however, is complicated by manifold echo contributions leading to a complicated signal dependency on relaxation times (T_1 and T_2), as well as on sequence parameters, such as the repetition time (TR) or the flip angle (α). Quantification was, nevertheless, shown to be feasible in vivo in the fast-transverse-decay regime (that is for repetition times $TR > T_2$), provided that T_1 can be estimated [54]. In this regime, only the shortest coherence pathways contribute to the signal and thus signal attenuation from diffusion becomes independent of T_2 [60]. Clinically, however, this limit seems of rather low interest since signal-to-noise and scanning efficiency is substantially reduced from the required long echo times ($TE \sim 2 \times TR \gg T_2$) and far from what

is considered to be optimal. This is in contrast to SSFP-Echo DWI in the very-rapid-pulsing regime (that is for TR $\ll T_2$), offering substantially increased signal-to-noise and sequence efficiency. This regime has recently shown great promise for characterization of cartilage function and repair [63–65], but quantification of diffusion effects was complicated not only by the aforementioned pronounced sensitivity on relaxation but also due to a failure of the common Wu-Buxton model (and thus the KBE ansatz) in this limit [66]. This issue can be resolved by using an accurate SSFP diffusion model, as proposed by Freed et al. in the context of spectroscopy [67], and only recently, it was shown that for low flip angles, diffusion sensitivity in the SSFP-Echo arises mainly from longitudinal modes, effectively decreasing its relaxation sensitivity to T_1 only, similar to what can be achieved in the fast-transverse-decay regime. As a result, a new approach for quantitative SSFP-Echo DWI in the very-rapid-pulsing regime was proposed [66], allowing to probe diffusion properties of human articular cartilage in the knee joint in a clinical setup (Fig. 2.1)

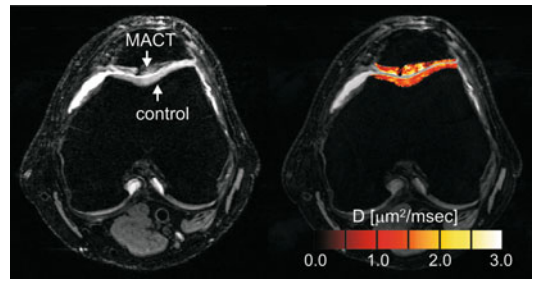

Fig. 2.1 In vivo axial sample image of a nondiffusion (*left*) and diffusion-weighted (*right*, averaged over three orthogonal directions) 3D SSFP-Echo scans with fused diffusivity map (using estimated T_1 information) of in vivo cartilage in the knee joint of a patient after matrix-associated autologous cartilage transplantation (MACT) at 3.0 T. A mean diffusivity of $1.42 \pm 0.24 \times 10^{-3}$ mm^2/s was found for the control cartilage and $1.73 \pm 0.54 \times 10^{-3}$ mm^2/s for the transplant (MACT). Scans were performed with 0.5×0.5 mm^2 inplane resolution and 3 mm slice thickness; for other details, cf. [66]

A completely different approach for DWI with SSFP-Echo was proposed by Zur et al. [68], using bipolar rather than unipolar diffusion-sensitizing crusher gradients to reduce sensitivity to bulk motion. This concept was recently revisited and extended by Deimling [69], proposing a double-echo steady state (DESS) imaging technique for DWI with SSFP rather than a single echo method based on SSFP-Echo. Acquiring both primary SSFP modes with DESS, namely the Echo and the FID (also known as FISP, FAST, GRASS), offers the advance that diffusion effects are in combination with bipolar gradients and with respect to the Echo/FID signal ratio independent on relaxation times, as already noticed much earlier by Cho [70]. Unfortunately, however, bipolar gradient waveforms are not very diffusion-sensitive and thus generally require large moments and long repetition times.

Recently, a new and truly diffusion-weighted technique that is relaxation-independent SSFP technique was introduced based on a DESS approach using diffusion-sensitizing crusher moments [71]. It was shown that SSFP signal attenuation from diffusion becomes independent on relaxation with respect to the Echo-FID signal ratio, in complete analogy to what was observed by Cho et al. using bipolar gradients. As a result, quantitative SSFP DWI can be performed in the very-rapid-pulsing regime from two DESS scans, similar to what is proposed for SSFP-Echo but without the confounding influences of relaxation times, allowing high-resolution quantitative diffusion imaging of human articular cartilage in the knee joint at 3.0 T (see Fig. 2.2). Simultaneously, a similar approach for diffusion quantification was proposed by Staroswiecki et al. [72] allowing simultaneous estimation of T2 and of the apparent diffusion coefficient from two DESS acquisitions with different crusher gradients and flip angles.

In summary, diffusion-sensitized SSFP, either based on the acquisition of the Echo only or on the double-echo approach using the FID to correct for relaxation time sensitivities in the Echo, have shown great promise for in vivo high-resolution

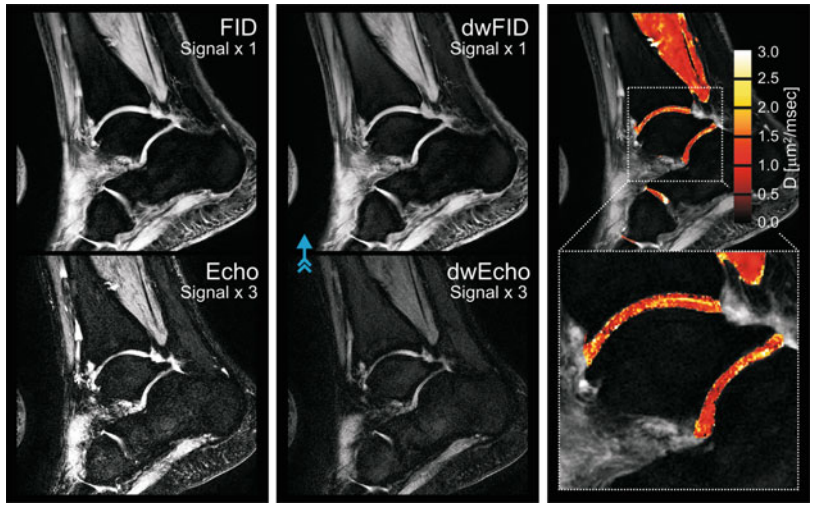

Fig. 2.2 High-resolution quantitative 3D DESS DWI of normal appearing cartilage in the ankle joint at 3.0 T. (*Left*) Sagittal nondiffusion-weighted DESS scan. (*Middle*) DESS scan with diffusion-sensitizing crusher moments along the direction indicated by the blue arrow. (*Right*) Fusion of the derived diffusion map onto a conventional DESS image (derived from the nondiffusion-weighted DESS scan). For cartilage, a diffusivity of $D = 1.21 \pm 0.48 \times 10^{-3}$ mm^2/s is found. Scans were performed with 0.4×0.4 mm^2 inplane resolution and 3 mm slice thickness; for other details, cf. [71]

quantitative DWI of cartilage in 3D and within reasonable scan times in a clinical setup. Sensitivity to bulk motion, however, is a major issue with diffusion-sensitized SSFP, and proper fixation seems not only mandatory but has carefully to be conducted prior to any measurement.

References

1. Locher S, Werlen S, Leunig M, Ganz R. [Inadequate detectability of early stages of coxarthrosis with conventional roentgen images]. Z Orthop Ihre Grenzgeb. 2001;139(1):70–4.
2. Burstein D, Gray ML. Is MRI fulfilling its promise for molecular imaging of cartilage in arthritis? Osteoarthritis Cartilage. 2006;14(11):1087–90.
3. Nieminen MT, Rieppo J, Toyras J, Hakumaki JM, Silvennoinen J, Hyttinen MM, Helminen HJ, Jurvelin JS. T2 relaxation reveals spatial collagen architecture in articular cartilage: a comparative quantitative MRI and polarized light microscopic study. Magn Reson Med. 2001;46(3):487–93.
4. White LM, Sussman MS, Hurtig M, Probyn L, Tomlinson G, Kandel R. Cartilage T2 assessment: differentiation of normal hyaline cartilage and reparative tissue after arthroscopic cartilage repair in equine subjects. Radiology. 2006;241(2):407–14.
5. Domayer SE, Kutscha-Lissberg F, Welsch G, Dorotka R, Nehrer S, Gabler C, Mamisch TC, Trattnig S. T2 mapping in the knee after microfracture at 3.0 T: correlation of global T2 values and clinical outcome—preliminary results. Osteoarthritis Cartilage. 2008;16(8):903–8.
6. Grunder W, Wagner M, Werner A. MR-microscopic visualization of anisotropic internal cartilage structures using the magic angle technique. Magn Reson Med. 1998;39(3):376–82.
7. Mosher TJ, Smith H, Dardzinski BJ, Schmithorst VJ, Smith MB. MR imaging and T2 mapping of femoral cartilage: in vivo determination of the magic angle effect. AJR Am J Roentgenol. 2001;177(3):665–9.
8. Li X, Benjamin Ma C, Link TM, Castillo DD, Blumenkrantz G, Lozano J, Carballido-Gamio J, Ries M, Majumdar S. In vivo T(1rho) and T(2) mapping of articular cartilage in osteoarthritis of the knee using 3 T MRI. Osteoarthritis Cartilage. 2007;15(7):789–97.
9. Trattnig S, Mamisch TC, Welsch GH, Glaser C, Szomolanyi P, Gebetsroither S, Stastny O, Horger W, Millington S, Marlovits S. Quantitative T2 mapping of matrix-associated autologous chondrocyte transplantation at 3 Tesla: an in vivo cross-sectional study. Invest Radiol. 2007;42(6):442–8.
10. Kurkijarvi JE, Mattila L, Ojala RO, Vasara AI, Jurvelin JS, Kiviranta I, Nieminen MT. Evaluation of cartilage repair in the distal femur after autologous chondrocyte transplantation using T2 relaxation time and dGEMRIC. Osteoarthritis Cartilage. 2007;15(4):372–8.
11. Welsch GH, Mamisch TC, Domayer SE, Dorotka R, Kutscha-Lissberg F, Marlovits S, White LM, Trattnig S. Cartilage T2 assessment at 3-T MR

imaging: in vivo differentiation of normal hyaline cartilage from reparative tissue after two cartilage repair procedures–initial experience. Radiology. 2008;247(1):154–61.
12. Quirbach S, Trattnig S, Marlovits S, Zimmermann V, Domayer S, Dorotka R, Mamisch TC, Bohndorf K, Welsch GH. Initial results of in vivo high-resolution morphological and biochemical cartilage imaging of patients after matrix-associated autologous chondrocyte transplantation (MACT) of the ankle. Skeletal Radiol. 2009;38(8):751–60.
13. Domayer SE, Welsch GH, Stelzeneder D, Hirschfeld C, Quirbach S, Nehrer S, Dorotka R, Mamisch TC, Trattnig S. Microfracture in the ankle: clinical results and MRI with T2-mapping at 3.0 T after 1 to 8 years. Cartilage. 2011;2(1):73–80.
14. Nehrer S, Domayer SE, Hirschfeld C, Stelzeneder D, Trattnig S, Dorotka R. Matrix-associated and autologous chondrocyte transplantation in the ankle: clinical and MRI follow-up after 2 to 11 years. Cartilage. 2011;2(1):81–91.
15. Maier CF, Tan SG, Hariharan H, Potter HG. T2 quantitation of articular cartilage at 1.5 T. J Magn Reson Imaging. 2003;17(3):358–64.
16. Pai A, Li X, Majumdar S. A comparative study at 3 T of sequence dependence of T2 quantitation in the knee. Magn Reson Imaging. 2008;26(9):1215–20.
17. Glaser C, Mendlik T, Dinges J, Weber J, Stahl R, Trumm C, Reiser M. Global and regional reproducibility of T2 relaxation time measurements in human patellar cartilage. Magn Reson Med. 2006;56 (3):527–34.
18. Glaser C, Horng A, Mendlik T, Weckbach S, Hoffmann RT, Wagner S, Raya JG, Horger W, Reiser M. [T2 relaxation time in patellar cartilage–global and regional reproducibility at 1.5 tesla and 3 tesla]. Rofo. 2007;179(2):146–52.
19. Mamisch TC, Hughes T, Mosher TJ, Mueller C, Trattnig S, Boesch C, Welsch GH. T2 star relaxation times for assessment of articular cartilage at 3 T: a feasibility study. Skeletal Radiol. 2012;41(3):287–92.
20. Bittersohl B, Miese FR, Hosalkar HS, Mamisch TC, Antoch G, Krauspe R, Zilkens C. T2* mapping of acetabular and femoral hip joint cartilage at 3 T: a prospective controlled study. Invest Radiol. 2012;47 (7):392–7.
21. Apprich S, Welsch GH, Mamisch TC, Szomolanyi P, Mayerhoefer M, Pinker K, Trattnig S. Detection of degenerative cartilage disease: comparison of high-resolution morphological MR and quantitative T2 mapping at 3.0 Tesla. Osteoarthritis Cartilage. 2010;18(9):1211–7.
22. Welsch GH, Apprich S, Zbyn S, Mamisch TC, Mlynarik V, Scheffler K, Bieri O, Trattnig S. Biochemical (T2, T2* and magnetisation transfer ratio) MRI of knee cartilage: feasibility at ultra-high field (7T) compared with high field (3T) strength. Eur Radiol. 2011;21(6):1136–43.
23. Apprich S, Mamisch TC, Welsch GH, Bonel H, Siebenrock KA, Kim YJ, Trattnig S, Dudda M. Evaluation of articular cartilage in patients with femoroacetabular impingement (FAI) using T2* mapping at different time points at 3.0 Tesla MRI: a feasibility study. Skeletal Radiol. 2012;41(8):987–95.
24. Guivel-Scharen V, Sinnwell T, Wolff SD, Balaban RS. Detection of proton chemical exchange between metabolites and water in biological tissues. J Magn Reson. 1998;133(1):36–45.
25. Ward KM, Aletras AH, Balaban RS. A new class of contrast agents for MRI based on proton chemical exchange dependent saturation transfer (CEST). J Magn Reson. 2000;143(1):79–87.
26. Ward KM, Balaban RS. Determination of pH using water protons and chemical exchange dependent saturation transfer (CEST). Magn Reson Med. 2000;44(5):799–802.
27. Zhou JY, van Zijl PCM. Chemical exchange saturation transfer imaging and spectroscopy. Prog Nucl Magn Reson Spectrosc. 2006;48(2–3):109–36.
28. Ling W, Regatte RR, Navon G, Jerschow A. Assessment of glycosaminoglycan concentration in vivo by chemical exchange-dependent saturation transfer (gagCEST). Proc Natl Acad Sci U S A. 2008;105 (7):2266–70.
29. Ayad S. The extracellular matrix factsbook. San Diego, CA: Academic; 1998. p. 301.
30. Roughley PJ. The structure and function of cartilage proteoglycans. Eur Cell Mater. 2006;12:92–101.
31. Roughley PJ, Lee ER. Cartilage proteoglycans—structure and potential functions. Microsc Res Tech. 1994;28(5):385–97.
32. Reddy R, Li SC, Noyszewski EA, Kneeland JB, Leigh JS. In vivo sodium multiple quantum spectroscopy of human articular cartilage. Magn Reson Med. 1997;38(2):207–14.
33. Borthakur A, Shapiro EM, Beers J, Kudchodkar S, Kneeland JB, Reddy R. Sensitivity of MRI to proteoglycan depletion in cartilage: comparison of sodium and proton MRI. Osteoarthritis Cartilage. 2000;8 (4):288–93.
34. Shapiro EM, Borthakur A, Dandora R, Kriss A, Leigh JS, Reddy R. Sodium visibility and quantitation in intact bovine articular cartilage using high field Na-23 MRI and MRS. J Magn Reson. 2000;142 (1):24–31.
35. Shapiro EM, Borthakur A, Gougoutas A, Reddy R. Na-23 MRI accurately measures fixed charge density in articular cartilage. Magn Reson Med. 2002;47 (2):284–91.
36. Krusche-Mandl I, Schmitt B, Zak L, Apprich S, Aldrian S, Juras V, Friedrich KM, Marlovits S, Weber M, Trattnig S. Long-term results 8 years after autologous osteochondral transplantation: 7 T gagCEST and sodium magnetic resonance imaging with morphological and clinical correlation. Osteoarthritis Cartilage. 2012;20(5):357–63.

37. Schmitt B, Zbyn S, Stelzeneder D, Jellus V, Paul D, Lauer L, Bachert P, Trattnig S. Cartilage quality assessment by using glycosaminoglycan chemical exchange saturation transfer and 23Na MR imaging at 7 T. Radiology. 2011;260(1):257–64.
38. Eckstein F, Burstein D, Link TM. Quantitative MRI of cartilage and bone: degenerative changes in osteoarthritis. NMR Biomed. 2006;19(7):822–54.
39. Trattnig S, Domayer S, Welsch GW, Mosher T, Eckstein F. MR imaging of cartilage and its repair in the knee—a review. Eur Radiol. 2009;19(7):1582–94.
40. Welsch GH, Trattnig S, Hughes T, Quirbach S, Olk A, Blanke M, Marlovits S, Mamisch TC. T2 and T2*mapping in patients after matrix-associated autologous chondrocyte transplantation: initial results on clinical use with 3.0-Tesla MRI. Eur Radiol. 2010;20 (6):1515–23.
41. Trattnig S, Ba-Ssalamah A, Pinker K, Plank C, Vecsei V, Marlovits S. Matrix-based autologous chondrocyte implantation for cartilage repair: noninvasive monitoring by high-resolution magnetic resonance imaging. Magn Reson Imaging. 2005;23 (7):779–87.
42. Trattnig S, Marlovits S, Gebetsroither S, Szomolanyi P, Welsch GH, Salomonowitz E, Watanabe A, Deimling M, Mamisch TC. Three-dimensional delayed gadolinium-enhanced MRI of cartilage (dGEMRIC) for in vivo evaluation of reparative cartilage after matrix-associated autologous chondrocyte transplantation at 3.0T: preliminary results. J Magn Reson Imaging. 2007;26(4):974–82.
43. Trattnig S, Welsch GH, Juras V, Szomolanyi P, Mayerhoefer ME, Stelzeneder D, Mamisch TC, Bieri O, Scheffler K, Zbyn S. 23Na MR imaging at 7 T after knee matrix-associated autologous chondrocyte transplantation: preliminary results. Radiology. 2010;257(1):175–84.
44. Varma G, Kourtelidis F, Madhurantakam A, Hackney DB, Lenkinski RE, Vinogradov E. Age-related assessment of intervertebral disc degeneration in the lumbar spine using gagCEST. Melbourne: ISMRM; 2012. p. 1460.
45. Kim M, Chan Q, Anthony MP, Samartzis D, Cheung KM, Khong PL. Chemical exchange saturation transfer and T2 mapping in subjects with intervertebral disc degeneration at 3 Tesla. Melbourne: ISMRM; 2012. p. 3331.
46. Singh A, Haris M, Cai K, Kassey VB, Kogan F, Reddy D, Hariharan H, Reddy R. Chemical exchange saturation transfer magnetic resonance imaging of human knee cartilage at 3 T and 7 T. Magn Reson Med. 2012;68(2):588–94.
47. Einstein A. Über die von der molekularkinetischen Theorie der Wärme geforderte Bewegung von in ruhenden Flüssigkeiten suspendierten Teilchen. Ann Phys. 1905;322(8):549–60.
48. von Smoluchowski M. Zur kinetischen Theorie der Brownschen Molekularbewegung und der Suspensionen. Ann Phys. 1906;326(14):756–80.
49. Tanner JE, Stejskal EO. Spin diffusion measurements: spin echoes in the presence of a time-dependent field gradient. J Chem Phys. 1965;42:288–92.
50. Le Bihan D, Breton E. Imagerie de diffusion in vivo par résonance magnétique nucléaire. C R Acad Sci Paris. 1985;301:1109–12.
51. Merboldt KD, Hanicke W, Frahm J. Self-diffusion NMR imaging using stimulated echoes. J Magn Reson. 1985;64:479–86.
52. Taylor DG, Bushell MC. The spatial mapping of translational diffusion coefficients by the NMR imaging technique. Phys Med Biol. 1985;30:345–9.
53. Mlynarik V, Sulzbacher I, Bittsansky M, Fuiko R, Trattnig S. Investigation of apparent diffusion constant as an indicator of early degenerative disease in articular cartilage. J Magn Reson Imaging. 2003;17 (4):440–4.
54. Miller KL, Hargreaves BA, Gold GE, Pauly JM. Steady-state diffusion-weighted imaging of in vivo knee cartilage. Magn Reson Med. 2004;51(2):394–8.
55. Deoni SC, Peters TM, Rutt BK. Quantitative diffusion imaging with steady-state free precession. Magn Reson Med. 2004;51(2):428–33.
56. Kaiser R, Bartholdi E, Ernst RR. Diffusion and field-gradient effects in NMR Fourier spectroscopy. J Chem Phys. 1974;60:2966–79.
57. Le Bihan D. Intravoxel incoherent motion imaging using steady-state free precession. Magn Reson Med. 1988;7(3):346–51.
58. Merboldt KD, Bruhn H, Frahm J, Gyngell ML, Hanicke W, Deimling M. MRI of “diffusion” in the human brain: new results using a modified CE-FAST sequence. Magn Reson Med. 1989;9(3):423–9.
59. Wu EX, Buxton RB. Effect of diffusion on the steady-state magnetization with pulsed field gradients. J Magn Reson. 1990;90(2):243–53.
60. Buxton RB. The diffusion sensitivity of fast steady-state free precession imaging. Magn Reson Med. 1993;29(2):235–43.
61. Patz S, Hawkes RC. The application of steady-state free precession to the study of very slow fluid flow. Magn Reson Med. 1986;3(1):140–5.
62. Merboldt KD, Hänicke W, Gyngell ML, Frahm J, Bruhn H. Rapid NMR imaging of molecular self-diffusion using a modified CE-FAST sequence. J Magn Reson. 1989;82(1):115–21.
63. Mamisch TC, Menzel MI, Welsch GH, Bittersohl B, Salomonowitz E, Szomolanyi P, Kordelle J, Marlovits S, Trattnig S. Steady-state diffusion imaging for MR in-vivo evaluation of reparative cartilage after matrix-associated autologous chondrocyte transplantation at 3 tesla–preliminary results. Eur J Radiol. 2008;65(1):72–9.
64. Welsch GH, Trattnig S, Domayer S, Marlovits S, White LM, Mamisch TC. Multimodal approach in the use of clinical scoring, morphological MRI and biochemical T2-mapping and diffusion-weighted imaging in their ability to assess differences between cartilage repair tissue after microfracture therapy and

matrix-associated autologous chondrocyte transplantation: a pilot study. Osteoarthritis Cartilage. 2009;17 (9):1219–27.
65. Friedrich KM, Mamisch TC, Plank C, Langs G, Marlovits S, Salomonowitz E, Trattnig S, Welsch G. Diffusion-weighted imaging for the follow-up of patients after matrix-associated autologous chondrocyte transplantation. Eur J Radiol. 2010;73(3):622–8.
66. Bieri O, Ganter C, Welsch GH, Trattnig S, Mamisch TC, Scheffler K. Fast diffusion-weighted steady state free precession imaging of in vivo knee cartilage. Magn Reson Med. 2012;67(3):691–700.
67. Freed DE, Scheven UM, Zielinski LJ, Sen PN, Hürlimann MD. Steady-state free precession experiments and exact treatment of diffusion in a uniform gradient. J Chem Phys. 2001;119(9):4249–58.
68. Zur Y, Bosak E, Kaplan N. A new diffusion SSFP imaging technique. Magn Reson Med. 1997;37 (5):716–22.
69. Deimling M. Method to determine the ADC coefficients in diffusion-weighted magnetic resonance imaging given use of steady-state sequences. US patent 6,891,373 B2; 2005.
70. Cho MH, Cho ZH. NMR diffusion coefficient mapping by use of fast steady-state free precession sequence. In: Proceedings of Society of Magnetic Resonance in Medicine, Amsterdam, The Netherlands; 1989. p 911.
71. Bieri O, Ganter C, Scheffler K. Quantitative in vivo diffusion imaging of cartilage using double echo steady-state free precession. Magn Reson Med. 2012;68(3):720–9.
72. Staroswiecki E, Granlund KL, Alley MT, Gold GE, Hargreaves BA. Simultaneous estimation of T(2) and apparent diffusion coefficient in human articular cartilage in vivo with a modified three-dimensional double echo steady state (DESS) sequence at 3 T. Magn Reson Med. 2012;67(4):1086–96.

Delayed Gadolinium-Enhanced MRI of Cartilage

3

Deborah Burstein

Delayed gadolinium-enhanced MRI of cartilage (dGEMRIC) was first described in 1996 as a nondestructive technique for quantitative measurements of glycosaminoglycan (GAG) concentration in articular cartilage samples [1]. Its translation to clinical platforms as a means of interrogating the molecular aspects of cartilage was demonstrated in 1997 with illustrative examples of apparent molecular degeneration in cartilage that was grossly intact morphologically [2]. Since then, over 150 reports of dGEMRIC involving in vitro and clinical studies have been published. These reports demonstrate the potential for molecular imaging techniques to illustrate new paradigms in the understanding of cartilage disease. However, along with the expanded applications come questions regarding appropriate protocols, possible sources of measurement and interpretation errors, and insight into directions for future study. This chapter describes the theoretical basis of dGEMRIC, protocols, pitfalls, and opportunities, focusing on the clinical aspects. Further details can be found in several reviews [3–7].

Biophysical Basis for dGEMRIC

dGEMRIC, like most biochemical methods for measuring cartilage GAG including radiotracer, histology with cationic dyes, and biochemical assays, is based on biophysical principles elucidated by Maroudas almost 40 years ago [8]. These principles rely on the fact that GAG is the source of the majority of the fixed charge on the cartilage extracellular matrix, due to the abundant carboxyl and sulfate groups on the GAG molecules. Mobile ions will distribute in tissue according to the GAG (negative fixed charge) concentration. The associated theories can be used to calculate the concentration of GAG based on the concentration of the mobile ion in the tissue. In dGEMRIC the mobile ion is the MRI contrast agent Gd-DTPA^{2-} (Gadopentetate Dimeglumine, Bayer Health Care).

If Gd-DTPA^{2-} is allowed time to equilibrate in tissue, theoretically the concentration of Gd-DTPA^{2-} can be determined from a measurement of the MRI parameter T1 in the presence of Gd-DTPA^{2-} (T1(Gd)), and the concentration of GAG can then be calculated from the determined concentration of the mobile Gd-DTPA^{2-} ion. In practice, the conditions for quantitation of absolute GAG are not met in clinical studies due to the contrast agent not being in steady state with the cartilage, and the relative distribution of T1 (Gd) is utilized as a metric for the relative distribution of cartilage GAG, as described below.

D. Burstein (✉)
Department of Radiology, Beth Israel Deaconess Medical Center, 4 Blackfan Circle, Boston, MA, USA
e-mail: dburstei@bidmc.harvard.edu

Y.-J. Kim (eds.), *Hip Magnetic Resonance Imaging*,
DOI 10.1007/978-1-4614-1668-5_3,

Protocol Considerations and Pitfalls

In order to determine the GAG concentration in cartilage from the concentration of Gd-DTPA^{2-}, Gd−DTPA^{2-} needs to be added to the system, and it needs time to penetrate the cartilage (which may take up to several hours in the avascular tissue). T1 measurements are then needed in order to assess the distribution of Gd-DTPA^{2-} concentration. There are several protocol considerations with respect to these steps:

T1 pre-contrast

Theoretically, calculation of Gd-DTPA^{2-} requires knowledge of T1 both before and after contrast agent administration. However, under some conditions the variation of T1 without contrast across the tissue in an individual, or between individuals, may be small enough relative to the changes induced by the contrast agent that it is possible to utilize the T1 post-contrast alone as a metric of Gd-DTPA^{2-} concentration. This has generally been found to be the case in dGEMRIC studies of native cartilage tissue of the knee, hip, and finger [9–12].

Administration of Gd-DTPA^{2-}

In clinical studies, the Gd-DTPA^{2-} is administered either by intra-articular or intravenous injection. Early studies demonstrated that in the thick cartilage of the patella of the knee, the kinetics of penetration of Gd-DTPA^{2-} was faster with intravenous administration due to its penetration from both the synovial and bone surfaces [2]. However, this may be less of an issue for the thinner cartilages of other aspects of the knee or of the hip.

An advantage of the intra-articular injection is the improved delineation of cartilage in addition to the dGEMRIC effect [13, 14]. However, intravenous is generally easier to implement and thus has been utilized in the majority of dGEMRIC studies to date of the knee, although a number of recent studies have utilized intra-articular injections for dGEMRIC of the hip [13–16].

Dose

Increasing dosage of Gd-DTPA^{2-} results in easier delineation of differences in GAG, as well as lower T1(Gd) and hence faster T1(Gd) measurement. Offsetting this is the concern for the safety issues of contrast agent at higher doses [17]. The majority of dGEMRIC studies have been done with "double dose" Gd-DTPA^{2-} (0.2 mmol/kg), although utility of single dose has also been illustrated [18].

Another consideration with dosing is that, since adipose tissue does not take up Gd-DTPA^{2-} as much as lean mass, dosing by weight results in individuals with higher BMI given an effectively larger dose of Gd-DTPA^{2-} [19]. Therefore, in studies including subjects with a large range of BMI, one can either adjust the dose, or "correct" the dGEMRIC values post-acquisition [19]. The BMI effect will not be an issue for longitudinal studies of individuals where BMI does not change during the study period. Alternatively, studies of relative dGEMRIC values within the knee at one time or across time will demonstrate effects apparent in localized regions of the knee even if BMI changes might be of concern [20].

Delay Period

Once injected, the Gd-DTPA^{2-} needs time to penetrate into the cartilage. Early studies demonstrated that 30–90 min were effective for penetration into hip cartilage, and 2–3 h into all the cartilages of the knee [21]. In particular, thicker cartilage would require a longer time for contrast agent penetration, and incomplete penetration of contrast in thick cartilage may result in higher T1(Gd) than would be obtained after longer equilibration times [22]. Therefore, early loss of GAG in thick cartilage may be underrepresented by this technique. Potentially offsetting the effect of longer penetration time in thick

cartilage and overestimation of the GAG concentration is the effect of faster penetration kinetics of contrast agent into degraded tissue [23].

The faster penetration of Gd-DTPA^{2-} into degraded cartilage also implies that earlier time points after contrast agent injection will result in a larger observed effect difference between healthy and diseased tissue [24] as the Gd-DTPA^{2-} will enter degraded tissue faster and will go to a higher concentration [25], and then wash out faster [26].

In interpreting clinical studies and clinical trials, the time after injection should be taken into account and consistency of this time noted. Most hip studies have been done with a delay time of about 30 min after injection; most knee studies have been done after 90 min.

Joint Motion

The initial clinical studies demonstrated that some form of motion of the joint is necessary for consistent penetration of the Gd-DTPA^{2-} into cartilage [21]. The protocols for this motion have varied from walking 10 min, to climbing stairs, to passive motion of the joint. No definitive study has yet been undertaken to define whether one type of motion is better than another.

T1 Imaging

Although T1 weighted images might demonstrate areas depleted of cartilage [2], quantitation of T1(Gd) allows for an absolute index for direct comparison across people and time points.

Calculated images of T1 can be obtained through some form of inversion recovery or saturation recovery pulse sequence. The most straightforward, although also the most time-consuming, are standard 2D inversion recovery pulse sequences. These are generally limited by the number of sections that can be imaged in a reasonable imaging time, and therefore are appropriate if a given section of the joint is of interest and can be localized to easily from scout scans.

More generally, three-dimensional pulse sequences allow for coverage of the joint and post-processing of the region of interest. This is particularly of value with the relatively spherical geometry of the hip joint. A number of studies have validated 3D T1 imaging compared to 2D sequences [27–31], and low versus high resolution imaging [32].

After the imaging data are obtained, calculated T1 maps are made through a number of software packages available. In general the data are reported as mean T1(Gd) from a region of interest.

An additional consideration for the hip is the visualization of T1(Gd) along the natural anatomic zones of the hip cartilage. In this regard, a number of studies have reported the radial distribution of T1(Gd) [33–35].

Field Strength

Both 1.5T and 3T are commonly used for musculoskeletal imaging applications. While generally 3T would have advantages in terms of achievable resolution, the higher T1 values at 3T result in a longer imaging time for dGEMRIC at that field strength. In addition, B1 inhomogeneity, which can be a factor in the accuracy of T1 measurements, is more problematic at 3T than at 1.5T. Correction schemes for B1 inhomogeneity have recently been proposed [36–38]. Pilot studies have also recently been reported at 7 T [39].

Combination with Other Pulse Sequences

A number of parameters have been proposed for interrogating the molecular aspects of cartilage, as discussed in other chapters in this book. There have been several proposals to utilize combined information from several parameters, which raises the issue of whether they can be measured in one scan session.

Since T2 is much more sensitive to tissue macromolecules than to Gd-DTPA^{2-}, T2 is not significantly impacted by Gd-DTPA^{2-}, and it is possible to measure both T2 and dGEMRIC after administration of Gd-DTPA^{2-} [40, 41]. This is not true for T1rho, which would be strongly affected by the concentration of Gd-DTPA^{2-}. Therefore, combined measures of T1rho and dGEMRIC would require imaging both before and after contrast agent administration.

The accuracy of cartilage thickness or volume measurements in the presence of Gd-DTPA^{2-} has been investigated for knee cartilage. Baseline measurements were found to be comparable with or without the contrast agent in the tissue [42]; however, a later study found that changes in thickness over time yielded disparate results depending on whether the measurements were made in the presence of Gd-DTPA^{2-} [43]. Improved accuracy may be a matter of optimizing the segmentation routines for post-Gd-DTPA^{2-} tissue contrast, and/or improving inherent errors in the volume measurement themselves.

Reproducibility of T1 Measurements

Reproducibility of studies needs to be interpreted in the context of the level of changes that need to be evaluated for a given study. Measurements of reproducibility of dGEMRIC are also complicated by the kinetics of the contrast agent washing in and out of cartilage. Due to the contrast agent administration, two complete studies immediately following one another are also not appropriate. Therefore, many of the reproducibility studies have been done with scans several weeks apart, and the results are a combination of actual measurement reproducibility and variation in the natural levels of cartilage molecular composition over these short time frames.

With this in mind, the reproducibility data can be evaluated. Early studies showed a reproducibility of about 15 % in the knee [21]. This has been improved with faster pulse sequences and better analysis routines. In the knee, the reproducibility has been shown to be between 5 and 8 % depending on the size of the regions of interest [44], while in the hip similar values were obtained (3.7–6.8 %) [45]. Interobserver variability in drawing standardized regions of interest was found to be better than 3 % in the different compartments of the knee [46]. Image registration was found to improve the reproducibility in the knee with ICC ranging from 0.85 to 0.9 [47, 48].

Since many of the clinically observed variations within a joint, between people, or changes over time are on the order of 20 % and higher (see sections below), the reported reproducibility values are sufficient for many applications.

Validation Studies

The theories developed by Maroudas [8] assume that the cartilage is in equilibration with a large "bath" (surrounding source) of the mobile ion, in this case Gd-DTPA^{2-}. These conditions are relatively easily achieved in vitro by placing the cartilage sample in a solution containing Gd-DTPA^{2-} for several hours, and a number of bench studies have validated the concentration of GAG as determined by dGEMRIC against biochemical and histological metrics [1, 49].

In clinical studies, the conditions of equilibrium and infinite bath surrounding the tissue do not hold. Therefore, the relative distribution of GAG within a joint, and between individuals, is inferred from the T1(Gd) maps. These distributions measured in vivo have compared well to histology from samples obtained after the imaging from total knee replacement surgeries [49]. Another means of validating the clinical dGEMRIC studies is to compare T1(Gd) images obtained with Gd-DTPA^{2-} to those obtained with a nonionic contrast agent. A small study initially demonstrated that the T1 distribution after administration of a nonionic contrast agent was uniform, compared with the "lesions" seen in the presence of Gd-DTPA^{2-} [2].

Opportunities

Within the context of the protocol and interpretation issues described above, the ability to distinguish molecular characteristics of morphologically intact tissue has the potential to greatly enhance our understanding of cartilage physiology and disease and impact therapeutic planning and evaluation. The majority of dGEMRIC studies have been in the knee and hip, although there are a number of reports of dGEMRIC applied to the finger joints [12, 50–52] and ankle [53]. dGEMRIC protocols have also been applied in the meniscus [54–56] and intervertebral discs [57, 58]; however, the considerations of transport are much more of a concern in these thick tissues, and the interpretation of the studies is likely to be different than those in the articular cartilages.

Applications of dGEMRIC in the hip will be described in detail in a later chapter; here we briefly present evidence for general types of opportunities that have been demonstrated in the hip as well as other joints that might be applicable to the hip in future studies.

Cartilage Physiology and Pathophysiology

While imaging studies tend to focus on disease, a better understanding of physiology might lead to lifestyle changes or interventions that might prevent degeneration of the joint. For example, adherence to an exercise regimen was shown to increase the dGEMRIC Index [48, 59, 60]. Similarly, in obese subjects, quadriceps strength was shown to correlate positively with dGEMRIC [61], as did weight loss [20]. The implication of biomechanics in alterations in molecular metrics is further strengthened by the observation that knee malalignment has been shown to correlate to medial/lateral ratios of the dGEMRIC Index [62]. Similarly, different types of femoroacetabular impingement had different distributions of dGEMRIC across the hip [63]. The observations regarding the impact of biomechanics may provide a window for therapeutics such as modifying the mechanical tissue conditions.

Pre-radiographic Disease

The most straightforward application of dGEMRIC or any molecular imaging technique is simply to demonstrate and follow "lesions" in otherwise apparently normal-appearing cartilage. Detection and monitoring of these lesions demonstrate a number of paradigm-changing concepts in the evaluation of cartilage physiology and pathophysiology. In particular, molecular scans such as dGEMRIC have demonstrated "lesions" or generally low values in radiographically normal compartments [51, 62, 64], which has implications for the enrollment of such individuals as "controls" in natural history or intervention trials for cartilage disease.

The prior reliance on radiographic abnormalities which only progress has led to the paradigm that arthritis only progresses with worsening disease. The observation of molecular level lesions in radiographically normal or stable states also allows for monitoring of regression as well as progression of disease or injury. In one case report, a posterior cruciate ligament injury was found to result in a dGEMRIC decrease over the first month but then a return to baseline after several months of rehabilitation [65].

Prediction of Disease Progression, Regression, or Success of Intervention

A determination of the molecular status of cartilage might enable one to predict whether the joint is progressing towards worse disease, improving in status, or whether the cartilage is in sufficiently good state such that an intervention can be effective.

One study showed that low dGEMRIC values preceded radiographic OA [66], and another showed that decreasing dGEMRIC in chronic rheumatoid arthritis despite treatment, leading to joint replacement [67]. Similarly several

studies have shown the negative impact of ACL injuries, exacerbated by meniscal injuries [68, 69]. Conversely, there are examples of studies demonstrating protective effects, such as muscle strength in knees with meniscal injuries [70] and collagen hydrolysate over a period of 6 months [71].

Summary

Molecular imaging of cartilage has the potential to improve understanding of joint disease, and the evaluation of protective and interventional procedures. dGEMRIC was designed as a method of measuring the GAG component of cartilage. Certain protocol considerations must be taken into account, and data interpretation in relation to actual GAG content needs to consider the nonequilibrium state of contrast distribution in vivo. With these considerations, changes in the dGEMRIC index have been used to compare cartilage status across individuals and monitor cartilage status over time for a given individual. In total, these studies have illustrated the dynamic, responsive, reversible nature of cartilage molecular structure, and hence the potential to impact cartilage health with lifestyle and therapeutic interventions.

References

1. Bashir A, Gray ML, Burstein D. Gd-DTPA2- as a measure of cartilage degradation. Magn Reson Med. 1996;36:665–73.
2. Bashir A, Gray ML, Boutin RD, Burstein D. Glycosaminoglycan in articular cartilage: in vivo assessment with delayed Gd(DTPA)(2-)-enhanced MR imaging. Radiology. 1997;205:551–8.
3. Gray ML, Burstein D, Kim YJ, Maroudas A. 2007 Elizabeth Winston Lanier Award Winner. Magnetic resonance imaging of cartilage glycosaminoglycan: basic principles, imaging technique, and clinical applications. J Orthop Res. 2008;26:281–91.
4. Crema MD, Roemer FW, Marra MD, Burstein D, Gold GE, Eckstein F, Baum T, Mosher TJ, Carrino JA, Guermazi A. Articular cartilage in the knee: current MR imaging techniques and applications in clinical practice and research. Radiographics. 2011;31:37–61.
5. Dahlberg A, Lammentausta E, Tiderius CJ, Nieminen MT. In vivo monitoring of joint cartilage—lessons to be learned by delayed gadolinium enhanced magnetic resonance imaging of cartilage. Eur Musculoskelet Rev. 2012;7:58–62.
6. Burstein D. Tracking longitudinal changes in knee degeneration and repair. J Bone Joint Surg. 2009;91 Suppl 1:51–3.
7. Burstein D, Gray M, Mosher T, Dardzinski B. Measures of molecular composition and structure in osteoarthritis. Radiol Clin North Am. 2009;47:675–86.
8. Maroudas A. Physicochemical properties of articular cartilage. In: Freeman M, editor. Adult articular cartilage. London: Pitman Medical; 1979. p. 215–90.
9. Williams A, Mikulis B, Krishnan N, Gray M, McKenzie C, Burstein D. Suitability of T(1GD) as the dGEMRIC index at 1.5T and 3.0T. Magn Reson Med. 2007;58:830–4.
10. Li W, Du H, Scheidegger R, Wu Y, Prasad PV. Value of precontrast T(1) for dGEMRIC of native articular cartilage. J Magn Reson Imaging. 2009;29:494–7.
11. Bittersohl B, Hosalkar HS, Kim YJ, Werlen S, Siebenrock KA, Mamisch TC. Delayed gadolinium-enhanced magnetic resonance imaging (dGEMRIC) of hip joint cartilage in femoroacetabular impingement (FAI): are pre- and postcontrast imaging both necessary? Magn Reson Med. 2009;62:1362–7.
12. Buchbender C, Scherer A, Kropil P, Korbl B, Quentin M, Reichelt D, Lanzman RS, Mathys C, Blondin D, Bittersohl B, Zilkens C, Hofer M, Wittsack HJ, Schneider M, Antoch G, Ostendorf B, Miese F. Cartilage quality in rheumatoid arthritis: comparison of T2* mapping, native T1 mapping, dGEMRIC, deltaR1 and value of pre-contrast imaging. Skeletal Radiol. 2012;41:685–92.
13. Boesen M, Jensen KE, Qvistgaard E, Danneskiold-Samsoe B, Thomsen C, Ostergaard M, Bliddal H. Delayed gadolinium-enhanced magnetic resonance imaging (dGEMRIC) of hip joint cartilage: better cartilage delineation after intra-articular than intravenous gadolinium injection. Acta Radiol. 2006;47:391–6.
14. Kwack KS, Cho JH, Kim MM, Yoon CS, Yoon YS, Choi JW, Kwon JW, Min BH, Sun JS, Kim SY. Comparison study of intraarticular and intravenous gadolinium-enhanced magnetic resonance imaging of cartilage in a canine model. Acta Radiol. 2008;49:65–74.
15. Bittersohl B, Hosalkar HS, Kim YJ, Werlen S, Trattnig S, Siebenrock KA, Mamisch TC. T1 assessment of hip joint cartilage following intra-articular gadolinium injection: a pilot study. Magn Reson Med. 2010;64:1200–7.
16. Bittersohl B, Hosalkar HS, Werlen S, Trattnig S, Siebenrock KA, Mamisch TC. Intravenous versus intra-articular delayed gadolinium-enhanced magnetic resonance imaging in the hip joint: a comparative analysis. Invest Radiol. 2010;45:538–42.

17. Abujudeh HH, Kaewlai R, Kagan A, Chibnik LB, Nazarian RM, High WA, Kay J. Nephrogenic systemic fibrosis after gadopentetate dimeglumine exposure: case series of 36 patients. Radiology. 2009; 253:81–9.
18. Nojiri T, Watanabe N, Namura T, Narita W, Ikoma K, Suginoshita T, Takamiya H, Komiyama H, Ito H, Nishimura T, Kubo T. Utility of delayed gadolinium-enhanced MRI (dGEMRIC) for qualitative evaluation of articular cartilage of patellofemoral joint. Knee Surg Sports Traumatol Arthrosc. 2006;14:718–23.
19. Tiderius C, Hori M, Williams A, Sharma L, Prasad PV, Finnell M, McKenzie C, Burstein D. dGEMRIC as a function of BMI. Osteoarthritis Cartilage. 2006;14:1091–7.
20. Anandacoomarasamy A, Leibman S, Smith G, Caterson I, Giuffre B, Fransen M, Sambrook PN, March L. Weight loss in obese people has structure-modifying effects on medial but not on lateral knee articular cartilage. Ann Rheum Dis. 2012;71:26–32.
21. Burstein D, Velyvis J, Scott KT, Stock KW, Kim YJ, Jaramillo D, Boutin RD, Gray ML. Protocol issues for delayed Gd(DTPA)(2-)-enhanced MRI (dGEMRIC) for clinical evaluation of articular cartilage. Magn Reson Med. 2001;45:36–41.
22. Hawezi ZK, Lammentausta E, Svensson J, Dahlberg LE, Tiderius CJ. In vivo transport of Gd-DTPA(2-) in human knee cartilage assessed by depth-wise dGEMRIC analysis. J Magn Reson Imaging. 2011;34:1352–8.
23. Gillis A, Gray M, Burstein D. Relaxivity and diffusion of gadolinium agents in cartilage. Magn Reson Med. 2002;48:1068–71.
24. Salo EN, Nissi MJ, Kulmala KA, Tiitu V, Toyras J, Nieminen MT. Diffusion of Gd-DTPA(2)(−) into articular cartilage. Osteoarthritis Cartilage. 2012; 20:117–26.
25. Tiderius CJ, Jessel R, Kim YJ, Burstein D. Hip dGEMRIC in asymptomatic volunteers and patients with early osteoarthritis: the influence of timing after contrast injection. Magn Reson Med. 2007;57:803–5.
26. Tiderius CJ, Olsson LE, Leander P, Ekberg O, Dahlberg L. Delayed gadolinium-enhanced MRI of cartilage (dGEMRIC) in early knee osteoarthritis. Magn Reson Med. 2003;49:488–92.
27. Kimelman T, Vu A, Storey P, McKenzie C, Burstein D, Prasad P. Three-dimensional T1 mapping for dGEMRIC at 3.0 T using the look locker method. Invest Radiol. 2006;41:198–203.
28. McKenzie CA, Williams A, Prasad PV, Burstein D. Three-dimensional delayed gadolinium-enhanced MRI of cartilage (dGEMRIC) at 1.5T and 3.0T. J Magn Reson Imaging. 2006;24:928–33.
29. Li W, Scheidegger R, Wu Y, Vu A, Prasad PV. Accuracy of T1 measurement with 3-D look-locker technique for dGEMRIC. J Magn Reson Imaging. 2008;27:678–82.
30. Mamisch TC, Dudda M, Hughes T, Burstein D, Kim YJ. Comparison of delayed gadolinium enhanced MRI of cartilage (dGEMRIC) using inversion recovery and fast T1 mapping sequences. Magn Reson Med. 2008;60:768–73.
31. Szumowski J, Durkan MG, Foss EW, Brown DS, Schwarz E, Crawford DC. Signal polarity restoration in a 3D inversion recovery sequence used with delayed gadolinium-enhanced magnetic resonance imaging of cartilage (dGEMRIC). J Magn Reson Imaging. 2012;35(5):1248–55.
32. Sur S, Mamisch TC, Hughes T, Kim YJ. High resolution fast T1 mapping technique for dGEMRIC. J Magn Reson Imaging. 2009;30:896–900.
33. Bittersohl B, Steppacher S, Haamberg T, Kim YJ, Werlen S, Beck M, Siebenrock KA, Mamisch TC. Cartilage damage in femoroacetabular impingement (FAI): preliminary results on comparison of standard diagnostic vs delayed gadolinium-enhanced magnetic resonance imaging of cartilage (dGEMRIC). Osteoarthritis Cartilage. 2009;17:1297–306.
34. Bittersohl B, Hosalkar HS, Werlen S, Trattnig S, Siebenrock KA, Mamisch TC. dGEMRIC and subsequent T1 mapping of the hip at 1.5 tesla: normative data on zonal and radial distribution in asymptomatic volunteers. J Magn Reson Imaging. 2011; 34:101–6.
35. Domayer SE, Mamisch TC, Kress I, Chan J, Kim YJ. Radial dGEMRIC in developmental dysplasia of the hip and in femoroacetabular impingement: preliminary results. Osteoarthritis Cartilage. 2010;18: 1421–8.
36. Siversson C, Tiderius CJ, Dahlberg L, Svensson J. Local flip angle correction for improved volume T1-quantification in three-dimensional dGEMRIC using the look-locker technique. J Magn Reson Imaging. 2009;30:834–41.
37. Lattanzi R, Glaser C, Mikheev AV, Petchprapa C, Mossa DJ, Gyftopoulos S, Rusinek H, Recht M, Kim D. A B1-insensitive high resolution 2D T1 mapping pulse sequence for dGEMRIC of the HIP at 3 tesla. Magn Reson Med. 2011;66:348–55.
38. Siversson C, Chan J, Tiderius CJ, Mamisch TC, Jellus V, Svensson J, Kim YJ. Effects of B1 inhomogeneity correction for three-dimensional variable flip angle T1 measurements in hip dGEMRIC at 3 T and 1.5 T. Magn Reson Med. 2012;67:1776–81.
39. Welsch GH, Mamisch TC, Hughes T, Zilkens C, Quirbach S, Scheffler K, Kraff O, Schweitzer ME, Szomolanyi P, Trattnig S. In vivo biochemical 7.0 tesla magnetic resonance: preliminary results of dGEMRIC, zonal T2, and T2* mapping of articular cartilage. Invest Radiol. 2008;43:619–26.
40. Nieminen MT, Menezes NM, Williams A, Burstein D. T2 of articular cartilage in the presence of Gd-DTPA2. Magn Reson Med. 2004;51:1147–52.
41. Taylor C, Carballido-Gamio J, Majumdar S, Li X. Comparison of quantitative imaging of cartilage for osteoarthritis: T2, T1rho, dGEMRIC and contrast-

enhanced computed tomography. Magn Reson Imaging. 2009;27:779–84.
42. Eckstein F, Buck RJ, Wyman BT, Kotyk JJ, Le Graverand MP, Remmers AE, Evelhoch JL, Hudelmaier M, Charles HC. Quantitative imaging of cartilage morphology at 3.0 tesla in the presence of gadopentate dimeglumine (Gd-DTPA). Magn Reson Med. 2007;58:402–6.
43. Eckstein F, Wyman BT, Buck RJ, Wirth W, Maschek S, Hudelmaier M, Le Graverand MP. Longitudinal quantitative MR imaging of cartilage morphology in the presence of gadopentetate dimeglumine (Gd-DTPA). Magn Reson Med. 2009; 61:975–80.
44. Multanen J, Rauvala E, Lammentausta E, Ojala R, Kiviranta I, Hakkinen A, Nieminen MT, Heinonen A. Reproducibility of imaging human knee cartilage by delayed gadolinium-enhanced MRI of cartilage (dGEMRIC) at 1.5 tesla. Osteoarthritis Cartilage. 2009;17:559–64.
45. Bittersohl B, Hosalkar HS, Haamberg T, Kim YJ, Werlen S, Siebenrock KA, Mamisch TC. Reproducibility of dGEMRIC in assessment of hip joint cartilage: a prospective study. J Magn Reson Imaging. 2009;30:224–8.
46. Tiderius CJ, Tjornstrand J, Akeson P, Sodersten K, Dahlberg L, Leander P. Delayed gadolinium-enhanced MRI of cartilage (dGEMRIC): intra- and interobserver variability in standardized drawing of regions of interest. Acta Radiol. 2004;45:628–34.
47. Bron EE, van Tiel J, Smit H, Poot DH, Niessen WJ, Krestin GP, Weinans H, Oei EH, Kotek G, Klein S. Image registration improves human knee cartilage T1 mapping with delayed gadolinium-enhanced MRI of cartilage (dGEMRIC). Eur Radiol. 2013;23(1): 246–52.
48. Van Ginckel A, Baelde N, Almqvist KF, Roosen P, McNair P, Witvrouw E. Functional adaptation of knee cartilage in asymptomatic female novice runners compared to sedentary controls. A longitudinal analysis using delayed gadolinium enhanced magnetic resonance imaging of cartilage (dGEMRIC). Osteoarthritis Cartilage. 2010;18:1564–9.
49. Bashir A, Gray ML, Hartke J, Burstein D. Nondestructive imaging of human cartilage glycosaminoglycan concentration by MRI. Magn Reson Med. 1999;41:857–65.
50. Williams A, Shetty SK, Burstein D, Day CS, McKenzie C. Delayed gadolinium enhanced MRI of cartilage (dGEMRIC) of the first carpometacarpal (1CMC) joint: a feasibility study. Osteoarthritis Cartilage. 2008;16:530–2.
51. Miese F, Buchbender C, Scherer A, Wittsack HJ, Specker C, Schneider M, Antoch G, Ostendorf B. Molecular imaging of cartilage damage of finger joints in early rheumatoid arthritis with delayed gadolinium-enhanced magnetic resonance imaging. Arthritis Rheum. 2012;64:394–9.
52. Miese F, Kropil P, Ostendorf B, Scherer A, Buchbender C, Quentin M, Lanzman RS, Blondin D, Schneider M, Bittersohl B, Zilkens C, Jellus V, Ch Mamisch T, Wittsack HJ. Motion correction improves image quality of dGEMRIC in finger joints. Eur J Radiol. 2011;80:e427–31.
53. Domayer SE, Trattnig S, Stelzeneder D, Hirschfeld C, Quirbach S, Dorotka R, Nehrer S, Pinker K, Chan J, Mamisch TC, Dominkus M, Welsch GH. Delayed-gadolinium-enhanced MRI of cartilage in the ankle at 3 T: feasibility and preliminary results after matrix-associated autologous chondrocyte implantation. J Magn Reson Imaging. 2010;31:732–9.
54. Krishnan N, Shetty SK, Williams A, Mikulis B, McKenzie C, Burstein D. Delayed gadolinium-enhanced magnetic resonance imaging of the meniscus: an index of meniscal tissue degeneration? Arthritis Rheum. 2007;56:1507–11.
55. Mayerhoefer ME, Welsch GH, Riegler G, Mamisch TC, Materka A, Weber M, El-Rabadi K, Friedrich KM, Dirisamer A, Trattnig S. Feasibility of texture analysis for the assessment of biochemical changes in meniscal tissue on T1 maps calculated from delayed gadolinium-enhanced magnetic resonance imaging of cartilage data: comparison with conventional relaxation time measurements. Invest Radiol. 2010;45:543–7.
56. Mayerhoefer ME, Mamisch TC, Riegler G, Welsch GH, Dobrocky T, Weber M, Apprich S, Scheurecker G, Szomolanyi P, Puchner S, Trattnig S. Gadolinium diethylenetriaminepentaacetate enhancement kinetics in the menisci of asymptomatic subjects: a first step towards a dedicated dGEMRIC (delayed gadolinium-enhanced MRI of cartilage)-like protocol for biochemical imaging of the menisci. NMR Biomed. 2011;24:1210–5.
57. Vaga S, Brayda-Bruno M, Perona F, Fornari M, Raimondi MT, Petruzzi M, Grava G, Costa F, Caiani EG, Lamartina C. Molecular MR imaging for the evaluation of the effect of dynamic stabilization on lumbar intervertebral discs. Eur Spine J. 2009;18 Suppl 1:40–8.
58. Vaga S, Raimondi MT, Caiani EG, Costa F, Giordano C, Perona F, Zerbi A, Fornari M. Quantitative assessment of intervertebral disc glycosaminoglycan distribution by gadolinium-enhanced MRI in orthopedic patients. Magn Reson Med. 2008; 59:85–95.
59. Tiderius CJ, Svensson J, Leander P, Ola T, Dahlberg L. dGEMRIC (delayed gadolinium-enhanced MRI of cartilage) indicates adaptive capacity of human knee cartilage. Magn Reson Med. 2004;51:286–90.
60. Roos EM, Dahlberg L. Positive effects of moderate exercise on glycosaminoglycan content in knee cartilage: a four-month, randomized, controlled trial in patients at risk of osteoarthritis. Arthritis Rheum. 2005;52:3507–14.

61. Anandacoomarasamy A, Giuffre BM, Leibman S, Caterson ID, Smith GS, Fransen M, Sambrook PN, March LM. Delayed gadolinium-enhanced magnetic resonance imaging of cartilage: clinical associations in obese adults. J Rheumatol. 2009;36:1056–62.
62. Williams A, Sharma L, McKenzie CA, Prasad PV, Burstein D. Delayed gadolinium-enhanced magnetic resonance imaging of cartilage in knee osteoarthritis: findings at different radiographic stages of disease and relationship to malalignment. Arthritis Rheum. 2005;52:3528–35.
63. Mamisch TC, Kain MS, Bittersohl B, Apprich S, Werlen S, Beck M, Siebenrock KA. Delayed gadolinium-enhanced magnetic resonance imaging of cartilage (dGEMRIC) in femoacetabular impingement. J Orthop Res. 2011;29:1305–11.
64. Pollard TC, McNally EG, Wilson DC, Wilson DR, Madler B, Watson M, Gill HS, Carr AJ. Localized cartilage assessment with three-dimensional dGEMRIC in asymptomatic hips with normal morphology and cam deformity. J Bone Joint Surg. 2010;92:2557–69.
65. Young AA, Stanwell P, Williams A, Rohrsheim JA, Parker DA, Giuffre B, Ellis AM. Glycosaminoglycan content of knee cartilage following posterior cruciate ligament rupture demonstrated by delayed gadolinium-enhanced magnetic resonance imaging of cartilage (dGEMRIC). A case report. J Bone Joint Surg. 2005;87:2763–7.
66. Owman H, Tiderius CJ, Neuman P, Nyquist F, Dahlberg LE. Association between findings on delayed gadolinium-enhanced magnetic resonance imaging of cartilage and future knee osteoarthritis. Arthritis Rheum. 2008;58:1727–30.
67. Tiderius CJ, Sandin J, Svensson J, Dahlberg LE, Jacobsson L. Knee cartilage quality assessed with dGEMRIC in rheumatoid arthritis patients before and after treatment with a TNF inhibitor. Acta Radiol. 2010;51:1034–7.
68. Fleming BC, Oksendahl HL, Mehan WA, Portnoy R, Fadale PD, Hulstyn MJ, Bowers ME, Machan JT, Tung GA. Delayed gadolinium-enhanced MR imaging of cartilage (dGEMRIC) following ACL injury. Osteoarthritis Cartilage. 2010;18:662–7.
69. Neuman P, Tjornstrand J, Svensson J, Ragnarsson C, Roos H, Englund M, Tiderius CJ, Dahlberg LE. Longitudinal assessment of femoral knee cartilage quality using contrast enhanced MRI (dGEMRIC) in patients with anterior cruciate ligament injury–comparison with asymptomatic volunteers. Osteoarthritis Cartilage. 2011;19:977–83.
70. Ericsson YB, Tjornstrand J, Tiderius CJ, Dahlberg LE. Relationship between cartilage glycosaminoglycan content (assessed with dGEMRIC) and OA risk factors in meniscectomized patients. Osteoarthritis Cartilage. 2009;17:565–70.
71. McAlindon TE, Nuite M, Krishnan N, Ruthazer R, Price LL, Burstein D, Griffith J, Flechsenhar K. Change in knee osteoarthritis cartilage detected by delayed gadolinium enhanced magnetic resonance imaging following treatment with collagen hydrolysate: a pilot randomized controlled trial. Osteoarthritis Cartilage. 2011;19:399–405.

Clinical Application of Biochemical Imaging of Cartilage

4

Goetz H. Welsch, Friedrich F. Hennig, and Andreas Mauerer

Introduction

These recent advances in MR sequences together with the implementation of high-resolution MRI due to high-field MR systems as well as sophisticated coil technology have overcome existing limitations and led to promising in vivo approaches in morphological, however, especially in biochemical MRI of cartilage [1–3]. Significant advances have been made in characterizing, quantifying, and standardizing the specific morphological as well as biochemical changes in patients with cartilage pathologies. Besides the exact evaluation of the cartilage defect, respectively, the cartilage degeneration, also the specific therapeutical approaches, can be assessed in best possible fashion noninvasively [4–6]. This precise assessment of the biochemical composition of articular cartilage was initially used in clinical approaches in the knee joint [7–9] and some years later also in the thinner articular cartilage of the hip joint [10, 11].

Concerning articular cartilage, standard MRI can visualize morphological alterations such as reduction in cartilage volume, cartilage contour irregularities, fissures, and cartilage thinning [12]. As structural cartilage damage is preceded by biochemical alterations such as proteoglycan loss, or changes in the collagen matrix, there is a substantial interest in detecting such changes in the course of cartilage disease/injury or after cartilage repair [13–15].

The biochemical MRI techniques most often reported to visualize cartilage ultra-structure are delayed Gadolinium-enhanced MRI of cartilage (dGEMRIC) and T2 mapping [16, 17]. Using dGEMRIC, biochemical MRI has the ability to quantify functionally relevant macromolecules within articular cartilage such as glycosaminoglycans (GAG). GAG are the main source of fixed charge density (FCD) in cartilage, which are often decreased in the early stages of cartilage degeneration and are considered as a key factor in the progression of cartilage damage. In a clinical background, the role of GAG is comparably important in the follow-up after cartilage repair procedures where hyaline-like repair tissue with a normal or nearly normal amount of proteoglycans is seen to have a positive predictive value [18]. In hip disorders like hip dysplasia, the GAG content as a quantifiable measure of cartilage health has also a positive predictive value on the outcome of hip joint preserving surgeries [19].

T2 relaxation time mapping reflects the interaction of water and the extracellular matrix. Changes in hydration as well as collagen anisotropy, reported to be early indicators of cartilage

G.H. Welsch (✉)
Department of Trauma Surgery, University Hospital of Erlangen, Krankenhausstr. 12, Erlangen 91054, Germany

Department of Radiology, MR Center, Medical University of Vienna, Vienna, Austria
e-mail: goetz.welsch@uk-erlangen.de

Y.-J. Kim (eds.), *Hip Magnetic Resonance Imaging*,
DOI 10.1007/978-1-4614-1668-5_4,

deterioration, can be visualized by T2 relaxation time mapping. In cartilage repair, quantitative T2 mapping is able to assess the zonal structure of the repair tissue, and hence the maturation of the repair tissue over time [20]. In osteoarthritis, T2 mapping techniques can be correlated to the different grades and thus the progression of the disease [21, 22], whereas, e.g., in hip dysplasia T2 mapping with loading enables for the detection of site-specific cartilage changes [23].

Aim of this manuscript was to review the current literature and present own ideas and studies how biochemical MR techniques can be of clinical use in daily patient care. Hence, with the focus on the knee and the hip joint in cartilage repair as well as in degenerative cartilage changes possible advantages of biochemical MR techniques will be presented. These advantages might offer the possibility to gain new insights into cartilage pathologies and their joint preserving therapy.

Prerequirements for the Clinical Application of Biochemical Cartilage Imaging

When working on an optimal protocol for advanced cartilage imaging, the first question is which MR system to use. Commonly available systems are of different vendors and have field strengths of 1.0, 1.5, or 3.0 T. There are different studies available to compare different field strengths in there ability to diagnose knee or hip pathologies as well as providing information on the benefits of higher fields [24–26].

Although at 1.0 or 1.5 T MRI is able to detect cartilage irregularities in high quality, the 3.0 T examinations provided a better visibility especially of smaller structures and cartilage was better delineated as well as offers more possibilities for biochemical MR techniques [26]. This is usually based on an increased average signal-to-noise and contrast-to-noise ratio at higher fields. Concluding, at 3.0 T, imaging is faster and/or a higher visibility (and resolution) of anatomic structures can be reached [25, 26]. In cartilage injury or repair, the highest available field strength should be used to provide the best available quality of the MR protocol. Especially in the hip joint by adding completely new joint preserving surgical procedures to the clinical treatment protocols, cartilage injuries or focal chondral defects can be addressed, e.g., arthroscopically which was not possible some years ago. These surgical procedures nevertheless pre-require high-resolution, high-quality diagnosis and the thin hip cartilage needs to be delineated by MRI. Hence, especially in the hip, the role of MR hardware (e.g., field strength) is important.

Furthermore when, e.g., at 3 T the clinical (needed) morphological protocol can be optimized and the MR protocol is shortened, biochemical techniques might be added. Furthermore, most of the biochemical techniques, especially in their assessment of the thin cartilage layers, need also high-resolution and enough signal-to-noise. This is especially important as these biochemical techniques are often very sensitive and if too much noise is present, their interpretation hard and the validity of the results is of inferior quality. Concluding comparable to morphological MR measurements, also for biochemical MRI of the thin cartilage layers of the hip, high resolution and the highest available field strength has to be used for the MR measurements.

Besides the field strength, however, the selection of a dedicated, multi-channel coil is possibly even more important [25, 26]. Most available MR scanners today come with an 8 or 15 channel knee coil. To use these coils in cartilage patients will improve the image quality and provide also in 1.0 or 1.5 T the ability to end up in high-resolution MR protocols in an acceptable acquisition time. The benefit of multi-channel coils lies (in parts) in the possibility of parallel-imaging where basically more information can be acquired in less time. In a study by Zou et al. it was demonstrated that parallel-imaging can be applied to current knee cartilage protocols with an acceleration factor of 2 (reduces acquisition time by 50 %) without degrading measurement

accuracy and good reproducibility [27]. Also in the hip new coils which are more dedicated for the hip joint will be available and together with a new generation of MR scanners these coils will be easier to use and more signal will be available for morphological and biochemical MRI techniques of the hip.

The prerequirement of an optimal MR scan is using the right sequences and plans the sequences on the localizer (initial landmark scan of the knee or hip) in the right direction. Hence, in a standard 2D MR evaluation, to gain - high-quality, high-resolution images, the anatomical curvature and localization of, e.g., the femoral neck in correlation to the acatabular labrum have to be taken into consideration. Hence, to take the goal of the respective MR scan into consideration, before planning the sequences protocol, enables for including biochemical techniques which then will provide additional information in a clinical setup. When only specific questions have to be answered by the biochemical sequences, the scan time might not be too long which is in the most hospitals or institutes, one of the most important points which have to be taken into consideration. Concluding by optimizing the hardware (scanner and coils), by optimizing the basic (morphological) MR protocol, and by including only one or two biochemical sequences in a specific orientation or anatomical region, biochemical MRI can be added to clinical MRI in diagnosis and in the follow-up of treated patients.

Diagnosis of Cartilage Pathologies Preoperatively Using Isotropic Morphological and Biochemical MRI

The quality of the diagnosis is naturally one of the most important parts when treating patients. When a cartilage pathology is diagnosed, besides the age of the patient, the activity level, the symptoms, and other clinical findings, the suspected dimension of this cartilage defect is one of the most important things especially when planning surgery. Furthermore, e.g., by focal cartilage defects, the surrounding cartilage and/or the corresponding cartilage surfaces have to be assessed. Hence, the MRI needs to be of high quality, especially as existing studies show that radiologic reports based on standard morphological MRI frequently underestimate the actual size of a lesion (which were then found intra-operatively) [28, 29]. In the study of Gomoll and coworkers, cartilage lesions were underestimated up to 300 % in the patellofemoral joint [29]. Based on a high-quality MRI, this should not be the case and cartilage lesions should be graded better. For sure it will never be possible that a 100 % match is reached between noninvasive diagnosis and the following surgery; nevertheless for preparing a tailored surgical or nonsurgical approach, the match has to be in the range of the real defect. The estimation of the cartilage pathology is even more demanding in the hip joint. Reasons for the preoperative underestimation of the cartilage lesion are based on different reasons. Besides an optimal, high-resolution MR protocol, possibly better results can be reached by exploiting isotropic MR sequences which have the potential to assess the three-dimensional anatomy of the hip joint isotropically in 3D (Fig. 4.1) and not only in two dimensions where the differences in between the anatomical orientation of the acetabulum and the femoral head and neck will always be a problem [3, 30]. Besides this biochemical MR sequences are enabling for a more precise and better diagnosis of cartilage pathologies in the specific joint. Although a full thickness cartilage defect that is filled by synovial fluid cannot be evaluated, biochemical MRI is a very promising tool to (1) assess the borders of the cartilage defect regarding to their quality, (2) assess the cartilage defect itself if there is not a full-thickness defect, and (3) assess the cartilage quality of the surrounding and the corresponding/opposing cartilage (Fig. 4.2). Although nearly no studies are available on this topic, all given examples will be topics of future research and will help in clinical decision making. To evaluate a more chronic and not full-thickness cartilage defect in its quality of the thin remaining cartilage layer is another possible option for the preoperative use OB biochemical MRI. Hence, the biochemical and

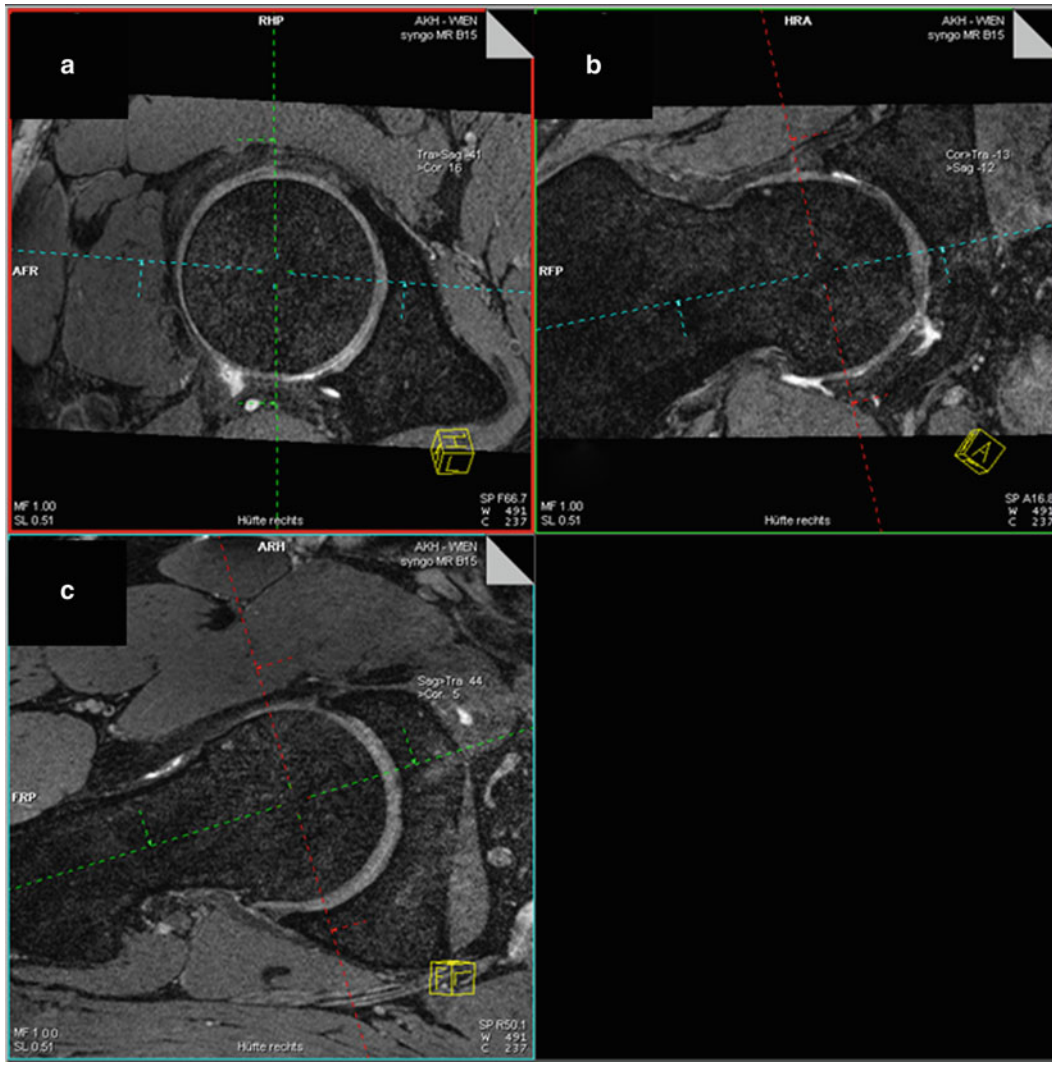

Fig. 4.1 A 3D isotropic fsPD SPCAE sequence of a 26-year-old soccer player with symptomatic FAI is provided with its multi-planar reconstruction in different planes (**a**–**c**). If in a clinical study only a few biochemical slides can be obtained, e.g., in a patient with CAM impingement, the interesting anterior-lateral orientation can be reconstructed in the isotropic sequences, and the thicker (~ 3 mm) biochemical slides can be obtained

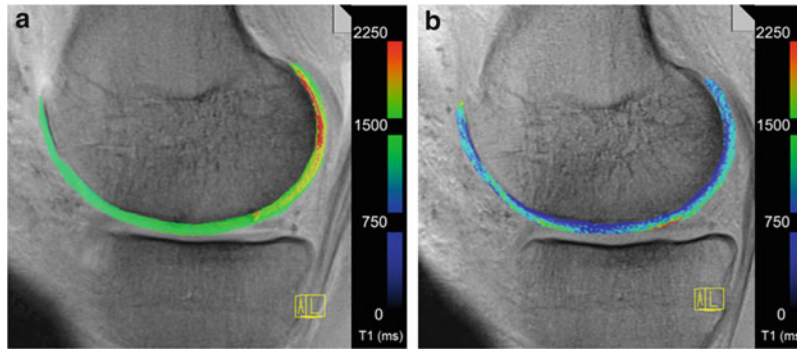

Fig. 4.2 A gradient echo T1 mapping sequence before (**a**) and after (**b**) i.v. Gadolinium (dGEMRIC) of a 36-year-old patient with suspicious early OA after repetitive smaller injuries of the lower extremity and chronic pain during running

biomechanical quality of these cartilage areas can be assessed. This is in initial studies already possible where a dGEMRIC index is used in the preoperative assessment of the cartilage quality before hip preserving surgery [10]. By including biomechanical MRI, initial studies showed that early cartilage changes can be quantified and detected [21, 31].

Concluding preoperative MRI (respectively, optimal cartilage diagnosis) should contain of a set of cartilage-sensitive MR sequences, and if possible, a 3D-isotropic MR sequence and as well as (if possible) of biochemical MR sequences. Moreover, the rest of the joint has to be diagnosed in comparably high quality.

Clinical Applications to Visualize the Glycosaminoglycan Content

dGEMRIC displays the distribution of glycosaminoglycans (GAGs), one of the major macromolecular constituents of cartilage which appears to be a key factor for its mechanical function. GAGs are lost at early stages of OA and would need to be replenished with therapy [32]. To quantify GAGs, dGEMRIC utilizes the anionic contrast agent gadopentetate dimeglumine (Magnevist; Schering AG, Berlin, Germany). Due to abundant carboxyl and sulfate groups, GAGs are negatively charged too. Therefore, lost GAGs will be replaced by Gd $(DTPA)^{2-}$, if given time to penetrate cartilage tissue. The distribution of $Gd(DTPA)^{2-}$ in tissues can be determined through MR measurements of the longitudinal relaxation time T1 for which an approximately linear inverse relationship with the GAG concentration has been demonstrated [16].

Recent clinical applications highlight the ability of dGEMRIC to demonstrate cartilage changes in patients with early OA [33], the influence of traumatic knee injuries, such as anterior cruciate ligament injuries, on the GAG content of cartilage [34], and differences in the tissue matrix of native cartilage and cartilage implants during follow-up of therapy [13, 35]. These studies show the applicability of dGEMRIC in a clinical background with different benefits in clinical studies and patient care:

- The GAG content can be quantified and in larger patient cohorts it is possible (when a comparable protocol is used at a comparable magnet and coil) to get a noninvasive information of the quality of the cartilage layers.
- Early grades of OA can be diagnosed and quantified which provides another measure in decision making, e.g., when planning a joint preserving surgery. Using this possibility, predictive values are available before treating the patient.
- Therapy monitoring after various surgical or nonsurgical treatments is possible on a histological level without the need of a biopsy.
- After cartilage repair, the maturation of the repair tissue can be assessed over time, and possible biomechanical statements (e.g., when the patient can return to high impact sports) can be answered.
- After cartilage repair the quality of the repair tissue can be assessed noninvasively which provides a predictive value on the durability of the cartilage transplant and helps to assess the probability of failures [18, 36].
- New therapeutical approaches can be assessed in their ability to treat cartilage pathologies noninvasively which is important for nonsurgical and surgical options. Especially upcoming treatment options might be assessed easier and in more detail (on a histological level).

These options are based on initial clinical studies in smaller patient groups [14, 37–43] and have to be verified in larger patient cohorts. Although these clinical applications are all preliminary, the strength of assessing the GAG content noninvasively by means of MRI and not by means of histological biopsies is not questionable. However, it has to be stated clearly that comparable analysis might be able in future approaches with other biochemical MR sequences possibly without the need for administering a gadolinium-based contrast agent and possiblenephrotoxicity.

In an investigation of the dGEMRIC technique in a clinical setup, a high-resolution, fast dual angle T1 mapping technique for 3D

isotropic imaging was introduced to assess dGEMRIC index of the hip at 1.5 T, which provides sufficient resolution for accurate 2D reformatting [38, 44]. Previous studies on dGEMRIC have primarily used T1 maps of the cartilage from single-slice two-dimensional (2D) inversion recovery fast spin-echo (IR-FSE) sequences. This method has been validated in vitro and in vivo [45]; however, in a clinical setup and for the in vivo clinical application several shortcomings of the single slices acquisition sequence such as the lack of joint coverage, long acquisition times, and the need for post-processing have limited its clinical use and its accuracy for follow-up of localized lesions. Therefore, the 3D sequence for T1 and the dGEMRIC index was introduced for the hip [38, 44]. In an additional study the reproducibility of dGEMRIC was evaluated at the hip [46]. Two independent dGEMRIC examinations using the above high-resolution, fast dual angle T1 mapping were performed in ten asymptomatic adult volunteers with a very high interclass correlation coefficient (ICC) which proves the clinical applicability as well as the reproducibility in longitudinal patient measurements. Based on these results, a specific hip protocol could be introduced by the group around Kim and Mamisch and the cartilage degradation FAI patients could be quantified in a patient cohort [47]. In this study, OA grading according to Tönnis based on standard radiographs and morphological MRI was compared with quantitative dGEMRIC measurements in ten asymptomatic young adults and 26 FAI patients. Compared to asymptomatic volunteers, cam- and pincer-type FAI patients had significantly lower T1 values in the group without radiographic evidence of OA proving that a biochemical MRI technique like dGEMRIC is able to assess a subtle decrease in the GAG content of cartilage before morphological changes begin. In an earlier study, the research group of Kim et al. applied dGEMRIC technique in a large patient cohort suffering from hip dysplasia prior to hip preserving surgery by PAO and correlated it with clinically relevant parameters like pain (assessed with WOMAC questionnaire) and severity of dysplasia [10]. In a subsequent study, the same research group performed a cohort study on patients undergoing PAO for the treatment of hip dysplasia with the goal to identify radiographic, clinical, and magnet resonance imaging findings that best predict treatment failure [19]. Multivariate analysis identified the dGEMRIC index as the most important predictor of failure of the osteotomy. For each 100-ms increase in the dGEMRIC value, the likelihood of failure decreased by 77 %, indicating a dramatically improved chance of success in the early postoperative period if the patient had a higher dGEMRIC value prior to the surgery.

However as mentioned above due to the significant limitation of using contrast agent for dGEMRIC including very sever side effects like nephrogenic systemic fibrosis (NSF), it has a limitation in its use in large scale clinical trials or for screening of OA. Therefore, none-contrast techniques would be preferable in long term.

Here 23(Na)-sodium imaging allows measurement of the FCD and hence quantification of the GAG content which offers a method for noninvasive in vivo evaluation of joint cartilage similar to the dGEMRIC technique [48, 49]. However, sodium MRI is up to now based on its low signal (in contrast to standard MRI) dependent on ultra-high fields if an in vivo evaluation of joint cartilage has to be performed. Initial studies on its use in the knee and the ankle are available, whereas in the hip joint, based on the thin cartilage layers and the lack of availability of dedicated multi-channel coils, clinical sodium imaging protocols are not yet available. Another possible non-contrast measure of the GAG content in cartilage is chemical exchange saturation transfer (CEST). CEST is a versatile contrast enhancement mechanism for MR imaging, where the CEST effect depends on the molecular group that provides the exchanging proton(s). One application of the CEST contrast is biochemical cartilage imaging, where the CEST contrast is generated by protons of glycosaminoglycans (gagCEST) [50]. However, also CEST imaging has still its drawbacks in clinical routine mainly because of the relatively long scan times necessary to obtain a

reliable CEST contrast in multi-slice examinations. Based on new CEST imaging methods, providing consistent contrast in 3D scans within clinically acceptable measurement times, its clinical applicability nevertheless has been shown in initial studies [48, 51]. The high correlation between the introduced gagCEST method and [23] Na imaging implies that gagCEST is a potentially useful biomarker for glycosaminoglycans. Initial, ongoing studies will prove its applicability not only in the knee joint, but also in the GAG quantification of hip joint cartilage.

Another biochemical MR marker, relaxation time in the rotating frame (T1 rho), has been reported to be a sensitive marker of the loss of proteoglycans in articular cartilage [52–54]. T1rho is a time constant that characterizes the magnetic relaxation of spins under the influence of a radiofrequency field that is parallel to the spin magnetization. Changes in T1 rho were observed in cartilage plugs that were chemically or enzymatically depleted of GAG, but not in collagenase-treated tissue [54]. On the other hand, Menezes et al. found no correlation between the cartilage $T_1\rho$ and GAG concentration [55]. Hence, T1rho has to be shown a valuable parameter in biochemical MR imaging of joint cartilage in the last years [53, 56]; its role as a replacement of dGEMRIC, however, is questionable. In a recent study, the clinical application of T1rho in the hip joint in patients with FAI has been shown and [57] acetabular hyaline cartilage changes in patients with FAI could be shown.

Concluding in the clinical applications to visualize the glycosaminoglycan content, dGEMRIC is still the standard, however, with the given disadvantages. Other sequences will show their potential in the quantification of GAG in knee and hip cartilage.

Clinical Applications to Visualize the Collagen Content and Orientation

Perhaps the most frequently implemented biochemical MR technique is the transverse relaxation time (T2) of cartilage as a sensitive parameter for the evaluation of changes in water and collagen content and tissue anisotropy [17]. Cartilage T2 reflects the interaction of water and the extracellular matrix on a molecular level. The collagen fiber orientation defines the layers of articular cartilage. Thus, the three-dimensional organization and curvature of the collagen network, influenced by water mobility, the proteoglycan orientation, and the resulting magic angle at 55° (with respect to the main magnetic field (B0)), influence the appearance of T2[26,71]. Many studies especially in the knee joint, however also in the hip joint, show different clinical applications of T2 mapping and hence collagen-sensitive biochemical MRI [15, 22, 23, 58–61]. These studies show the applicability of T2 mapping in a clinical background with different benefits in clinical studies and patient care:

- The collagen orientation and (in parts) the collagen content can be quantified and in larger patient cohorts it is possible (when a comparable protocol is used at a comparable magnet and coil) to get a noninvasive information of the quality of the cartilage layers.
- Early grades of OA can be diagnosed and quantified which provides another measure in decision making, e.g., when planning a joint preserving surgery. However in comparison to dGEMRIC, for T2 mapping there is no uni-directional when degeneration is taking place. This makes it harder to really interpret slightly increased or decreased T2 values.
- Therapy monitoring after various surgical or nonsurgical treatments is possible on a histological level without the need of a biopsy.
- Especially for T2 mapping and all other collagen-sensitive MR techniques, a zonal evaluation of the cartilage is essential to provide a precise information if a hyaline-like cartilage structure is present.
- Biomechanical MRI is relatively easily possible in clinical patient care and loading- or unloading can be visualized.
- After cartilage repair, the maturation of the repair tissue can be assessed over time, and possible biomechanical statements (e.g., when the patient can return to high impact sports) can be answered.

- After cartilage repair the quality of the repair tissue can be assessed noninvasively which provides a predictive value on the durability of the cartilage transplant and helps to assess the probability of failures [18, 36].
- New therapeutical approaches can be assessed in their ability to treat cartilage pathologies noninvasively which is important for nonsurgical and surgical options. Especially upcoming treatment options might be assessed easier and in more detail (on a histological level).

Hence, collagen-sensitive biochemical MR techniques provide roughly comparable possibilities than GAG-sensitive techniques. A drawback of, e.g., T2 mapping, however, is the problem in the interpretation of, e.g., slightly decreased or increased values [62]; a clear benefit is the relatively easy clinical use and the relatively robust sequence without the need of contrast agent. A further advantage is the various biomechanical applications which are already available for clinical applications. For example, loading or unloading of cartilage areas can be assessed noninvasively and in vivo, where initial studies show a clearly different biomechanical response of healthy and altered (OA or after cartilage repair) articular cartilage to unloading [21, 63]. In biochemical or biomechanical collagen-sensitive MRI, the zonal evaluation of cartilage plays an important role. In healthy articular cartilage, an increase in T2 values from deep to superficial cartilage layers can be observed. Histologically validated animal studies have shown this zonal increase in T2 values as a marker of hyaline or hyaline-like cartilage structure after cartilage repair procedures within the knee[73,74]. To visualize this zonal variation in vivo, high spatial resolution is essential. In combination with a dedicated (multi-channel) coil nevertheless, T2 mapping in clinically applicable scan time could be achieved on most available MR magnets. In the hip joint, however, the resolution of the cartilage has to be mainly high enough to really delineate the femoral and the acetabular cartilage. Within e.g., the femoral cartilage it nevertheless remains challenging to assess a deep and a superficial cartilage layer.

In cartilage repair tissue T2 values have shown an increase in the early postoperative follow-up, which enables for visualization of cartilage repair tissue maturation[20]. Furthermore it has been shown that a zonal T2 evaluation is able to differentiate cartilage repair tissue after MFX and MACT [15]. Whereas cartilage repair tissue after MFX–histologically seen as fibrocartilage–shows no clear zonal increase from deep to superficial cartilage aspects, repair tissue after MACT—histologically reported as hyaline-like–shows a significant stratification.

In addition to standard 2D multi-echo spin-echo T2 relaxation, T2*- weighted 3D gradient-echo articular cartilage imaging has shown reliable results in the evaluation of chondromalacia of the knee [64]. In recent studies, T2* mapping, with its potentially short scan times, was correlated to standard T2, and showed information comparable to that obtained for articular cartilage in the knee, but with overall lower T2* values (ms) [65, 66]. Furthermore, also for T2*, a clear zonal variation between deep and superficial cartilage layers was described for healthy cartilage; after cartilage repair using MFX, however, this stratification could not be found [65]. Thus, for standard T2, as well as for comparable techniques, zonal assessment of healthy and altered articular cartilage is crucial in the thick cartilage layers of the knee joint. In the hip joint compared to standard T2 mapping, T2* mapping has several benefits with its potential higher signal and its ability for 3D imaging. In a recent study by Bittersohl and coworkers, T2* values could be correlated in various histological severities of osteoarthritis [22]. However, and this has to be seen contrary to standard multi-echo spin-echo T2 (Fig. 4.3), T2* values decreased significantly with increasing cartilage degeneration (Fig. 4.4) [22]. This study is nevertheless a good example that all results and conclusions of biochemical MRI have to be seen with caution and that more histological

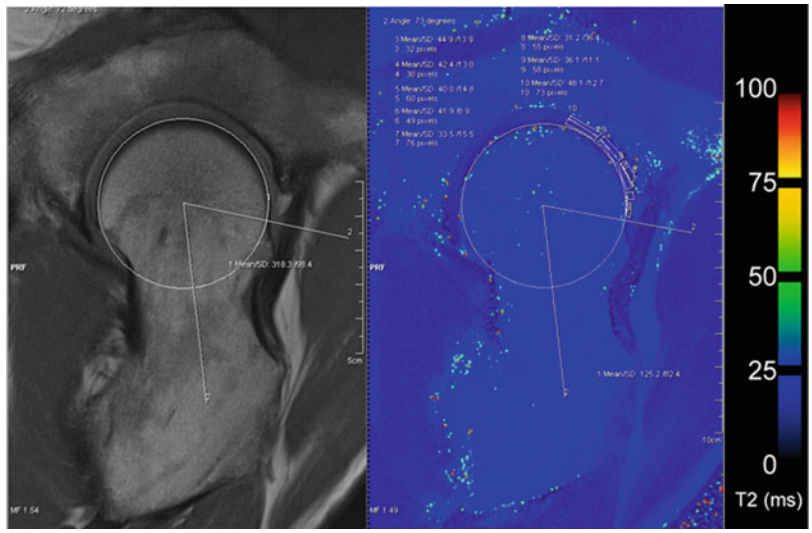

Fig. 4.3 A multi-echo spin-echo T2 mapping sequence of a 33-year-old soccer player with symptomatic FAI. The images out of a clinical cohort were planned on an isotropic sequence (see above), and by using quantitative T2 values, the cartilage quality was scored

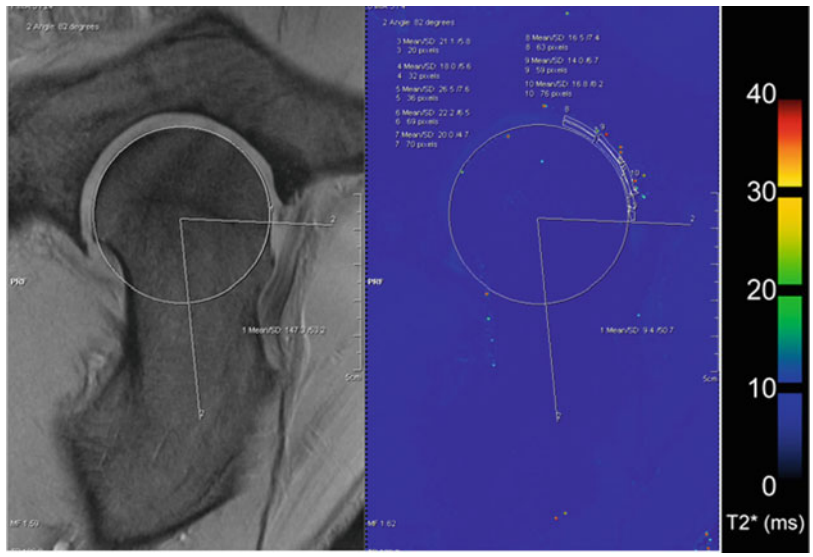

Fig. 4.4 A gradient echo T2* sequence of the same patient than provided in Fig. 4.2. Comparably to the standard T2 values, also the T2* values are provided in the impingement-specific cartilage areas

"gold-standard" studies are needed in future. Hence, when applying biochemical MRI to clinical studies or to patient care, the physicians have to learn to interpret the results. Nonetheless these results will for sure provide new insights into the pathophysiological pathway of, e.g., cartilage degeneration.

In addition to T2 or T2 star mapping, magnetization transfer contrast has been shown reliable in the evaluation of the collagen organization and might be more sensitive to the collagen content and less dependent on the hydration of the tissue [67].

References

1. Potter HG, Black BR, le Chong R. New techniques in articular cartilage imaging. Clin Sports Med. 2009;28:77–94.
2. Welsch GH, Trattnig S, Domayer S, Marlovits S, White LM, Mamisch TC. Multimodal approach in the use of clinical scoring, morphological MRI and biochemical T2-mapping and diffusion-weighted imaging in their ability to assess differences between cartilage repair tissue after microfracture therapy and matrix-associated autologous chondrocyte transplantation: a pilot study. Osteoarthritis Cartilage. 2009;17:1219–27.
3. Welsch GH, Zak L, Mamisch TC, Resinger C, Marlovits S, Trattnig S. Three-dimensional magnetic resonance observation of cartilage repair tissue (MOCART) score assessed with an isotropic three-dimensional true fast imaging with steady-state precession sequence at 3.0 Tesla. Invest Radiol. 2009;44:603–12.
4. Potter HG, le Chong R, Sneag DB. Magnetic resonance imaging of cartilage repair. Sports Med Arthrosc. 2008;16:236–45.
5. Trattnig S, Millington SA, Szomolanyi P, Marlovits S. MR imaging of osteochondral grafts and autologous chondrocyte implantation. Eur Radiol. 2007;17:103–18.
6. Welsch GH, Mamisch TC, Hughes T, Domayer S, Marlovits S, Trattnig S. Advanced morphological and biochemical magnetic resonance imaging of cartilage repair procedures in the knee joint at 3 Tesla. Semin Musculoskelet Radiol. 2008;12:196–211.
7. Gillis A, Bashir A, McKeon B, Scheller A, Gray ML, Burstein D. Magnetic resonance imaging of relative glycosaminoglycan distribution in patients with autologous chondrocyte transplants. Invest Radiol. 2001;36:743–8.
8. Mosher TJ, Smith H, Dardzinski BJ, Schmithorst VJ, Smith MB. MR imaging and T2 mapping of femoral cartilage: in vivo determination of the magic angle effect. AJR Am J Roentgenol. 2001;177:665–9.
9. Smith HE, Mosher TJ, Dardzinski BJ, et al. Spatial variation in cartilage T2 of the knee. J Magn Reson Imaging. 2001;14:50–5.
10. Kim YJ, Jaramillo D, Millis MB, Gray ML, Burstein D. Assessment of early osteoarthritis in hip dysplasia with delayed gadolinium-enhanced magnetic resonance imaging of cartilage. J Bone Joint Surg Am. 2003;85A:1987–92.
11. Watanabe A, Boesch C, Siebenrock K, Obata T, Anderson SE. T2 mapping of hip articular cartilage in healthy volunteers at 3T: a study of topographic variation. J Magn Reson Imaging. 2007;26:165–71.
12. Recht M, Bobic V, Burstein D, et al. Magnetic resonance imaging of articular cartilage. Clin Orthop Relat Res. 2001;391 Suppl:S379–396.
13. Trattnig S, Marlovits S, Gebetsroither S, et al. Three-dimensional delayed gadolinium-enhanced MRI of cartilage (dGEMRIC) for in vivo evaluation of reparative cartilage after matrix-associated autologous chondrocyte transplantation at 3.0T: preliminary results. J Magn Reson Imaging. 2007;26:974–82.
14. Watanabe A, Boesch C, Anderson SE, Brehm W, Mainil Varlet P. Ability of dGEMRIC and T2 mapping to evaluate cartilage repair after microfracture: a goat study. Osteoarthritis Cartilage. 2009;17:1341–9.
15. Welsch GH, Mamisch TC, Domayer SE, et al. Cartilage T2 assessment at 3-T MR imaging: in vivo differentiation of normal hyaline cartilage from reparative tissue after two cartilage repair procedures–initial experience. Radiology. 2008;247:154–61.
16. Burstein D, Velyvis J, Scott KT, et al. Protocol issues for delayed Gd(DTPA)(2-)-enhanced MRI: (dGEMRIC) for clinical evaluation of articular cartilage. Magn Reson Med. 2001;45:36–41.
17. Mosher TJ, Dardzinski BJ. Cartilage MRI T2 relaxation time mapping: overview and applications. Semin Musculoskelet Radiol. 2004;8:355–68.
18. Knutsen G, Drogset JO, Engebretsen L, et al. A randomized trial comparing autologous chondrocyte implantation with microfracture. Findings at five years. J Bone Joint Surg Am. 2007;89:2105–12.
19. Cunningham T, Jessel R, Zurakowski D, Millis MB, Kim YJ. Delayed gadolinium-enhanced magnetic resonance imaging of cartilage to predict early failure of Bernese periacetabular osteotomy for hip dysplasia. J Bone Joint Surg Am. 2006;88:1540–8.
20. Welsch GH, Mamisch TC, Marlovits S, et al. Quantitative T2 mapping during follow-up after matrix-associated autologous chondrocyte transplantation (MACT): full-thickness and zonal evaluation to visualize the maturation of cartilage repair tissue. J Orthop Res. 2009;27:957–63.
21. Apprich S, Welsch GH, Mamisch TC, et al. Detection of degenerative cartilage disease: comparison of high-resolution morphological MR and quantitative T2 mapping at 3.0 Tesla. Osteoarthritis Cartilage. 2011;18:1211–7.
22. Bittersohl B, Miese FR, Hosalkar HS, et al. T2* mapping of hip joint cartilage in various histological grades of degeneration. Osteoarthritis Cartilage. 2012;20:653–60.
23. Nishii T, Shiomi T, Tanaka H, Yamazaki Y, Murase K, Sugano N. Loaded cartilage T2 mapping in patients with hip dysplasia. Radiology. 2010;256:955–65.
24. Bolog N, Nanz D, Weishaupt D. Muskuloskeletal MR imaging at 3.0 T: current status and future perspectives. Eur Radiol. 2006;16:1298–307.
25. Kornaat PR, Reeder SB, Koo S, et al. MR imaging of articular cartilage at 1.5T and 3.0T: comparison of SPGR and SSFP sequences. Osteoarthritis Cartilage. 2005;13:338–44.
26. Schoth F, Kraemer N, Niendorf T, Hohl C, Gunther RW, Krombach GA. Comparison of image quality in

magnetic resonance imaging of the knee at 1.5 and 3.0 Tesla using 32-channel receiver coils. Eur Radiol. 2008;18:2258–64.
27. Zuo J, Li X, Banerjee S, Han E, Majumdar S. Parallel imaging of knee cartilage at 3 Tesla. J Magn Reson Imaging. 2007;26:1001–9.
28. Azer NM, Winalski CS, Minas T. MR imaging for surgical planning and postoperative assessment in early osteoarthritis. Radiol Clin North Am. 2004;42: 43–60.
29. Gomoll AH, Yoshioka H, Watanabe A, Dunn JC, Minas T. Preoperative measurement of cartilage defects by MRI underestimates lesion size. Cartilage. 2011;2(4):389–393.
30. Welsch GH, Zak L, Mamisch TC, et al. Advanced morphological 3D magnetic resonance observation of cartilage repair tissue (MOCART) scoring using a new isotropic 3D proton-density, turbo spin echo sequence with variable flip angle distribution (PD-SPACE) compared to an isotropic 3D steady-state free precession sequence (True-FISP) and standard 2D sequences. J Magn Reson Imaging. 2010;33: 180–8.
31. Apprich S, Mamisch TC, Welsch GH, et al. Quantitative T2 mapping of the patella at 3.0T is sensitive to early cartilage degeneration, but also to loading of the knee. Eur J Radiol. 2012;81:e438–43.
32. Pollard TC, Gwilym SE, Carr AJ. The assessment of early osteoarthritis. J Bone Joint Surg Br. 2008;90: 411–21.
33. Tiderius CJ, Olsson LE, Leander P, Ekberg O, Dahlberg L. Delayed gadolinium-enhanced MRI of cartilage (dGEMRIC) in early knee osteoarthritis. Magn Reson Med. 2003;49:488–92.
34. Tiderius CJ, Olsson LE, Nyquist F, Dahlberg L. Cartilage glycosaminoglycan loss in the acute phase after an anterior cruciate ligament injury: delayed gadolinium-enhanced magnetic resonance imaging of cartilage and synovial fluid analysis. Arthritis Rheum. 2005;52:120–7.
35. Trattnig S, Mamisch TC, Pinker K, et al. Differentiating normal hyaline cartilage from post-surgical repair tissue using fast gradient echo imaging in delayed gadolinium-enhanced MRI (dGEMRIC) at 3 Tesla. Eur Radiol. 2008;18:1251–9.
36. Knutsen G, Engebretsen L, Ludvigsen TC, et al. Autologous chondrocyte implantation compared with microfracture in the knee. A randomized trial. J Bone Joint Surg Am. 2004;86-A:455–64.
37. Domayer SE, Welsch GH, Nehrer S, et al. T2 mapping and dGEMRIC after autologous chondrocyte implantation with a fibrin-based scaffold in the knee: preliminary results. Eur J Radiol. 2010;73:636–42.
38. Mamisch TC, Dudda M, Hughes T, Burstein D, Kim YJ. Comparison of delayed gadolinium enhanced MRI of cartilage (dGEMRIC) using inversion recovery and fast T1 mapping sequences. Magn Reson Med. 2008;60:768–73.
39. Mayerhoefer M, Welsch GH, Mamisch TC, Szomolanyi P, Trattnig S. The in vivo effects of mechanical compression on T1-Gd (dGEMRIC) and T2 relaxation times in healthy meniscal tissue at 3.0 Tesla: feasibility of texture analysis. Invest Radiol. 2010.
40. Mayerhoefer ME, Welsch GH, Mamisch TC, et al. The in vivo effects of unloading and compression on T1-Gd (dGEMRIC) relaxation times in healthy articular knee cartilage at 3.0 Tesla. Eur Radiol. 2010;20: 443–9.
41. Trattnig S, Burstein D, Pinker K, Szomolanyi P, Welsch GH, Mamisch TC. T1(Gd) gives comparable information as delta T1 relaxation rate in dGEMRIC evaluation of cartilage repair tissue. Invest Radiol. 2009;44:598–602.
42. Welsch GH, Mamisch TC, Hughes T, et al. In vivo biochemical 7.0 Tesla magnetic resonance: preliminary results of dGEMRIC, zonal T2, and T2* mapping of articular cartilage. Invest Radiol. 2008; 43:619–26.
43. Zilkens C, Miese F, Bittersohl B, et al. Delayed gadolinium-enhanced magnetic resonance imaging of cartilage (dGEMRIC), after slipped capital femoral epiphysis. Eur J Radiol. 2011;79:400–6.
44. Sur S, Mamisch TC, Hughes T, Kim YJ. High resolution fast T1 mapping technique for dGEMRIC. J Magn Reson Imaging. 2009;30:896–900.
45. Trattnig S, Mlynarik V, Breitenseher M, et al. MRI visualization of proteoglycan depletion in articular cartilage via intravenous administration of Gd-DTPA. Magn Reson Imaging. 1999;17:577–83.
46. Bittersohl B, Hosalkar HS, Haamberg T, et al. Reproducibility of dGEMRIC in assessment of hip joint cartilage: a prospective study. J Magn Reson Imaging. 2009;30:224–8.
47. Bittersohl B, Steppacher S, Haamberg T, et al. Cartilage damage in femoroacetabular impingement (FAI): preliminary results on comparison of standard diagnostic vs delayed gadolinium-enhanced magnetic resonance imaging of cartilage (dGEMRIC). Osteoarthritis Cartilage. 2009;17:1297–306.
48. Trattnig S, Zbyn S, Schmitt B, et al. Advanced MR methods at ultra-high field (7 Tesla) for clinical musculoskeletal applications. Eur Radiol. 2012;22: 2338–46.
49. Zbyn S, Stelzeneder D, Welsch GH, et al. Evaluation of native hyaline cartilage and repair tissue after two cartilage repair surgery techniques with 23Na MR imaging at 7 T: initial experience. Osteoarthritis Cartilage. 2012;20:837–45.
50. Ling W, Regatte RR, Navon G, Jerschow A. Assessment of glycosaminoglycan concentration in vivo by chemical exchange-dependent saturation transfer (gagCEST). Proc Natl Acad Sci USA. 2008; 105:2266–70.
51. Schmitt B, Zbyn S, Stelzeneder D, et al. Cartilage quality assessment by using glycosaminoglycan

chemical exchange saturation transfer and (23)Na MR imaging at 7 T. Radiology. 2011;260:257–64.
52. Borthakur A, Mellon E, Niyogi S, Witschey W, Kneeland JB, Reddy R. Sodium and T1rho MRI for molecular and diagnostic imaging of articular cartilage. NMR Biomed. 2006;19:781–821.
53. Regatte RR, Akella SV, Lonner JH, Kneeland JB, Reddy R. T1rho relaxation mapping in human osteoarthritis (OA) cartilage: comparison of T1rho with T2. J Magn Reson Imaging. 2006;23:547–53.
54. Regatte RR, Akella SV, Wheaton AJ, Borthakur A, Kneeland JB, Reddy R. T 1 rho-relaxation mapping of human femoral-tibial cartilage in vivo. J Magn Reson Imaging. 2003;18:336–41.
55. Menezes NM, Gray ML, Hartke JR, Burstein D. T2 and T1rho MRI in articular cartilage systems. Magn Reson Med. 2004;51:503–9.
56. Regatte RR, Akella SV, Borthakur A, Kneeland JB, Reddy R. In vivo proton MR three-dimensional T1rho mapping of human articular cartilage: initial experience. Radiology. 2003;229:269–74.
57. Rakhra KS, Lattanzio PJ, Cardenas-Blanco A, Cameron IG, Beaule PE. Can T1-rho MRI detect acetabular cartilage degeneration in femoroacetabular impingement?: a pilot study. J Bone Joint Surg Br. 2012;94:1187–92.
58. Bittersohl B, Miese FR, Hosalkar HS, et al. T2* mapping of acetabular and femoral hip joint cartilage at 3 T: a prospective controlled study. Invest Radiol. 2012;47:392–7.
59. Miese FR, Zilkens C, Holstein A, et al. Assessment of early cartilage degeneration after slipped capital femoral epiphysis using T2 and T2* mapping. Acta Radiol. 2011;52:106–10.
60. Trattnig S, Mamisch TC, Welsch GH, et al. Quantitative T2 mapping of matrix-associated autologous chondrocyte transplantation at 3 Tesla: an in vivo cross-sectional study. Invest Radiol. 2007;42:442–8.
61. Welsch GH, Trattnig S, Hughes T, et al. T2 and T2* mapping in patients after matrix-associated autologous chondrocyte transplantation: initial results on clinical use with 3.0-Tesla MRI. Eur Radiol. 2010; 20:1515–23.
62. Burstein D, Gray ML. Is MRI fulfilling its promise for molecular imaging of cartilage in arthritis? Osteoarthritis Cartilage. 2006;14:1087–90.
63. Mamisch TC, Trattnig S, Quirbach S, Marlovits S, White LM, Welsch GH. Quantitative T2 mapping of knee cartilage: differentiation of healthy control cartilage and cartilage repair tissue in the knee with unloading–initial results. Radiology. 2010;254: 818–26.
64. Murphy BJ. Evaluation of grades 3 and 4 chondromalacia of the knee using T2*-weighted 3D gradient-echo articular cartilage imaging. Skeletal Radiol. 2001;30:305–11.
65. Hughes T, Welsch GH, Trattnig S, Brandi L, Domayer S, Mamisch TC. T2-star relaxation as a means to diffrentiatie cartilage repair tissue after microfracturing therapy. Intern Soc Magn Reson Med. 2007;15:183.
66. Wietek B, Martirosian P, Machann J, Mueller-Horvath C, Claussen CD, Schick F. T2 and T2* mapping of the human femoral-tibial cartilage at 1.5 and 3 Tesla. Intern Soc Magn Reson Med. 2007; 15:516.
67. Welsch GH, Trattnig S, Scheffler K, et al. Magnetization transfer contrast and T2 mapping in the evaluation of cartilage repair tissue with 3T MRI. J Magn Reson Imaging. 2008;28:979–86.

Section II

Hip Joint Anatomy and Diseases

Normal Articular Anatomy

5

Luis Perez Carro, Pau Golano, Natalia Fernandez Escajadillo, Miguel Ruperez Vallejo, Victor de Diego, and Luis Cerezal Pesquera

The Hip Joint

The hip is a diarthrotic joint formed by the surface of the acetabulum and the head of the femur. The acetabulum is a confluence of the ilium superiorly, the ischium laterally and inferiorly, and the pubis medially. These three bones fuse at the triradiate cartilage during growth and development to form the coxal or innominate bone. The acetabulum is hemispheric in shape and is partially covered at the weight-bearing surface by articular cartilage, creating a lunate-shaped cartilage configuration with a nonarticular portion in the center and inferior regions (Fig. 5.1). At the anteroinferior region of the acetabulum, there is a focal bone indentation, the acetabular notch, which is spanned by the transverse ligament. The central, nonarticular cavity, often referred to as the cotyloid fossa, contains the pulvinar and ligamentum teres. The bony acetabulum has a fibrocartilaginous rim, the labrum, which increases the depth and extension of the cotyloid fossa. The ball portion of the hip joint is comprised of the femoral head, which is reciprocally shaped to the acetabular socket, but is not perfectly congruent. In the area posterior and slightly inferior to the true center of the femoral head there is a small depression corresponding to the femoral insertion site of the ligamentum teres. This area is the only area of the femoral head that is not covered by articular cartilage.

Hip Arthroscopy

Even though arthroscopy of the hip was first performed as early as 1931 [1], its clinical application has developed rather slowly [2, 3]. Clinical assessment of the hip is improving and arthroscopic indications are therefore increasing. As hip arthroscopy becomes more common, it is vital that accurate knowledge of the anatomy of the hip and how to establish the common portals is combined with correct patient selection, sound preoperative planning, and consistent arthroscopic technique in order to maximize clinical outcomes. From an arthroscopic point of view, Dorfmann and Boyer [4] divided the hip into two compartments separated by the acetabular labrum: the central compartment and the peripheral compartment. Recently two new compartments have been described: The peritrochanteric space and the deep gluteal space [5, 6]. The central compartment includes the acetabular fossa, ligamentum teres, lunate cartilage, and articular surface of the femoral head in the weight-bearing area (Fig. 5.2). The peripheral compartment is formed of the non-weight-bearing cartilage of the femoral head,

L. Perez Carro (✉)
Servicio Cirugia Ortopédica y Traumatología, Clínica Mompía, Hospital Universitario Marqués de Valdecilla, C/Lealtad 20 2ºIZ, Santander, Cantabria 39002, Spain
e-mail: lpcarro@gmail.com

Y.-J. Kim (eds.), *Hip Magnetic Resonance Imaging*,
DOI 10.1007/978-1-4614-1668-5_5,

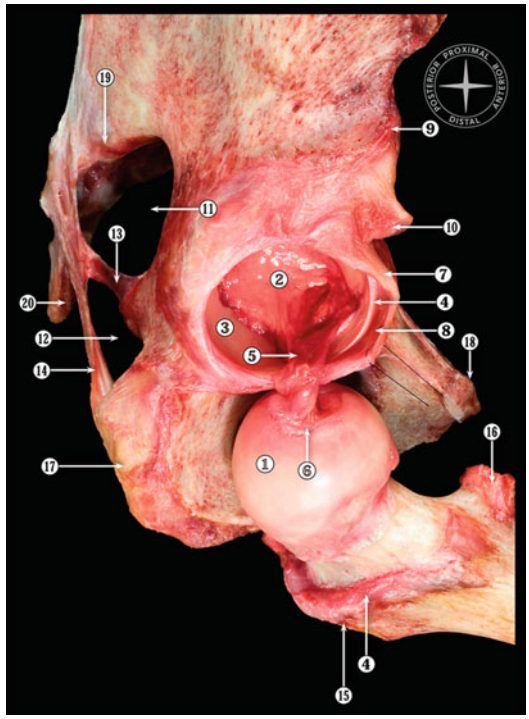

Fig. 5.1 Osteoarticular dissection of the hip joint (lateral view). (*1*) Head of femur. (*2*) Acetabular fossa or cotyloid fossa, with the pulvinar. (*3*) Lunate articular surface. (*4*) Acetabular labrum. (*5*) Ligamentum teres. (*6*) Fovea capitis. (*7*) Capsule of the hip joint (resected). (*8*) Paralabral sulcus, labrum-capsular sulcus, or perilabral recess. (*9*) Anterior inferior iliac spine. (*10*) Rectus femoris tendon cut (reflected and straight heads of the rectus femurs tendon). (*11*) Greater sciatic foramen. (*12*) Lesser sciatic foramen. (*13*) Sacrospinous ligament. (*14*) Sacrotuberous ligament. (*15*) Greater trochanter. (*16*) Lesser trochanter. (*17*) Ischial tuberosity. (*18*) Pubic tubercle. (*19*) Sacroiliac joint. (*20*) Coccyx

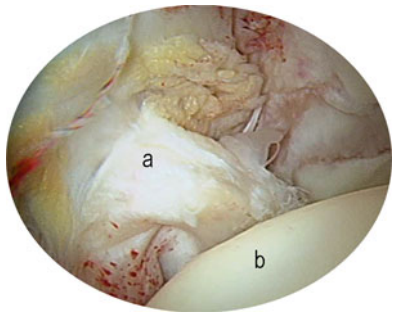

Fig. 5.2 View of the central compartment of the hip: (*a*) Ligamentum teres (*b*) Articular surface of the femoral head in the weight-bearing area

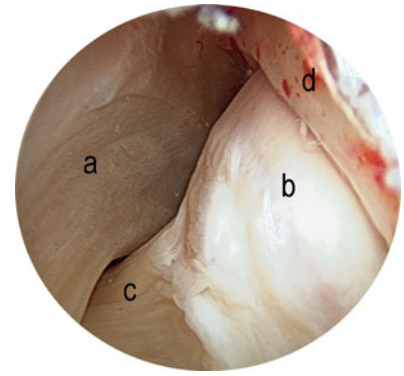

Fig. 5.3 View of the peripheral compartment of the hip: (*a*) Zona orbicularis (*b*) Non-weight-bearing cartilage of the femoral head (*c*) Femoral neck (*d*) Peripheral labrum

the femoral neck with its synovial folds, and the joint capsule (Fig. 5.3).To access and visualize the central compartment, traction must be applied to the joint, whereas the peripheral compartment is examined better without traction [7]. After releasing traction, flexion of the hip relaxes the anterior capsuloligamentous complex (Fig. 5.4), giving easy access to the anterior peripheral compartment [8].

Intracapsular Anatomy of the Hip and Arthroscopic Hip Examination

Femoral Head

The femoral head forms approximately two thirds of a sphere and is covered throughout with articular cartilage, except at the fovea. Anteriorly, the articular surface extends to the neck. It faces anterosuperomedially and geometrically resembles part of the surface of an ovoid (Fig. 5.5). Kurrat and Oberlander [9] found maximal thickness of the articular cartilage on the anterolateral portion of the femoral head. Normal hyaline cartilage, as in other joints, has a shining white appearance on direct inspection. The only fixed landmark on its surface is the insertion of the ligamentum teres on the fovea (Fig. 5.6). This area is located on the anteromedial portion

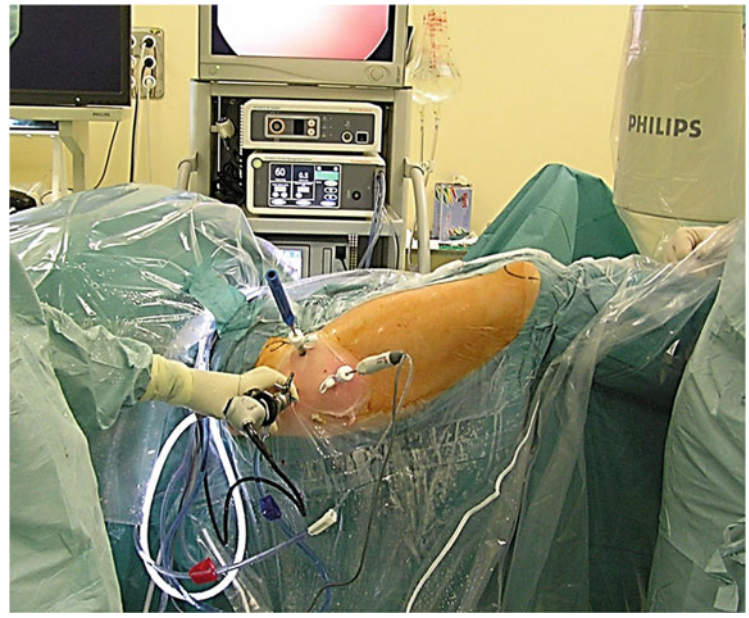

Fig. 5.4 Supine position for hip arthroscopy. Flexion of the hip relaxes the anterior capsuloligamentous complex giving easy access to the peripheral compartment

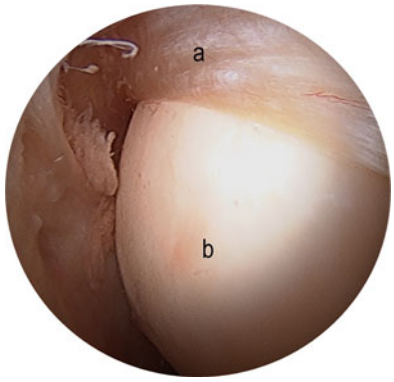

Fig. 5.5 Peripheral compartment viewing superiorly. (*a*) Anterior labrum. (*b*) Femoral head resembles part of the surface of an ovoid

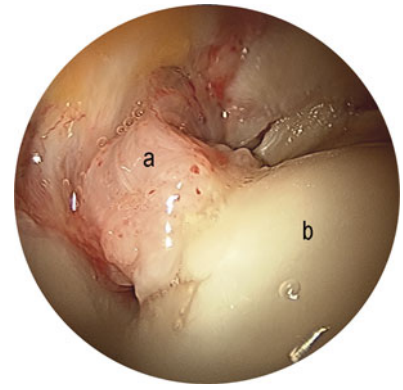

Fig. 5.6 Arthroscopic view of the insertion of the ligamentum teres on the fovea. (*a*) Ligamentum teres (*b*) Femoral head

of the head and was previously known as the bare area.

Acetabulum

The horseshoe shape of the acetabulum is a fixed landmark and allows easy orientation within the joint. It can be divided into a superior part, an anterior column, and a posterior column. The inner borders of the articular surface of the acetabulum have a rounded cartilage edge; these form the margins of the acetabular fossa or cotyloid fossa (Figs. 5.7 and 5.8). The thickness of the articular cartilage is reported [9] to be maximal on the anterosuperior quadrant. The acetabulum cartilage can be divided in rim cartilage and non-rim cartilage (Figs. 5.9 and 5.10).

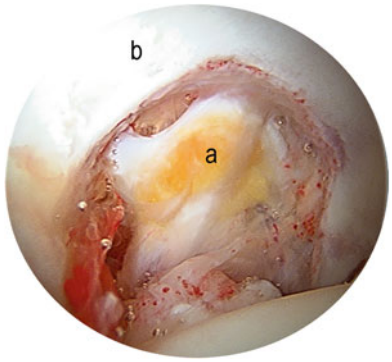

Fig. 5.7 (*a*) Cotyloid fossa (*b*) Acetabulum

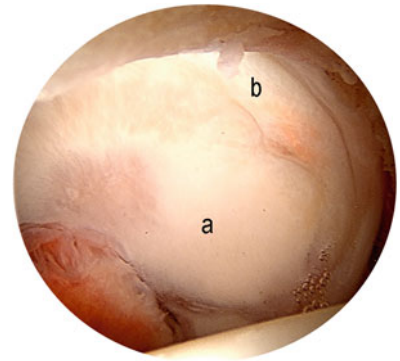

Fig. 5.9 The acetabulum cartilage can be divided in (*a*) Non-rim cartilage and (*b*) Rim cartilage. View of the wave sign at the rim cartilage

Fig. 5.8 The central, nonarticular cavity of the acetabulum, often referred to as the cotyloid fossa, contains the pulvinar and ligamentum teres

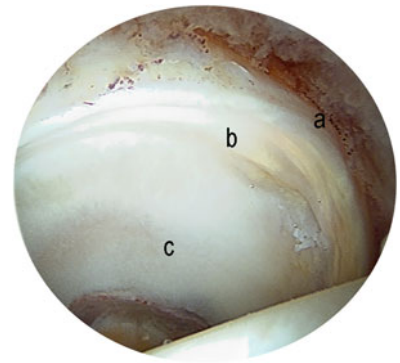

Fig. 5.10 The horseshoe shape of the acetabulum is a fixed landmark and allows easy orientation within the joint. (*a*) Labrum (*b*) Rim cartilage (*c*) Non-rim cartilage

The Acetabular Labrum

The acetabular labrum or cotyloid ligament is found on the rim of the bony acetabulum (Fig. 5.11). The labrum is a fibrocartilage with a triangular cross section; it increases the depth and coverage of the acetabulum, thus favoring stability of the hip joint by forming slightly more than a hemisphere. The labrum has three faces: (1) The base or adherent face is the part that inserts onto the rim of the acetabulum. (2) The internal or articular face is continuous with the articular surface of the acetabulum, such that it is occasionally difficult to distinguish on simple arthroscopic vision (Fig. 5.12). (3) The external face inserts onto the joint capsule, leaving a free border that can be observed during arthroscopic examination (Figs. 5.13 and 5.14). The size of the labrum varies; it is thicker superiorly and posteriorly than it is inferiorly and anteriorly [10, 11]. Classic anatomic studies observed variations of between 6 and 10 mm in the height of the labrum. Average width of the acetabular labrum is reported to be 5.3 mm (SD, 2.6 mm) [12]. In the young adult, the labrum has an avascular, meniscus-like, elastic appearance, whereas in the elderly it can appear yellow and degenerate.

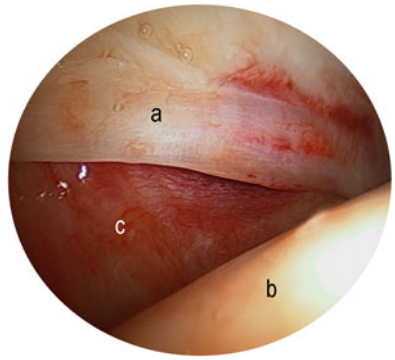

Fig. 5.11 The labrum is a fibrocartilage with a triangular cross section; it increases the depth and coverage of the acetabulum. (*a*) Labrum (*b*) Femoral head (*c*) Anterior capsule

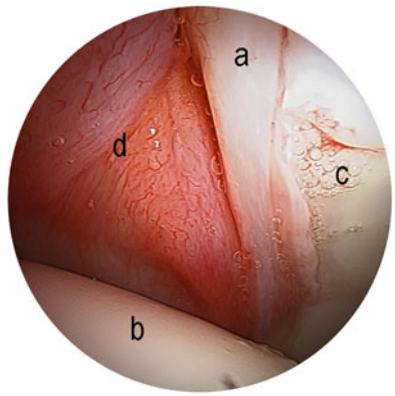

Fig. 5.12 Arthroscopic view of the internal or articular face of the labrum. (*a*) Labrum (*b*) Femoral head (*c*) Acetabulum (*d*) Anterior capsule

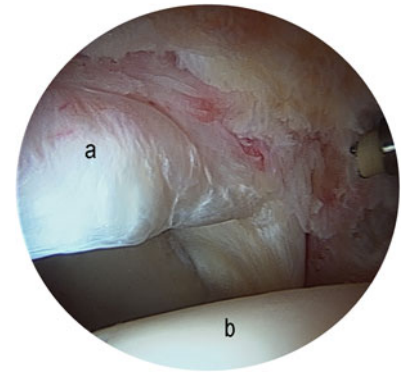

Fig. 5.13 View of the external face of the labrum with traction (*a*) Labrum (*b*) Femoral head

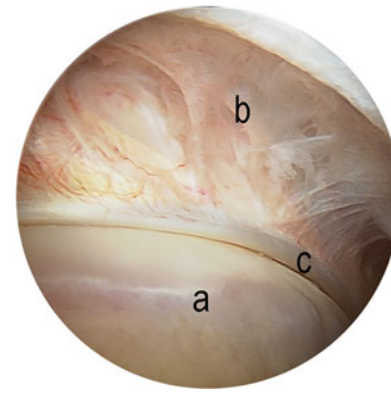

Fig. 5.14 View of the external face of the labrum without traction. The external face of the labrum inserts onto the joint capsule, leaving a free border (*a*) Femoral head (*b*) Capsule (*c*) Labrum

Sometimes the labrum is thin, poorly developed, and hypoplastic, and at other times it may appear enlarged. Superiorly, there is a slight separation between the insertion of the capsule and the acetabular rim, creating a space between the labrum and the capsule known as the paralabral sulcus, labrum-capsular sulcus, or perilabral recess [13] (Figs. 5.15 and 5.16). It is important to get used to the normal arthroscopic appearance of the paralabral sulcus, as certain disorders commonly give rise to adhesions at this site, obliterating the sulcus. On the inner lip of the acetabulum lies the cartilage-labrum junction, which is the most common site for labral pathology. However, it must be remembered that a partial separation of the labrum may be observed at the superior part of the acetabulum as an anatomic variant [14]. This separation is called the sublabral sulcus and should not be confused with a labral lesion. In vivo observation by hip arthroscopy shows the most common site for labral injury to be the anterior and anterosuperior regions [15]. However, the distinction between the sublabral sulcus and a labral lesion is not always clear; a labral lesion should be considered when there are compatible symptoms, or when there is an associated image of labral hemorrhage in acute disorders or granulation tissue indicating

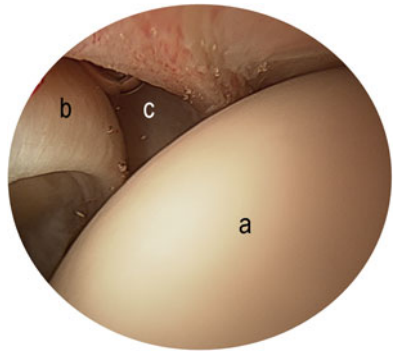

Fig. 5.15 View of a normal paralabral sulcus or perilabral recess (*a*) Femoral head (*b*) Labrum (*c*) Perilabral recess

Fig. 5.17 Paralabral cyst an associated labral hemorrhage

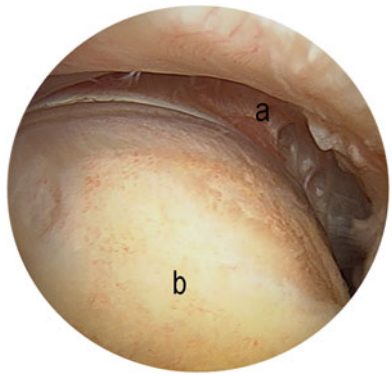

Fig. 5.16 Arthroscopic view of the peripheral compartment: (*a*) Superior sulcus above the lateral labrum (*b*) Femoral neck

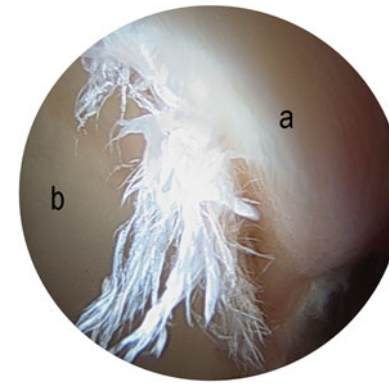

Fig. 5.18 Typical appearance of a labral tear in the anterosuperior weight-bearing zone (*a*) Labrum (*b*) Acetabulum

attempted healing in chronic disorders [14] (Figs. 5.17 and 5.18).

The Ligamentum Teres

The ligamentum teres or ligamentum capitis femoris [16] is an intra-articular ligament that attaches the head of the femur to the acetabulum. It arises in the inferior part of the acetabular fossa and runs inferiorly and anteriorly across the joint space to insert into the fovea capitis of the head of the femur (Figs. 5.19 and 5.20). The ligamentum teres is trapezoid; its base, which is thickened into two bands, inserts onto the border of the acetabular notch and onto the transverse ligament of the acetabulum. As it runs towards the femoral head, it becomes progressively round or oval in shape before inserting into the fovea capitis at a site slightly posterior and inferior to the true center of the head. In cross section, the ligamentum teres is pyramidal, with a fascicular appearance formed by an anterior and a posterior bundle; it follows a spiral course from its acetabular attachment to its femoral insertion. Dynamic hip examination shows that the ligament becomes tense during external rotation of the hip and relaxed on internal rotation. The ligamentum teres may have a function similar to that of the anterior cruciate ligament in the knee [17]. When considering reconstruction of

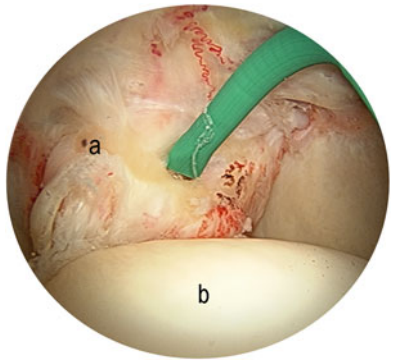

Fig. 5.19 Arthroscopic view of ligamentum teres being probed with a curved radiothermal instrument around the femoral head (*a*) Ligamentum teres (*b*) Femoral head

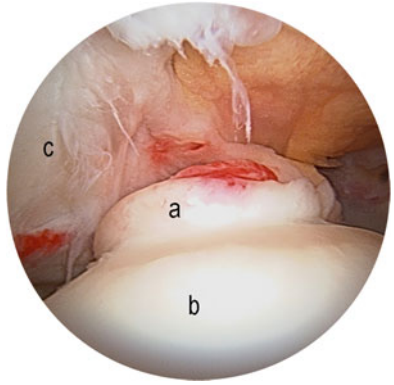

Fig. 5.20 Ligamentum teres, or ligamentum capitis femoris, is an intra-articular ligament that attaches the head of the femur to the acetabulum (*a*) Ligamentum teres (*b*) Femoral head (*c*) Acetabulum

this ligament, anchors should be placed in areas of the acetabulum that provide the best bone stock for purchase, while minimizing the risk of damage to vital intrapelvic structures [18].

The Synovial Folds

As the neck of the femur is intra-articular, it is covered by synovial membrane. This synovial tissue forms a series of folds that descend along the femoral neck, from the border of the cartilage of the femoral head to the insertion of the joint capsule on the femur. These folds are variable in number and size, and it is important to distinguish them from possible adhesions.

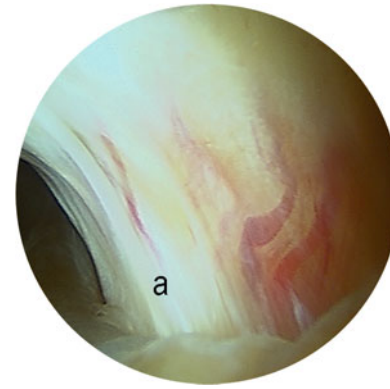

Fig. 5.21 (*a*) Retinacular vessels at the femoral neck important for vascularization of the femoral head

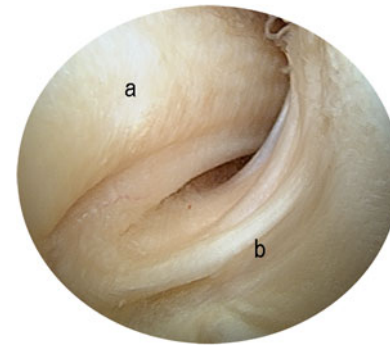

Fig. 5.22 Vincula-like structures representing branches of the medial femoral circumflex artery to the inferior portion of the femoral head (*a*) Zona orbicularis (*b*) Retinacular vessels

Synovial folds, which may be large, are usually observed medially and laterally; an anterior fold is less common. The anterior synovial fold is adherent to the neck and only recognizable by its single fibers covering the bone of the neck. The lateral fold indicates the site of entry of the perforating arterioles, which are important for vascularization of the femoral head [19]. It is important to remember this vascularization, as damage to it, whether in open or arthroscopic procedures, can lead to necrosis of the femoral head (Figs. 5.21, 5.22, and 5.23).

The medial fold is an important reference for initial orientation and usually indicates the medial limit for performing osteochondroplasty in cases of femoroacetabular impingement, while the lateral fold marks the lateral limit for this

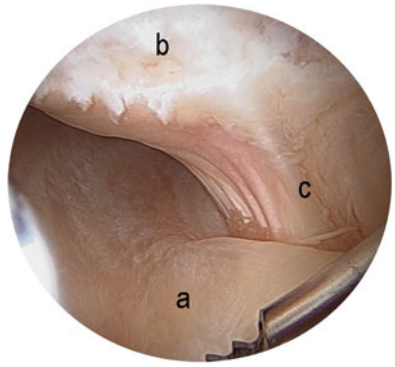

Fig. 5.23 Arthroscopic view of the anterolateral femoral neck and lateral synovial fold. (*a*) Zona orbicularis (*b*) Femoral head (*c*) Vincula

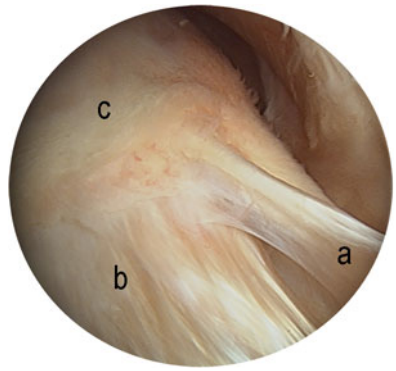

Fig. 5.24 View of the medial synovial fold (*a*) Medial synovial fold (*b*) Femoral neck (*c*) Femoral head

resection. The medial synovial fold can be found consistently. It is usually not adhering to the femoral neck and passes proximally from the medial border of the femoral head distally to the lesser trochanter (Figs. 5.24 and 5.25). This structure is a helpful landmark, especially if visibility within the peripheral compartment is limited by synovial disease [20].

A Systematic Arthroscopic Exam of the Hip

A systematic arthroscopic examination of the central and peripheral compartments of the hip increases the accuracy and reproducibility of

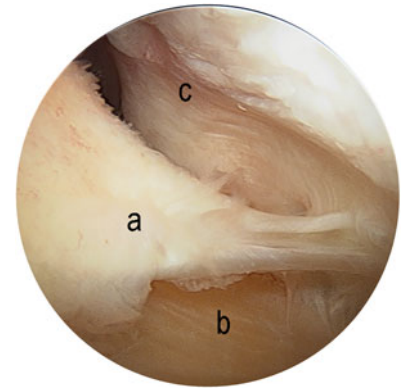

Fig. 5.25 The medial fold is an important reference for initial orientation and usually indicates the medial limit for performing osteochondroplasty in cases of femoroacetabular impingement (*a*) Medial synovial fold (*b*) Femoral neck (*c*) Zona orbicularis

each hip arthroscopy. The use of a standardized, systematic approach ensures that all components of the hip are carefully inspected and makes it possible to document the procedure correctly so that it can be reviewed in the future. The arthroscopic portals of the hip can be classified into two groups according to their relationship to the greater trochanter: paratrochanteric (anterolateral, posterolateral, accessory anterolateral), and anterior (anterior, accessory distal anterior, accessory proximal anterior, and midanterolateral).

Examination of the Central Compartment

The central compartment must be explored starting from the central region of the joint. The anterior region is then examined, followed by the posterior region. The structures visualized are, in order, the acetabular fossa, the posteromedial acetabular cartilage and labrum, the anterior triangle, the anterior labrum and paralabral sulcus, the posterolateral labrum, the posterior capsule, and the femoral head. Beginning with the arthroscope introduced through the anterolateral portal into the central compartment, the first landmark is easily reached by slowly withdrawing the

Fig. 5.26 Anterior triangle on a left hip with a spinal needle establishing the anterior portal. (*a*) Labrum (*b*) Femoral head (*c*) Capsule (*d*) Acetabulum

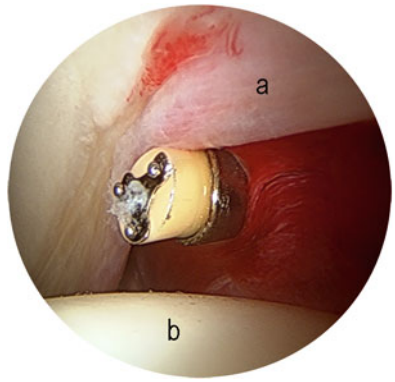

Fig. 5.27 Anterior triangle on a right hip with a radiothermal instrument through it (*a*) Labrum with associated labral hemorrhage (*b*) Femoral head

arthroscope to get a view of the components of the medial wall of the acetabulum, including the acetabular or cotyloid fossa, pulvinar, and ligamentum teres. It is important to use this view for general orientation; in addition, synovitis of the acetabular fossa and tears of the ligamentum teres are commonly seen from this position [21]. The camera is then moved to visualize the posteromedial horn of the acetabular cartilage and labrum. With adequate distraction, the posterior capsular reflection can also be observed behind. The lens is then rotated superiorly and the camera is raised and retracted gently to visualize the anterior triangle, which is

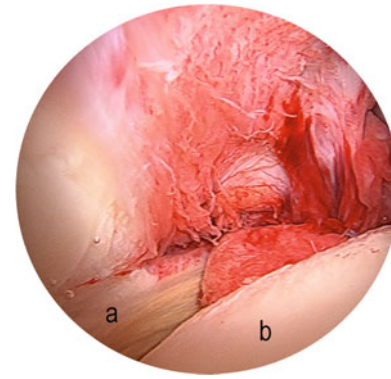

Fig. 5.28 (*a*) View of the transverse acetabular ligament at the inferior most aspect of the acetabulum. This ligament is hard to see unless the patient has hyperlaxity (*b*) Femoral head

composed of the anterior capsule, anterior labrum, and femoral head (Figs. 5.26 and 5.27). The anterior triangle is a very helpful landmark and will give direct visualization of the spinal needle when establishing the anterior portal. Once the anterior portal is established, the camera is withdrawn further and the anterior labrum and paralabral sulcus come into view. The triangular anterior labrum usually fuses with the acetabular cartilage inferiorly and the paralabral sulcus superiorly. The anterior portal gives the best view of the ligamentum teres as it arises from the posteroinferior margin of the acetabulum and inserts onto the medial aspect of the femoral head. Even minor tears can be diagnosed with gentle rotation of the lower extremity. With adequate distraction, the camera can be carefully maneuvered posteriorly to view the posterior aspect of the transverse ligament where it inserts onto the posteromedial labrum (Fig. 5.28). This is a site where articular loose bodies can lodge. Pulling the camera back, anterior to the ligament, reveals the anterior aspect of the transverse ligament and its attachment to the anterior labrum. By rotating the lens laterally, the superior acetabular cartilage is seen. The posterolateral portal gives a good view of the posterior capsule, the weight-bearing part of the acetabulum, the anterolateral labrum, and the femoral head. From the medial notch, the arthroscope is slowly

Fig. 5.29 Byfid labrum (*a*) Femoral head

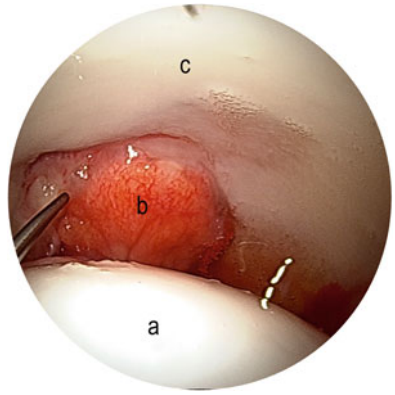

Fig. 5.30 The stellate crease is frequently found directly superior to the acetabular fossa characterized by a stellate pattern of chondromalacia. (*a*) Femoral head (*b*) Acetabular fossa (*c*) Acetabulum

withdrawn and moved inferiorly over the posterior labrum into the inferior gutter, which runs from the capsular attachment on the posterior and medial acetabulum to the thickened cylindrical sleeve of the orbicular ligament that surrounds the femoral neck. The lens of the scope is then rotated cranially and advanced to see the weight-bearing dome of the acetabulum. Cartilage degeneration and cyst formation within the acetabulum are often best appreciated in this area. The camera is then moved superiorly to view the anterolateral labrum from a different angle. Finally, rotating the lens, the posterior aspect of the femoral head can be examined. The camera should be drawn tangentially over the surface of

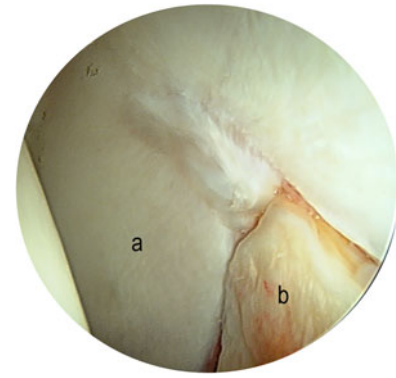

Fig. 5.31 View of the stellate crease immediately above the acetabular fossa. (*a*) Acetabulum (*b*) Acetabular fossa

the cartilage in an effort to observe as much of the femoral head as possible.

Normal Variants in the Central Compartment

Although the acetabular labrum was described as a homogeneous ring-shaped structure, its posterior part can be bifid [22] (Fig. 5.29). Adjacent to anterior or posterior apex of the acetabular fossa, within its lunate surface, a stellate-appearing articular lesion immediately above the acetabular fossa, referred to as the *stellate crease,* is frequently seen (Figs. 5.30 and 5.31). The inexperienced surgeon must be aware of its existence so as not to confuse it with early degenerative changes. When seen, it is unlikely to be of clinical significance as a contributing cause of pain and must be distinguished from traumatic articular lesions. Remnants of the triradiate cartilage may be evident in adulthood as a physeal scar, extending in a linear fashion along the medial aspect of the acetabulum anterior and/or posterior to the fossa. This should not be misinterpreted as an old fracture line (Fig. 5.32). There is usually also a normal groove or indentation at 2–3/8–9 o'clock in the anterior lip of the acetabulum where the psoas crosses it. Sometimes the psoas tendon indents the medial joint capsule at this point (Capsule hour-glass restriction) (Fig. 5.33).

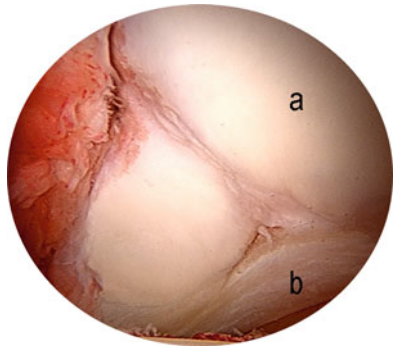

Fig. 5.32 The physeal scar is an area devoid of articular surface demarcating the area of the old triradiate physis. (*a*) Acetabulum (*b*) Labrum

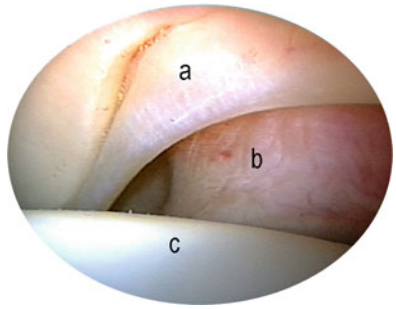

Fig. 5.33 Normal groove or indentation in the anterior lip of the acetabulum where the psoas crosses (*a*) Labrum (*b*) Reflection of the iliopsoas tendon on the capsule. (*c*) Femoral head

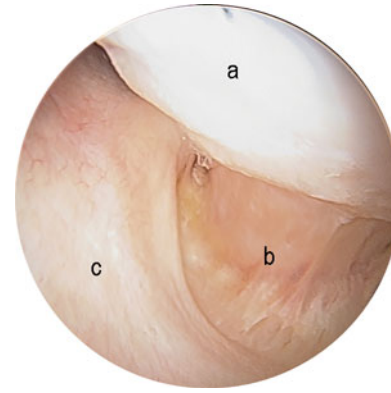

Fig. 5.34 Peripheral compartment and the femoral neck (*a*) Femoral head (*b*) Femoral neck (*c*) Zona orbicularis

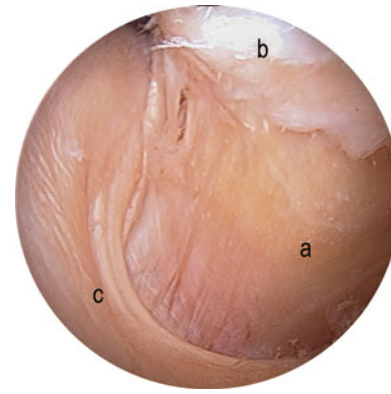

Fig. 5.35 (*a*) Arthroscopic view of the femoral neck (*b*) Femoral head (*c*) Zona orbicularis

Examination of the Peripheral Compartment

After the appropriate treatment of any condition diagnosed in the central compartment, the limb is taken out of traction and the hip is positioned in approximately 35° of flexion. This relaxes the anterior capsuloligamentous complex and permits adequate inspection of the peripheral compartment to be performed. Once inside the peripheral compartment, the visual field should be moved from medial to lateral over the femoral head and then from lateral to medial along the femoral neck (Figs. 5.34 and 5.35). There are six landmarks commonly inspected within the peripheral compartment: the medial femoral neck, the medial femoral head, the anterior femoral head, the lateral femoral head, the lateral femoral neck, and the anterior femoral neck. Upon entering the peripheral compartment from the AL portal, the initial view is typically of the medial neck. If the camera is oriented so that it is looking down upon the femoral neck, the first anatomic complex is a very consistent landmark, comprising the orbicular ligament, medial synovial fold, and femoral neck. Like the acetabular fossa and the ligamentum teres in the central compartment, the medial synovial fold and orbicular ligament serve as excellent landmarks in the peripheral compartment. From the medial neck, the camera is directed superiorly and is slowly withdrawn as it is gently maneuvered under the orbicular ligament, sliding into the medial gutter.

Fig. 5.36 Synovial chondromatosis. Loose bodies under the orbicular ligament. (*a*) Orbicular ligament

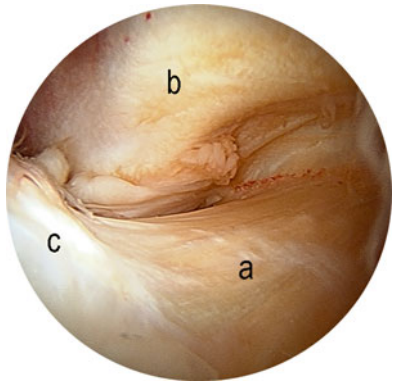

Fig. 5.37 Arthroscopic view of the zona orbicularis: Circular fibers extension of the iliofemoral ligament. (*a*) Femoral neck (*b*) Orbicular ligament. (*c*) Femoral head

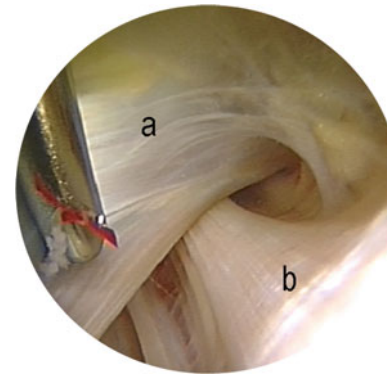

Fig. 5.38 View of the insertion of the gluteus maximus tendon running posterior to the vastus lateralis into the linea aspera (*a*) Vastus lateralis (*b*) Gluteus maximus tendon

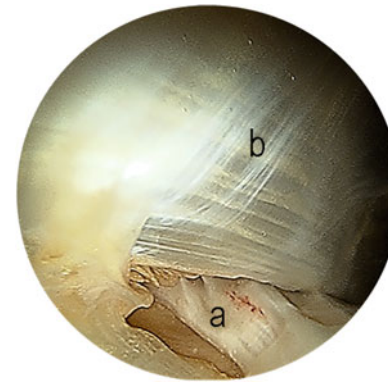

Fig. 5.39 Peritrochanteric compartment: The sciatic nerve lies approximately 3–4 cm posterior to the maximus insertion. (*a*) Gluteus maximus tendon (*b*) Vastus lateralis

It is not uncommon to find hidden loose bodies in this area (Fig. 5.36). From the lateral aspect of the femoral head, the camera is withdrawn distally to reach the lateral aspect of the femoral neck. From here, fibers of the orbicular ligament can be seen from the peripheral compartment side and correspond well to the previous view from the central compartment (Fig. 5.37). This is also the most common area for the cam lesion commonly seen with femoroacetabular impingement [23, 24].

Examination of the Peritrochanteric Compartment

Voos et al. [5] described the arthroscopic anatomy of the hip in the peritrochanteric compartment: The borders of the peritrochanteric compartment consist of the tensor fascia lata and iliotibial band laterally, the abductor tendons superomedially, the vastus lateralis inferomedially, the gluteus maximus muscle superiorly, and its tendon posteriorly. Within the space exist the trochanteric bursae and the gluteus medius and minimus tendons at their attachment on the greater trochanter. Three portals provide optimal visualization within the peritrochanteric compartment. Visualizing through the anterior portal, the examination begins at the gluteus maximus insertion at the linea aspera (Figs. 5.38 and 5.39). Fibrous tissue

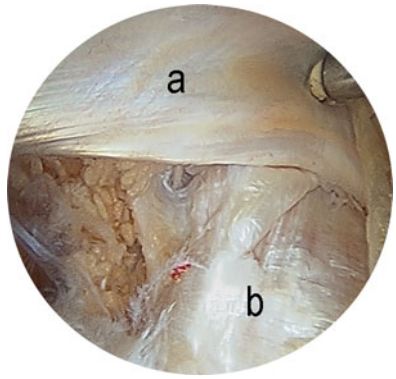

Fig. 5.40 Peritrochanteric compartment initial view: (*a*) Vastus lateralis (*b*) Gluteus maximus tendon running toward the iliotibial band and posterior femur

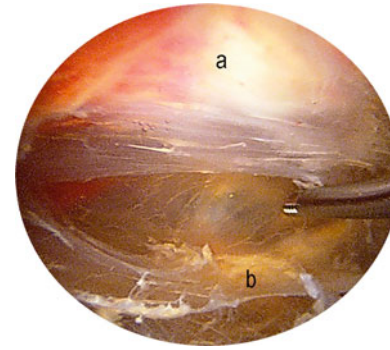

Fig. 5.42 Gluteus medius muscle and tendon inserting on the greater trochanter. Fibrous bands from the trochanteric bursa may need to be removed in order to best visualize the medius attachment (*a*) Gluteus medius (*b*) Fatty tissue over the sciatic nerve

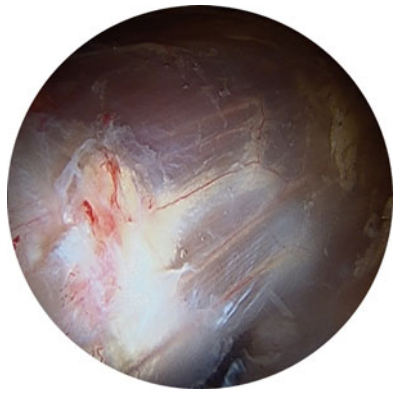

Fig. 5.41 Vastus lateralis fibers are identified and can be traced toward its insertion on the vastus tubercle

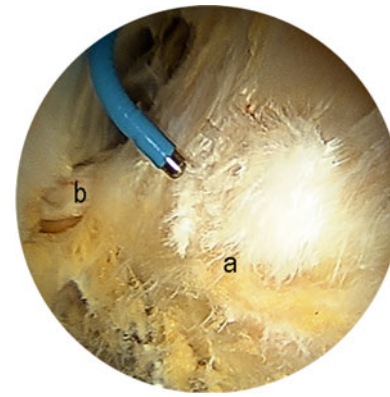

Fig. 5.43 View of the ileotibial band looking distally in the peritrochanteric space. (*a*) IIiotibial band with abrasive changes in a syntomatic coxa saltans externus. (*b*) Gluteus maximus tendon

bands may need to be removed from the space in this location to visualize the coalescence. Rotating proximally, the vastus lateralis fibers (Figs. 5.40 and 5.41) are identified and can be traced toward its insertion on the vastus tubercle. Rotating the arthroscope anterior and superior, the gluteus minimus tendon is visualized anteriorly. Moving anteriorly above the gluteus minimus lies the gluteus medius tendon and its attachment to the greater trochanter (Fig. 5.42). Fibrous bands from the trochanteric bursa may need to be removed in order to best visualize the medius attachment to the greater trochanter. The ileotibial band sits posteriorly and can be seen (Fig. 5.43) with a small posterior maneuver of the arthroscope and rotation: The posterior one third of the ileotibial is implicated in external snapping hip (coxa saltans) and can be released (Fig. 5.44).

Hip arthroscopy has expanded to treatment of peritrochanteric space: External snapping hip, trochanteric bursitis, and treatment of gluteus medius and gluteus minimus tears (Fig. 5.45).

Examination of the Subgluteal Space

The subgluteal space is anterior and beneath the gluteus maximus and posterior to the posterior border of the femoral neck, with the linea aspera

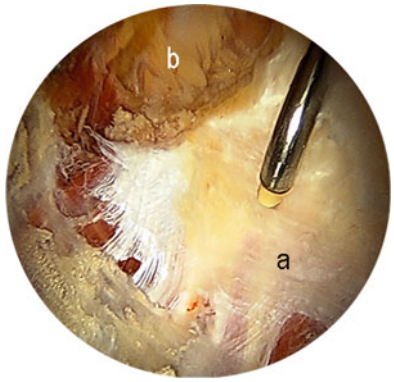

Fig. 5.44 Arthroscopic release of the iliotibial band can be performed if necessary to decompress a symptomatic coxa saltans externus. (*a*) Iliotibial band (*b*) Release of the iliotibial band

Fig. 5.45 Gluteus medius tendon torn from the greater trochanter

Fig. 5.46 Endoscopic view of the sciatic nerve behind the greater trochanter. (*a*) Sciatic nerve

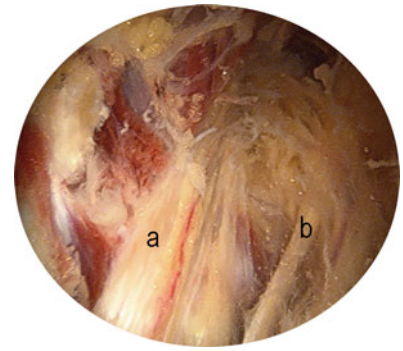

Fig. 5.47 Subgluteal space. (*a*) Sciatic nerve (*b*) Posterior femoral cutaneous nerve

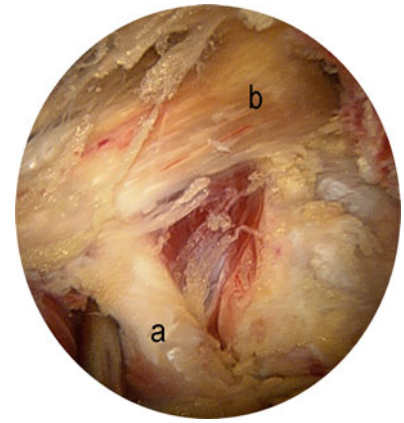

Fig. 5.48 Endoscopic view of the obturator internus tendon (*a*) Obturator internus (*b*) Sciatic nerve

(lateral), the sacrotuberous and falciform fascia (medial), the inferior margin of the sciatic notch (superior), and the hamstring origin (inferior). Within this region of great importance are the sciatic nerve (Figs. 5.46 and 5.47), piriformis, obturator internus/externus (Fig. 5.48), gemelli, quadratus femoris, hamstrings, superior and inferior gluteal nerves, lateral ascending vessels of the medial femoral circumflex artery, ischium, sacrotuberous and sacrospinous ligaments, and origin of the ischiofemoral ligament. The subgluteal space is a recently defined anatomic region for endoscopic access [6] that can treat different disorders and allows release of the piriformis tendon with exploration of relationship between piriformis and sciatic nerve, assessing

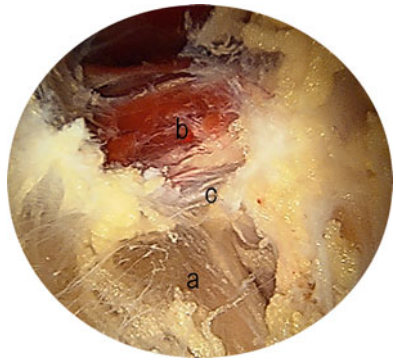

Fig. 5.49 Endoscopic view of sciatic nerve entrapment by the piriformis (*a*) Sciatic nerve (*b*) Piriformis muscle (*c*) Piriformis tendon

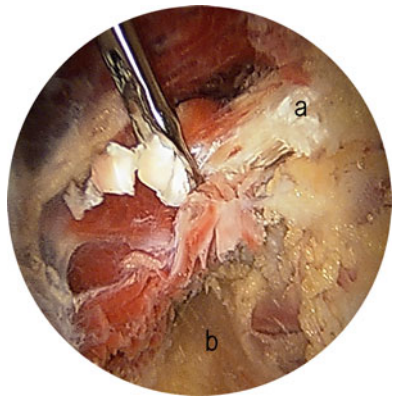

Fig. 5.50 Endoscopic view of surgical release of the piriformis. (*a*) Piriformis tendon (*b*) Sciatic nerve

and accounting for anatomic variations that may exist (Figs. 5.49, 5.50, and 5.51).

Summary

Currently, there is unprecedented enthusiasm for hip arthroscopy, as this modality is transforming the management of hip injuries. Careful preoperative planning, precise portal placement, a knowledge of the anatomy and potential complications, and a methodical sequence of arthroscopic examination, progressing from one part of the joint cavity to another systematically in each operative case, are essential for effective arthroscopy of any joint. This standard arthroscopic method also helps differentiate normal

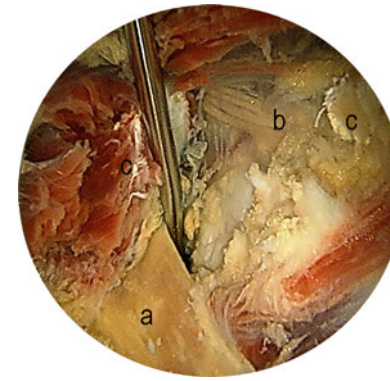

Fig. 5.51 Endoscopic view after surgical decompression of the sciatic nerve. (*a*) Sciatic nerve (*b*) Superior gluteal nerve (*c*) Piriformis tendon released

structures from their pathologic counterparts. Furthermore, it allows us to correlate arthroscopic findings with clinical presentations, enhancing our diagnostic abilities and providing better clinical outcomes.

References

1. Burman M. Arthroscopy or the direct visualization of joints. J Bone Joint Surg. 1931;4:669–95.
2. Kelly BT, Riley III JW, Philippon MJ. Hip arthroscopy: current indications, treatment options, and management issues. Am J Sports Med. 2003;31:1020–37.
3. Byrd JWT. The role of hip arthroscopy in the athletic hip. Clin Sports Med. 2006;25:255–78.
4. Dorfmann H, Boyer T. Hip arthroscopy utilizing the supine position. Arthroscopy. 1996;12:264–7.
5. Voos JE, Rudzki JR, Shinkdle MK, et al. Arthroscopic anatomy and surgical techniques for peritrochanteric space disorders in the hip. Arthroscopy. 2007;23:1246.e1–e5.
6. Martin HD, Shears SA, Johnson JC, Smathers AM, Palmer IJ. The endoscopic treatment of sciatic nerve entrapment/deep gluteal syndrome. Arthroscopy. 2011;27:172–81.
7. Dienst M, Gödde S, Seil R, Hammer D, Kohn D. Hip arthroscopy without traction. In vivo anatomy of the peripheral hip joint cavity. Arthroscopy. 2001;17:924–31.
8. Guanche CA, Bare AA. Arthroscopic treatment of femoroacetabular impingement. Arthroscopy. 2006;22:95–106.
9. Kurrat HJ, Oberlander W. The thickness of the cartilage in the hip joint. J Anat. 1978;126:145–55.
10. Petersilge CA, Haque MA, Petersilge WJ, Lewin JS, Lieberman JM, Buly R. Acetabular labral tears:

evaluation with MR arthrography. Radiology. 1996;200:231–5.
11. Ghebontni L, Roger B, El-Khoury J, Brasseur JL, Grenier PA. MR arthrography of the hip: normal intra-articular structures and common disorders. Eur Radiol. 2000;10:83–8.
12. Tan V, Seldes RM, Katz MA, et al. Contribution of acetabular labrum to articulating surface area and femoral head coverage in adult hip joints: an anatomic study in cadavera. Am J Orthop. 2001;30:809–12.
13. Petersilge CA. MR arthrography for evaluation of the acetabular labrum. Skeletal Radiol. 2001;30:423–30.
14. Byrd JWT. Labral lesions: an elusive source of hip pain case reports and literature review. Arthroscopy. 1996;12:603–12.
15. McCarthy J, Noble P, Aluisio FV, Schuck M, Wright J, Lee J. Anatomy, pathologic features, and treatment of acetabular labral tears. Clin Orthop. 2003;406:38–47.
16. Brewster S. The development of the ligament of the head of the femur. Clin Anat. 1991;4:245–55.
17. Wenger D, Miyanji F, Mahar A, Oka R. The mechanical properties of the ligamentum teres. A pilot study to assess its potential for improving stability in children's hip surgery. J Pediatr Orthop. 2007;4:408–10.
18. Perez-Carro L, Golano P, Vega J, Escajadillo FN, Rubin CG, Cerezal L. The ligamentum capitis femoris: anatomic, magnetic resonance and computed tomography study. Hip Int. 2011;21:367–72.
19. Beaulé P, Campbell P, Lu Z, Leunig-Ganz K, Beck M, Leunig M, et al. Vascularity of the arthritic femoral head and hip resurfacing. J Bone Joint Surg Am. 2006;88A:85–96.
20. Dorfmann H, Boyer T. Arthroscopy of the hip: 12 years of experience. Arthroscopy. 1999;15:67–72.
21. Byrd JWT. Avoiding the labrum in hip arthroscopy. Arthroscopy. 2000;16:770–3.
22. Miller R, Villar RN. The bifid posterior labrum: an anatomic variant of the acetabular labrum. Arthroscopy. 2009;25:413–5.
23. Lavigne M, Parvizi J, Beck M. Anterior femoroacetabular impingement. Part I: technique of joint preserving surgery. Clin Orthop. 2004;413:61–6.
24. Beck M, Leunig M, Parvizi J. Anterior femoroacetabular impingement. Part II: midterm results of surgical treatment. Clin Orthop. 2004;418:67–73.

Abnormal Osseous Anatomy

6

Lisa M. Tibor and Michael Leunig

Introduction

The cause of "primary" or "idiopathic" osteoarthritis was, for most of the twentieth century, widely thought to be unknown. Although Murray, Harris, and Solomon each proposed a mechanical etiology for hip arthrosis [1–3], most research energy and attention during the past 4 decades was directed towards improving total hip arthroplasty. At present, there is a resurgence of interest in the relationship between hip deformity and osteoarthrosis (OA) due to advances in surgical techniques to correct the deformity and improved understanding of the role of deformity in the development of OA.

Hip deformities that may cause mechanical damage to the joint and resultant OA range from acetabular dysplasia which causes instability and static overload of the joint to femoroacetabular impingement (FAI) which causes dynamic overload of the cartilage and labrum due to abnormal contact between the femur and the acetabulum during motion. Much of the renewed interest and improvement in understanding of the importance of hip arthrokinematics in the development of OA is attributed to Ganz et al.'s observation of the link between osseous abnormalities, hip pain, chondrolabral damage, and eventual osteoarthrosis [4]. Ganz and colleagues postulated that "most, if not all hip osteoarthrosis is secondary, often secondary to subtle but definite and commonly overlooked, ignored, or not recognized dysplasia or pistol grip deformities (FAI)." [5] This chapter will summarize the current understanding of the prevalence of hip deformity as it relates to the development of hip OA.

Proximal Femoral Anatomy

There are a number of subtle alterations in proximal femoral anatomy that affect the biomechanics of the hip. In patients with FAI, decreased offset at the head–neck junction [6] or a cam deformity [4], which is thought to be an extension of the epiphysis onto the femoral neck [7, 8], cause cam impingement and damage at the chondrolabral junction. The prevalence of this deformity is quite high and varies with the population being studied (Fig. 6.1) and the radiographic studies used. Specifically, studies that only evaluate an AP image or only use radiographs likely underestimate the prevalence and the magnitude of the deformity [9]. This is because the maximal alpha angle is usually located between 1 and 3 o'clock at the anterosuperior aspect of the femoral neck [6, 9–12] and is best detected with either three-dimensional computerized tomography (CT) or radial slices through the femoral neck on either CT or magnetic resonance imaging (MRI).

L.M. Tibor (✉)
San Diego, CA, USA
e-mail: lisa.tibor@gmail.com

Y.-J. Kim (eds.), *Hip Magnetic Resonance Imaging*,
DOI 10.1007/978-1-4614-1668-5_6,

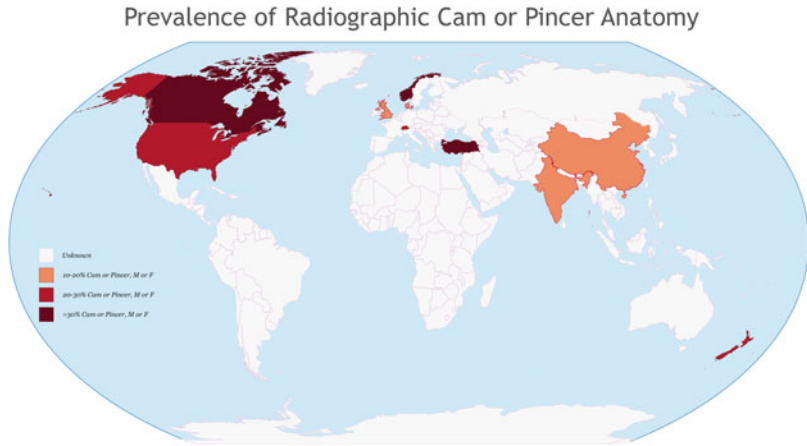

Fig. 6.1 International prevalence of femoroacetabular impingement morphology

In a study of asymptomatic male Swiss army recruits, the prevalence of the cam deformity detected on radial MRI slices was 24 % overall [13]. When the recruits with limited hip internal rotation were selected from the entire group, the prevalence of the cam deformity increased to 50 % [13]. A separate study of this same cohort found that cam deformities were associated with an increased risk of damage to the labrum and cartilage (relative risk 2–3 depending on the specific type of lesion) [14]. A study of asymptomatic Swiss females found that no female had a definite cam deformity, but the prevalence of a possible or mild cam deformity was 22 % [15]. Labral lesions were observed in 19 % of these women, but given the smaller nature of the cam deformity no statistical correlations between cam deformities and labral tears were found [15]. Other studies examining the prevalence of the cam deformity or decreased head–neck offset have found rates ranging from 12 to 35 % in the normal population, with males having three to five times the rates of those seen for females (Table 6.1) [16–19]. Similarly, males also seem to have higher rates of bilateral deformities than females, with 25 % of males and 6 % of females having bilateral cam deformities in one series [19]. When femoral asphericity was evaluated in a series of patients who had abdominal CTs for reasons unrelated to their hips, 74 % of the cohort had asphericity in at least one plane, and for 66 % of the cohort the asphericity was bilateral [18].

Femoral version also affects the biomechanics of the hip. Femoral retroversion is thought to exacerbate the inclusion damage caused by cam impingement by limiting the amount of flexion and internal rotation that is possible before impingement occurs [20–22]. Conversely, femoral anteversion may mitigate the effect of an anterior cam deformity, but may be a cause of increased static stress or instability at the anterior acetabulum [20, 21] or psoas tendon [23]. Femoral version has been examined in several studies. In the Hahmann-Todol osteologic collection, adult males less than 40 were found to have an average version of 8.9 ± 8.3°, while females had slightly more anteversion, with an average of 11.4 ± 7.5° [24]. A CT-based study of femoral version found an average version of 4.5–5 ± 8° [25]. There may also be some ethnic variation to femoral version. A study comparing Caucasians to ethnic Chinese in Hong Kong observed average versions of 7° and 10° in Caucasian males and females, respectively, whereas the average version in the ethnic Chinese cohort was 14° and 16° for males and females, respectively [26]. The normal distribution of femoral version has also been characterized (Fig. 6.2) [27, 28]. Femoral version has a bell-shaped distribution, ranging from −17° to 38° [28]. In these studies, between 9 and 15 % of femurs were retroverted—i.e., with version ≤0° [27, 28]. Similar percentages of femurs were excessively anteverted, with 8–13 % having version >20° [27, 28].

Table 6.1 International prevalence of FAI pathoanatomy

Country/ region	Prevalence	References
China (Beijing)	CEA >35°: 11 % (F); impingement angle <70°: 3.5 %	Dudda et al. [33]
India	11.8 % (low head–neck offset)	Malhotra et al. [78]
Denmark	Deep socket M: 15.2 %, F: 19.4 %	Gosvig et al. [16]
	Pistol grip M: 19.6 %, F: 5.2 %	
UK	Cam M: 18 %, F: 11.9 %	Pollard et al. [74]
	Pincer M: 16.7 %, F: 21.1 %	
New Zealand	Retroversion 14 %	Kang et al. [18]
	Overcoverage 16 %	
	Cam 22 %	
Switzerland	M: 24 % definite cam, F: 22 % mild/possible cam	Reichenbach et al. [13], Leunig et al. [15]
US	M: 29 % (AP image only)	Dudda et al. [33], Jung et al. [79]
	F: 23 % CEA >35°, 12 % impingement angle <70°	
Turkey	CEA >35°: 32.5 %	Sahin et al. [40]
	Alpha angle >50°: 45 %	
Norway	Cam M: 35.0 %, F: 10.2 %	Laborie et al. [19]
	Pincer M: 34.3 %, F: 16.6 %	
Canada	Cam M: 51.7 %, F: 18.9 %	Hack et al. [17]

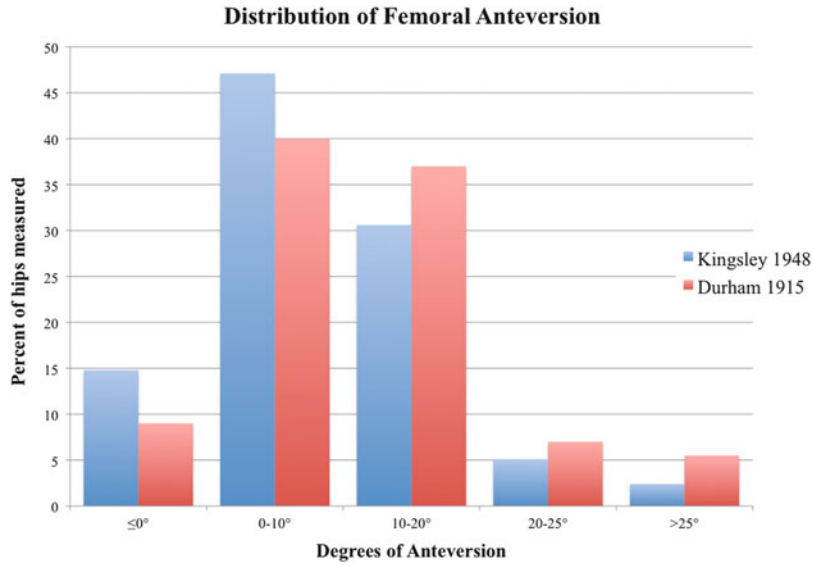

Fig. 6.2 Distribution of normal femoral version from a total of 830 cadaveric femora, as measured by Durham in 1915 [27] and Kingsley and Olmstead in 1948 [28]

Acetabular Anatomy

Acetabular anatomy has historically been studied in the context of acetabular dysplasia, with the lateral center-edge angle (CEA) on an anteroposterior (AP) pelvis X-ray used as the most common measure of acetabular coverage. Studies using CT to measure lateral CEA in a normal asymptomatic adult population found average CEAs of 30–31 ± 4° [25] and 37–38 ± 7° [29], with an overall range of

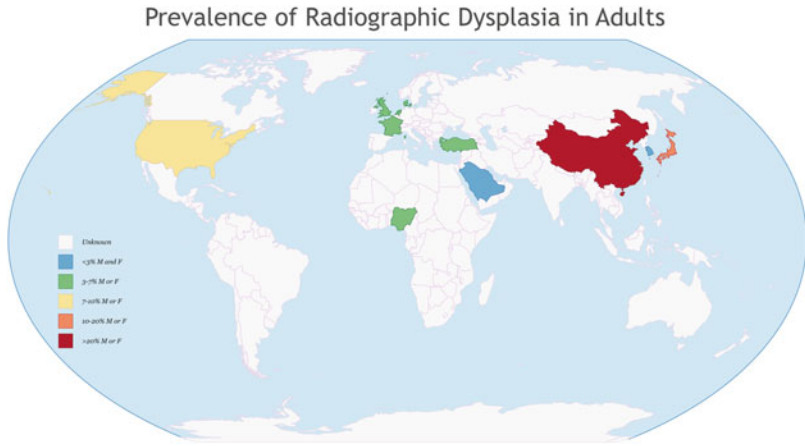

Fig. 6.3 International prevalence of adult hip dysplasia

Table 6.2 International prevalence of adult dysplasia

Country/region	Prevalence	References
Saudi Arabia	1.4 % (all mild w/CEA <25°, no <20°)	Moussa and Alomran [31]
Korea	M: 1.3 % (CEA <20°), F: 2.2 %	Han et al. [104]
Turkey	M: 2.5–9.8 % (CEA <25°), F: 1.0–9.8 % (CEA <25°)	Goker et al. [105], Aktas et al. [30]
France	M: 1.8 %, F: 5.6 %	Inoue et al. [93]
UK	M: 2.4 % (CEA <25°), F: 4 %	Yoshimura et al. [88]
Nigeria	M: 3.3 % (CEA <25°)	Ali-Gombe et al. [90]
Denmark	3.5–5.5 % (CEA <20°)	Jacobsen and collaborators [56, 57], Gosvig et al. [16]
	M: 4.3 %, F: 3.6 %	
Netherlands	4.8 % (CEA <25°)	Reijman et al. [55]
Hong Kong	M: 4.5 % (CEA <25°) 10 % (majority w/CEA 20–25°), F: 9.9 %	Lau et al. [85], Hoaglund et al. [86]
US	7 % (F, CEA <20°)	Dudda et al. [33]
Singapore	7.3 % (CEA <20°)	Umer et al. [106]
Malawi	M: 11.5 %, F: 13.2 %	Msamati et al. [107]
Japan	M: 5.1–16 % (CEA <25°), F: 11.6–41 %	Inoue et al. [93], Yoshimura et al. [88]
Norway (Sámi, above Arctic Circle)	17 % (CEA <20°)	Johnsen et al. [32]
	38 % (CEA <25°)	
China (Beijing)	21.7 % (F, CEA <20°)	Dudda et al. [33]

22–55° [26, 29]. The prevalence of dysplasia in both newborns and adults is known to vary widely, depending on the population being studied (Fig. 6.3, Table 6.2), and the average CEA varies accordingly. In adults, rates of dysplasia (CEA less than 20°) range from 1 % of females in Turkey [30] and 1.4 % of Saudi Arabian adults [31], to 17 % in the Sami population [32] and 22 % in Chinese women around Beijing [33]. For infants, rates of hip instability as detected by clinical exam range from 0 % in the Bantu people of South Africa and Zimbabwe to 33 % in the Cree-Ojibwa Native American tribes [34].

In contrast, there are only a few studies that have evaluated the prevalence of acetabular overcoverage and acetabular retroversion, which is the pathoanatomy on the acetabular side that can contribute to FAI. In studies of Caucasians, acetabular overcoverage or increased acetabular depth was observed in 10–15 % of hips [15, 16, 18, 19] and

was bilateral in 75–77 % of these patients [16, 18]. Although the most precise way to measure acetabular version is with axial MRI or CT images of the pelvis, a centered AP pelvis X-ray can also provide information about version. The crossover sign is present when the shadow of the anterior acetabular wall crosses over that of the posterior wall. The posterior wall sign is present when the posterior wall lies medial to the center of rotation of the femoral head. A CT study of the acetabular version in asymptomatic adults found the average version to be 26–27 ± 6° [25]. The prevalence of the crossover sign is extremely variable and somewhat technique-dependent; in one study 51 % of males and 45 % of females had a crossover sign on AP pelvis images [19], whereas other studies have observed the crossover sign in only 14 % [18] and 6 % [35] of asymptomatic adults. When the posterior wall sign was assessed in a larger population, it was observed on the AP pelvis images of 23 % of males and 11 % of females [19]. Regardless of the radiographic measure, acetabular retroversion is not uncommon and may be associated with other hip disorders, including osteoarthritis, dysplasia, and Perthes' disease [35].

Association Between Hip Deformity and OA in the General Population

The prevalence of FAI is known to be greatly increased in patients presenting with hip pain, adductor strain, labral tears, and athletic pubalgia, and in some series is seen in as many as 90 % of these patients [36–38]. In a multicenter study of French patients presenting with hip pain and who were candidates for hip arthroscopy, 63 % had evidence of FAI. Of the FAI patients, 58 % were found to have pure cam impingement, 19 % had pure pincer impingement, and 23 % had evidence of mixed impingement [39]. The prevalence of FAI is also increased in the contralateral hip of patients who have previously undergone total hip arthroplasty, with 84 % of arthroplasty patients having cam deformities as compared to 32 % of controls with no past history of hip pain [40]. One caveat to these findings is that reactive osteophytes also can form at the head–neck junction and be misinterpreted as a primary cam deformity. Similarly, reactive osteophytes also form on the acetabular rim obscuring the original anatomy that initiated the arthrosis.

The prevalence of dysplasia in patients presenting with hip pain is also significant. In the UK, 24 % of patients over 40 presenting with new hip pain were found to have a lateral CEA <25° [41] and 35 % of patients in the French study of potential hip arthroscopy candidates were found to have dysplasia [39]. In the French study, a total of 95 % of patients presenting with hip pain were found to have either dysplasia or FAI [39].

As part of the work developing the mechanical concept of hip arthrosis, Harris, Solomon, and Murray looked at the prevalence of subtle deformities in "primary" osteoarthritis, finding rates of deformity ranging from 65 to 79 % [1–3]. It is likely that the prevalence of subtle deformity is actually higher, however, as these early studies evaluated only AP pelvis X-rays and there was no evaluation of acetabular overcoverage or acetabular retroversion.

Mild dysplasia was observed in 20–39 % of patients with idiopathic hip arthrosis [1–3]. All of these series found a much higher prevalence of dysplasia in females as compared to males. Murray's series had a male to female ratio of 10:41 for mild dysplasia [1], Solomon's series had a male to female ratio of 1:10 [2], and Harris observed mild dysplasia in 15 % of males but 68 % of females [3]. The gender ratio was reversed when looking at the "head tilt" and "pistol grip" deformities. Harris carefully described the spectrum of pistol grip deformities as flattening of the normally concave surface of the lateral femoral neck, development of a bump on the anterolateral surface of the femoral neck, the formation of a sharp transition or "hook" at the junction of the articular surface of the femoral head with the femoral neck, and failure of the femoral head to be centered over the femoral neck in either the AP pelvis, frog, or true lateral X-rays [3]. These deformities currently would be considered cam morphology, but at that time were considered "deformities that occurred after minimal slipping

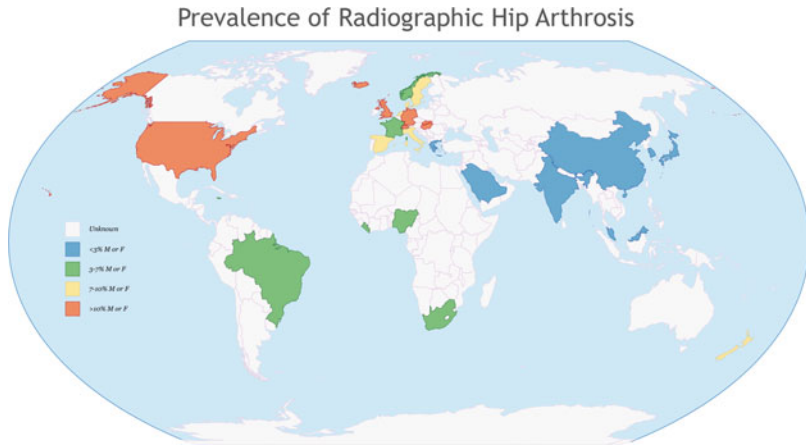

Fig. 6.4 International prevalence of primary hip arthrosis

of the capital femoral epiphysis and mild cases of Legg–Perthes disease" [3]. In both Murray and Harris' series, 40 % of patients with primary osteoarthrosis had pistol grip deformities, with a male to female ratio of 66:10 for Harris [3] and 67:12 for Murray [1]. Solomon's series included patients with secondary causes of arthrosis, but he also observed a predominance of the head tilt in males, with a male to female ratio of 14:1 [2].

Contemporary studies have examined the radiographs of younger patients (<55 or 60 years old) undergoing total hip arthroplasty for osteoarthritis. All of the currently available literature is, however, level III or IV prognostic evidence [42] from X-ray data. When patients who have dysplasia, Perthes' disease, and inflammatory arthropathy are excluded, the prevalence of FAI in the remaining population is exceedingly high—96–97 % [43, 44]. Looking specifically at the anatomy of the acetabulum, retroversion or overcoverage is seen in 20–45 % of these patients [35, 44].

While the cam deformity is easily and classically seen in males, the anatomy causing idiopathic arthrosis in females may be a subtler radiographic finding. In elderly white females, lateral flattening of the femoral head on an AP pelvis X-ray was associated with progressive arthrosis [45]. Females are known to have smaller cam deformities than males [6, 46, 47] and this may be the female equivalent of a subtle pistol grip deformity. Femoral head flattening is also seen in dysplasia [48, 49]. Without additional imaging, the precise anatomy causing the femoral head flattening and subsequent arthrosis is unclear.

Radiographic rates of arthrosis progression for patients with FAI are also variable. In a study of Greek patients who had radiographic evidence of FAI, after 10 years only 18 % had radiographic progression of arthrosis, regardless of whether they had cam, pincer, or mixed-type FAI [50]. When compared to other European countries, however, the overall prevalence of hip arthrosis in Greece is very low (Fig. 6.4, Table 6.3) [51]. Thus, some other environmental or genetic factor may also be influencing the progression of arthrosis in this population. In contrast, other studies have found much higher rates of progression. Of US patients who underwent unilateral total hip arthroplasty for FAI-related arthrosis, 73 % showed either progression of at least one grade of radiographic arthrosis or underwent total hip arthroplasty at an average of 5 years after their first arthroplasty [43]. Another study of FAI patients in the UK observed radiographic progression of osteoarthritis in 65 % of patients over 10 years [52]. A population-based case–control study of women in the UK obtained AP pelvis radiographs 19 years apart, allowing the investigators to evaluate risk factors for hip arthroplasty [53]. There was a higher prevalence of both acetabular dysplasia and of cam deformities in women who underwent arthroplasty [53]. There is one study that attempted to determine if the size of the cam deformity or amount of

Table 6.3 International prevalence of "idiopathic" or primary hip osteoarthritis

Country/region	Prevalence	References
Saudi Arabia	0.04 %	Ahlberg et al. [80]
India	M: 0.08 %, F: 0.1 %	Mukhopadhaya and Barooah [81]
Greece	0.9 % M: 0.3 %, F: 1.5 %	Andrianakos et al. [51]
Malaysia	M: 0.7–1.7 %, F: 1.2–4.4 %	Veerapen et al. [82]
China (Beijing)	0.03–2.0 %, M: 1.1 %, F: 0.9 %	Nevitt et al. [83], Zeng et al. [84]
Hong Kong	M (>70): 1.2–5.4 %, F: 0.8 %	Lau et al. [85], Hoaglund et al. [86]
Korea	M: 1.7 %, F: 1.8 %	Chung et al. [87]
Japan	M: 0–1.4 %, F: 2–3.5 %	Yoshimura et al. [88]
Jamaica	M: 1–2 %, F: 4 %	Lawrence and Sebo [89]
Liberia	M: 3 %, F: 2 %	Lawrence and Sebo [89]
Nigeria	M: 3–7.0 %, F: 2 %	Lawrence and Sebo [89], Ali-Gombe et al. [90]
South Africa (Black, Tswana, Phokeng)	M: 3–4.9 %, F: 0.7–3 %	Solomon et al. [91], Lawrence and Sebo [89]
Brazil	4.7 %	Senna et al. [92]
France	M: 5.7 %, F: 2.5 %	Inoue et al. [93]
Norway (Oslo)	M: 4.6 %, F: 6.2 %	Grotle et al. [94]
Norway (Sámi, above Arctic Circle)	M: 3.9–8.8 %, F: 6.3–11.1 %	Johnsen et al. [59]
Denmark	M: 4.9–7.5 %, F: 2.0–7.9 %	Jacobsen and collaborators [56, 57]
Sweden (Malmö)	1.1–9.8 %	Danielsson and Lindberg [95]
Netherlands	M: 2.8–11.8 %, F: 1.7–14.8 %	Van Saase et al. [96]
Spain	7.4 % M: 6.7 %, F: 8.0 %	Quintana et al. [97]
Italy (Tuscany)	7.7 %	Mannoni et al. [98]
Canada (British Columbia, Haida)	M: 7 %	Lawrence and Sebo [89]
New Zealand	F: 8.45 %	Yoshida et al. [99]
Iceland	10.8 % M: 12 %, F: 10 %	Ingvarsson et al. [100]
US		
Caucasian	M: 4.5 %, 23.8 %, F: 3.8–5.5 %, 29.1 %	Nevitt et al. [83], Jordan et al. [101]
Pima Indians	M: 3.7–7.3 %, F: 2.5–3.9 %	Hirsch et al. [102]
Native American, Montana	M: 8 %, F: 11 %	Lawrence and Sebo [89]
Native American, Arizona	M: 12 %, F: 5 %	Lawrence and Sebo [89]
African American	M: 33.2 %, F: 31.2 %	Jordan et al. [101]
UK		
North Staffordshire, Southampton	M: 11.0 %, F: 4.8 %	Yoshimura et al. [88]
Wensleydale	M: 22 %, F: 16–18 %	Lawrence and Sebo [89]
Leigh	M: 22–25 %, F: 14–15 %	Lawrence and Sebo [89]
Watford	M: 10–12 %, F: 7–9 %	Lawrence and Sebo [89]
Germany (Oberhörlen)	M: 16 %, F: 10 %	Lawrence and Sebo [89]
Hungary	16.49 %	Horváth et al. [103]
Slovakia (Piestany)	M: 17 %, F: 10 %	Lawrence and Sebo [89]
Switzerland (Azmoos)	M: 17 %, F: 7 %	Lawrence and Sebo [89]

acetabular coverage correlated with the age at the time of total hip arthroplasty. With the numbers available, however, no variable was predictive of the age at surgery [54].

Contemporary studies have also examined the association between dysplasia or CEA and the risk of arthrosis. Large population-based studies in the Netherlands and Denmark have observed

that CEAs of <20–25° are associated with an increased risk of joint space narrowing and osteoarthrosis (adj OR 4.3, CI[2.2–8.7] [55]; OR 2.6–3.4, CI[1.2–6.0] [56, 57]). In the Japanese population, the majority of hip arthrosis seems to be due to dysplasia rather than FAI, with a peak age of presentation in ages 50–59 and females making up 80–90 % of arthroplasty patients [58]. A population-based study of the Sámi people in Norway who have high rates of neonatal and adult dysplasia did not observe a significant association between arthrosis and dysplasia, but the population studied had an average age of 48 [59]. It is likely that with such a young sample, the prevalence of arthrosis was low, making an association with dysplasia difficult to discern (Table 6.2).

With dysplasia, the amount of undercoverage and steepness of the acetabular roof is related to the risk of arthrosis. In a multicenter study of Japanese hip arthrosis patients, the risk of arthrosis was doubled for patients with an acetabular index (described as roof obliquity) of more than 10° or patients with less than 80 % femoral head coverage [60]. In a similar vein, radiographic follow-up of the contralateral hip in patients undergoing arthroplasty for dysplasia compared the hips of patients who had radiographic progression of arthrosis to those hips that did not show progression. In the group that progressed, the average CEA was 7 ± 12°, with an average acetabular index of 25 ± 10°, as compared to an average CEA of 34 ± 9° and an average acetabular index of 6° in the non-progression group [61].

Prevalence of Hip Arthrosis and FAI in Athletic Populations

Numerous studies have observed an increased rate of hip arthrosis and, in some cases, arthroplasty for men and women who participated in sports. When the exposure to sport was examined, men and women with high exposures to sports had a significantly increased likelihood of developing hip arthrosis as compared to people with moderate and low exposure to sport. For men, the relative risk of arthrosis was 4.5 [CI 2.7–7.6] for high exposure as compared to low exposure [62], and for women the relative risk was 2.3 [CI 1.5–3.7] [63]. A study of former national or professional level male athletes found that athletes who played impact sports—soccer, handball, and hockey—had a higher risk of hip arthrosis and total hip arthroplasty than control patients, with age-adjusted odds ratios ranging from 2.01 to 3.13, depending on the sport [64]. Athletes who played non-impact sports also had a higher risk of arthrosis, but the difference was not statistically significant (OR 1.35, [CI 0.63–2.92]) [64]. Other studies have also noted the increased incidence of arthrosis in former elite athletes as compared with controls, with former handball players having a 60 % incidence of radiographic OA compared to 13 % of controls [65] and former elite soccer players having an odds ratio of 2.1 [CI 1.0–4.2] for hip arthrosis as compared to controls [66]. Studies of former dancers have yielded conflicting results. One study of former professional dancers from Scandinavia showed an increased incidence of hip arthrosis compared to the general population [67], but a similar cohort from the Netherlands had no statistically significant difference in the prevalence of hip arthrosis between dancers and controls [68].

As early as 1971, Murray and Duncan noted that the "tilt deformity" was more common in young males with higher rates of activity. Presently, this deformity would be interpreted as a cam deformity [69]. Contemporary studies of asymptomatic collegiate, national level, and professional athletes have observed high rates of pathoanatomy that could cause FAI, which may ultimately be responsible for the high rates of arthrosis observed in former elite athletes. A study of American collegiate football players found that 61 % had a crossover sign and 91 % had decreased femoral head–neck offset or a cam deformity [70]. Asymptomatic professional and collegiate hockey players were found to have high rates of soft tissue abnormalities on MRI, with 77 % having evidence of labral tears, osteochondral lesions, or common adductor-rectus tendon dysfunction. In addition, 39 % of these players had an abnormally high alpha angle [71]. A study of professional soccer players revealed that 72 % of men and 50 % of women

had at least one radiographic abnormality that could cause FAI. Although these athletes were asymptomatic at the time of the X-ray, 50 % of men and 25 % of women reported a past groin or hip injury, indicating that these athletes may have intermittently symptomatic FAI or compensatory pathology [47].

There is some evidence that increased stress on the proximal femoral physis around the time of closure is responsible for the cam deformity [8]. Accordingly, in elite adolescent soccer players ages 12–19, 26 % had an alpha angle >60°, 13 % had a prominence at the head–neck junction, and 53 % had flattening, as compared to rates of 17, 0, and 18 % for these measures in control patients who did not play sports [72]. Elite club basketball players in Germany who had played basketball year-round since age 8 were found to have greater mean alpha angles than normal controls and larger mean alpha angles after physeal closure [73]. In the athletes, 89 % had an alpha angle >55° in at least one site after physeal closure. In the control patients, there was no increase in the mean alpha angle after physeal closure. Clinical examination of these athletes revealed that 48 % had pain on impingement testing (flexion, adduction, and internal rotation) and 19 % of athletes reported hip or groin pain in the preceding 6 months. In comparison, 1.3 % of the controls had a positive impingement test [73].

Genetic Influences

There is evidence suggesting that genetic factors influence the development of both FAI and dysplasia, although it appears the evidence is stronger for dysplasia than for FAI. A study of FAI patients and their siblings found that the siblings had an increased risk of both cam and pincer morphology (RR 2.8, [CI 1.8–4.2] for cam; RR 2.0, [CI 1.3–3.0] for pincer) relative to unrelated controls [74]. Studies performed 2 to 4 decades previously of children with neonatal hip dislocation due to dysplasia found that their parents also had radiographically shallower acetabuli than those of the normal population [75, 76]. More recent studies of patients with dysplasia provide a comparison to the FAI study. Siblings of patients with dysplasia have an up to 12-fold increased risk of dysplasia as compared to the general population [77].

At present, there has been only one study comparing the prevalence of FAI morphology between various ethnic groups in different countries. In elderly women with non-arthritic hips, 24 % of US women had a cam deformity as compared to 7 % of Chinese women. In addition, 46 % of the US women had a CEA >35°, or evidence of overcoverage, in comparison to 22 % of Chinese women. In contrast, there have been multiple studies comparing the prevalence of dysplasia between ethnic groups (Fig. 6.3, Table 6.2) and it varies widely. The development of hip dysplasia is multifactorial, however, with environmental or cultural factors that may affect physeal development, e.g., swaddling practices for newborns or prolonged periods of time spent in deep hip flexion as part of the activities of daily life in these countries.

Summary

The prevalence of FAI in the younger asymptomatic population is high. In addition, FAI is likely responsible for the majority of what was formerly considered idiopathic arthrosis. The prevalence rates of FAI in younger patients are not, however, the same as the prevalence rates for hip arthrosis, indicating that additional factors also play a role. The prevalence of dysplasia is quite variable, but like FAI, does not automatically cause hip arthrosis. Nonetheless, FAI and dysplasia are both common causes of hip pain in young people. Improvements in the biomechanical understanding of the anatomy and motion or static stress required to cause chondrolabral damage will help to explain which patients ultimately develop pain or arthrosis. Additional studies using high-quality axial CT or MR images and incorporating long-term follow-up are needed for determining the true prevalence of both FAI and dysplasia as well as monitoring disease progression.

References

1. Murray RO. The aetiology of primary osteoarthritis of the hip. Br J Radiol. 1965;38:810–24.
2. Solomon L. Patterns of osteoarthritis of the hip. J Bone Joint Surg Br. 1976;58-B:176–83.
3. Harris WH. Etiology of osteoarthritis of the hip. Clin Orthop Relat Res. 1986;213:20–33.
4. Ganz R, Parvizi J, Beck M, Leunig M, Nötzli H, Siebenrock KA. Femoroacetabular impingement: a cause for osteoarthritis of the hip. Clin Orthop Relat Res. 2003;417:112–20.
5. Ganz R, Leunig M, Leunig-Ganz K, Harris WH. The etiology of osteoarthritis of the hip: an integrated mechanical concept. Clin Orthop Relat Res. 2008; 466:264–72.
6. Ito K, Minka MA, Leunig M, Werlen S, Ganz R. Femoroacetabular impingement and the cam-effect. A MRI-based quantitative anatomical study of the femoral head-neck offset. J Bone Joint Surg Br. 2001;83-B:171–6.
7. Siebenrock KA, Wahab KHA, Werlen S, Kalhor M, Leunig M, Ganz R. Abnormal extension of the femoral head as a cause of cam impingement. Clin Orthop. 2004;418:54–60.
8. Kienle KP, Keck J, Werlen S, Kim YJ, Siebenrock KA, Mamisch TC. Femoral morphology and epiphyseal growth plate changes of the hip during maturation: MR assessments in a 1-year follow-up on a cross-sectional asymptomatic cohort in the age range of 9-17 years. Skeletal Radiol. 2012;41:1381–90.
9. Dudda M, Albers C, Mamisch TC, Werlen S, Beck M. Do normal radiographs exclude asphericity of the femoral head-neck junction? Clin Orthop Relat Res. 2009;467:651–9.
10. Meyer DC, Beck M, Ellis T, Ganz R, Leunig M. Comparison of six radiographic projections to assess femoral head/neck asphericity. Clin Orthop Relat Res. 2006;445:181–5.
11. Pfirrmann CWA, Mengiardi B, Dora C, Kalberer F, Zanetti M, Hodler J. Cam and pincer femoroacetabular impingement: characteristic MR arthrogram findings in 50 patients. Radiology. 2006;240: 778–85.
12. Rakhra KS, Sheikh AM, Allen D, Beaulé PE. Comparison of MRI alpha angle measurement planes in femoroacetabular impingement. Clin Orthop Relat Res. 2009;467:660–5.
13. Reichenbach S, Jüni P, Werlen S, Nüesch E, Pfirrmann CW, Trelle S, Odermatt A, Hofstetter W, Ganz R, Leunig M. Prevalence of cam-type deformity on hip magnetic resonance imaging in young males. A cross-sectional study. Arthritis Care Res. 2010;62: 1319–27.
14. Reichenbach S, Leunig M, Werlen S, Nüesch E, Pfirrmann CW, Bonel H, Odermatt A, Hofstetter W, Ganz R, Jüni P. Association between cam-type deformities and magnetic resonance imaging-detected structural hip damage. A cross-sectional study in young men. Arthritis Rheum. 2011;63: 4023–30.
15. Leunig M, Jüni P, Werlen S, Limacher A, Nüesch E, Pfirrmann CW, Trelle S, Odermatt A, Hofstetter W, Ganz R, Reichenbach S. Prevalence of cam and pincer-type deformities on hip MRI in an asymptomatic young Swiss female population: a cross-sectional study. Osteoarthritis Cartilage. 2013;21: 544–50.
16. Gosvig KK, Jacobsen S, Sonne-Holm S, Palm H, Troelsen A. Prevalence of malformations of the hip joint and their relationship to sex, groin pain, and risk of osteoarthritis. J Bone Joint Surg Am. 2010; 92-A:1162–9.
17. Hack K, DiPrimio G, Rakhra K, Beaulé PE. Prevalence of cam-type femoroacetabular impingement morphology in asymptomatic volunteers. J Bone Joint Surg Am. 2010;92:2436–44.
18. Kang ACL, Gooding AJ, Coates MH, Goh TD, Armour P, Rietveld J. Computed tomography assessment of hip joints in asymptomatic individuals in relation to femoroacetabular impingment. Am J Sports Med. 2010;38:1160–5.
19. Laborie LB, Lehmann TG, Engesæter I, Eastwood DM, Engesæter LB, Rosendahl K. Prevalence of radiographic findings thought to be associated with femoroacetabular impingement in a population-based cohort of 2081 healthy young adults. Radiology. 2011; 260:494–502.
20. Tönnis D, Heinecke A. Acetabular and femoral anteversion: relationship with osteoarthritis of the hip. J Bone Joint Surg Am. 1999;81-A:1747–70.
21. Bedi A, Dolan M, Leunig M, Kelly BT. Static and dynamic mechanical causes of hip pain. Arthroscopy. 2011;27:235–51.
22. Sutter R, Dietrich TJ, Zingg PO, Pfirrmann CWA. Femoral antetorsion: comparing asymptomatic volunteers and patients with femoroacetabular impingement. Radiology. 2012;263:475–83.
23. Fabricant PD, Bedi A, DeLaTorre K, Kelly BT. Clinical outcomes after arthroscopic psoas lengthening: the effect of femoral version. Arthroscopy. 2012;28: 965–71.
24. Unnanuntana A, Toogood P, Hart D, Cooperman D, Grant RE. Evaluation of proximal femoral geometry using digital photographs. J Orthop Res. 2010;28: 1399–404.
25. Buller LT, Rosneck J, Monaco FM, Butler R, Smith T, Barsoum WK. Relationship between proximal femoral and acetabular alignment in normal hip joints using 3-dimensional computed tomography. Am J Sports Med. 2012;40:367–75.
26. Hoaglund FT, Low WD. Anatomy of the femoral neck and head, with comparative data from Caucasians and Hong Kong Chinese. Clin Orthop Relat Res. 1980;152:10–6.

27. Durham HA. Anteversion of the femoral neck in the normal femur and its relationship to congenital dislocation of the hip. JAMA. 1915;65:223–4.
28. Kingsley PC, Olmsted KL. A study to determine the angle of anteversion of the neck of the femur. J Bone Joint Surg Am. 1948;30-A:745–51.
29. Tallroth K, Lepisto J. Computed tomography measurement of acetabular dimensions. Normal values for correction of dysplasia. Acta Orthop. 2006;77(4): 598–602.
30. Aktas S, Pekindil G, Ercan S, Pekindil Y. Acetabular dysplasia in normal Turkish adults. Bull Hosp Jt Dis. 2000;59:158–62.
31. Moussa M, Alomran A. Acetabular dysplasia in adult hips of a Saudi population. A possible relation to coxarthrosis. Saudi Med J. 2007;28:1059–61.
32. Johnsen K, Goll R, Reikerås O. Acetabular dysplasia in the Sami population: a population study among Sami in North Norway. Int J Circumpolar Health. 2008;67:147–53.
33. Dudda M, Kim YJ, Zhang Y, Nevitt MC, Xu L, Niu J, Goggins J, Doherty M, Felson DT. Morphologic differences between the hips of Chinese women and white women. Arthritis Rheum. 2011;63:2992–9.
34. Loder RT, Skopelja EN. The epidemiology and demographics of hip dysplasia. ISRN Orthop. 2011; 2011:238607.
35. Ezoe M, Naito M, Inoue T. The prevalence of acetabular retroversion among various disorders of the hip. J Bone Joint Surg Am. 2006;88-A:372–9.
36. Ochoa LM, Dawson L, Patzkowski JC, Hsu JR. Radiographic prevalence of femoroacetabular impingement in a young population with hip complaints is high. Clin Orthop Relat Res. 2010;468:2710–4.
37. Dolan MM, Heyworth BE, Bedi A, Duke G, Kelly BT. CT reveals a high incidence of osseous abnormalities in hips with labral tears. Clin Orthop Relat Res. 2011;469:831–8.
38. Weir A, de Vos RJ, Moen M, Hölmich P, Tol JL. Prevalence of radiological signs of femoroacetabular impingement in patients presenting with long-standing adductor-related groin pain. Br J Sports Med. 2011;45:6–9.
39. Nogier A, Bonin N, May O, Gedouin JE, Bellaiche L, Boyer T, Lequesne M. The French arthroscopy society. Descriptive epidemiology of mechanical hip pathology in adults under 50 years of age. Prospective series of 292 cases: clinical and radiological aspects and physiopathological review. Orthop Traumatol Surg Res. 2010;96S:S53–8.
40. Sahin N, Atici T, Özturk A, Özkaya G, Özkan Y, Avcu B. Prevalence of femoroacetabular impingement in asymptomatic contralateral hips in patients with unilateral idiopathic osteoarthritis. J Int Med Res. 2011;39:790–7.
41. Birrell F, Silman A, Croft P, Cooper C, Hosie G, Macfarlane G. Syndrome of symptomatic adult acetabular dysplasia (SAAD syndrome). Ann Rheum Dis. 2003;62:356–8.
42. Wright JB, Swiontkowski MF, Heckman JD. Introducing levels of evidence to the journal. J Bone Joint Surg Am. 2003;85-A:1–3.
43. Clohisy JC, Dobson MA, Robison JF, Warth LC, Zheng J, Liu SS, Yehyawi TM, Callaghan JJ. Radiographic structural abnormalities associated with premature, natural hip-joint failure. J Bone Joint Surg Am. 2011;93 Suppl 2:3–9.
44. Ipach I, Mittag F, Syha R, Kunze B, Wolf P, Kluba T. Indications for total hip arthroplasty in young adults—idiopathic osteoarthritis seems to be overestimated. Rofo. 2012;184:239–47.
45. Lynch JA, Parimi N, Chaganti K, Nevitt MC, Lane NE. The association of proximal femoral shape and incident radiographic hip OA in elderly women. Osteoarthritis Cartilage. 2009;17:1313–8.
46. Nakahara I, Takao M, Sakai T, Nishii T, Yoshikawa H, Sugano N. Gender differences in 3D morphology and bony impingement of human hips. J Orthop Res. 2011; 29:333–9.
47. Gerhardt MB, Romero AA, Silvers HJ, Harris DJ, Watanabe D, Mandelbaum B. The prevalence of radiographic hip abnormalities in elite soccer players. Am J Sports Med. 2012;40:584–8.
48. Myers SR, Eijer H, Ganz R. Anterior femoroacetabular impingement after periacetabular osteotomy. Clin Orthop Relat Res. 1999;363:93–9.
49. Steppacher SD, Tannast M, Werlen S, Siebenrock KA. Femoral morphology differs between deficient and excessive acetabular coverage. Clin Orthop Relat Res. 2008;466:782–90.
50. Hartofilakidis G, Bardakos NV, Babis GC, Georgiades G. An examination of the association between different morphotypes of femoroacetabular impingement in asymptomatic subjects and the development of osteoarthritis of the hip. J Bone Joint Surg Br. 2011;93:580–6.
51. Andrianakos AA, Kontelis LK, Karamitsos DG, Aslanidis SI, Georgountzos AI, Kaziolas GO, Pantelidou KV, Vafiadou EV, Dantis PC. Prevalence of symptomatic knee, hand, and hip osteoarthritis in Greece. The ESORDIG study. J Rheumatol. 2006;33:2507–14.
52. Bardakos NV, Villar RN. Predictors of progression of osteoarthritis in femoroacetabular impingement: a radiological study with a minimum of ten years follow-up. J Bone Joint Surg Br. 2009;91:162–9.
53. Nicholls AS, Kiran A, Pollard TCB, Hart DJ, Arden CPA, Spector T, Gill HS, Murray DW, Carr AJ, Arden NK. The association between hip morphology parameters and nineteen-year risk of end-stage osteoarthritis of the hip. A nested case-control study. Arthritis Rheum. 2011;63:3392–400.
54. Audenaert EA, Peeters I, VanOnsem S, Pattyn C. Can we predict the natural course of femoroacetabular impingement? Acta Orthop Belg. 2011; 77:188–96.

55. Reijman M, Hazes JMW, Pols HAP, Koes BW, Bierma-Zeinstra SMA. Acetabular dysplasia predicts incident osteoarthritis of the hip. The Rotterdam study. Arthritis Rheum. 2005;52:787–93.
56. Jacobsen S, Sonne-Holm S, Søballe K, Gebuhr P, Lund B. Hip dysplasia and osteoarthrosis. Acta Orthop. 2005;76:149–58.
57. Jacobsen S, Sonne-Holm S. Hip dysplasia: a significant risk factor for the development of hip osteoarthritis. A cross-sectional survey. Rheumatology. 2005;44:211–8.
58. Jingushi S, Ohfuji S, Sofue M, Hirota Y, Itoman M, Matsumoto T, Hamada Y, Shindo H, Takatori Y, Yamada H, Yasunaga Y, Ito H, Mori S, Owan I, Fujii G, Ohashi H, Iwamoto Y, Miyanishi K, Iga T, Takahira N, Sugimori T, Sugiyama H, Okano K, Karita T, Ando K, Hamaki T, Hirayama T, Iwata K, Nakasone S, Matsuura M, Mawatari T. Multiinstitutional epidemiological study regarding osteoarthritis of the hip in Japan. J Orthop Sci. 2010;15: 626–31.
59. Johnsen K, Goll R, Reikerås O. Acetabular dysplasia as an aetiological factor in development of hip osteoarthritis. Int Orthop. 2009;33:653–7.
60. Jingushi S, Ohfuji S, Sofue M, Hirota Y, Itoman M, Matsumoto T, Hamada Y, Shindo H, Takatori Y, Yamada H, Yasunaga Y, Ito H, Mori S, Owan I, Fujii G, Ohashi H, Iwamoto Y, Miyanishi K, Iga T, Takahira N, Sugimori T, Sugiyama H, Okano K, Karita T, Ando K, Hamaki T, Hirayama T, Iwata K, Nakasone S, Matsuura M, Mawatari T. Osteoarthritis hip joints in Japan: involvement of acetabular dysplasia. J Orthop Sci. 2011;16:156–64.
61. Murphy SB, Ganz R, Müller ME. The prognosis in untreated dysplasia of the hip. A study of radiographic factors that predict outcome. J Bone Joint Surg Am. 1995;77-A:985–9.
62. Vingard E, Alfredsson L, Goldie I, Hogstedt C. Sports and osteoarthritis of the hip. An epidemiologic study. Am J Sports Med. 1993;21:195–200.
63. Vingard E, Alfredsson L, Malchau H. Osteoarthrosis of the hip in women and its relationship to physical load from sports activities. Am J Sports Med. 1998; 26:78–82.
64. Tveit M, Rosengren BE, Nilsson JA, Karlsson MK. Former male elite athletes have a higher prevalence of osteoarthritis and arthroplasty in the hip and knee than expected. Am J Sports Med. 2012;40:527–33.
65. L'Hermette M, Polle G, Tourny-Chollet C, Dujardin F. Hip passive range of motion and frequency of radiographic hip osteoarthritis in former elite handball players. Br J Sports Med. 2006;40:45–9.
66. Lindberg H, Roos H, Gärdsell P. Prevalence of coxarthrosis in former soccer players; 286 players compared with matched controls. Acta Orthop Scand. 1993;64:165–7.
67. Andersson S, Nilsson B, Hessell T, Saraste M, Noren A, Stevens-Andersson A, Rydholm D. Degenerative joint disease in ballet dancers. Clin Orthop Relat Res. 1989;236:233–6.
68. van Dijk CN, Lim LSL, Poortman A, Strübbe EH, Marti RK. Degenerative joint disease in female ballet dancers. Am J Sports Med. 1995;23:295–300.
69. Murray RO, Duncan C. Athletic activity in adolescence as an etiological factor in degenerative hip disease. J Bone Joint Surg Br. 1971;53-B:406–19.
70. Kapron AL, Anderson AE, Aoki SK, Phillips LG, Petron DJ, Toth R, Peters CL. Radiographic prevalence of femoroacetabular impingement in collegiate football players. AAOS exhibit selection. J Bone Joint Surg Am. 2011;93:e111(1-10).
71. Silvis ML, Mosher TJ, Smetana BS, et al. High prevalence of pelvic and hip magnetic resonance imaging findings in asymptomatic collegiate and professional hockey players. Am J Sports Med. 2011;39:715–21.
72. Agricola R, Bessems JHJM, Ginai AZ, Heijboer MP, van der Heijden RA, Verhaar JAN, Weinans H, Waarsing JH. The development of cam-type deformity in adolescent and young male soccer players. Am J Sports Med. 2012;40:1099–106.
73. Siebenrock KA, Ferner F, Noble PC, Santore RF, Werlen S, Mamisch TC. The cam-type deformity of the proximal femur arises in childhood in response to vigorous sporting activity. Clin Orthop Relat Res. 2011;469:3229–40.
74. Pollard TCB, Villar RN, Norton MR, Fern ED, Williams MR, Murray DW, Carr AJ. Genetic influences in the aetiology of femoroacetabular impingement. A sibling study. J Bone Joint Surg Br. 2010;92-B:209–16.
75. Wynne-Davies R. Acetabular dysplasia and familial joint laxity: two etiological factors in congenital dislocation of the hip. J Bone Joint Surg Br. 1970; 52-B:704–16.
76. Hoaglund FT, Healey JH. Osteoarthrosis and congenital dysplasia of the hip in family members of children who have congenital dysplasia of the hip. J Bone Joint Surg Am. 1990;72-A:1510–8.
77. Stevenson DA, Mineau G, Kerber RA, Viskochil DH, Schaefer C, Roach JW. Familial predisposition to developmental dysplasia of the hip. J Pediatr Orthop. 2009;29:463–6.
78. Malhotra R, Kannan A, Kancherla R, Khatri D, Kumar V. Femoral head-neck offset in the Indian population: a CT based study. Indian J Orthop. 2012; 46:212–5.
79. Jung KA, Restrepo C, Hellman M, AbdelSalam H, Morrison W, Parvizi J. The prevalence of cam-type femoroacetabular deformity in asymptomatic adults. J Bone Joint Surg Br. 2011;93-B:1303–7.
80. Ahlberg A, Linder B, Binhemd TA. Osteoarthritis of the hip and knee in Saudi Arabia. Int Orthop. 1990; 14:29–30.
81. Mukhopadhaya B, Barooah B. Osteoarthritis of hip in Indians. An anatomical and clinical study. Indian J Orthop. 1967;1:55–62.

82. Veerapen K, Wigley RD, Valkenburg H. Musculoskeletal pain in Malaysia: a COPCORD survey. J Rheumatol. 2007;34:207–13.
83. Nevitt MC, Xu L, Zhang Y, Lui LY, Yu W, Lane NE, Quin M, Hochberg MC, Cummings SR, Felson DT. Very low prevalence of hip osteoarthritis among Chinese elderly in Beijing, China, compared with whites in the United States. Arthritis Rheum. 2002;46: 1773–9.
84. Zeng QY, Chen R, Darmawan J, Xiao ZY, Chen SB, Wigley R, Chen SL, Zhang NZ. Rheumatic diseases in China. Arthritis Res Ther. 2008;10:R17.
85. Lau EMC, Lin F, Lam D, Silman A, Croft P. Hip osteoarthritis and dysplasia in Chinese men. Ann Rheum Dis. 1995;54:965–9.
86. Hoaglund FT, Yau ACMC, Wong WL. Osteoarthritis of the hip and other joints in southern Chinese in Hong Kong. J Bone Joint Surg Am. 1973;55-A: 545–57.
87. Chung CY, Park MS, Lee KM, Lee SH, Kim TK, Kim KW, Park JH, Lee JJ. Hip osteoarthritis and risk factors in elderly Korean population. Osteoarthritis Cartilage. 2010;18:312–6.
88. Yoshimura N, Campbell L, Hashimoto T, Kinoshita H, Okayasu T, Wilman C, Coggon D, Croft P, Cooper C. Acetabular dysplasia and hip osteoarthritis in Britain and Japan. Br J Rheumatol. 1998;37:1193–7.
89. Lawrence JS, Sebo M. The geography of osteoarthritis. In: Nuki G, editor. The aetiopathogenesis of osteoarthritis. Baltimore, MD: University Park Press; 1980. p. 155–83.
90. Ali-Gombe A, Croft PR, Silman AJ. Osteoarthritis of the hip and acetabular dysplasia in Nigerian men. J Rheumatol. 1996;23:512–5.
91. Solomon L, Beighton P, Lawrence JS. Rheumatic disorders in the South African Negro. Part II. Osteo-arthrosis. S Afr Med J. 1975;49:1737–40.
92. Senna ER, de Barros ALP, Silva EO, Costa IF, Pereira LVB, Ciconelli RM, Ferraz MB. Prevalence of rheumatic diseases in Brazil: a study using the COPCORD approach. J Rheumatol. 2004;31:594–7.
93. Inoue K, Wicart P, Kawasaki T, Huang J, Ushiyama T, Hukuda S, Courpied JP. Prevalence of hip osteoarthritis and acetabular dysplasia in French and Japanese adults. Rheumatolgy. 2000;39:745–8.
94. Grotle M, Hagen KB, Natvig B, Dahl FA, Kvien TK. Prevalence and burden of osteoarthritis: results from a population survey in Norway. J Rheumatol. 2008; 35:677–84.
95. Danielsson L, Lindberg H. Prevalence of coxarthrosis in an urban population during four decades. Clin Orthop Relat Res. 1997;342:106–10.
96. van Saase JLCM, van Romunde LKJ, Cats A, Vandenbroucke JP, Valkenburg HA. Epidemiology of osteoarthritis: Zoetermeer survey. Comparison of radiological osteoarthritis in a Dutch population with that in 10 other populations. Ann Rheum Dis. 1989; 48:271–80.
97. Quintana JM, Arostegui I, Escobar A, Azkarate J, Goenaga I, Lafuente I. Prevalence of knee and hip osteoarthritis and the appropriateness of joint replacement in an older population. Arch Intern Med. 2008;168:1576–84.
98. Mannoni A, Briganti MP, DiBari M, Ferrucci L, Costanzo S, Serni U, Masotti G, Marchionni N. Epidemiological profile of symptomatic osteoarthritis in older adults: a population based study in Dicomano, Italy. Ann Rheum Dis. 2003;62:576–8.
99. Yoshida Y, Gregory JS, Mason B, Reid I, Reid DM. Prevalence and incidence of hip osteoarthritis identified from dual energy Xray absorptimetry images in the Auckland Calcium Study cohort. Rheumatology. 2011;50:iii88.
100. Ingvarsson T, Hägglund G, Lohmander LS. Prevalence of hip osteoarthritis in Iceland. Ann Rheum Dis. 1999;58:201–7.
101. Jordan JM, Helmick CG, Renner JB, Luta G, Dragomir AD, Woodard J, Fang F, Schwartz TA, Nelson AE, Abbate LM, Callahan LF, Kalsbeek WD, Hochberg MC. Prevalence of hip symptoms and radiographic and symptomatic hip osteoarthritis in African Americans and Caucasians: The Johnston County Osteoarthritis Project. J Rheumatol. 2009;36:809–15.
102. Hirsch R, Fernandes RJ, Pillemer SR, Hochberg MC, Lane NE, Altman RD, Bloch DA, Knowler WC, Bennett PH. Hip osteoarthritis prevalence estimates by three radiographic scoring systems. Arthritis Rheum. 1998;41:361–8.
103. Horváth G, Koroknai G, Ács B, Than P, Bellyei A, Illés T. Prevalence of radiographic primary hip and knee osteoarthritis in a representative Central European population. Int Orthop. 2011;35:971–5.
104. Han CD, Yoo JH, Lee WS, Choe WS. Radiographic parameters of the acetabulum for dysplasia in Korean adults. Yonsei Med J. 1998;39:404–8.
105. Goker B, Sancak A, Haznedaroglu S. Radiographic hip osteoarthritis and acetabular dysplasia in Turkish men and women. Rheumatol Int. 2005;25:419–22.
106. Umer M, Thambyah A, Tan WTJ, De Das S. Acetabular morphology for determining hip dysplasia in the Singaporean population. J Orthop Surg. 2006;14: 27–31.
107. Msamati BC, Igbigbi PS, Lavy CBD. Geometric measurements of the acetabulum in adult Malawians: radiographic study. East Afr Med J. 2003;80:546–9.

Abnormal Articular Anatomy

7

Courtney E. Scher and Ira Zaltz

Introduction

The first reports of labral tears were associated with posterior hip dislocations and described by Paterson in 1957 and Dameron in 1959 [1, 2]. In 1977, Altemberg reported two cases of non-traumatic labral tears, which were treated with open resection of the torn fragments [3]. In the late 1970s, a link was postulated between labral tears of the hip and the development of osteoarthrosis [4]. In 1986, Suzuki et al. reported successful arthroscopic diagnosis of labral tears [5]. More recently, there has been continued emphasis placed on the importance of the acetabular capsular–labral complex in the biomechanical properties of the hip [6]. In the setting of developmental dysplasia of the hip (DDH), femoroacetabular impingement (FAI), or trauma, lesions of the acetabular labrum can be sources of pain and loss of function [6]. In order to accurately identify and diagnose pathology involving the labrochondral complex of the hip, knowledge of the variable appearance and pathology of these structures is necessary.

C.E. Scher (✉)
Department of Musculoskeletal Radiology, Henry Ford Hospital, 2799 West Grand Boulevard, Detroit, MI 48202, USA
e-mail: courtneys@rad.hfh.edu

Diagnostic Imaging

Historically, single contrast arthrography was used to evaluate for the presence of labral tears, with varying success [7]. CT arthrography and MRI without arthrography have also been used, but with limitations. The current standard of practice is the use of MR arthrography (MRa) with radial sequencing when possible [7, 8]. 3T imaging without arthrography has recently been shown to have high sensitivity and accuracy in the diagnosis of labral pathology and chondral lesions [9]. Ultrasound is emerging as an alternative modality to dynamically evaluate labral tears and proximal femoral anatomy in the setting of impingement [10].

Labrum

Variation in asymptomatic patients. The acetabular labrum is typically triangular in shape and shows low signal intensity on all MRI sequences; however, there is known variability in asymptomatic patients. The shape of the labral–capsular complex can be triangular with a sharp edge centrally, rounded with a round edge, irregular in shape, or absent. With age, the labrum tends to become more round and irregular in morphology [11]. Internal signal characteristics of the labrum can also vary in asymptomatic patients. MRI signal of the normal labrum is most commonly homogeneously

Y.-J. Kim (eds.), *Hip Magnetic Resonance Imaging*,
DOI 10.1007/978-1-4614-1668-5_7,

Fig. 7.1 Sublabral sulcus. Posterior sublabral sulcus (*thin arrow*) (axial PD arthrogram images)

hypointense, but can also be heterogeneous with central intermediate or high signal, heterogeneous with central hyperintense signal communicating with the articular surface, or diffusely hyperintense. The heterogeneity and abnormal signal of the labrum also increase with age in the asymptomatic population [11].

Sublabral sulcus. One pitfall in diagnosing labral tears is the presence of a sublabral sulcus (labrocartilagenous cleft). A sublabral sulcus is seen intraoperatively as a smooth, well-defined groove at the labral base where it attaches to the underlying chondral surface, with no associated irregularity or fraying of the labrum, and no signs of healing [12, 13]. Direct probing of the sulcus at surgery results in no instability of the labrum [14]. In contrast, at surgery, labral tears appear irregular with fraying, instability to probing, and, in some cases, signs of healing [12, 13]. On MRa, a sublabral sulcus is seen as contrast material insinuating partially between the labral base and chondral surface (Fig. 7.1). The defect appears smooth, in contrast to the irregularities seen with pathologic or degenerative labral tears. Contrast that spans the entire labral base, or extends into the substance of the labrum, should be considered abnormal. Dinauer et al. found the prevalence of a posteroinferior labral sulcus to be approximately 22 % [14]. However, over 90 % of labral tears occur anteriorly or anterosuperiorly; therefore, the presence of a posteroinferior labral sulcus should not be confused with a labral tear.

Studler et al. have described the presence of a sublabral sulcus located in the anterior hip, which makes the distinction between the sulcus and a tear more difficult [15]. However, the anterior sublabral sulcus and labral tears can be differentiated by location and appearance. Using a clock face with 12 o'clock located superiorly toward the head of the patient, 3 o'clock posterior, 6 o'clock inferior, and 9 o'clock anterior, the anterior sublabral sulcus occurs at the 8 o'clock position most commonly (located within the anteroinferior quadrant). Defects occurring at the 9 o'clock and 10 o'clock positions (in the anterosuperior quadrant) are more typical for labral tears, which helps with the distinction. In addition, the sublabral sulcus is typically smooth, without contrast material extending into the substance of the labrum or across the entire labral base with MRa. There is no associated cartilage loss, labral signal abnormality, underlying osseous lesion, or para-labral cyst seen in conjunction with sublabral sulci, while these are common findings associated with labral tears [15].

There is also a normal perilabral recess, occurring between the labrum and the overlying joint capsule, which can become distended with contrast material during MRa [6, 12] (Fig. 7.2). However, given its location, superficial to the chondrolabral junction, mistaking this normal variant for a tear would be unlikely.

Absence of the labrum. Early MR imaging of the pediatric and adult hip demonstrated certain patients with complete absence of the labrum, thought to be a congenital variant [6]. However, these early studies used MR scanners with lower resolution and larger slice thickness than used in current imaging techniques. Furthermore, older MR imaging of the labrum was done without intra-articular contrast material, which greatly aids in evaluating the acetabular labrum. Findings of congenitally absent labra were likely the result of early imaging limitations, rather than true abnormalities.

The labrum becomes more heterogeneous with age, demonstrating increased signal intensity and irregular morphology. Apparent absence of the labrum in the older population is likely a

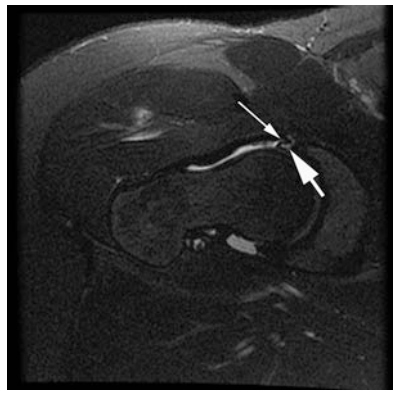

Fig. 7.2 Normal variant perilabral recess (*thin white arrow*) between the joint capsule and the underlying labrum. Tear of the underlying acetabular labrum is also present (*thick arrow*) (axial PD arthrogram image)

result of significant degenerative change and tearing, as opposed to congenital absence.

Labral tears. Tears of the acetabular labrum can be associated with the development of cartilage loss, progressive cartilage damage, and subsequent development of osteoarthrosis. When it occurs, this process is initiated by shear forces or impingement within the hip causing excessive loading of the labrum. Inciting pathology includes acetabular dysplasia or morphology associated with FAI. Initial shear forces or impingement may then result in fraying of the acetabular labrum along its articular margin, progressing to labral tearing at the chondrolabral junction. Delamination of the articular cartilage may then occur, resulting in cartilage flaps at the level of the labral abnormality, leading to further progression of labral and chondral degeneration, and, eventually, osteoarthrosis [16, 17].

When evaluating the acetabular labrum with MRa, the labrum should be assessed for its morphology, the presence of abnormal signal, the presence of contrast material within an adjacent cleft/defect, as well as the presence of contrast material extending into the labrum itself, or across the entire labral base. Care must be taken to distinguish perilabral recess and sublabral sulcus, which are normal findings, from true labral tears.

Labral tears and associated cartilage lesions occur most commonly in the anterosuperior quadrant of the hip, and may be of partial or full thickness [12] (Figs. 7.3 and 7.4), with occasional extension into other quadrants. Concurrent labral tears at multiple sites are seen relatively infrequently, and have been reported only 7 % of the time [12]. When this occurs, the tears typically occur anteriorly and posteriorly. The posterior tear is thought to represent a countre-coup injury secondary to the change in biomechanics of the hip caused by the anterior tear [12]. Isolated posterior labral tears in the Western population most commonly occur in the setting of trauma and posterior hip dislocation [18]. However, a higher incidence of non-traumatic posterior labral tears has been reported in Japan, possibly due to the increased amounts of time spent squatting or sitting on the floor [12, 19].

Labral tears occur most commonly at the chondrolabral junction and are often described as labral detachments. Histologically, this type of tear occurs at the transition zone between the fibrocartilage of the labrum and the underlying hyaline articular cartilage [19]. Tears confined to the substance of the labrum, occurring along the course of the circumferentially oriented fibers, are less common [12]. Histologically, these types of tears involve cleavage planes of variable depths within the substance of the labrum, perpendicular to the internal surface of the labrum [19].

Acute tears. Classically, labral tears in the setting of trauma have been described with posterior hip dislocations. Transverse acetabular fractures are associated with avulsion of the labrum from the acetabular rim [12]. More commonly, labral tears occur in the setting of repetitive micro-trauma at extremes of motion in certain athletes. Soccer, hockey, golf, martial arts, and ballet involve extremes of abduction, extension, flexion, and external rotation, and have been associated with labral tears [19]. The most common movement associated with acute labral tears is hyperextension with concurrent external rotation. In this position, the labrum is subject to increased strain and the forces that are transmitted across the labrummay result in a tear. Damage to the adjacent hyaline cartilage is the

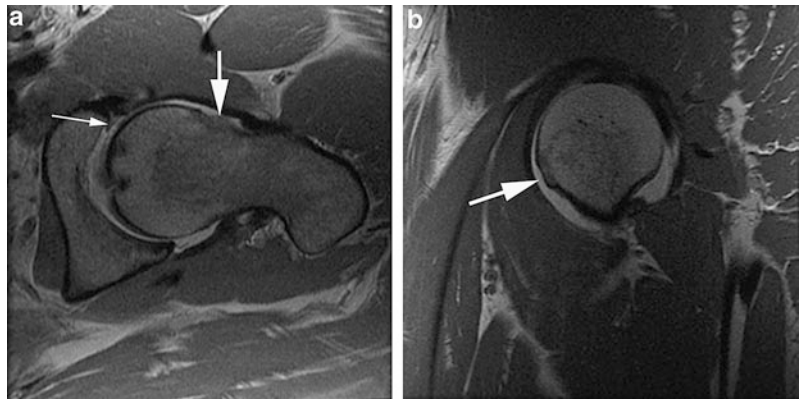

Fig. 7.3 Full-thickness labral tear at the chondrolabral junction. (**a**) Labral tear (*thin white arrow*) in the setting of FAI. Note the prominent osseous excrescence at the femoral head–neck junction (*short thick white arrow*). (**b**) Prominent osseous excrescence of the femoral head–neck junction (*thick white arrow*) is seen in sagittal plane (axial T2 and sagittal PD arthrogram images)

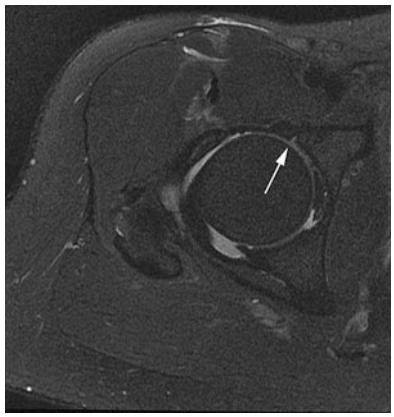

Fig. 7.4 Partial thickness labral tear—small partial defect at the chondrolabral junction (*white arrow*). Axial T2 fat-saturated arthrogram image

most common associated injury seen in the setting of a labral tear [19].

Femoroacetabular impingement. FAI has been characterized as abutment of the proximal femoral head–neck junction with the anterosuperior acetabulum. FAI can be classified as CAM type (osseous excresence at the femoral head–neck junction), pincer type (overcoverage of the femoral head by the acetabulum), or mixed. Impingement between the proximal femur and acetabulum damages the interposed labrum and cartilage and has been associated with the development of osteroarthrosis.

Developmental hip dysplasia. Patients with DDH are prone to distinct labrochondral and acetabular pathology, known as the "acetabular rim syndrome," described by Klaue [20]. There are two subtypes of acetabular rim syndrome. Type I involves a shallow and vertically oriented acetabulum, with an incongruent femoral head. This incongruence shifts the weight-bearing load to the labrum resulting in shear stresses across the labrum and secondary hypertrophy and separation from the adjacent acetabulum (Fig. 7.5). In this situation, para-labral cysts may form, which should alert the clinician to the possibility of an underlying labral tear [13].

In Type II, the joint is congruent, but the acetabular roof is small and fails to adequately cover the femoral head. Consequently, increased stress on the diminutive acetabulum and chondrolabral structures results in cartilaginous tearing and subchondral injury. Joint fluid undermines the tears within the cartilage resulting in intraosseous/subchondral cyst formation [13].

Classification of labral tears. Czerney et al. and Hoffmann et al. have classified the MRI appearance of labral tears by using three stages of posttraumatic (IA, IIA, IIIA) and dysplastic lesions(IB, IIB, IIIB) as below [21, 22]:

Stage 0 (*normal*)—Homogeneous low signal intensity, a triangular shape, and continuous attachment to the lateral margin of the acetabulum without a notch or a sulcus.

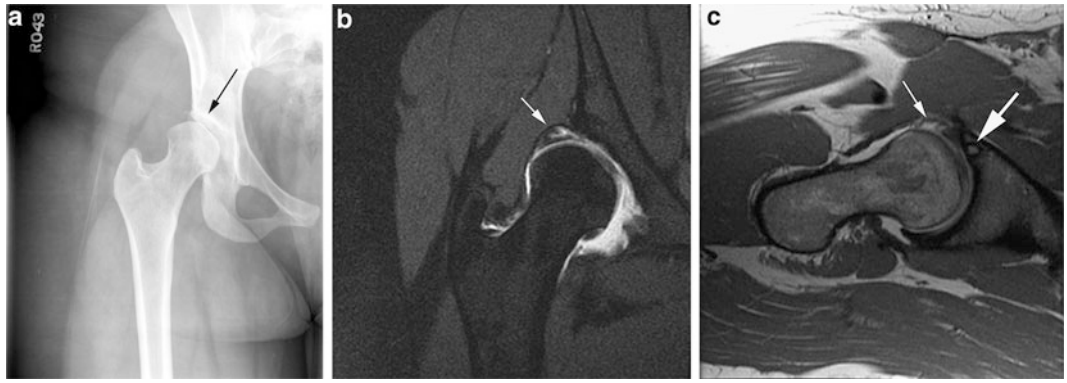

Fig. 7.5 Developmental hip dysplasia. (**a**) Radiographs showing a shallow acetabulum (*black arrow*) with uncovering of the femoral head. (**b**) Hypertrophied and torn labrum (*white arrow*), with incongruence of the femoral head within the acetabulum. (**c**) Subchondral cysts are seen indicating early degenerative changes (*thick white arrow*). Hypertrophied and torn labrum is seen with lack of a perilabral recess (*thin arrow*) (coronal fat-saturated T1, axial PD arthrogram images)

Stage IA—Area of increased signal intensity within the center of the triangular-shaped labrum.

Stage IB—Similar to IA, but the labrum is thickened and there is no perilabral recess.

Stage IIA—Extension of contrast material into the labrum without detachment, and the presence of a triangular shape and a recess (Fig. 7.2).

Stage IIB—Same as IIA, but the labrum is thickened and a recess is not present (Fig. 7.5).

Stage IIIA—The labrum is detached, and there is a triangular shape and a recess.

Stage IIIB—Same as IIIA, but the labrum is thickened and there is no recess.

Athroscopically, labral tears may be classified according to their structure. A radial flap tear involves the free edge of the labrum with formation of a separate flap. A radial fibrillated tear shows fraying at the free edge of the labrum. A longitudinal peripheral tear occurs along the acetabular insertion of the labrum and is considered unstable [19]. A bucket-handle tear occurs when there is separation of the labrum from the acetabular rim at the chondrolabral junction [19].

Articular Cartilage

Cartilage appearance on MRI. Cartilage damage in the hip occurs initially along the acetabular surface, whereas the femoral cartilage is typically preserved until late in degeneration. Since the acetabular cartilage is thinner than in other joints of the body, detection of pathology is challenging. The use of 3T MRI has improved detection of focal chondral lesions in the hip [12]. The normal articular cartilage in the hip demonstrates homogeneous intermediate signal, with the acetabular and femoral surfaces separated by a thin band of high signal intensity, representing joint fluid or gadolinium [12]. Pathology in the cartilage manifests as inhomogeneity of signal, thinning, and irregular morphology, most commonly in the anterosuperior quadrant.

Supraacetabular fossa. The supraacetabular fossa (SAF) is a normal variation in the acetabular roof, which can mimic a focal cartilage defect (Fig. 7.6). It is located at the 12 o'clock position in coronal and sagittal planes, and can appear as a focal notch devoid of cartilage, or in some instances it can be filled with cartilage. Occasionally, the SAF is large enough that it can fill with contrast at arthrography and can be seen on conventional radiographs [23]. Another variation of the acetabulum is the superior acetabular roof notch, also known as the stellate crease, when seen arthroscopically. The roof notch is more linear in morphology, located at the apex of the acetabulum, and is devoid of cartilage [23, 24] (Fig. 7.7).

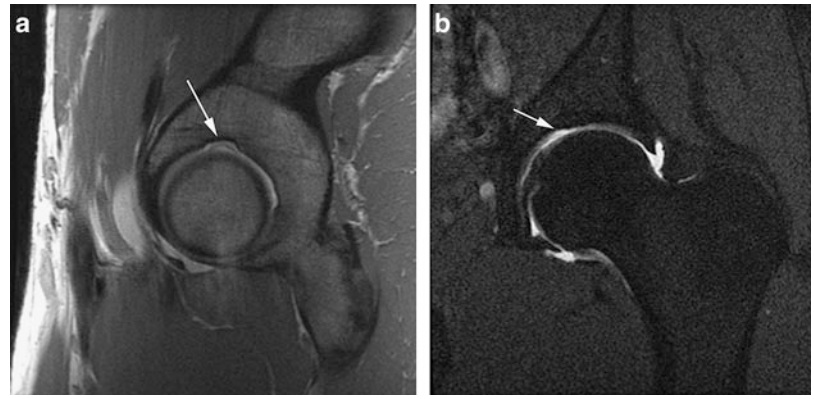

Fig. 7.6 Supraacetabular fossa devoid of cartilage (*white arrows*) (**a**, **b**) which should not be mistaken for pathology of the cartilage (sagittal PD and coronal T1 fat-saturated post-arthrogram images)

Fig. 7.7 Superior acetabular roof notch (*black arrows* in (**a**) and (**b**)) in two different patients (AP and frog-leg lateral radiographs). The larger roof notch fills with contrast at arthrography (*white arrow* in (**c**)) (sagittal PD post-arthrogram image). When seen arthroscopically, the roof notch is termed a stellate crease

Association of cartilage damage with labral tears. Labral tears in the hip, in the setting of DDH or FAI, are associated with damage to the hyaline cartilage. Pathologic forces generated within the hip are transmitted across the labrum, which leads to fraying of the labrum peripherally along the joint margin. This fraying eventually gives way to tearing of the labrum at the articular margin, with subsequent delamination of the underlying articular cartilage. This delamination leads to the formation of a cartilage flap adjacent to the labral pathology (Fig. 7.8), leading to more widespread labral and chondral injury and progressive osteoarthrosis (Fig. 7.9) [12].

Cartilage defects and surgical classification. Cartilage damage is classically described surgically using the Outerbridge classification, which was developed for use in the knee and does not account for the pattern of damage that is unique to the hip. Beck et al. developed a staging classification for cartilage damage in the hip, as follows [19]:

Stage 0—Normal—Macroscopically sound cartilage

Stage 1—Malacia—Roughening of surface, fibrillation

Stage 2—Pitting malacia—Roughening, partially thinning and full-thickness defects or deep fissuring to the bone

Stage 3—Debonding—Loss of fixation to the subchondral bone, macroscopically sound cartilage; carpet phenomenon

Stage 4—Cleavage—Loss of fixation to the subchondral bone; frayed edges, thinning of cartilage

Stage 5—Defect—Full-thickness defect

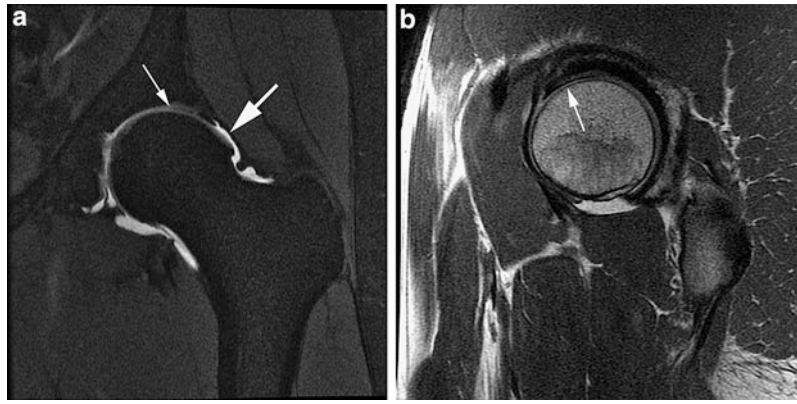

Fig. 7.8 Chondral flap (**a**, **b**) (*thin white arrows*) in the setting of FAI and a labral tear. Note the prominent osseous excrescence at the femoral head–neck junction indicating underlying FAI (*thick white arrow*) (coronal T1 fat-saturated; sagittal PD arthrogram images)

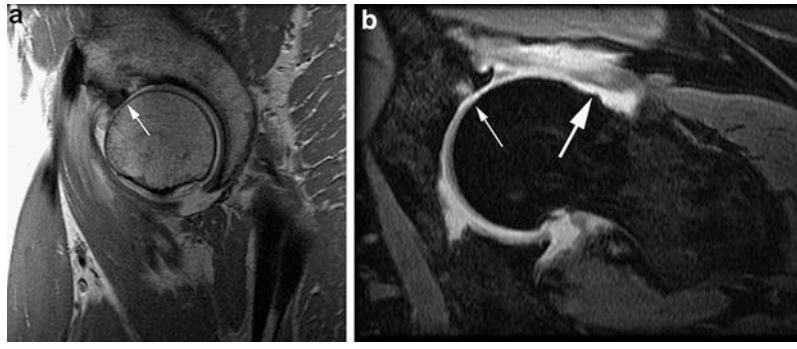

Fig. 7.9 Hip OA secondary to long-standing FAI (**a**, **b**) with complete loss of cartilage of the anterosuperior hip (*thin white arrow*). Note prominent osseous excrescence at the femoral head–neck junction (*thick white arrow*) indicating underlying FAI (sagittal PD, axial 3D arthrogram images)

References

1. Paterson I. The torn acetabular labrum: a block to reduction of a dislocated hip. J Bone Joint Surg. 1957;39-B:306–9.
2. Dameron TB. Bucket-handle tear of acetabular labrum accompanying posterior dislocation of the hip. J Bone Joint Surg. 1959;41-A:131–4.
3. Altenberg AR. Acetabularlabral tears: a cause of hip pain and degenerative arthritis. South Med J. 1977;70 (2):174–5.
4. Harris WH, Bourne RB, Oh I. Intra-articular acetabular labrum: a possible etiological factor in certain cases of osteoarthrosis of the hip. J Bone Joint Surg. 1979;61-A:510–4.
5. Suzuki S, et al. Arthroscopic diagnosis of ruptured acetabular labrum. Acta Orthop Scand. 1986; 57:513–5.
6. Czerny C, et al. MR arthrography of the adult acetabular capsular-labral complex: correlation with surgery and anatomy. Am J Radiol. 1999;173:345–9.
7. Plötz GMJ, Brossman J, Schünke M, Heller M, Kurz B, Hassenpflug J. Magnetic resonance arthrography of the acetabular labrum—macroscopic and histologic correlation in 20 cadavers. J Bone Joint Surg. 2000;82:426–32.
8. Horii M, Toshikazu T, Hirasawa Y. Radial MRI of the hip with moderate osteoarthritis. J Bone Joint Surg. 2000;82-B:364–8.
9. Sundberg TP, Toomayan GA, Major NM. Evaluation of acetabular labrum at 3.0T MR imaging compared with 1.5T MR arthrography: preliminary experience. Radiology. 2006;238(2):706–11.
10. Buck FM, Hodler J, Zanetti M, Dora C, Pfirrmann CWA. Ultrasound for the evaluation of femoroacetabular impingement of the cam type. Diagnostic performance of qualitative criteria and alpha angle measurements. Eur Radiol. 2011;21:167–75.

11. Abe I, et al. Acetabular labrum: abnormal findings at MR imaging in asymptomatic hips. Radiology. 2000;216:576–81.
12. Saddik D, Troupis J, Tirman P, O'Donnell J, Howells R. Prevalence and location of acetabular sublabral sulci at hip arthroscopy with retrospective MRI review. Am J Radiol. 2006;187:W507–11.
13. Petersilge C. Imaging of the acetabular labrum. MRI Clin N Am. 2005;13:641–52.
14. Dinauer PA, Murphy KP, Carroll JF. Sublabral sulcus at the posteriorinferior acetabulum: a potential pitfall in MR arthrography diagnosis of acetabular labral tears. Am J Radiol. 2004;183:1745–53.
15. Studler U, et al. MR arthrography of the hip: differentiation between an anterior sublabral recess as a normal variant and a labral tear. Radiology. 2008; 249:947–54.
16. McCarthy JC, et al. The role of labral lesions to development of early degenerative hip disease. Clin Orthop Relat Res. 2001;393:25–37.
17. Pfirrmann CWA, Duc SR, Zanetti M, Dora C, Hodler J. MR arthrography of acetabular cartilage delamination in femoroacetabular cam impingement. Radiology. 2008;249(1):236–41.
18. Byrd JW. Labral lesions: an elusive source of hip pain case reports and literature review. Arthroscopy. 1996;12:603–12.
19. Tzaveas A, Villar R. Acetabular labral and chondral pathology. Open Sports Med J. 2010;4:64–74.
20. Klaue K, Durnin CW, Ganz R. The acetabular rim syndrome. J Bone Joint Surg. 1991;73B:423–9.
21. Czerny C, et al. Lesions of the acetabular labrum: accuracy of MR imaging and MR arthrography in detection and staging. Radiology. 1996;200:225–30.
22. Hofmann S, Tschauner C, Urban M, Eder T, Czerny C. Clinical and diagnostic imaging of labrum lesions in the hip joint. Orthopade. 1998;27:681–9.
23. Dietrich TJ, Suter A, Pfirrmann CWA, Dora C, Fucentese SF, Zanetti M. Supraacetabular fossa (pseudodefect of acetabular cartilage): frequency at MR arthrography and comparison of findings at MR arthrography and arthroscopy. Radiology. 2012;263:484–91.
24. Johnstone WH, Keats TE, Lee ME. The anatomic basis for the superior acetabular roof notch "Superior Acetabular Notch". Skeletal Radiol. 1982;8:25–7.

Developmental Hip Disorders

8

Jeffrey J. Nepple and Young-Jo Kim

Introduction

Symptomatic hip pain in adults is increasingly recognized as sequelae of residual deformity from pediatric hip disease. Common developmental hip disorders include developmental hip dysplasia, slipped capital femoral epiphysis (SCFE), and Legg–Calve–Perthes (LCP) disease. Additionally, the recent recognition of femoroacetabular impingement (FAI) as a cause of hip pain and intra-articular damage also appears to be the result of deformity formation during adolescence, possibly in response to overexposure to certain athletic activities. While FAI plays a role in the pathophysiology of both SCFE and LCP disease, the common presentation of FAI in the absence of symptomatic pediatric hip disease is discussed in detail elsewhere. This chapter will review the characteristic deformity, epidemiology, and natural history of developmental hip dysplasia, SCFE, and LCP disease.

Developmental Dysplasia of the Hip

Developmental hip dysplasia is a result of abnormal formation of acetabular and/or femoral structure that results in abnormal loads across the femoral-acetabular articulation. Acetabular dysplasia is more commonly treated than femoral deformities. Wiberg [1] first recognized the association of hip dysplasia with the development of osteoarthritis and reported measurement of the lateral center edge angle (LCEA) for characterization of acetabular coverage. His original description defined a LCEA less than 20° as dysplasia, while a LCEA of 20–25° indicates borderline dysplasia and a LCEA greater than 25° is normal.

Epidemiology

Acetabular dysplasia remains the most common pediatric hip disorder and the most common reason for osteoarthritis in young adults undergoing hip arthroplasty [2, 3]. Jacobsen et al. [4] reported rates of acetabular dysplasia of 5.5 % (as defined by LCEA $< 20°$) in a cross-sectional cohort over 3,500 Caucasians in Denmark. Similarly, Engesaeter et al. [5] found a prevalence of 3.3 % in a large Norwegian cohort, including 4.2 % in females and 2.4 % in males. Nunley et al. [6] reported that 72 % of patients presenting with symptomatic adult acetabular dysplasia were female, compared to 28 % male.

Acetabular Deformity

Acetabular dysplasia is most commonly recognized by relative lateral deficiency of the acetabulum and increased inclination of the weight-bearing surface.

J.J. Nepple (✉)
Department of Orthopaedic Surgery, Washington University School of Medicine, 1 Barnes-Jewish Hospital Plaza, St. Louis, MO 63110, USA
e-mail: jeff.nepple@gmail.com

Y.-J. Kim (eds.), *Hip Magnetic Resonance Imaging*,
DOI 10.1007/978-1-4614-1668-5_8,

Fig. 8.1 Range of acetabular dysplasia seen in hip dysplasia. The *right panel* shows a mild acetabular dysplasia with no evidence of hip subluxation. The *left panel* shows a severe acetabular dysplasia with subluxation of the hip and an acetabular rim fracture

The acetabular weight-bearing surface has a decreased surface area and is maloriented. Yet, the acetabular deformity is variable, encompassing a spectrum from a mildly shallow socket to frank dislocation (Fig. 8.1). Acetabular dysplasia can be subclassified as anterior, posterior, or global deficiencies, based on the presence of relative anterior and posterior deficiency. Global and anterior deficiencies are most commonly seen. Unlike femoral version, acetabular version is on average similar in dysplastic hips compared to normal controls. Acetabular retroversion has been reported to be present in 18 % of dysplastic hips. The presence of acetabular retroversion in dysplastic hips indicates posterior acetabular deficiency, in addition to anterosuperior deficiency [7]. Posterior deficiency may play a role in earlier and more severe symptomatology in dysplastic hips [7]. Acetabular retroversion in dysplastic hips is unlike deformity present in patients with FAI and acetabular retroversion, where anterosuperior overcoverage is generally present. Recognition of acetabular retroversion is important for surgical planning in acetabular dysplasia.

Femoral Deformity

Although less commonly treated than acetabular deformities, femoral deformities are commonly present in patients with hip dysplasia. Deformities of femoral version and femoral head/neck morphology are most apparent. Dysplastic hips generally have increased femoral anteversion compared to non-dysplastic hips. Several studies have demonstrated average increases of 10–20° of femoral anteversion compared to controls (which average approximately 15°). However, the degree of femoral anteversion in dysplastic hips is extremely variable and can even include femoral retroversion [8]. An increased valgus orientation (increased neck-shaft angle) to the femoral neck is present on AP pelvis radiographs in almost half of cases [9]. However, in some cases apparent coxa valga may be projectional and not truly present. Noble et al. [10] demonstrated that this valgus orientation of the femoral neck is commonly seen in dysplastic hips with a normal neck-shaft angle due to an increased femoral anteversion when the femoral neck is not placed perpendicular to the plane of the AP pelvis radiograph.

Nearly 75 % of hips with acetabular dysplasia have evidence of aspherical femoral heads or insufficient femoral head–neck offset (Fig. 8.2). Abnormalities of the femoral head–neck junction in dysplastic hips can resemble typical femoral deformities seen in FAI. While impingement can occur at the extremes of motion in dysplastic hips, it is not generally thought to play a major role in the pathophysiology of hip dysplasia.

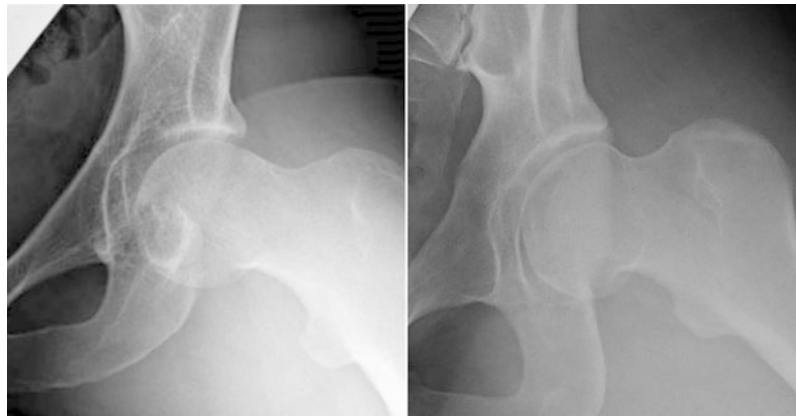

Fig. 8.2 The range of femoral head and head–neck offset deformity seen in acetabular dysplasia. The *left panel* shows a decrease in head–neck offset seen in a mildly dysplastic hip, while the *right panel* shows a femoral head deformity in a hip with significant acetabular dysplasia

However, impingement after redirectional acetabular osteotomies has been recognized and is influenced by the presence of dysplastic femoral morphologies. Dysplastic hips commonly have smaller femoral heads, femoral necks, and femoral intramedullary canals than non-dysplastic hips. Significant rotational deformities of the proximal femur are commonly present as well, including relatively more posterior location to the greater trochanter.

Natural History

In some series, developmental hip dysplasia remains the most common cause of osteoarthritis in young adults undergoing total hip arthroplasty, accounting for nearly half of all cases [2, 3]. Cooperman et al. [11] demonstrated the development of osteoarthritis in all hips with a LCEA less than 20° at 22-year follow-up. Similarly, Murphy et al. investigated the long-term outcome of the contralateral hip in patients undergoing arthroplasty due to hip dysplasia. Osteoarthritis developed by the age of 65 in all hips with a LCEA less than 16° or an acetabular inclination of greater than 15°. The natural history of hips with borderline acetabular dysplasia (LCEA 20–25°) is more controversial. It appears that some hips with borderline dysplasia develop osteoarthritis, while others do not. Further research is needed to clarify the natural history in this population.

Delayed gadolinium-enhanced magnetic resonance imaging of cartilage (dGEMRIC) has been introduced as a measure of cartilage biochemistry and has been shown to correlate with pain and degree of acetabular deformity in dysplastic populations [12]. dGEMRIC has been shown to be a sensitive means of detecting early degenerative changes not seen on radiographs in this population. A dGEMRIC index of less than 390 ms is generally indicative of early osteoarthritis. Jessel and colleagues [13] demonstrated using dGEMRIC studies that degenerative changes were more strongly correlated with anterior acetabular deficiency, than lateral acetabular deficiency.

Pattern of Articular Damage

Klaue et al. [14] provided an improved understanding of the pathological process of dysplastic hips in their description of "acetabular rim syndrome." Biomechanical alterations in these hips produce dynamic hip instability and subsequent anterosuperior acetabular rim overload that may lead to acetabular labral and chondral injury and eventual osteoarthritis. Biomechanical analyses have demonstrated increased peak contact stresses at the acetabular rim in dysplastic

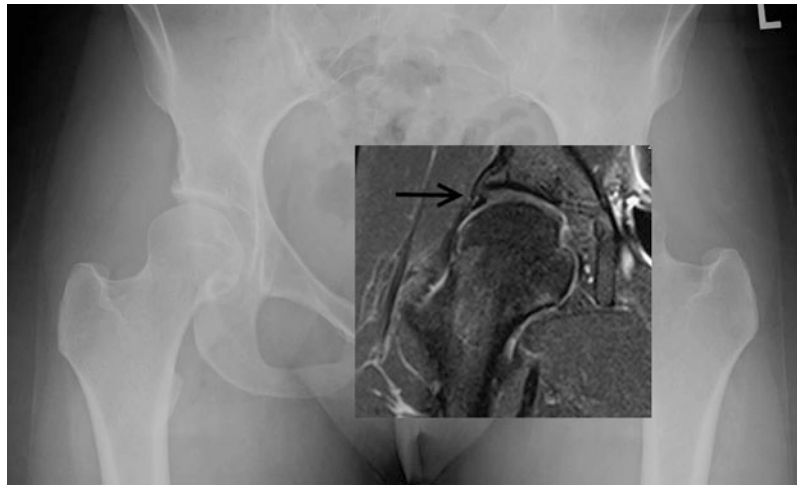

Fig. 8.3 Patient with acetabular dysplasia seen on radiograph. On MRI, the acetabular labrum and cartilage is enlarged

hips. Elevated contact stresses are due to multiple factors including a lateralized hip center, increased body-weight level arm, and decreased acetabular surface area. The acetabular labrum has a weight-bearing role in the dysplastic hip, unlike the non-dysplastic hip, and generally becomes hypertrophic in response to this stress (Fig. 8.3). This makes the acetabular labrum more prone to labrochondral separation or tearing. Subsequent loss of labral function can lead to increased overload of the acetabular rim and degenerative changes. Ross et al. [15] reported acetabular labral tears and anterosuperior rim articular cartilage lesions in over two-thirds of patients undergoing combined hip arthroscopy and periacetabular osteotomy. Hips with a LCEA less than 15° were more likely to have major articular cartilage damage.

Slipped Capital Femoral Epiphysis

SCFE involves an injury to the immature proximal femoral physis leading to varying degrees of displacement of the femoral neck relative to the epiphysis. The femoral metaphysis generally displaces anteriorly and externally rotates, leading to relative posterior displacement of the epiphysis (Fig. 8.4). Appropriate timely clinical diagnosis and treatment is important to minimize the degree of deformity present. SCFE is commonly classified based on acuity of symptoms [acute (<3 weeks) or chronic (>3 weeks)] and ability to bear weight with crutches (stable or unstable) at presentation. Loder et al. [16] reported no cases of osteonecrosis in stable slips, compared to a 47 % rate of osteonecrosis in unstable slips. However, clinical categorization of stable and unstable slips has been shown to poorly correlate with intraoperative assessment of stability [17, 18].

Historically, SCFE has been most commonly treated with in situ fixation, as attempts at reduction have been associated with high rates of avascular necrosis. However, advances in surgical technique, including surgical hip dislocation with an extended retinacular flap, allow for protection of the blood supply to femoral head during reduction and have been advocated in some cases [19] (Fig. 8.5). Residual proximal femoral deformity after in situ fixation of a SCFE has been reported to undergo variable degrees of remodeling. Long-term follow-up studies of SCFE have generally shown good hip function, but with significant self-limitation of activities. Recent evidence suggests that FAI occurs in patients with residual deformity and may lead to acetabular chondral and labral damage. Femoral head–neck osteoplasty (Fig. 8.6) has been utilized to address mild residual deformity, while

Fig. 8.4 Slipped capital femoral epiphysis seen in the right hip. The femoral neck displaces anteriorly and is externally rotated relative to a femoral head that is in place

proximal femoral osteotomy (Fig. 8.7) is required for more severe cases. Further research is needed to determine if the long-term outcomes of these procedures alter the natural history of the disease.

MRI plays a role in the detection of the early occult SCFE with normal plain radiographs (pre-slip). In these cases, MRI demonstrates physeal widening, adjacent bony edema, joint effusion, and synovitis (Fig. 8.8). MRI has a limited role in the presence of radiographic evidence of deformity. MRI may play a role in the detection and characterization of subsequent osteonecrosis, but its role is limited by the degree of metallic artifact present postoperatively.

Epidemiology

SCFE is among the most common pediatric hip disorders with a reported incidence of 10.8 per 100,000 children in the United States in 2000, with a mean age at presentation of 12.1 years [20]. SCFE more commonly occurs in males (13.4/100,000) compared to females (8.1/100,000). The cumulative risk among males approaches 1 per 1,000. The increased prevalence in males is likely due to hormonal factors during puberty. Estrogen generally results in strengthening of the physis, while testosterone decreases the strength of the physis. Mean age at presentation was 12.7 years in males, compared to 11.1 years in females. While the chronologic age of patients with SCFE is variable, the physiologic age has been demonstrated to be narrower [21]. Bilateral SCFE is present at presentation in approximately 20 % of cases, while an additional 10–20 % develop a contralateral SCFE at a later point. Obesity is currently recognized as the most common risk factor for development of SCFE, with more than 80 % of all patients with SCFE being obese. Trends of increasing obesity in children have been mirrored by increasing rates of SCFE. SCFE is more common among African-American and Hispanic populations, reflecting increased rates of obesity in these populations. Other recognized risk factors include endocrine disorders, renal osteodystrophy, and previous radiation therapy. Endocrine abnormalities are present in 5–8 % of SCFEs, including hypothyroidism, panhypopituitarism, growth hormone deficiency, and hypogonadism.

Femoral Deformity

Subtle changes in femoral morphology may predispose some individuals to the development of SCFE. Decreased femoral anteversion is commonly present in hips with SCFE at presentation and may play a role in the development of SCFE due to increasing shear force across the physis. Pritchett et al. [22] reported that relative femoral retroversion in SCFE patients results in increased shear stress on the physis by 3.3 times body weight in the sagittal plane during fast walking. Gelberman et al. [23] reported a mean femoral neck anteversion of 1° as measured by CT in a cohort of 39 slips, compared to standard reference values of 15–20° in this age group. Similar levels of anteversion were present in slips at presentation and at follow-up after operative treatment. Additionally, decreased femoral anteversion has been noted in populations of obese patients with an average of 0° of anteversion compared to 11° in normal contrals.

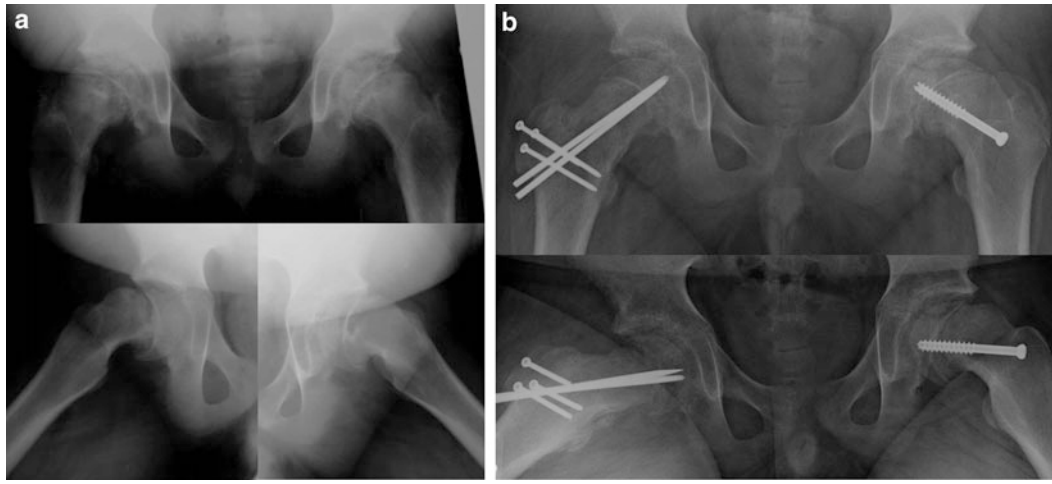

Fig. 8.5 Patient with bilateral slipped capital femoral epiphysis (**a**). The right hip (**b**) underwent a modified Dunn procedure to realign the femoral head onto the femoral neck. The milder left hip underwent in situ screw fixation

This association may partially explain the link of obesity and SCFE. Similarly, a mild varus alignment of the femoral neck results in a more vertical orientation of the physis and may increase shear force and contribute to the development of SCFE. The physeal orientation in the contralateral hips of patients with SCFE has been shown to be 8–11° more oblique than normal.

Anterior displacement of the proximal femoral metaphysis is the primary deformity present in SCFE. This has been traditionally described as posterior displacement of the proximal femoral epiphysis, despite the unchanged relationship between the epiphysis and the acetabulum. Medial displacement of the epiphysis is variably present on anteroposterior radiographs, but may be a result of the relatively externally rotated posture of the leg that is commonly present. The severity of the deformity is commonly classified using measurement of the Southwick slip angle on frog-leg lateral radiographs (Fig. 8.9), in which the femoral epiphyseal-shaft angle is measured on the affected side and subtracted from the measurement of the contralateral normal hip. SCFE is classified as mild with angle 0–30°, moderate 30–60°, and severe 60°.

The metaphyseal prominence in the residual SCFE is considered the major residual deformity and may result in FAI. Rab characterized the residual SCFE deformity and its role in FAI utilizing three-dimensional modeling of walking and sitting positions [24]. Two types of FAI were noted: "impaction" and "inclusion." Impaction-type impingement occurs in moderate to severe deformities where a large metaphyseal prominence impacts the acetabular rim preventing further motion. This type of impingement results in severe alterations of range of motion, including the classic obligatory external rotation that occurs with hip flexion. Additionally, external rotation of the leg may be required during walking to prevent impingement. Inclusion-type impingement occurs with milder deformities where a smaller metaphyseal prominence is able to enter the acetabulum but may result in chondrolabral damage, similar to the mechanism seen in cam-type FAI. In a CT-based model of bony impingement, Mamisch et al. [25] demonstrated that the relative head–neck offset, in addition to degree of slip, influences range of motion to impingement.

In 1926, Key [26] first described radiographic evidence of remodeling after SCFE, including resorption of the anterior-superior metaphyseal bone and new bone formation along the posterior-inferior neck. Remodeling of the metaphyseal prominence in SCFE after in situ

Fig. 8.6 The anterior metaphyseal prominence seen on the *top right panel* after in situ fixation was removed (osteoplasty) via a surgical dislocation approach

fixation has been demonstrated by multiple studies, but is variable. Remodeling potential is generally greater in individuals with an open proximal femoral physis and significant remaining growth potential. O'Brien et al. [27] reported on the remodeling of 12 patients with moderate or severe slips treated with in situ fixation. Remodeling was observed in 83 % of hips, generally in the presence of an open triradiate cartilage. However, radiographic evidence of remodeling in these patients would be viewed as incomplete by modern standards. Jones et al. [28] described a classification system for residual deformity of the anterior head–neck junction. Type A hips demonstrate a normal transition from the convexity of the femoral head to the concavity of the anterior femoral neck. In type B hips the transition from femoral head to femoral neck is straight. Type C hips demonstrate convexity of the head–neck junction with the anterior margin of the femoral head projecting posterior to the anterior prominence of the neck (Fig. 8.10). Unlike by modern standards, type A and B hips were defined as completely remodeled (90 % of mild, 50 % of moderate or severe slips). Siegel et al. [29] demonstrated remodeling reductions in slip angle from 44° to 30° as measured by computed tomography at 2 years postoperatively. Significant gains in flexion and internal rotation range of motion generally occurred by 6 months postoperatively without associated changes in femoral version. Changes in range of motion after 6 months postoperatively were minimal. While multiple studies demonstrate the remodeling does occur after in situ fixation of SCFE, the remodeling is generally incomplete with significant residual deformity present [30].

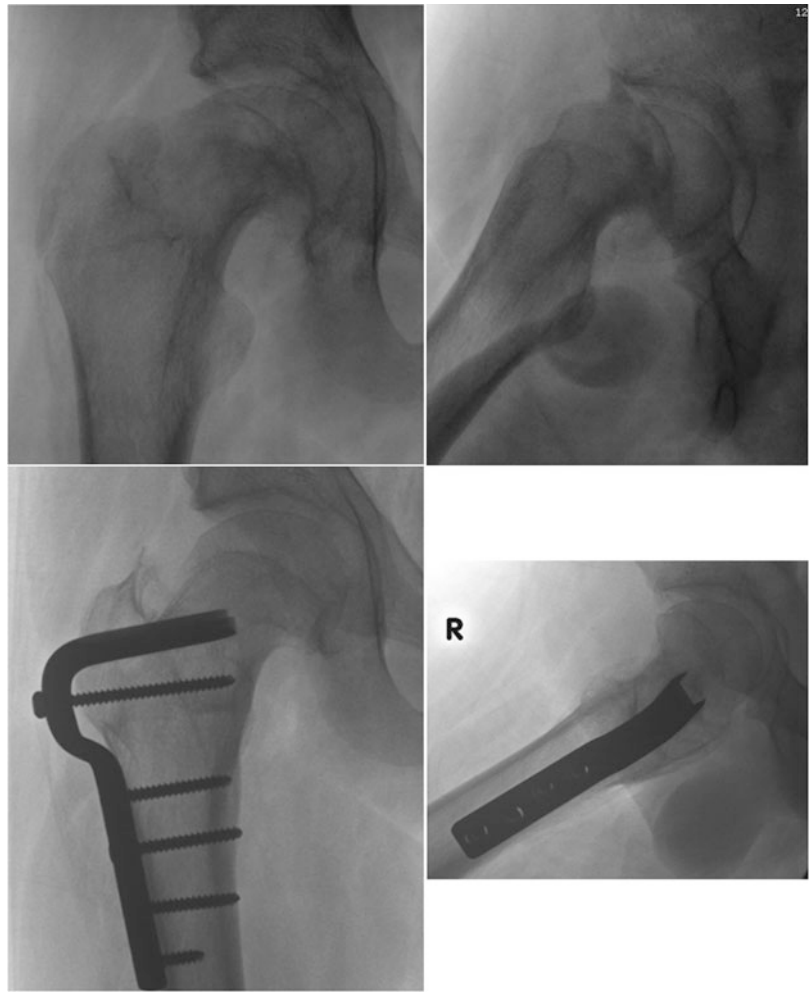

Fig. 8.7 Severe healed SCFE deformity (*top panels*) corrected via an intertrochanteric flexion osteotomy and an osteoplasty (*bottom panels*)

Femoral deformities in cam-type FAI have been speculated to be the result of mild or subclinical slips [31]. However, recent evidence suggests that while the deformity in cam-type FAI may result from physeal stresses, the deformity does not appear to occur from displacement of the epiphysis as seen in SCFE. Utilizing MRI, Siebenrock et al. [32] demonstrated that the typical anterosuperior cam deformity is a result of abnormal extension of the proximal femoral physis, compared to controls (Fig. 8.11). Additionally, this study established that the proximal femoral epiphysis is otherwise normally oriented relative to the femoral neck, without evidence of posterior epiphyseal displacement seen in SCFE.

Acetabular Deformity

The presence of acetabular deformity in patients with SCFE has been variably reported. Unlike other pediatric hip disorders, SCFE generally occurs at an age when limited remodeling capabilities of the acetabulum exist. Acetabular overcoverage or retroversion could play a role in the etiology of SCFE in some patients, as well as worsening FAI occurring in patients with

Fig. 8.8 Patient with left hip pain. Plain radiographs show minimal evidence of a SCFE. The T1 weighted image (*middle panel*) shows some physeal widening in the left hip. The T2 weight image (*bottom panel*) shows edema around the physis

residual deformity. Kitadai et al. reported a slightly increased acetabular coverage in patients with SCFE compared to matched controls (LCEA 37° vs. 34°). Several studies have showed no significant difference in acetabular version between involved and uninvolved hips in patients with SCFE. Monazzam et al. [33] demonstrated increased prevalence of cranial acetabular retroversion on CT, increased rates of acetabular overcoverage in hips with SCFE, as well as contralateral unaffected hips. Utilizing plain radiographs, Sankar et al. [34] found significantly increased coverage (LCEA 33° vs. 20°) and prevalence of acetabular retroversion (positive crossover sign 78 % vs. 21 %) in the contralateral hip of patients with SCFE compared to a control group.

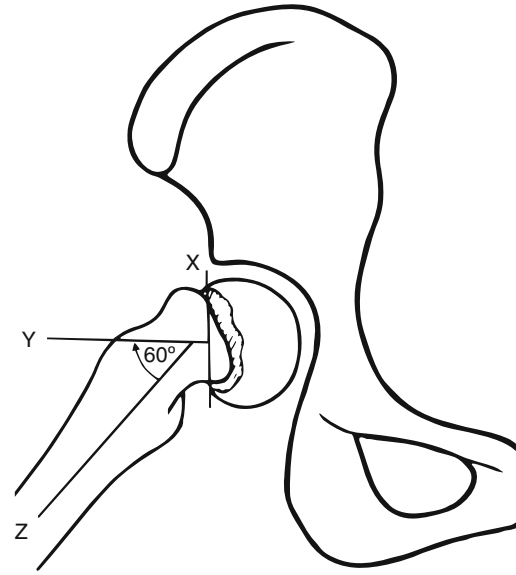

Fig. 8.9 The Southwick slip angle measured on the frog lateral view

Natural History

Rates of osteoarthritis in mild slips treated with in situ fixation at 31- to 41-year follow-up have been reported from 16 to 64 %, with 7–10 % rates of severe osteoarthritis. Similarly, in severe slips rates of osteoarthritis were reported from 60 to 100 %, with 33–40 % rates of severe osteoarthritis. Carney et al. [35] reported a series of 155 hips with SCFE at a mean follow-up of 41 years. The authors concluded the natural history in this population was characterized by "mild deterioration related to the severity of slip and complications." Osteonecrosis and chondrolysis occurred more commonly after reduction attempts. Twenty-eight percent of patients underwent further surgery (generally arthroplasty) at a median of 28 years postoperatively. Further surgery was more common with more severe slips (12 % mild, 30 % moderate, 53 % severe). Fraitzl et al. [36] reported on a cohort of 16 patients with average age of 28 years after in situ pinning of mild slips. Tegner activity scores averaged 5.2, with more than half be 4 or less (implying minimal sporting activities). Residual deformity was more prominent at the lateral head–neck junction (mean

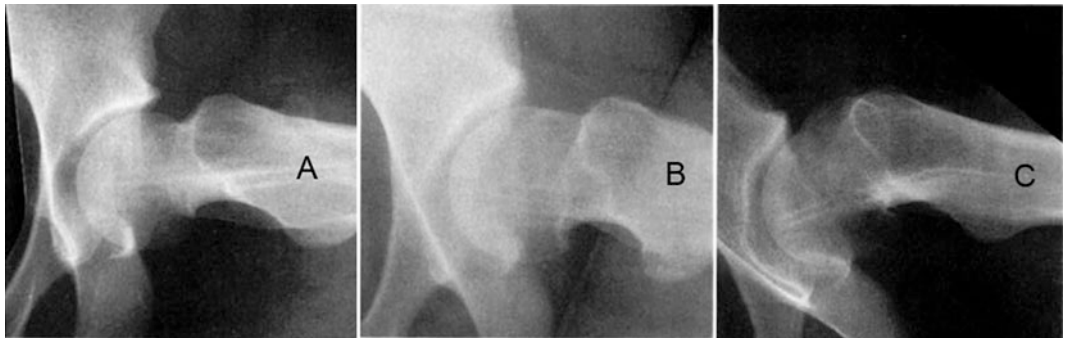

Fig. 8.10 Metaphyseal remodeling after SCFE can be classified as Jones type: (**A**) normal convexity in head–neck junction, (**B**) straight transition from head to neck, and (**C**) convex projection of the head–neck junction

alpha 86°), than the anterior head–neck junction (mean alpha 55°). Goodman et al. [31] investigated the association of "post-slip" morphology and the development of osteoarthritis in the Hamann–Todd collection of nearly 3,000 cadavers. A prevalence of post-slip morphology was seen in 8 % of hips. Severe osteoarthritis was present in 38 % of hips with post-slip morphology, compared to 26 % for controls. A 68 % prevalence of severe osteoarthritis was seen in hips with mild post-slip morphology that were greater than 56 years old. Wensaas et al. [37] reported on a group of 36 patients (43 hips) treated with in situ fixation at a mean follow-up of 37 years. Six hips had undergone total hip arthroplasty, while four additional hips had radiographic evidence of osteoarthritis. Higher alpha angles were found to correlate with a poorer outcome.

FAI Pathology

Several recent studies have demonstrated substantial rates (75–100 %) of intra-articular chondral and labral pathology in hips with SCFE. The degree of intra-articular damage does not appear to correlate with the degree of femoral deformity. Inclusion-type impingement seen in mild deformities may actually be more destructive than impaction-type impingement. Similarly, rates of articular cartilage damage have been reported at 87–96 % in stable slips, compared to 73 % for unstable slips [17, 38, 39]. Ziebarth et al. [17] reported a 75 % prevalence of moderate–severe articular cartilage damage in stable slips. Sink et al. reported on a cohort of 39 hips (36 patients) undergoing surgical hip dislocation for persistent symptoms after in situ fixation of SCFE (34 hips, average 20 months after initial procedure) or chronic stable SCFE without previous surgery (five hips with severe slips). The cohort included 8 mild, 20 moderate, and 11 severe slips. Intraoperatively, labral injury was present in 87 % of hips, including 33 % with complete or partial labral detachments. Acetabular cartilage injury was present in 85 % of hips, including 36 % with full-thickness cartilage damage. Labrochondral injury was most commonly present from the 3:00 position anteriorly to the 11:00 position posteriorly, similar to other causes of FAI. Leunig et al. [40] and Lee et al. [41] demonstrated significant chondral and labral pathology in a group of five patients with mild slips (slip angle $< 30°$) undergoing hip arthroscopy.

Legg–Calve–Perthes Disease

LCP disease is a pediatric osteonecrosis of the proximal femoral epiphysis that commonly results in residual hip deformity in the adult. Since its original independent descriptions in 1910 by Legg, Calve, and Perthes, significant advances in the understanding of LCP have occurred but the etiology remains unknown. Animal models have demonstrated that the

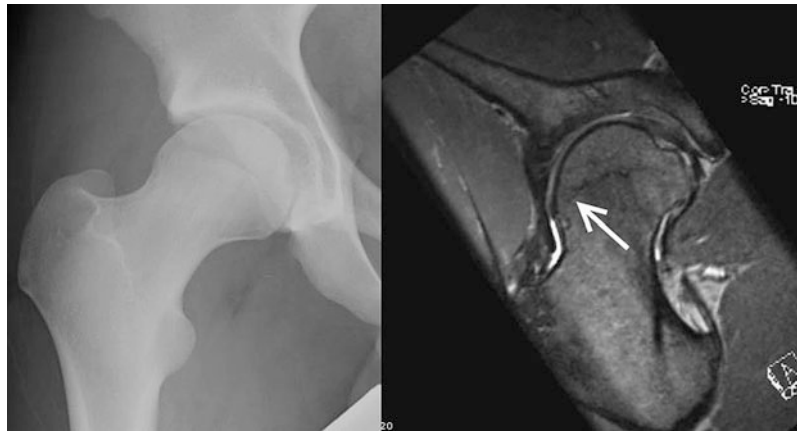

Fig. 8.11 Physeal extension seen on the MRI scan of a patient with cam impingement. Deformity is distinctly different from a SCFE

deformities of residual LCP generally result from more than one vascular insult. LCP disease is commonly classified into four stages using radiographs: initial, fragmentation, reossification, and healed. The extent of femoral head involvement is commonly apparent during the fragmentation stage and is an important prognostic factor to the eventual outcome. Revascularization of the proximal femoral epiphysis invariably occurs, but variable components of femoral head deformity remain. Secondary acetabular remodeling is also variable and plays an important role in the eventual outcome of LCP. Residual deformities are highly variable and may contribute to FAI, hip instability, or both. Precise characterization of both femoral and acetabular morphology is extremely important in order to understand the underlying causes of pain. Modern surgical techniques also allow for detailed intraoperative assessment of the presence of impingement and instability. The risk of hip osteoarthritis has generally been shown to correlate with the degree of residual femoral head deformity and hip congruency (Fig. 8.12). Most individuals with LCP maintain reasonable hip function into adulthood. However, the degree of residual deformity and the altered biomechanics of the hip lead to symptoms in some young adults.

MRI has a role in the identification of early stages of LCP prior to the presence of radiographic changes, as well as defining the extent of necrosis present. MRI also defines the extent of deformity present in early stages by characterizing the cartilaginous portion of the femoral head and may detect subluxation not apparent on plain radiographs. However, at present MRI currently does not play a role in staging disease in LCP. Additionally, MRI is useful in evaluating the extent of labral and chondral (and osteochondral) changes present in patients with residual deformity. Significant degenerative changes may be seen on MRI despite an apparently preserved joint space on plain radiographs.

Epidemiology

The peak age of onset of LCP is approximately 7 years [42], with most cases presenting between 4 and 8 years of age. Males are affected five times more commonly than females, while females are generally thought to have a worse prognosis. Bilateral involvement occurs in 10–12 % of cases. The incidence of LCP has been reported to be from 0.4 to 15.6 per 100,000, with significant geographical and socioeconomic variation. LCP is more common in Caucasians.

Femoral Deformity

Residual femoral deformities in LCP are a result of complex interactions of several factors including premature physeal closure, asymmetric

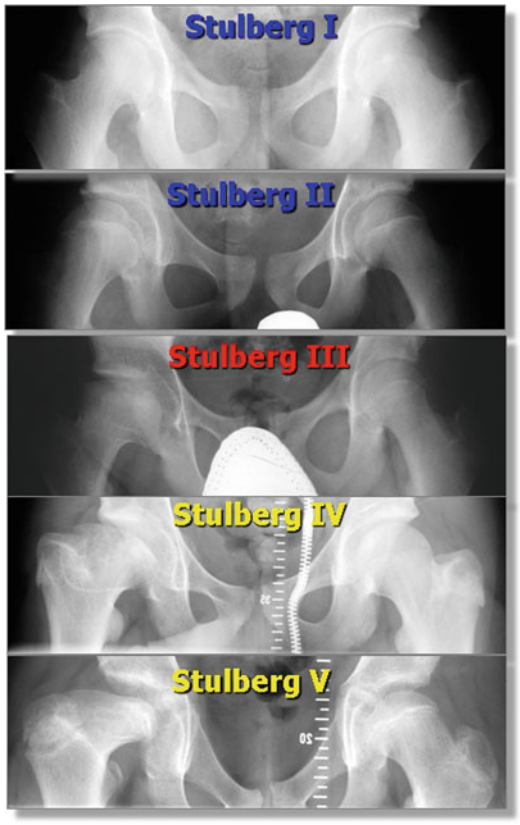

Fig. 8.12 Long-term risk of osteoarthritis in hips with LCPD is a function of femoral head sphericity and joint congruency which is classified using the Stulberg classification: *I*—normal, *II*—spherical but with coxa magna, coxa breva, or acetabular dysplasia, *III*—nonspherical but not flat head, *IV*—flat femoral head with congruent acetabulum, and *V*—flat femoral head with incongruent acetabulum

healing, abnormal remodeling secondary to stresses, and remodeling secondary to acetabular impingement. Typical deformities include asphericity of the femoral head, coxa magna, coxa plana, coxa breva, and trochanteric overgrowth (Fig. 8.13). Central physeal closure may result in coxa breva with maintained sphericity of the femoral head, while lateral physeal closure additionally creates significant irregularity of the femoral head shape. The femoral articular surface orientation is commonly altered and located on the superior posteromedial portion of the head. While the relationship of the femoral neck to shaft in patients with LCP may represent normal or increased femoral anteversion, the relative retrotorsion of the articulating femoral head to the femoral neck creates "functional retroversion" (Fig. 8.14). The inferior anterolateral head ("false head") is extruded outside of the acetabulum and commonly represents a block to internal rotation. In the presence of significant lateral deformity hinged abduction may occur. Hinged abduction occurs when impingement of the lateral femoral head on the acetabulum occurs during abduction, resulting in the medial femoral head levering out of the acetabulum. The presence of coxa breva and trochanteric overgrowth contributes to a reduced lever arm for the abductor mechanism that contributes to a Trendelenburg gait and abductor fatigue frequently seen in these patients.

Mose et al. [43] classified the degree of residual asphericity of the femoral head into four groups: (1) normal, (2) flattened spherical (1–2 mm asphericity), (3) irregular (2–4 mm asphericity), and (4) very irregular (>4 mm asphericity). In 1981, Stulberg classified the residual deformity at skeletal maturity as (1) normal, (2) spherical but with coxa magna, coxa breva, or abnormally steep acetabulum, (3) nonspherical but not flat femoral head, (4) flat femoral head with coxa magna/breva and steep acetabulum, and (5) flat femoral head with normal femoral neck and acetabulum [44].

FAI in hips with residual deformity of LCP is most commonly a result of significant femoral head deformity. Similar to "inclusion" and "impaction" types of impingement seen after SCFE, both mechanisms of impingement are seen in LCP depending on the degree of the residual deformity. Significant variability in the location of the femoral head deformity and impingement exists with some deformities more prominent anteriorly and other laterally. Continued remodeling can occur until the cessation of skeletal growth. Trochanteric overgrowth and coxa breva result in altered biomechanics of the abductor mechanism and can contribute to extra-articular impingement. The trochanteric position results in relative overwork of the abductor mechanism and contributes to the clinical presentation of abductor fatigue and Trendelenburg gait. The presence of extra-articular impingement in hips

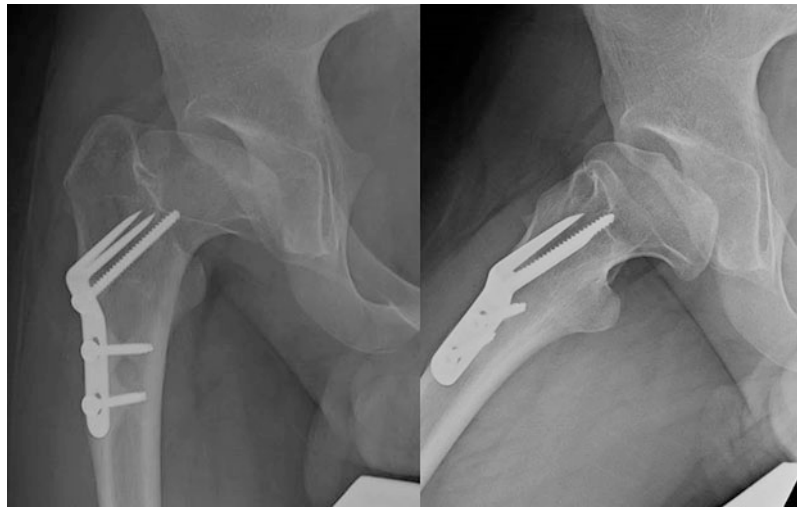

Fig. 8.13 Healed LCPD with oval femoral head, high riding greater trochanter, and short femoral neck (coxa breva)

with LCP has been increasingly recognized. Tannast et al. [45] utilizing CT-based range of motion simulations demonstrated extra-articular impingement was present in 86 % of hips, while intra-articular impingement was present in 79 %. During abduction, the greater trochanter can cause impingement against the supraacetabular bone. During extension and external rotation, the greater trochanter can similarly impinge against the ischium. Osteochondritis dissecans lesions of the femoral head can occur but are relatively uncommon (3 %). Leg length discrepancies may occur in cases of significant epiphyseal collapse and premature physeal closure.

Acetabular Deformity

Secondary acetabular deformity in LCP is highly variable and may include components of acetabular dysplasia, acetabular retroversion, and articular incongruency. Acetabular remodeling is complex and generally necessary to maintain congruency of the joint in the setting of significant femoral deformity. Acetabular growth is generally slowed after the age of 8 and this likely plays a role in the limited acetabular remodeling potential in patients with LCP onset at a later age. Acetabular hyperemia and in some cases premature triradiate cartilage closure has been shown relative to the contralateral hip [46]. Acetabular dysplasia in LCP is signified by a steep acetabular orientation. Traditional measures of acetabular coverage can be difficult to measure when severe femoral head deformity exists. Significant acetabular dysplasia may result in dynamic instability and lateral acetabular rim overload with subsequent labral and chondral damage. Clohisy et al. [47] utilized a periacetabular osteotomy (in addition to other concomitant surgical procedures) to address instability in 46 % of a series of 97 consecutive hips treated for residual Perthes-like hip deformity. Evidence of acetabular dysplasia as indicated by measurements of LCEA, anterior center edge angle, and acetabular inclination were predictive of the presence of clinical instability. In the presence of femoral head deformity, the absence of acetabular dysplasia may result in incongruity of the femoroacetabular articulation.

Acetabular retroversion is present in 31–42 % of hips with residual LCP based on plain radiographs (compared to 6 % of controls) and may result in pincer-type impingement. Three-dimensional imaging is important to confirm apparent acetabular retroversion, when alterations of pelvic tilt or rotation are present on plain radiographs. Cranial acetabular retroversion occurs fairly commonly in LCP and correlates

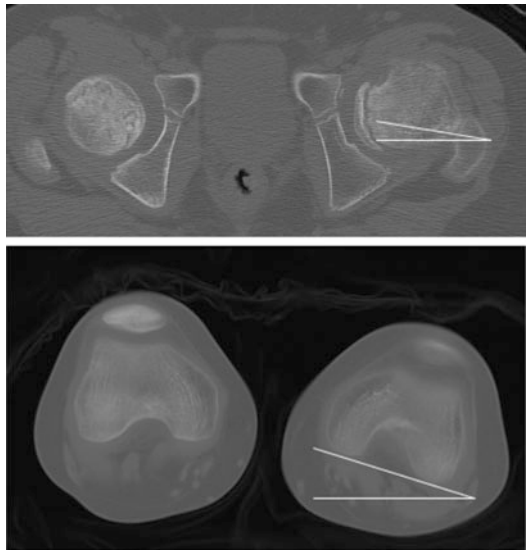

Fig. 8.14 Example of functional femoral retroversion in LCPD. The anteriorly extruded femoral head is not functional. If the femoral version is calculated using the functional femoral head in the acetabulum, the effective femoral version is retroverted

with the presence of a crossover sign. Central acetabular retroversion is uncommon in LCP. Larson et al. demonstrated a 90 % rate of a prominent ischial spine sign (generally indicating acetabular retroversion) in the early stages of LCP, prior to ossification of the anterior and posterior acetabular walls on radiographs. This suggests the acetabular retroversion present in hips with residual deformity may be present at onset of disease, rather than being the result of remodeling. However, Sankar et al. reported rates of central acetabular retroversion of 2 % prior to triradiate cartilage fusion, compared to 31 % after fusion. When present, acetabular retroversion can worsen the underlying impingement (pincer type) in hips with residual Perthes-like deformities.

Natural History

The natural history of LCP disease is significantly affected by several factors. The age at onset is strongly associated with outcome. Onset before the age of 5 is associated with a generally favorable outcome. Similarly, young age at reossification offers a favorable prognosis as the potential for remodeling is greater. The extent of epiphyseal involvement is also predictive of outcome, with involvement of the entire head having the most unfavorable prognosis. Sparing of the lateral column of the epiphysis implies a good prognosis, as it may prevent additional collapse of the epiphysis and subsequent deformity. Additional, radiographic features that are associated with poor outcome include the Gage sign, calcification lateral to the epiphysis, metaphyseal radiolucencies, lateral subluxation, and a horizontal growth plate orientation [48].

At 20- to 40-year follow-up, most patients are pain-free despite radiographic evidence of deformity. Development of hip pain has been associated with irregularity and flattening of the femoral head, as well as deformities secondary to physeal closure (coxa breva, trochanteric overgrowth) that contribute to biomechanical overload. At longer term follow-up, the long-term outcomes of LCP appear to deteriorate. Mcandrew et al. [49] reported on the 48-year follow-up of a cohort and found that 50 % had disabling pain and 40 % had already undergone arthroplasty. Mose et al. [50] reported follow-up of a cohort of LCP greater than 60 years old and found that all hips with irregular femoral heads developed osteoarthritis, and nearly two-thirds of those with spherical femoral heads also had evidence of osteoarthritis. Lecuire [51] reported long-term follow-up of 51 hips at a mean follow-up of 50.2 years. Twenty-four percent had undergone total hip arthroplasty, with an additional 33 % reporting mild to severe pain. Three degree of deformity correlated with long-term outcome. Irregular and very irregular hips generally had significant pain and frequently required arthroplasty. Significant deterioration was noted between the 34- and 50-year outcomes of this cohort.

Stulberg et al. [44] reported long-term outcomes of cohorts of LCP patients from three centers. They found that the degree of femoral head deformity and the presence of acetabular incongruity strongly correlated with the risk and timing of development of osteoarthritis. Hips with "aspherical incongruency" (Class V) develop osteoarthritis at an early age. These

hips are generally thought to be the result of LCP in older patients where compensatory acetabular remodeling fails to occur. Hips with "aspherical congruency" (Class III–IV) also generally develop osteoarthritis at a later age. Secondary acetabular remodeling occurs in these hips to allow congruency.

Ross et al. [52] demonstrated high rates of chondral and labral pathology in a cohort of patients with hip pain and residual Perthes deformities. Labral pathology was present in 76 %, acetabular chondral pathology in 59 %, and femoral head chondral pathology in 81 %. The presence of acetabular dysplasia correlated with less severe chondral changes, while trochanteric overgrowth was associated with more severe chondral changes.

Conclusion

Hip pain in adults is commonly the result of residual deformity from pediatric hip disease, including developmental hip dysplasia, slipped capital femoral epiphysis (SCFE), and Legg–Calve–Perthes (LCP) disease. Each of these disorders has unique epidemiology, proximal femoral and acetabular deformity, and the natural history that are important to recognize.

References

1. Wiberg G. Studies on dysplastic acetabula and congenital subluxation of the hip joint. With special reference to the complication of osteoarthritis. Acta Chir Scand Suppl. 1939;58:7–38.
2. Harris WH. Etiology of osteoarthritis of the hip. Clin Orthop Relat Res. 1986;213:20–33.
3. Clohisy JC. Radiographic structural abnormalities associated with premature, natural hip-joint failure. J Bone Joint Surg Am. 2011;93 Suppl 2:3. doi:10.2106/JBJS.J.01734.
4. Jacobsen S, Sonne-Holm S. Hip dysplasia: a significant risk factor for the development of hip osteoarthritis. A cross-sectional survey. Rheumatology. 2005;44(2):211–8. doi:10.1093/rheumtology/keh436.
5. Engesæter IØ, Laborie LB, Lehmann TG, et al. Prevalence of radiographic findings associated with hip dysplasia in a population-based cohort of 2081 19-year-old Norwegians. Bone Joint J. 2013;95-B(2):279–85. doi:10.1302/0301-620X.95B2.30744.
6. Nunley RM. Clinical presentation of symptomatic acetabular dysplasia in skeletally mature patients. J Bone Joint Surg Am. 2011;93 Suppl 2:17. doi:10.2106/JBJS.J.01735.
7. Fujii M. Acetabular retroversion in developmental dysplasia of the hip. J Bone Joint Surg Am. 2010;92(4):895. doi:10.2106/JBJS.I.00046.
8. Kiyama T, Naito M, Shiramizu K, Shinoda T. Postoperative acetabular retroversion causes posterior osteoarthritis of the hip. Int Orthop. 2007;33(3):625–31. doi:10.1007/s00264-007-0507-6.
9. Clohisy JC, Nunley RM, Carlisle JC, Schoenecker PL. Incidence and characteristics of femoral deformities in the dysplastic hip. Clin Orthop Relat Res. 2008;467(1):128–34. doi:10.1007/s11999-008-0481-3.
10. Noble PC, Kamaric E, Sugano N, et al. Three-dimensional shape of the dysplastic femur: implications for THR. Clin Orthop Relat Res. 2003;417:27–40.
11. Cooperman DR, Wallensten R, Stulberg SD. Acetabular dysplasia in the adult. Clin Orthop Relat Res. 1983;175:79–85.
12. Kim Y-J, Jaramillo D, Millis MB, Gray ML, Burstein D. Assessment of early osteoarthritis in hip dysplasia with delayed gadolinium-enhanced magnetic resonance imaging of cartilage. J Bone Joint Surg Am. 2003;85-A(10):1987–92.
13. Jessel RH, Zurakowski D, Zilkens C, Burstein D, Gray ML, Kim YJ. Radiographic and patient factors associated with pre-radiographic osteoarthritis in hip dysplasia. J Bone Joint Surg Am. 2009;91(5):1120–9. doi:10.2106/JBJS.G.00144.
14. Klaue K, Durnin CW, Ganz R. The acetabular rim syndrome. A clinical presentation of dysplasia of the hip. J Bone Joint Surg Br. 1991;73(3):423–9.
15. Ross JR, Zaltz I, Nepple JJ, Schoenecker PL, Clohisy JC. Arthroscopic disease classification and interventions as an adjunct in the treatment of acetabular dysplasia. Am J Sports Med. 2011;39 Suppl 1:72S–8. doi:10.1177/0363546511412320.
16. Loder RT, Richards BS, Shapiro PS, Reznick LR, Aronson DD. Acute slipped capital femoral epiphysis: the importance of physeal stability. J Bone Joint Surg Am. 1993;75(8):1134–40.
17. Ziebarth K, Leunig M, Slongo T, Kim Y-J, Ganz R. Slipped capital femoral epiphysis: relevant pathophysiological findings with open surgery. Clin Orthop Relat Res. 2013;471:2156–62. doi:10.1007/s11999-013-2818-9.
18. Slongo T. Treatment of slipped capital femoral epiphysis with a modified Dunn procedure. J Bone Joint Surg Am. 2010;92(18):2898. doi:10.2106/JBJS.I.01385.
19. Ganz R, Huff TW, Leunig M. Extended retinacular soft-tissue flap for intra-articular hip surgery: surgical technique, indications, and results of application. Instr Course Lect. 2009;58:241–55.
20. Lehmann CL, Arons RR, Loder RT, Vitale MG. The epidemiology of slipped capital femoral epiphysis: an update. J Pediatr Orthop. 2006;26(3):286–90. doi:10.1097/01.bpo.0000217718.10728.70.

21. Loder RT, Farley FA, Herzenberg JE, Hensinger RN, Kuhn JL. Narrow window of bone age in children with slipped capital femoral epiphyses. J Pediatr Orthop. 1993;13(3):290–3.
22. Pritchett JW, Perdue KD. Mechanical factors in slipped capital femoral epiphysis. J Pediatr Orthop. 1988;8(4):385–8.
23. Gelberman RH, Cohen MS, Shaw BA, Kasser JR, Griffin PP, Wilkinson RH. The association of femoral retroversion with slipped capital femoral epiphysis. J Bone Joint Surg Am. 1986;68(7):1000–7.
24. Rab GT. The geometry of slipped capital femoral epiphysis: implications for movement, impingement, and corrective osteotomy. J Pediatr Orthop. 1999;19(4):419–24.
25. Mamisch TC, Kim Y-J, Richolt JA, Millis MB, Kordelle J. Femoral morphology due to impingement influences the range of motion in slipped capital femoral epiphysis. Clin Orthop Relat Res. 2008;467(3):692–8. doi:10.1007/s11999-008-0477-z.
26. Key JA. Epiphyseal coxa vara or displacement of the capital epiphysis of the femur in adolescence. J Bone Joint Surg Am. 2013;8:53–117. doi:10.1007/s11999-013-2907-9.
27. O'Brien ET, Fahey JJ. Remodeling of the femoral neck after in situ pinning for slipped capital femoral epiphysis. J Bone Joint Surg Am. 1977;59(1):62–8.
28. Jones JR, Paterson DC, Hillier TM, Foster BK. Remodelling after pinning for slipped capital femoral epiphysis. J Bone Joint Surg Br. 1990;72(4):568–73.
29. Siegel DB, Kasser JR, Sponseller P, Gelberman RH. Slipped capital femoral epiphysis. A quantitative analysis of motion, gait, and femoral remodeling after in situ fixation. J Bone Joint Surg Am. 1991;73(5):659–66.
30. DeLullo JA, Thomas E, Cooney TE, McConnell SJ, Sanders JO. Femoral remodeling may influence patient outcomes in slipped capital femoral epiphysis. Clin Orthop Relat Res. 2007;457:163–70. doi:10.1097/BLO.0b013e31802d8aaa.
31. Goodman DA, Feighan JE, Smith AD, Latimer B, Buly RL, Cooperman DR. Subclinical slipped capital femoral epiphysis. Relationship to osteoarthrosis of the hip. J Bone Joint Surg Am. 1997;79(10):1489–1497.
32. Siebenrock KA, Wahab KHA, Werlen S, Kalhor M, Leunig M, Ganz R. Abnormal extension of the femoral head epiphysis as a cause of cam impingement. Clin Orthop Relat Res. 2004;418:54–60.
33. Monazzam S, Krishnamoorthy V, Bittersohl B, Bomar JD, Hosalkar HS. Is the acetabulum retroverted in slipped capital femoral epiphysis? Clin Orthop Relat Res. 2013;471:2145–50. doi:10.1007/s11999-012-2697-5.
34. Sankar WN, Brighton BK, Kim Y-J, Millis MB. Acetabular morphology in slipped capital femoral epiphysis. J Pediatr Orthop. 2011;31(3):254–8. doi:10.1097/BPO.0b013e31820fcc81.
35. Carney BT, Weinstein SL, Noble J. Long-term follow-up of slipped capital femoral epiphysis. J Bone Joint Surg Am. 1991;73(5):667–74.
36. Fraitzl CR, Käfer W, Nelitz M, Reichel H. Radiological evidence of femoroacetabular impingement in mild slipped capital femoral epiphysis: a mean follow-up of 14.4 years after pinning in situ. J Bone Joint Surg Br. 2007;89(12):1592–6.
37. Wensaas A, Gunderson RB, Svenningsen S, Terjesen T. Femoroacetabular impingement after slipped upper femoral epiphysis: the radiological diagnosis and clinical outcome at long-term follow-up. J Bone Joint Surg Br. 2012;94(11):1487–93. doi:10.1302/0301-620X.94B11.29569.
38. Leunig M, Horowitz K, Ganz R. Femoroacetabular impingement after slipped capital femoral epiphysis: does slip severity predict clinical symptoms? Dodds et Al. J Pediatr Orthop. 2009 September; 29(6). J Pediatr Orthop. 2011;31(1):6.
39. Sink EL, Zaltz I, Heare T, Dayton M. Acetabular cartilage and labral damage observed during surgical hip dislocation for stable slipped capital femoral epiphysis. J Pediatr Orthop. 2010;30(1):26–30. doi:10.1097/BPO.0b013e3181c6b37a.
40. Leunig M, Horowitz K, Manner H, Ganz R. In situ pinning with arthroscopic osteoplasty for mild SCFE: a preliminary technical report. Clin Orthop Relat Res. 2010;468(12):3160–7. doi:10.1007/s11999-010-1408-3.
41. Lee CB, Matheney T, Yen Y-M. Case reports: acetabular damage after mild slipped capital femoral epiphysis. Clin Orthop Relat Res. 2013;471:2163–72. doi:10.1007/s11999-012-2715-7.
42. Ippolito E, Tudisco C, Farsetti P. The long-term prognosis of unilateral Perthes' disease. J Bone Joint Surg Br. 1987;69(2):243–50.
43. Mose K. Methods of measuring in Legg-Calvé-Perthes disease with special regard to the prognosis. Clin Orthop Relat Res. 1980;150:103–9.
44. Stulberg SD, Cooperman DR, Wallensten R. The natural history of Legg-Calvé-Perthes disease. J Bone Joint Surg Am. 1981;63(7):1095–108.
45. Tannast M, Hanke M, Ecker TM, Murphy SB, Albers CE, Puls M. LCPD: reduced range of motion resulting from extra- and intraarticular impingement. Clin Orthop Relat Res. 2012;470(9):2431–40. doi:10.1007/s11999-012-2344-1.
46. Joseph B. Morphological changes in the acetabulum in Perthes' disease. J Bone Joint Surg Br. 1989;71(5):756–63.
47. Clohisy JC, Ross JR, North JD, Nepple JJ, Schoenecker PL. What are the factors associated with acetabular correction in Perthes-like hip deformities? Clin Orthop Relat Res. 2012;470(12):3439–45. doi:10.1007/s11999-012-2507-0.
48. Kim HK, Herring JA. Prognostic factors and outcome measures in Perthes disease. Orthop Clin North Am. 2011;42(3):303–15. doi:10.1016/j.ocl.2011.03.004.
49. McAndrew MP, Weinstein SL. A long-term follow-up of Legg-Calvé-Perthes disease. J Bone Joint Surg Am. 1984;66(6):860–9.

50. Mose K, Hjorth L, Ulfeldt M, Christensen ER, Jensen A. Legg Calvé Perthes disease. The late occurrence of coxarthrosis. Acta Orthop Scand Suppl. 1977;169:1–39.
51. Lecuire F. The long-term outcome of primary osteochondritis of the hip (Legg-Calvé-Perthes' disease). J Bone Joint Surg Br. 2002;84(5):636–40.
52. Ross JR, Nepple JJ, Baca G, Schoenecker PL, Clohisy JC. Intraarticular abnormalities in residual Perthes and Perthes-like hip deformities. Clin Orthop Relat Res. 2012;470(11):2968–77. doi:10.1007/s11999-012-2375-7.

Extra-articular Hip Conditions and Sports Injuries

9

Kathleen L. Davenport, Peter J. Moley, and Bryan T. Kelly

Introduction

The hip is a dynamic joint that has been implicated in sports injury. While the hip joint, and more specifically the interplay between the acetabulum and the femoral head/neck junction, has been implicated in the injury of the joint, there are also significant injuries that occur outside of the joint. In this chapter, we review some of the more common extra-articular injuries of the hip in the athlete. Hip pathology can be viewed in a layered approach, with the layers involving osteochondral, inert, dynamic (muscular), and neural pathology. We subdivide the muscular pathology into anterior, lateral, posterior, and medial regions.

Osteochondral Pathology

Stress Fractures

Stress fractures of the femoral neck are an important consideration for hip pain in the athlete. In this population, fractures are considered to be due to repetitive stress causing fatigue of normal bone [1, 2]. Essentially, new bone formation is unable to adequately respond to increased demands required by new or increased activity [3]. Female athletes, particularly those with negative energy balance, low bone density, and dysmenorrhea (female athlete triad), are at increased risk of developing stress fractures [4]. Runners are also at increased risk, primarily due to training errors and excessive mileage [4, 5] (Fig. 9.1).

Athletes frequently complain of anterior groin pain that worsens with activity and weight bearing and improves with rest. A stress fracture can be difficult to diagnose since symptoms are often vague [5]. Physical exam may demonstrate antalgic gait or even inability to bear weight on the affected limb [6]. Hip range of motion can be decreased [3]. A hop test, where pain is reproduced with single leg hop, has shown to have increased sensitivity compared to other physical exam findings [5]. However, a hop test should be used cautiously to prevent progression of a stress reaction or cause outright fracture.

Treatment is dependent on the type of fracture. Femoral neck fractures are subdivided into compression (inferior surface, less than 50 % of the femoral neck) and tension (superior surface) types [1, 2, 6, 7]. Compression type stress fractures generally respond to conservative care, with placing the athlete non-weight bearing until asymptomatic and then gradually returning to activity [3, 4, 6]. Conversely, tension-sided stress fractures require surgical fixation due to risk of fracture resulting in malunion, avascular necrosis, and deformity [4, 6]. Any displaced fracture

K.L. Davenport (✉)
Spine and Sports Medicine, Hospital for Special Surgery, East 75th Street, New York, NY, USA
e-mail: davenportk@hss.edu

Y.-J. Kim (eds.), *Hip Magnetic Resonance Imaging*,
DOI 10.1007/978-1-4614-1668-5_9,

Fig. 9.1 Compression side stress fracture of the left femoral neck

should be considered for urgent surgical fixation [3]. In either type, addressing training factors, biomechanics, and nutritional balance is essential [4]. Return to play may be allowed when an athlete has achieved pain-free range of motion, asymptomatic full weight bearing, and often healing on repeat MRI [7].

Stress fractures in the pelvis, particularly the ischiopubic ramus, can also occur and can present similarly to adductor tendinopathy, osteitis pubis, and athletic pubalgia. Similar to femoral stress fractures, runners have an increased incidence as well as women with the female athlete triad [7]. Recovery and return to sport is often successfully achieved with decreased weight bearing, possibly requiring crutches, and gradual activity progression [7].

True fractures and fracture dislocations of the hip and pelvis, although uncommon in sports, can occur, particularly in contact sports such as football, rugby, and wrestling. Diagnosis is typically not difficult due to the limb deformity and immobility. Appropriate imaging is critical for complete analysis of the injury pattern, and should include AP Pelvis, Judet views, Inlet/Outlet views, and AP and lateral views of the femur. Fractures of the femoral neck, intertrochanteric or subtrochanteric regions, and displaced pelvic or acetabular fractures require urgent surgical management.

Inert Layer

Capsular Injury

The capsule encompasses most of the femoral neck and extends from the intertrochanteric ridge to the acetabular rim. The capsule is then reinforced by surrounding ligamentous and muscular structures. Injury to the capsule can occur in athletic participation or in traumatic hip dislocation [1]. Sports involving axial loading with hip rotation, such as golf, football, and gymnastics, place the capsule at increased risk for capsule stretch or rupture injury [6, 8]. If there is laxity in the hip capsule from previous injury or innate factors, the surrounding soft tissues, such as the iliopsoas muscle, may compensate and become an additional source of anterior groin pain (see iliopsoas tendinopathy below) [6, 9]. Secondary injuries, such as labral pathology, can arise from chronic capsular laxity with resultant suboptimal joint mechanics [9].

Patients generally report anterior groin pain, which worsens with passive external rotation and extension [6]. Treatment is initially conservative with anti-inflammatory medications and physical therapy [6]. If conservative measures are unsuccessful, arthroscopy may be considered for capsular plication [10].

Adhesive capsulitis, while more common in the shoulder, can also be a source of hip pain and decreased range of motion. It may be seen idiopathically, in association with diabetes, or secondary to intra-articular lesions [11]. Similar to shoulder adhesive capsulitis, pathology in the hip is most commonly seen in middle-aged women [12]. Patients often have decreased, painful range of motion, similar to findings in the shoulder [11, 12]. Our experience has been that loss of external rotation is the most pathognomonic feature. However, painful restriction in hip joint motion is a nonspecific clinical finding, and diagnosis can be challenging. Treatment is conservative with range of motion and intra-articular steroid injection, but arthroscopy with manipulation can be considered [11, 12].

Labrum and Femoroacetabular Impingement

Femoroacetabular impingement (FAI) occurs when there is increased contact between the proximal femur and acetabulum, most evident during flexion and adduction of the hip [13]. FAI is the result of anatomical variants of the femoral head–neck junction (CAM), acetabular rim (pincer), or both [14–18]. CAM lesions present as an inclusion injury with increased radius of the femoral head with loss of sphericity, causing shearing over the anteriosuperior acetabular rim and resultant chondral destruction [14, 15, 17, 19]. Pincer impingement is considered an impaction injury and occurs when there is acetabular overcoverage or focal anterior retroversion, which results in labral injury and bone apposition at the acetabular rim [14, 15, 17, 20]. Most commonly, there is a combination of CAM and pincer type impingement [18, 19].

Athletes with FAI often present with gradual onset of decreased range of motion and anterior groin pain, which is worse with prolonged sitting [13, 17, 18, 21, 22]. It is more common in young, active athletes who participate in sports requiring repetitive hip flexion and rotation, such as hockey, golf, martial arts, and dance [15, 21, 23–25]. These movements place the athlete at risk due to the increased stress placed on the labrum during extreme positions. The chondrolabral junction is a vulnerable location for trauma and damage during end range hip movements. When these positions are repeated frequently, the athlete may be at increased risk for early hip osteoarthritis or bone apposition at the acetabular rim, increasing the amount of impingement [20, 26]. Therefore, a careful history regarding training techniques, cross-training activities, hours of training, and sports positions is essential. Pain is reproduced on physical exam with flexion–adduction–internal rotation (FADIR) maneuver [15, 17, 18, 25]. Additional physical exam findings include decreased hip range of motion, particularly to flexion and internal rotation [18, 25].

Initial treatment of FAI involves activity modification with attempt to avoid exacerbated movements and with optimizing the stabilizing hip and core musculature [15, 17, 25, 27]. Anti-inflammatory medications and intra-articular steroid injections may also be considered for diagnostic and therapeutic pain relief [15]. Surgical correction of FAI is often required in high level athletes with the goal to provide increased clearance between the femoral head and the acetabulum [17]. With appropriate postoperative rehabilitation, there have been high rates of successful outcomes in athletes after FAI surgical correction [6]. Importantly, if surgery is considered for other concurrent soft tissue injuries, such as labral tears, it is essential that FAI correction is considered in order to correct the possible underlying etiology [16, 19]. It is important to recognize and treat FAI in athletes as there is often a delay in diagnosis [18] and FAI can be a risk factor for early osteoarthritis of the hip [14, 21, 22, 24, 27].

Some athletes with underlying FAI may be at risk for FAI-induced posterior hip instability [28]. The mechanism of this injury can be non-contact as well as contact and is related to premature anterior contact of the femoral head against the acetabulum with posterior levering of the head out of the socket. This can be associated with a posterior lip fracture, analogous to a bony bankart of the posterior acetabulum, or with posterior capsular stripping off of the acetabulum [28]. A high index of suspicion should be maintained for athletes with continued pain with passive motion after hip injury, as frequently these injuries are mis-diagnosed as simple muscle strains. Loose bodies from cartilaginous or bony fragmentation may be present [28].

FAI is directly related to injuries involving the surrounding hip soft tissue structures, which may become pathological either from underlying abnormalities or from direct mechanical stress [13, 14, 18, 29]. These soft tissue injuries will be dependent on the specific repetitive activity an athlete utilizes for his or her sport. FAI can result in cartilage destruction, labral injury, and compensatory tendinopathies, which will be reviewed in this chapter.

Ischiofemoral Impingement

Ischiofemoral impingement occurs when the quadratus femoris muscle is compressed between the ischium and the lesser trochanter [30, 31]. The psoas insertion and hamstring origin may also be affected. The reduced space can be congenital or acquired, such as after fractures, degenerative arthritis, proximal femoral osteotomy, or total-hip arthroplasty [30, 32]. Ischiofemoral impingement has also been described in conjunction with snapping hip syndrome and has been associated with hamstring and gluteal injuries [33].

Athletes often report buttock pain and medial thigh pain. In some cases, it has been reported to closely mimic hamstring origin pain [33]. Pain can be reproduced on physical exam by placing the hip in extension, adduction, and external rotation [30, 31]. Treatment focuses on optimizing biomechanical forces, and appropriate stretching and strengthening of the quadratus femoris muscle [33]. Guided injection may be beneficial for both diagnostic and therapeutic pain relief. As partial tears have been demonstrated in the quadratus femorus muscle, autologous blood products may be a theoretical consideration for future treatment options [30, 32, 33]. Surgical resection of the lesser trochanter has been described to provide pain relief, but this population was less active, postsurgical, and older [34], and therefore this larger surgery should be used with caution in younger, active athletes [31, 33].

Subspine Impingement

Subspine impingement occurs when the anterior inferior iliac spine (AIIS) impinges inferiorly on the femoral neck [35–37]. The impingement occurs during hip flexion and results in compression of the AIIS against the anterior femoral neck. It has been associated with avulsion fractures of the AIIS, the origin of the rectus femoris muscle [38], but it has also been described without prior AIIS injury [35–37].

Patients typically report pain with activities requiring repetitive or prolonged hip flexion. Physical examination reveals pain with straight hip flexion and with palpation over the AIIS. Diagnosis can be assisted with intra-articular hip injection resulting in 50 % or greater pain relief to provocative maneuvers [35–37]. Conservative treatment with activity modification, intra-articular injections, and rehabilitation may be sufficient and should be trialed prior to surgical consideration. However, arthroscopic decompression of the AIIS may be necessary and has shown good results in improving function and decreasing pain scores [35–37].

Anterior Muscular Pathology

Rectus Femoris

The hip flexors include the rectus femoris (straight and reflected head) and the sartorius generally occurs at the myotendinous junction.

In addition, muscles that cross two joints are at higher risk for strains [39]. Both have also been implicated in apophyseal avulsion injuries in skeletally immature patients [39, 40]. Although relatively rare in the adult population, avulsions of the rectus femoris can occur in the setting of strong eccentric contraction of the direct head. A case report demonstrated a proximal avulsion in two NFL kickers [41] soon followed by a larger NFL survey [42]. Investigators surmise that these injuries occur in kickers going from a hip-extended/knee-flexed starting point to a hip-flexed/knee-extended position. These injuries can be managed conservatively most of the time; however, some studies suggest that operative treatment should be considered in kickers and soccer players. One complication of non-operative treatment is the development of extra-articular impingement due to heterotopic bone formation along the tract of injury, resulting in prominent subspine impingement [36].

Iliopsoas Tendinopathy

The psoas and iliacus muscles originate from the lumbar spine and pelvis, respectively, and combine to insert onto the lesser trochanter where it acts as one of the primary hip flexors [43]. Iliopsoas tendinopathy occurs with repetitive hip flexion movements or hip hyperextension moments [44, 45]. Iliopsoas tendinopathy may occur with iliopsoas bursitis or internal snapping hip (internal coxa saltans).

The iliopsoas bursa, the largest bursa in the body, may become inflamed from internal coxa saltans [2, 43]. This occurs when the iliopsoas tendon rubs over the iliopectineal eminence, anterior femoral head, or anterior hip capsuloligamentous structures [43, 44]. Often there is audible or palpable snapping [2, 43]. Snapping can occur from several mechanisms, but often results from the femur moving from flexion/external rotation into extension/internal rotation and causes the iliopsoas tendon to snap over the iliacus muscle [45, 46].

Patients often present with anterior hip pain or inguinal pain which is worse with activity [43, 44]. They may describe an audible or palpable snap if internal coax saltans is present. On physical exam, there may be tenderness to palpation over the iliopsoas myotendinous junction, pain with resisted hip flexion, positive Thomas test, and pain with FADIR test [43, 44, 47]. Additionally, if internal coxa saltans is present, the patient may have a positive fan test where snapping and pain is reproduced when the limb is moved from flexion/external rotation into extension/internal rotation.

The majority of treatment is conservative and includes correcting muscle imbalances with a targeted strengthening and stretching rehabilitation regime [43–45]. If this alone is ineffective, ultrasound-guided injections into the iliopsoas tendon bursa may be effective [43, 44]. Surgery is rarely indicated, but hip arthroscopy can be considered when all conservative measures have failed [43, 44, 47].

Lateral Muscular Pathology

Abductor Dysfunction

The greater trochanter is the attachment site for five muscles: the gluteus medius, gluteus minimus, piriformis, obturator externus, and obturator internus [48]. Hip abductor dysfunction from chronic overload can result in trochanteric bursitis, gluteus medius/minimus tendinopathy, and snapping iliotibial band (ITB) syndrome [49]. This combination of factors has been grouped into the "greater trochanteric pain syndrome" [49, 50]. Hip abductor dysfunction is more common in women than men, possibly due to the wider female pelvis [48–51] (Fig. 9.2).

Patients typically report lateral hip pain, which is worse with direct pressure, walking, and stair climbing [51, 52]. Back pain is often associated with hip abductor dysfunction, and patients may be treated for lumbar spine pain generators prior to correct diagnosis [50, 51]. Physical exam often reveals tenderness to palpation over the greater trochanter, posterior pain

Fig. 9.2 Gluteus medius and minimus tendonosis

with the flexion–abduction–external rotation (FABER) test, positive Ober test, and weakness with reproduction of pain with resisted hip abduction [48, 51, 52]. A Trendelenburg sign or gait pattern may be present [52].

Most patients respond to conservative treatment and muscle imbalances, particularly including gluteus medius weakness, and should be addressed in any treatment protocol [48, 51, 52]. To facilitate physical therapy participation, decreasing inflammation can be achieved with ice, oral or topical anti-inflammatory medications, or steroid injection [48, 51, 52]. Recalcitrant cases may be addressed with trochanteric bursectomy, with or without ITB release [48, 51]. More recently, platelet-rich plasma (PRP) has been used for the treatment of gluteus minimus and medius tendinopathy and has shown some successes [53] but larger studies are needed. In patients with complete rupture of the tendon insertion or chronic high grade partial tendinopathy that has failed to respond to non-operative measures, surgical repair of the injured tendon can be performed with good and excellent outcomes [54].

Iliotibial Band Dysfunction

ITB syndrome is a cause of lateral hip pain and lateral knee pain in athletes, particularly runners and cyclists [55–57]. The ITB originates from the iliac crest and attaches to Gerdy's tubercle at the fibular head [57, 58]. Anatomically, it is connective tissue sheath comprising the tensor fascia lata (TFL) and gluteus maximus fascia. ITB pain results from the friction of the ITB over the lateral femoral condyle as the knee moves from flexion into extension [7, 56, 57]. Strength deficits, particularly involving the hip abductors, and increased strain of the ITB are believed to contribute to ITB pain [7, 58, 59]. Additionally, running downhill and running at slower speeds are felt to increase the risk of developing ITB syndrome due to increased friction of the ITB over the lateral femoral condyle [57].

External snapping hip, or external coxa saltans, can be associated with ITB dysfunction [60, 61]. External coxa saltans is most often attributed to the ITB snapping over the greater trochanter [60, 61]. Snapping of the gluteus maximus muscle has also been described [61]. A snap is felt or

heard in the lateral thigh and can be accentuated if thickening of the posterior aspect of the ITB or anterior aspect of the gluteus maximus has occurred [61]. The band snaps anteriorly over the grater trochanter from its posterior position as the hip is moved from extension into flexion [60]. External coxa saltans may be one etiology of ITB dysfunction and should be considered during an evaluation for lateral hip pain.

Athletes generally report pain along the lateral hip and thigh, but particularly at the lateral knee [7, 58]. Often, patients report an increase in training regimen, a change in hill running, or a change in footwear prior to development of ITB symptoms. Pain is often worse with activity, particularly running, or shortly after exercise. On physical examination, there is often pain over the ITB to palpation [55]. Ober's test is often positive and weakness in hip abduction is common [55].

Treatment should be conservative and focus on restoring gluteus medius strength and flexibility imbalances [55]. Decreasing inflammation with ice, anti-inflammatory medications, or steroid injection may also facilitate participation with physical therapy. In some recalcitrant cases that have failed conservative treatments, surgical release may be warranted [56]. Return to running should be accomplished in a gradual, stepwise manner with continued exercises to minimize recurrence [55]. In addition to correcting biomechanics, training factors, such as hills, stairs, and cadence speed, should also be addressed to return the athlete to running.

Posterior Muscular Pathology

Hamstring Tendinopathy

Acute and chronic hamstring tendon dysfunction can affect both professional and recreational athletes. The hamstring comprises the semimembranosus, semitendinosus, and biceps femoris muscles, all originating from the ischial tuberosity with the exception of the short head of the biceps femoris [62–64]. Acute injury is often the result of a sudden eccentric contraction or extreme hip flexion with knee extension [62, 63, 65–68]. Chronic tendinopathy is thought to be the result of mild, low-grade microtrauma, usually from sports such as long-distance and mid-distance running [64, 68].

Both acute and chronic hamstring tendon dysfunctions are most likely to occur immediately adjacent to the myotendinous junction of the long head of the biceps femoris muscle [2, 63, 64]. Athletes typically present with lower gluteal pain or posterior thigh pain that is exacerbated by activity [62, 66]. On physical exam, pain may be elicited by palpation over the ischial tuberosity and bruising or palpable defect may be present in complete or partial hamstring tendon tears [62, 65, 69]. The hamstring acts primarily as a hip extensor and, to a lesser extent, as a knee flexor [62, 66, 70, 71]. Since strength imbalances and poor flexibility are risk factors for both acute and chronic hamstring tendinopathy, restoration and correction of these factors are essential for recovery [63, 66, 68, 71]. Eccentric hamstring strengthening has been shown to be beneficial in preventing new and recurrent hamstring injuries in male soccer players and should be part of any physical therapy program [70]. There is not sufficient evidence to recommend steroid injections into this area. However, preliminary results from our practice suggest a promising role for injection of autologous blood products combined with an eccentric strengthening physical therapy program.

Complete rupture of the hamstring tendons can lead to significant disability with resultant pain, sciatic nerve irritation, and functional deficit. Complete rupture of two tendons with retraction of more than 2–3 cm, or complete three-tendon tears should be considered for surgical repair [72, 73]. Acute repairs (within 3–4 weeks) are easier to repair due to less scarring and adhesions, although repair of chronic tears with allograft reconstruction has been shown to result in comparable functional outcome in some series [74].

Medial Muscular Pathology and Athletic Pubalgia

Adductor Tendinopathy

The hip adductors comprise six muscles: the adductor longus, adductor brevis, adductor magnus, gracilis, pectineus, and obturator externus [75]. Each muscle originates at the pubis, with the adductor magnus also inserting on the ischium, and inserts along the medial femur. Injuries to these muscles often involve sudden changes in direction or momentum [66, 76]. Risk factors for adductor injury include decreased adductor strength, decreased flexibility, and prior history of adductor strain [75].

Athletes generally present with groin pain, which may be acute or chronic in nature [75, 76]. Athletes may also report feeling weakness in the adductors [76]. Groin pain in the athlete can be a potentially confusing diagnosis and by itself is not specific for adductor tendinopathy. Other potential causes of groin pain in the athlete, such as osteitis pubis and athletic pubalgia, are discussed below. Similarly, tenderness to palpation on the pubic symphysis is not specific for adductor tendinopathy as this can also be seen in other diagnoses. Physical exam may also reveal pain and weakness with resisted adduction.

Treatment emphasizes strengthening of the adductor musculature with gradual return to sport [75]. Recurrent adductor tendinopathy is not uncommon, and therefore careful attention to adequate restoration of functional ability prior to return to play is essential [75]. Adductor tenotomy has been used in rare cases, but only after all other forms of groin pain have been ruled out.

Osteitis Pubis

Osteitis pubis is defined as a chronic overuse pain syndrome of the pubic symphysis [77]. Pain is exacerbated by physical activity and is most commonly seen in sports requiring cutting and twisting movements, such as football, ice hockey, soccer, and rugby [78]. These movements result in strain over the adductor attachment and irritation of the pubic symphysis [2, 79]. Limited hip range of motion and FAI have also been implicated in predisposing the athlete to osteitis pubis [77].

Athletes locate their pain in the anterior and medial groin [77]. There are often concomitant findings of athletic pubalgia, adductor and iliopsoas strain, core musculature weakness, and FAI [78]. Recent studies have shown a correlation between athletic pubalgia and FAI [37]. On physical exam, the pubic symphysis may be tender to palpation and there may also be tenderness to the adductor musculature, pain with resisted hip adduction, pain with utilization of lower abdominal musculature, and pain anteriorly with compression of the pelvis [77, 79]. There may be loss of hip range of motion in internal or external rotation, weakness in hip adductor or abductor strength, and antalgic gait [77].

Treatment initiates with relative rest and decreasing inflammation of the surrounding pubic structures [77, 78]. While many cases of osteitis pubis resolve with relative rest, this may not be an option in the high level athlete. Physical therapy begins with range of motion activities and then progresses to strengthening exercises, which should include core muscle retraining. Corticosteroid injections into the pubic symphysis may be used to decrease pain and inflammation with the goal of allowing increased participation with therapy [77, 78]. Surgery to stabilize the pubic symphysis is rarely considered if pain continues to limit function and only after the athlete has failed all conservative treatment options.

Athletic Pubalgia ("Sports Hernia")

Athletic pubalgia is a challenging diagnosis to make due to the multiple potential combinations of involved core musculature. Meyers et al. describe over 20 different subtypes of athletic pubalgia or "core muscle dysfunction," with varying presentation [80]. These conditions

refer to pathology involving the pubic joint, and do not involve a true inguinal hernia [29, 80]. The pubic joint has been defined as the right and left pubic symphyses with their surrounding musculature [29, 80]. Etiology of athletic pubalgia has also been described as inflammation of the conjoined tendon, rectus abdominis insertional injury, avulsion of the internal oblique musculature, and strain in the external oblique aponeurosis [80–83] and the literature can be confusing regarding this diagnosis [80]. Essentially, athletic pubalgia is an injury to the flexion and adduction mechanism of the hip and lower abdomen which results in lower abdominal and inguinal exertional pain [29, 80]. Similar underlying factors predisposing an athlete to adductor tendinopathy and osteitis pubis can also lead to athletic pubalgia [83, 84]. Specifically, FAI has been shown to be a risk factor for athletic pubalgia and as a cause for suboptimal recovery after treatment for athletic pubalgia [37].

Athletic pubalgia is commonly seen in male athletes participating in sports which require cutting and turning motions at high speeds such as rugby, tennis, ice and field hockey, and soccer [80–84]. Typically, a diagnosis is delayed due to the challenges of making this diagnosis. A patient will report insidious onset of lower abdominal and anterior/medial groin pain that is symptomatic with activity and resolves with rest [29, 81–83]. Aggravating movements often include kicking, sneezing, abdominal core exercises (sit-ups), sprinting, and sudden movement [29, 81, 82]. On physical exam, athletes often have pain to palpation over the pubic tubercle, conjoined tendon, and inguinal area [81]. There is no inguinal hernia palpable on physical exam and therefore the term hernia is misleading [85]. Pain is elicited on sit-up maneuver, resisted hip adduction, and during valsalva maneuver [29, 80, 81].

Similar to adductor strain and osteitis pubis, initial treatment for athletic pubalgia is relative rest followed by strengthening and stretching [81, 84]. However, unlike other causes of medial groin pain, athletic pubalgia often requires surgical correction [29, 80–84]. Intra-articular pathology, such as FAI, should be considered for correction at the time of athletic pubalgia surgery [37]. Surgery should be followed with an adequate stepwise postsurgical rehabilitation regimen to ensure full return to sports and decrease the risk of recurrence [80, 84].

Neural Pathology

Peripheral Nerve Injury

While less common, peripheral nerve injury can be a cause of extra-articular hip pain. Peripheral nerve injuries in athletes are most common in the upper extremity, but can occur in the lower extremity [86–88]. Peripheral nerve injuries are generally thought to be underdiagnosed in the athletic population and, when diagnosis occurs, it is often delayed [87]. Electromyography (EMG) and MRI may be considered for further diagnostic evaluation of a suspected peripheral nerve injury.

Lateral femoral cutaneous neuritis (meralgia paresthetica) has been described in the athletic population, generally associated with compression as the nerve is susceptible to compression throughout its course [88–91]. While athletic meralgia paresthetica is rare, it has been most commonly reported with thigh trauma and hematoma formation [91] and athletes participating in aggressive contact sports, such as American football and rugby, are at increased risk [88]. Athletes complain of numbness and paresthesias in the lateral thigh [89–91]. As the lateral femoral cutaneous nerve is only a sensory nerve, any complaints or exam findings of muscle weakness should prompt investigation of alternative diagnoses. Treatment is generally nonsurgical and often symptoms resolve spontaneously, but surgical treatment with neurolysis can be considered if symptoms become persistent [89, 91, 92].

Ilioinguinal nerve, iliohypogastric nerve, and genitofemoral nerve injury and irritation have presented as groin pain in athletes [93, 94]. Symptoms of neuritis are similar to those of athletic pubalgia and a nerve block can be considered for diagnosis, particularly after an athlete has failed all other conservative treatments for other causes of groin pain. Neuropathic symptoms are thought to be caused by the

neurovascular bundle becoming trapped in a tear of the external oblique muscle [93, 94]. Often, surgical repair of the external oblique defect is required to resolve neurological symptoms, and athletes generally return successfully to sport [94]. Neurolysis has also been shown to be effective in pain reduction after failure of conservative management of groin pain [92]. If athletic pubalgia surgery is required based on other diagnostic factors, ilioinguinal nerve ablation should be considered to be performed concomitantly [93].

Pudendal nerve injury has been described primarily in athletes participating in sports requiring prolonged sitting, particularly cyclists [95]. In the biking patient, the pudendal nerve is at risk of stretch injury from repeated pedaling as well as from compression injury after prolonged sitting [96]. The athlete most commonly reports perineal numbness and, in men, erectile dysfunction [96–98]. Treatment is generally conservative with focus on optimal seat fit and angle as well as optimizing the training regimen to include increased rest breaks from the seated position [95].

Conclusion

Extra-articular hip injury and sports injuries around the hip comprise a large range of injuries varying in severity to mild muscle strain to fracture and fracture dislocations. Oftentimes, due to the overlapping pathology, accurate diagnosis and treatment can be challenging. Systematic evaluation assessing each tissue layer, including the osseous layer, intra-articular layer (capsule, labrum, cartilage complex), muscular layer (core muscle dysfunction), and neural layer, allows for a more accurate clinical diagnosis and subsequent treatment plan.

References

1. Blankenbaker DG, De Smet AA. Hip injuries in athletes. Radiol Clin North Am. 2010;48(6):1155–78.
2. Overdeck KH, Palmer WE. Imaging of hip and groin injuries in athletes. Semin Musculoskelet Radiol. 2004;8(1):41–55.
3. Shin AY, Gillingham BL. Fatigue fractures of the femoral neck in athletes. J Am Acad Orthop Surg. 1997;5(6):293–302.
4. Paluska SA. An overview of hip injuries in running. Sports Med. 2005;35(11):991–1014.
5. Clement DB, Ammann W, Taunton JE, et al. Exercise-induced stress injuries to the femur. Int J Sports Med. 1993;14(6):347–52.
6. Tibor LM, Sekiya JK. Differential diagnosis of pain around the hip joint. Arthroscopy. 2008;24(12):1407–21.
7. Fredericson M, Jennings F, Beaulieu C, Matheson GO. Stress fractures in athletes. Top Magn Reson Imaging. 2006;17(5):309–25.
8. Greenberg E, Wells L. Hip joint capsule disruption in a young female gymnast. J Orthop Sports Phys Ther. 2010;40(11):761.
9. Kelly BT, Williams 3rd RJ, Philippon MJ. Hip arthroscopy: current indications, treatment options, and management issues. Am J Sports Med. 2003;31(6):1020–37.
10. Philippon MJ. The role of arthroscopic thermal capsulorrhaphy in the hip. Clin Sports Med. 2001;20(4):817–29.
11. Joassin R, Vandemeulebroucke M, Nisolle JF, Hanson P, Deltombe T. Adhesive capsulitis of the hip: three case reports. Ann Readapt Med Phys. 2008;51(4):301–14.
12. Byrd JW, Jones KS. Adhesive capsulitis of the hip. Arthroscopy. 2006;22(1):89–94.
13. Kuhlman GS, Domb BG. Hip impingement: identifying and treating a common cause of hip pain. Am Fam Physician. 2009;80(12):1429–34.
14. Ganz R, Leunig M, Leunig-Ganz K, Harris WH. The etiology of osteoarthritis of the hip: an integrated mechanical concept. Clin Orthop Relat Res. 2008;466(2):264–72.
15. Lequesne M, Bellaiche L. Anterior femoroacetabular impingement: an update. Joint Bone Spine. 2012;79(3):249–55.
16. Leunig M, Beaule PE, Ganz R. The concept of femoroacetabular impingement: current status and future perspectives. Clin Orthop Relat Res. 2009;467(3):616–22.
17. Keogh MJ, Batt ME. A review of femoroacetabular impingement in athletes. Sports Med. 2008;38(10):863–78.
18. Philippon MJ, Maxwell RB, Johnston TL, Schenker M, Briggs KK. Clinical presentation of femoroacetabular impingement. Knee Surg Sports Traumatol Arthrosc. 2007;15(8):1041–7.
19. Beck M, Kalhor M, Leunig M, Ganz R. Hip morphology influences the pattern of damage to the acetabular cartilage: femoroacetabular impingement as a cause of early osteoarthritis of the hip. J Bone Joint Surg Br. 2005;87(7):1012–8.
20. Corten K, Ganz R, Chosa E, Leunig M. Bone apposition of the acetabular rim in deep hips: a distinct finding of global pincer impingement. J Bone Joint Surg Am. 2011;93 Suppl 2:10–6.

21. Kassarjian A, Brisson M, Palmer WE. Femoroacetabular impingement. Eur J Radiol. 2007;63(1):29–35.
22. Laude F, Boyer T, Nogier A. Anterior femoroacetabular impingement. Joint Bone Spine. 2007;74(2):127–32.
23. Mason JB. Acetabular labral tears in the athlete. Clin Sports Med. 2001;20(4):779–90.
24. McCarthy JC, Noble PC, Schuck MR, Wright J, Lee J. The Otto E. Aufranc award: the role of labral lesions to development of early degenerative hip disease. Clin Orthop Relat Res. 2001;393:25–37.
25. Sink EL, Gralla J, Ryba A, Dayton M. Clinical presentation of femoroacetabular impingement in adolescents. J Pediatr Orthop. 2008;28(8):806–11.
26. Tannast M, Goricki D, Beck M, Murphy SB, Siebenrock KA. Hip damage occurs at the zone of femoroacetabular impingement. Clin Orthop Relat Res. 2008;466(2):273–80.
27. Jaberi FM, Parvizi J. Hip pain in young adults: femoroacetabular impingement. J Arthroplasty. 2007;22(7 Suppl 3):37–42.
28. Krych AJ, Thompson M, Larson CM, Byrd JW, Kelly BT. Is posterior hip instability associated with cam and pincer deformity? Clin Orthop Relat Res. 2012;470:3390–7.
29. Hammoud S, Bedi A, Magennis E, Meyers WC, Kelly BT. High incidence of athletic pubalgia symptoms in professional athletes with symptomatic femoroacetabular impingement. Arthroscopy. 2012;28:1388–95.
30. Patti JW, Ouellette H, Bredella MA, Torriani M. Impingement of lesser trochanter on ischium as a potential cause for hip pain. Skeletal Radiol. 2008;37(10):939–41.
31. Stafford GH, Villar RN. Ischiofemoral impingement. J Bone Joint Surg Br. 2011;93(10):1300–2.
32. Torriani M, Souto SC, Thomas BJ, Ouellette H, Bredella MA. Ischiofemoral impingement syndrome: an entity with hip pain and abnormalities of the quadratus femoris muscle. AJR Am J Roentgenol. 2009;193(1):186–90.
33. O'Brien SD, Bui-Mansfield LT. MRI of quadratus femoris muscle tear: another cause of hip pain. AJR Am J Roentgenol. 2007;189(5):1185–9.
34. Johnson KA. Impingement of the lesser trochanter on the ischial ramus after total hip arthroplasty. Report of three cases. J Bone Joint Surg Am. 1977;59(2):268–9.
35. Hetsroni I, Larson CM, Dela Torre K, Zbeda RM, Magennis E, Kelly BT. Anterior inferior iliac spine deformity as an extra-articular source for hip impingement: a series of 10 patients treated with arthroscopic decompression. Arthroscopy. 2012;28(11):1644–53.
36. Larson CM, Kelly BT, Stone RM. Making a case for anterior inferior iliac spine/subspine hip impingement: three representative case reports and proposed concept. Arthroscopy. 2011;27(12):1732–7.
37. Larson CM, Pierce BR, Giveans MR. Treatment of athletes with symptomatic intra-articular hip pathology and athletic pubalgia/sports hernia: a case series. Arthroscopy. 2011;27(6):768–75.
38. Pan H, Kawanabe K, Akiyama H, Goto K, Onishi E, Nakamura T. Operative treatment of hip impingement caused by hypertrophy of the anterior inferior iliac spine. J Bone Joint Surg Br. 2008;90(5):677–9.
39. Garrett Jr WE. Muscle strain injuries. Am J Sports Med. 1996;24(6 Suppl):S2–8.
40. Armfield DR, Kim DH, Towers JD, Bradley JP, Robertson DD. Sports-related muscle injury in the lower extremity. Clin Sports Med. 2006;25(4):803–42.
41. Hsu JC, Fischer DA, Wright RW. Proximal rectus femoris avulsions in national football league kickers: a report of 2 cases. Am J Sports Med. 2005;33(7):1085–7.
42. Gamradt SC, Brophy RH, Barnes R, Warren RF, Thomas Byrd JW, Kelly BT. Nonoperative treatment for proximal avulsion of the rectus femoris in professional American football. Am J Sports Med. 2009;37(7):1370–4.
43. Johnston CA, Wiley JP, Lindsay DM, Wiseman DA. Iliopsoas bursitis and tendinitis. A review. Sports Med. 1998;25(4):271–83.
44. Morelli V, Weaver V. Groin injuries and groin pain in athletes: part 1. Prim Care. 2005;32(1):163–83.
45. Wahl CJ, Warren RF, Adler RS, Hannafin JA, Hansen B. Internal coxa saltans (snapping hip) as a result of overtraining: a report of 3 cases in professional athletes with a review of causes and the role of ultrasound in early diagnosis and management. Am J Sports Med. 2004;32(5):1302–9.
46. Deslandes M, Guillin R, Cardinal E, Hobden R, Bureau NJ. The snapping iliopsoas tendon: new mechanisms using dynamic sonography. AJR Am J Roentgenol. 2008;190(3):576–81.
47. Domb BG, Shindle MK, McArthur B, Voos JE, Magennis EM, Kelly BT. Iliopsoas impingement: a newly identified cause of labral pathology in the hip. HSS J. 2011;7(2):145–50.
48. Strauss EJ, Nho SJ, Kelly BT. Greater trochanteric pain syndrome. Sports Med Arthrosc. 2010;18(2):113–9.
49. Segal NA, Felson DT, Torner JC, et al. Greater trochanteric pain syndrome: epidemiology and associated factors. Arch Phys Med Rehabil. 2007;88(8):988–92.
50. Tortolani PJ, Carbone JJ, Quartararo LG. Greater trochanteric pain syndrome in patients referred to orthopedic spine specialists. Spine J. 2002;2(4):251–4.
51. Williams BS, Cohen SP. Greater trochanteric pain syndrome: a review of anatomy, diagnosis and treatment. Anesth Analg. 2009;108(5):1662–70.
52. Bewyer DC, Bewyer KJ. Rationale for treatment of hip abductor pain syndrome. Iowa Orthop J. 2003;23:57–60.

53. Finnoff JT, Fowler SP, Lai JK, et al. Treatment of chronic tendinopathy with ultrasound-guided needle tenotomy and platelet-rich plasma injection. PM R. 2011;3(10):900–11.
54. Voos JE, Shindle MK, Pruett A, Asnis PD, Kelly BT. Endoscopic repair of gluteus medius tendon tears of the hip. Am J Sports Med. 2009;37(4):743–7.
55. Fredericson M, Weir A. Practical management of iliotibial band friction syndrome in runners. Clin J Sport Med. 2006;16(3):261–8.
56. Holmes JC, Pruitt AL, Whalen NJ. Iliotibial band syndrome in cyclists. Am J Sports Med. 1993;21 (3):419–24.
57. Orchard JW, Fricker PA, Abud AT, Mason BR. Biomechanics of iliotibial band friction syndrome in runners. Am J Sports Med. 1996;24(3):375–9.
58. Hamill J, Miller R, Noehren B, Davis I. A prospective study of iliotibial band strain in runners. Clin Biomech (Bristol, Avon). 2008;23(8):1018–25.
59. Noehren B, Davis I, Hamill J. ASB clinical biomechanics award winner 2006 prospective study of the biomechanical factors associated with iliotibial band syndrome. Clin Biomech (Bristol, Avon). 2007;22 (9):951–6.
60. Allen WC, Cope R. Coxa saltans: the snapping hip revisited. J Am Acad Orthop Surg. 1995;3(5):303–8.
61. Lewis CL. Extra-articular snapping hip: a literature review. Sports Health. 2010;2(3):186–90.
62. Ali K, Leland JM. Hamstring strains and tears in the athlete. Clin Sports Med. 2012;31(2):263–72.
63. Clanton TO, Coupe KJ. Hamstring strains in athletes: diagnosis and treatment. J Am Acad Orthop Surg. 1998;6(4):237–48.
64. Linklater JM, Hamilton B, Carmichael J, Orchard J, Wood DG. Hamstring injuries: anatomy, imaging, and intervention. Semin Musculoskelet Radiol. 2010;14 (2):131–61.
65. Askling CM, Tengvar M, Saartok T, Thorstensson A. Acute first-time hamstring strains during high-speed running: a longitudinal study including clinical and magnetic resonance imaging findings. Am J Sports Med. 2007;35(2):197–206.
66. Heiderscheit BC, Sherry MA, Silder A, Chumanov ES, Thelen DG. Hamstring strain injuries: recommendations for diagnosis, rehabilitation, and injury prevention. J Orthop Sports Phys Ther. 2010;40(2):67–81.
67. McSweeney SE, Naraghi A, Salonen D, Theodoropoulos J, White LM. Hip and groin pain in the professional athlete. Can Assoc Radiol J. 2012;63 (2):87–99.
68. Opar DA, Williams MD, Shield AJ. Hamstring strain injuries: factors that lead to injury and re-injury. Sports Med. 2012;42(3):209–26.
69. Anderson K, Strickland SM, Warren R. Hip and groin injuries in athletes. Am J Sports Med. 2001;29 (4):521–33.
70. Petersen J, Thorborg K, Nielsen MB, Budtz-Jorgensen E, Holmich P. Preventive effect of eccentric training on acute hamstring injuries in men's soccer: a cluster-randomized controlled trial. Am J Sports Med. 2011;39(11):2296–303.
71. Reurink G, Goudswaard GJ, Tol JL, Verhaar JA, Weir A, Moen MH. Therapeutic interventions for acute hamstring injuries: a systematic review. Br J Sports Med. 2012;46(2):103–9.
72. Cohen S, Bradley J. Acute proximal hamstring rupture. J Am Acad Orthop Surg. 2007;15(6):350–5.
73. Cohen SB, Rangavajjula A, Vyas D, Bradley JP. Functional results and outcomes after repair of proximal hamstring avulsions. Am J Sports Med. 2012;40 (9):2092–8.
74. Folsom GJ, Larson CM. Surgical treatment of acute versus chronic complete proximal hamstring ruptures: results of a new allograft technique for chronic reconstructions. Am J Sports Med. 2008;36 (1):104–9.
75. Nicholas SJ, Tyler TF. Adductor muscle strains in sport. Sports Med. 2002;32(5):339–44.
76. Grote K, Lincoln TL, Gamble JG. Hip adductor injury in competitive swimmers. Am J Sports Med. 2004;32 (1):104–8.
77. Hiti CJ, Stevens KJ, Jamati MK, Garza D, Matheson GO. Athletic osteitis pubis. Sports Med. 2011;41 (5):361–76.
78. Beatty T. Osteitis pubis in athletes. Curr Sports Med Rep. 2012;11(2):96–8.
79. Choi H, McCartney M, Best TM. Treatment of osteitis pubis and osteomyelitis of the pubic symphysis in athletes: a systematic review. Br J Sports Med. 2011;45(1):57–64.
80. Meyers WC, McKechnie A, Philippon MJ, Horner MA, Zoga AC, Devon ON. Experience with "sports hernia" spanning two decades. Ann Surg. 2008;248 (4):656–65.
81. Farber AJ, Wilckens JH. Sports hernia: diagnosis and therapeutic approach. J Am Acad Orthop Surg. 2007;15(8):507–14.
82. Litwin DE, Sneider EB, McEnaney PM, Busconi BD. Athletic pubalgia (sports hernia). Clin Sports Med. 2011;30(2):417–34.
83. Swan Jr KG, Wolcott M. The athletic hernia: a systematic review. Clin Orthop Relat Res. 2007;455:78–87.
84. Caudill P, Nyland J, Smith C, Yerasimides J, Lach J. Sports hernias: a systematic literature review. Br J Sports Med. 2008;42(12):954–64.
85. Zoga AC, Kavanagh EC, Omar IM, et al. Athletic pubalgia and the "sports hernia": MR imaging findings. Radiology. 2008;247(3):797–807.
86. Krivickas LS, Wilbourn AJ. Peripheral nerve injuries in athletes: a case series of over 200 injuries. Semin Neurol. 2000;20(2):225.
87. Toth C. Peripheral nerve injuries attributable to sport and recreation. Neurol Clin. 2008;26(1):89–113. viii–ix.
88. Lorei MP, Hershman EB. Peripheral nerve injuries in athletes—treatment and prevention. Sports Med. 1993;16(2):130–47.

89. Hayashi S, Nishiyama T, Fujishiro T, Kanzaki N, Kurosaka M. Avulsion-fracture of the anterior superior iliac spine with meralgia paresthetica: a case report. J Orthop Surg (Hong Kong). 2011;19(3):384–5.
90. Macgregor J, Moncur JA. Meralgia paraesthetica—a sports lesion in girl gymnasts. Br J Sports Med. 1977;11(1):16–9.
91. Otoshi K, Itoh Y, Tsujino A, Kikuchi S. Case report: meralgia paresthetica in a baseball pitcher. Clin Orthop Relat Res. 2008;466(9):2268–70.
92. Lee CH, Dellon AL. Surgical management of groin pain of neural origin. J Am Coll Surg. 2000;191 (2):137–42.
93. Brown RA, Mascia A, Kinnear DG, Lacroix V, Feldman L, Mulder DS. An 18-year review of sports groin injuries in the elite hockey player: clinical presentation, new diagnostic imaging, treatment, and results. Clin J Sport Med. 2008;18(3):221–6.
94. Ziprin P, Williams P, Foster ME. External oblique aponeurosis nerve entrapment as a cause of groin pain in the athlete. Br J Surg. 1999;86(4):566–8.
95. Kennedy J. Neurologic injuries in cycling and bike riding. Neurol Clin. 2008;26(1):271–9. xi–xii.
96. Leibovitch I, Mor Y. The vicious cycling: bicycling related urogenital disorders. Eur Urol. 2005;47 (3):277–86. discussion 286–7.
97. Durante JA, Macintyre IG. Pudendal nerve entrapment in an ironman athlete: a case report. J Can Chiropr Assoc. 2010;54(4):276–81.
98. Silbert PL, Dunne JW, Edis RH, Stewart-Wynne EG. Bicycling induced pudendal nerve pressure neuropathy. Clin Exp Neurol. 1991;28:191–6.

Section III

MRI Techniques to Detect Disease Conditions

Overview of Diagnostic Imaging of Hip Joint

10

Sarah D. Bixby

Introduction

Since its introduction in the 1970s, MRI has become one of the most powerful imaging tools for musculoskeletal imaging. With state-of-the-art advances in imaging technology, MRI provides remarkable soft tissue contrast with continually improving spatial resolution. MRI is ideally suited to evaluate muscles, tendons, ligaments, and other vital soft tissue structures not easily evaluated by any other imaging technique. MRI does not require ionizing radiation. This is particularly important for patients with chronic conditions who are likely to undergo multiple imaging examinations in their lifetime. With ongoing technologic advancements in MR sequence development, coil manufacturing, and high field strength magnets (e.g., 3.0 T), indications for imaging the hip with MRI continue to expand. It is common for institutions and imaging centers to have a variety of imaging protocols for the hip, utilizing a variety of different coils and often requiring specific magnet strengths (please refer to tables at the end of the chapter for several examples of indication-based protocols). This chapter will focus on the different coils, sequences, and protocols which are useful in imaging the hip.

S.D. Bixby (✉)
Department of Radiology, Boston Children's Hospital, 300 Longwood Avenue, Boston, MA 02115, USA
e-mail: Sarah.bixby@childrens.harvard.edu

Field Strength

The current standard field strength for MRI examinations of the musculoskeletal system in the United States is 1.5 Tesla (T), though 3.0 T imaging systems have become increasingly prevalent. A high field strength imaging system is important for detailed assessment of intra-articular structures such as labrum and cartilage, as the higher field strength systems allow increased SNR and/or reduced imaging times. A more global assessment of the hip and pelvis, such as in a patient with fever and white count with symptoms of infection, typically does not require a high field strength magnet in order to provide the necessary information for accurate diagnosis and treatment (Fig. 10.1). Lower field strength (1.0 T) open magnets or dedicated extremity scanners for patients with a large body habitus or claustrophobia may be useful for certain patients. The most important benefit of using a system with high field strength (e.g., 3.0 T) is the increase in SNR. Theoretically the SNR at 3 T should be double than that at 1.5 T, though the actual increase in SNR is between 30 and 60 % [1]. The increase in field strength from 1.5 to 3.0 T is associated with changes in tissue relaxation times and sensitivity to magnetic susceptibility. For these reasons, appropriate imaging parameters are not identical between 1.5 and 3.0 T systems. In general, T1 times are slightly higher at 3.0 T compared to 1.5 T [2, 3] because of the prolonged T1 relaxation of tissues at the higher field strength, and therefore

Y.-J. Kim (eds.), *Hip Magnetic Resonance Imaging*,
DOI 10.1007/978-1-4614-1668-5_10,

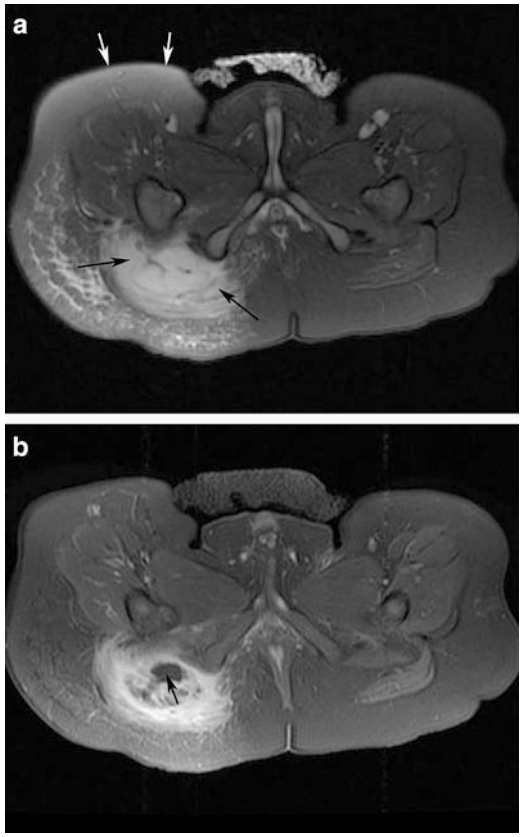

Fig. 10.1 MRI of the pelvis in an 8-month-old child with pyomyositis performed on a 1.5 T magnet with a cardiac coil. (**a**) Axial T2-FSE fs image through the lower pelvis demonstrates areas of poor fat suppression along the right thigh (*white arrows*). An area of confluent signal abnormality is clearly appreciated (*black arrows*) in the posterior soft tissues adjacent to the right ischium (*black arrows*). (**b**) Axial T1 fs image performed after intravenous contrast administration demonstrates abnormal enhancement in the same area, with a focal non-enhancing abscess (*arrow*)

the TR must be increased to achieve the same effect. For T2-weighted images the TE is decreased on 3.0 T field strengths compared to 1.5 T to adjust for the accelerated T2 decay and lower T2 relaxation times [3–6]. For gradient echo examinations the flip angle is lower at 3.0 T in light of the increased T1 relaxation times, and the TE is shorter to account for the doubled T2* effects [6]. The advantages of increased SNR are improved spatial or temporal resolution, thinner slices, and/or shorter imaging times [2]. Another advantage of 3.0 T systems over lower field strength magnets includes more efficient fat-saturation techniques secondary to wider frequency separation of fat and water [6]. Fat-suppression techniques are particularly important in musculoskeletal imaging examinations as the contrast between soft tissue structures is often increased after fat suppression is applied. The length of a fat-saturation pulse is shortened on 3.0 T compared to 1.5 T systems, leading to either slightly shorter imaging times or increased number of imaging slices [6]. Disadvantages of higher field strength magnets include increased magnitude of certain imaging artifacts, including chemical shift [7] and standing wave artifact [2]. Doubling the receiver bandwidth at 3.0 T results in a similar amount of chemical shift artifact compared to 1.5 T, though with an associated decrease in SNR [6]. Postoperative patients may have tiny pieces of metal in and around the joint that cause increased susceptibility artifact at 3.0 T compared to lower field strength systems [8]. These patients may be better served on a lower field strength magnet or by eliminating the use of gradient echo (GR) sequences. Certain open magnet configurations have the advantage of allowing for functional assessment of joints by imaging patients in both supine and weight-bearing positions [9]. Weight-bearing or load assessments of joints can be performed in vertically oriented open magnets or in systems that utilize special loading devices [10].

Coils

A variety of imaging coils are useful for imaging the hip. Most imaging coils are multichannel, phased-array coils. Coil selection depends on many factors, including the manufacturer of the imaging system, patient age and size, shape of the body part imaged, and desired field of view (FOV). Image quality is highly dependent on proper coil selection. Proper coil selection requires that the clinician or radiologist determines prior to imaging whether one or both hips should be included in the FOV. While it is possible to change the coil at any point during an examination, this adjustment costs

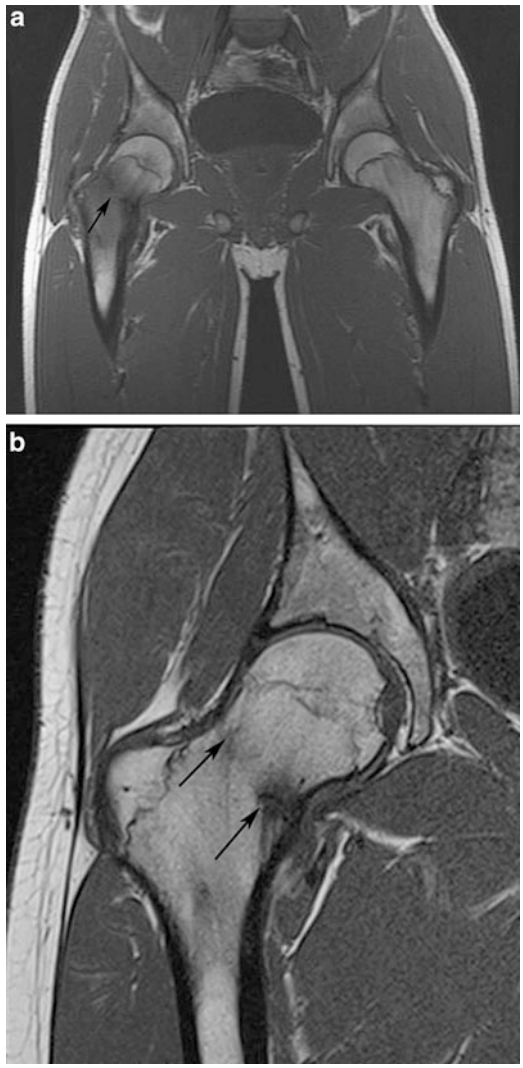

Fig. 10.2 Coronal T1-weighted images through the right hip in a 15-year-old male with femoral neck fracture. (**a**) Initial images performed with a large FOV through both hips using a body matrix coil demonstrate the fracture line (*black arrow*), but with poor spatial resolution. (**b**) A follow-up scan performed with a surface coil demonstrates the healing fracture (*black arrows*) with significantly improved spatial resolution. Both studies were performed on a 1.5 T magnet

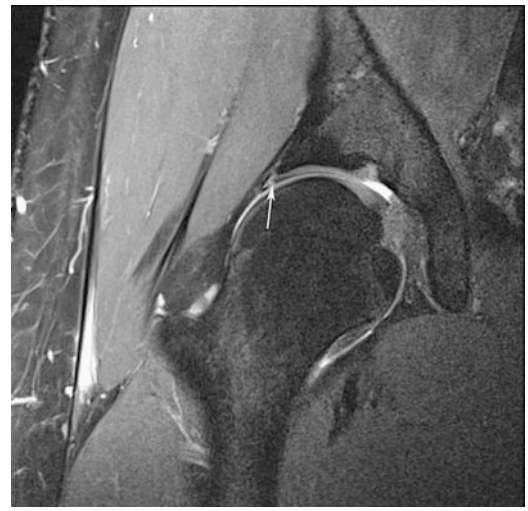

Fig. 10.3 Coronal PD-FSE fs sequence through the right hip in a 17-year-old male using a small surface coil with a 15 cm FOV achieves high-resolution imaging of the intra-articular structures such that a superior labral tear (*white arrow*) is easily visualized

valuable imaging time. In general, in an otherwise healthy patient with acute pain in one hip, dedicated imaging of the hip in question (excluding the other hip) is preferred in order to achieve high-resolution images (Fig. 10.2). Regional coils, such as phased-array torso, cardiac, or body matrix coils, should be considered when imaging of the entire pelvis is indicated, at the expense of high-resolution imaging of a single hip. Localized surface coils allow for improved spatial resolution and better detail of the anatomic structures such as femoral head, joint capsule, cartilage, and labrum (Fig. 10.3). Larger body coils allow for increased SNR and more uniform signal intensity throughout the image, though with decreased spatial resolution [11]. One must consider whether the benefit of increasing the FOV to include the contralateral hip outweighs the loss of resolution that will accompany the increase in coverage (Fig. 10.4). In some instances it may be useful to image one patient using several coils, depending on the indication. In a patient with unilateral hip pain with systemic disease such as sickle cell disease (SCD), a dedicated surface coil positioned over the painful hip will provide high-quality images of the hip while a single, additional sequence with a larger, body matrix coil may provide important additional information about the surrounding pelvis and contralateral hip (Fig. 10.5). It is often worthwhile to obtain one coronal image through both hips with a body

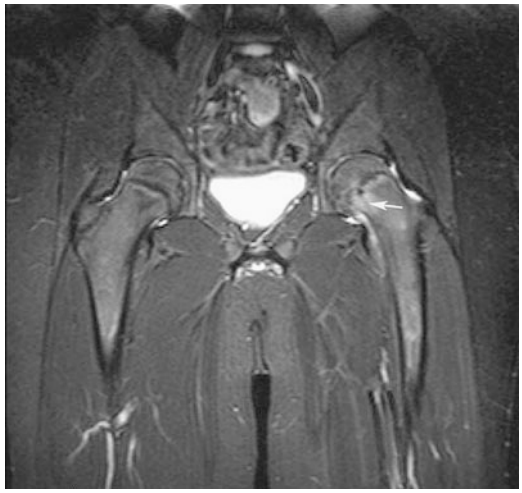

Fig. 10.4 Coronal STIR sequence on a 14-year-old male using a body matrix coil with a large 36 cm field of view. The mild left-sided slipped capital femoral epiphysis (*arrow*) and small associated left hip effusion are not well demonstrated given the large FOV

Fig. 10.5 Coronal T1 fs image after administration of intravenous contrast in a 9-year-old female with sickle cell anemia and avascular necrosis of the left hip (*arrows*). The large FOV was important for excluding disease on the contralateral hip

coil, which will serve as a guide for subsequent sequences, and also reveal whether there are bilateral or diffuse abnormalities [11]. Surface coils used for imaging of the hip joint and surrounding structures are flat or flexible so that they may be placed over the hip of interest. Some patients may not be able to hold still for extended periods of time, so it is often important to perform the most important imaging sequences early in an imaging protocol. Detailed clinical information about the patient's symptoms is extremely helpful in establishing an appropriate protocol.

For single hip imaging, coronal images should extend through the entire joint. If the clinical indication is to evaluate for intra-articular pathology, coronal images through the iliopsoas anteriorly and sciatic nerve posteriorly are often sufficient [12]. In many cases the clinical history is not specific, or the pathology may be extra-articular, and it is therefore prudent to enlarge the FOV to include all of the muscle groups. Likewise, sagittal imaging through the joint may be limited to the greater trochanter laterally and the medial acetabular wall medially when the pathology is intra-articular, but more often imaging through the entire area is recommended to evaluate the adjacent soft tissues. When imaging through both hips is indicated, the coronal images are performed straight rather than oblique, and images extend through the anterior and posterior muscle groups on both sides. Likewise, axial images should include the soft tissues surrounding the hip, and should extend cranially and caudally to cover the area of clinical interest.

Sequences

MR protocols are highly driven by clinical history and should be tailored to the indication for imaging. Certain sequences will be selected based on their ability to demonstrate anatomic structures with high detail, whereas other sequences may have poorer resolution but may provide additional information regarding the presence of edema, hemorrhage, or even molecular structure. Imaging time is also an important factor, particularly in pediatric patients who may be under sedation or anesthesia, or who have limited ability to hold still if unsedated. The workhorse of musculoskeletal MR imaging is the spin-echo sequence, including T1-weighted, T2-weighted, and proton-density (PD)-weighted images. The relative contrast of the image will

vary depending on the parameters of the particular imaging system. Spin-echo sequences have traditionally been performed as two-dimensional (2D) image acquisitions, though more recently three-dimensional (3D) spin-echo sequences have become available. The 3D sequences are volumetric acquisitions with isotropic voxel sizes allowing post-processing reformatting into any 2D imaging plane. This reformatting can be particularly helpful when imaging an obliquely oriented structure (such as the femoral neck) or a structure that is curved (such as the acetabular labrum).

Most multichannel phased-array coils allow for parallel imaging, which increases speed of imaging acquisition and thereby reduces imaging times. There are several types of parallel imaging techniques, including image-domain-based and k-space-based techniques [2]. Using either technique, each of the elements or channels in a phased-array coil provides separate image information which is combined with information from other elements to create an image. The advantage of parallel imaging is a reduction in overall imaging time, though with concomitant diminished SNR [2]. For this reason, common indications for applying parallel imaging techniques include high SNR sequence and/or those that require fast temporal resolution (such as contrast-enhanced dynamic imaging, breath-hold sequences, and volumetric acquisitions) [2].

Bone and Bone Marrow Sequences

Evaluation of bony contours is a critical piece of any musculoskeletal MRI examination, particularly in the hip where morphologic osseous abnormalities may contribute to hip pain and joint damage [13–16]. The "gold standard" for 3D bony imaging of the hip and pelvis remains multidetector computerized tomography (MDCT), as the significantly higher density of bony structures compared to the surrounding soft tissues allows for creation of beautiful 3D reconstructions. The images acquired with MDCT require the use of ionizing radiation directed at the pelvis, prompting clinicians and radiologists to answer as many clinical questions as possible using MRI in place of CT. At present it is generally not feasible to create 3D models of the proximal femur and/or pelvis from an MRI sequence (even a thin-section isotropic sequence) without rigorous and time-consuming segmentation techniques. The contrast between bone and soft tissues on MRI is significantly narrower than the vast contrast between these tissues at CT, which limits 3D volumetric modeling of MRI images. Rather than creating volumetric models of the bones, MRI is capable of evaluating structures in any imaging plane regardless of how the patient is positioned in the scanner. Images may be directly prescribed off of localizer sequences and acquired directly in a specific imaging plane, or they may be reformatted from an isotropic volumetric acquisition after the patient has left the scanner. One particular imaging technique that is useful for hip imaging is acquiring a rotating or "radial" plane of images. As both the femoral head and acetabulum are relatively spherical structures with curved surfaces, it is often helpful to rotate the imaging plane around the axis of either the femoral head or acetabulum, rather than acquiring contiguous parallel slices in any single plane. The most common indication for performing radial imaging of the hip is femoroacetabular impingement (FAI). By rotating the image along the axis of the femoral neck, cam lesions along the head/neck junction are easily detected and the extent of the deformity may be precisely mapped (Fig. 10.6). As an alternative to rotating the plane of imaging around the femoral neck axis, radial images may instead be oriented around the acetabulum to detect labral tears (this will be discussed in greater detail in the chapter on MR arthrography (MRA)). The improved SNR of a direct radial acquisition compared to a reformatted sequence from a thin, isotropic volumetric sequence is important for detection of subtle labral tears or cartilage lesions.

MRI also provides an important assessment of intramedullary bone marrow signal. A variety of disease processes manifest with alterations in the normal or expected bone marrow signal, and detection of marrow signal changes is often an

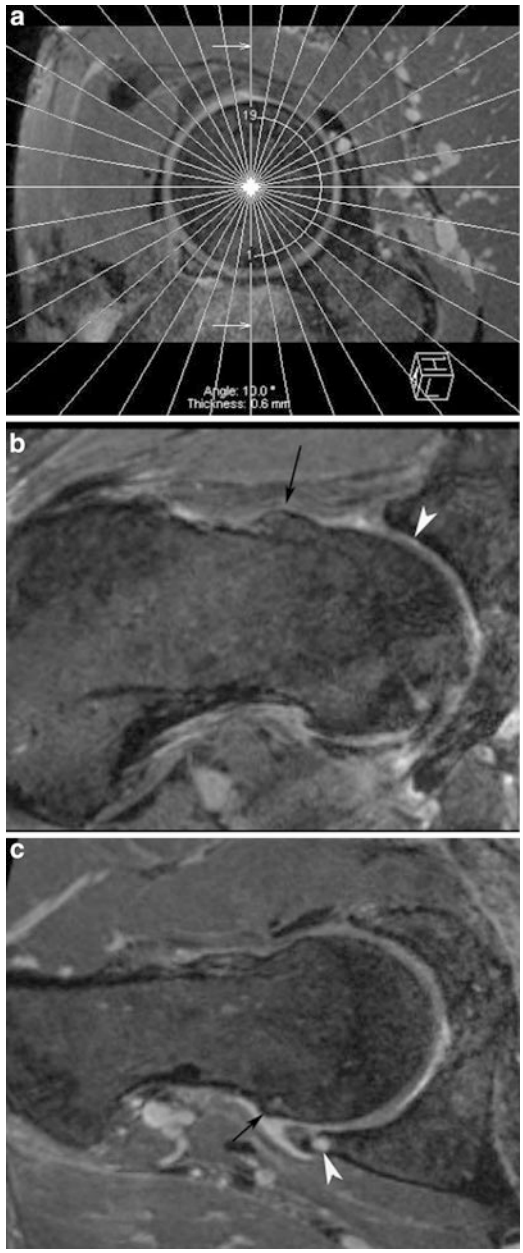

Fig. 10.6 Isotropic, thin-section sagittal oblique TrueFISP sequence through the right hip in a 34-year-old male with history of remote slipped capital femoral epiphysis, now with hip pain. (**a**) Radially oriented reformat rotating around the axis of the femoral neck was performed with 10° between images. (**b**) Anterosuperior image through the 11:00 position of the femoral head/neck junction demonstrates a prominent osseous bump (*black arrow*) and acetabular cartilage loss (*white arrowhead*). (**c**) Posterosuperior image at the 2:00 position demonstrates a bony bump (*black arrow*) and an acetabular rim cyst (*white arrowhead*)

important clue to underlying pathology. No other imaging modality is capable of providing as much meaningful imaging information about the bone marrow as MRI. Although bone-seeking radiopharmaceutical studies in nuclear medicine indicate areas of increased bone turnover or increased blood supply [17], the findings are relatively nonspecific and precise anatomic information is lacking. In order to accurately assess the marrow with MRI, it is important to understand normal marrow structure, and how marrow changes over time. Bone marrow consists of osseous matrix (trabeculae), red marrow (cellular, hematopoietic), and yellow marrow (fatty, hematopoietically inactive marrow). Marrow composition changes with age, with conversion of hematopoietic marrow to fatty marrow in predictable patterns. T1-weighted spin-echo sequences are well suited for differentiating between red and yellow marrow, as well as for detecting pathologic marrow replacement processes. T1-weighted images are characterized by low TR (<1,000 ms) and low TE (<30 ms). Hematopoietic marrow tends to have intermediate signal on T1-weighted images, while yellow marrow has bright signal. Fluid-sensitive sequences with fat suppression are also useful in assessment of bone marrow, as fatty marrow signal is lower than surrounding muscle, in contrast to the isointense hematopoietic marrow. Pathologic marrow processes (leukemia, lymphoma, marrow edema, osteomyelitis, metastases, post-chemotherapy changes, etc.) demonstrate bright signal intensity on T2-weighted images and decreased signal on T1-weighted images [18]. In adult patients the bone marrow in the hip should largely consist of yellow, fatty marrow. Variable amounts of hematopoietic marrow will remain in the femoral neck and metaphyseal equivalents depending on age and hematopoietic demands. T1-weighted images allow the best determination of normal red-marrow patterns versus pathologic marrow signal, given that normal red marrow tends to have a patchy distribution [18] or flame-shaped pattern, versus the more amorphous or confluent pattern of other marrow replacement processes

Fig. 10.7 (**a**) Coronal T1-weighted image through the pelvis and hips in a 17-year-old male with history of right hip pain reveals a normal marrow pattern, with predominantly fatty marrow with geographic or "flame-shaped" regions of residual hematopoietic marrow within the femoral metadiaphyseal region (*black arrows*) and superior acetabulum (*white arrows*). (**b**) The marrow is nearly completely replaced with intermediate signal intensity lesions on this T1-weighted image through the pelvis in an 8-year-old female with newly diagnosed leukemia

(Fig. 10.7). Pathologic marrow replacement processes do not respect boundaries such as the physeal scar of the proximal femur [19]. Pathologic marrow infiltrating lesions demonstrate dark signal on T1-weighted images relative to the surrounding marrow signal. These lesions are often more difficult to detect on T2-weighted images because of decreased contrast between normal and abnormal marrow. T1-weighted images also allow for assessment of fracture lines, which stand out from the surrounding bright, usually fatty marrow signal as a low-signal, linear signal abnormality (Fig. 10.2). T1-weighted images are also helpful in evaluation of bone or soft tissue lesions. Lesions containing fat, such as fat necrosis (Fig. 10.8), lipoma, or other fatty neoplasms, are best characterized by the bright signal on T1-weighted images that suppresses with fat-suppression techniques.

T1-weighted images are also performed after administration of the intravenous contrast agent gadolinium. The intrinsic T1-shortening effect of gadolinium allows tissues that take up gadolinium to appear brighter on T1-weighted images. The enhancement of such lesions is best appreciated by applying fat-suppression techniques so that the otherwise bright signal intensity of fat no longer is apparent. Gadolinium contrast is often administered to patients in whom there is concern for infection such as pelvic osteomyelitis or septic arthritis (Fig. 10.9), arthropathy, or neoplasm. Gadolinium is particularly useful for confirming that masses that have intrinsically bright signal on T2-weighted images are solid rather than complex cystic lesions (Fig. 10.10). It may be helpful to perform a T1-weighted sequence with fat suppression through a region of interest before the administration of gadolinium in order that the non-contrast image may later be subtracted (either mentally or with special software) from the post-contrast image. This is particularly helpful for lesions that often have intrinsically bright signal on T1-weighted images, such as hematoma or lymphatic malformation. The bright T1-signal in these lesions post-contrast may be mistaken for enhancement if pre-contrast imaging was not performed. Dynamic contrast-enhanced images are helpful for detection of perfusion abnormalities in the femoral head, such as in young patients with concern for Legg–Calvé–Perthes (LCP) disease [20], or differentiating transient synovitis from septic arthritis [21]. In order to perform multiple phases of imaging through the femoral heads in a short period of time, T1-weighted GR sequences are often performed in lieu of a spin-echo sequence. Both hips are imaged together in the coronal plane. Further investigation in this area is currently ongoing, as it has been postulated that the reperfusion pattern of the femoral head in

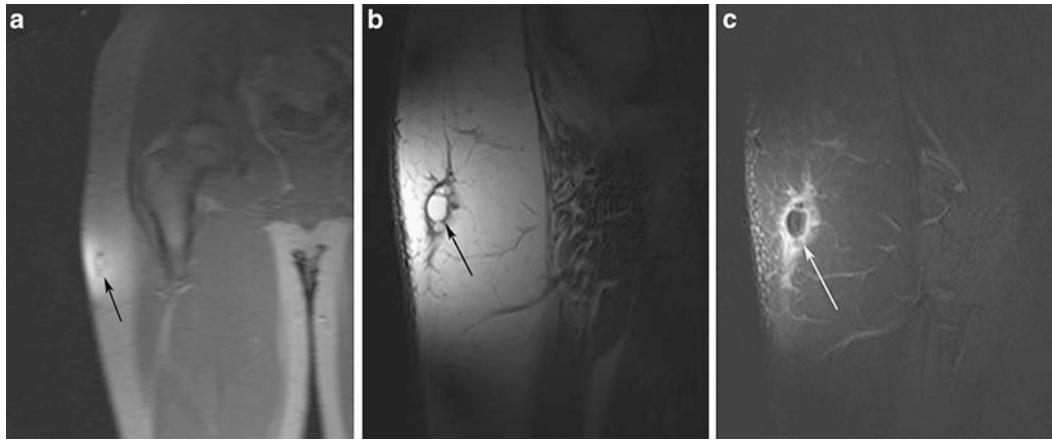

Fig. 10.8 Imaging of the right hip in a 15-year-old male with enlarging mass along the lateral aspect of the hip. (**a**) Initial GR localizer sequence through the right hip demonstrated a lesion confined to the superficial fat of the right upper thigh. A small surface coil (loop coil) was selected based on the superficial nature of the lesion. (**b**) T1-weighted image through the lesion demonstrated a multilobulated lesion within the subcutaneous fat which was isointense to the surrounding fat. (**c**) T1-weighted image with fat suppression after contrast demonstrated suppression of the signal within the lesion with peripheral enhancement. The diagnosis was fat necrosis and the patient improved with no further treatment

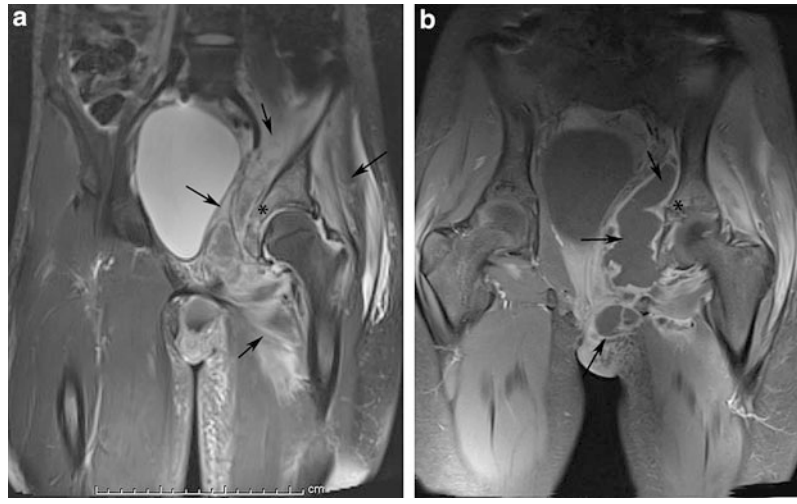

Fig. 10.9 Images through the hips and pelvis on a 3 T magnet in a 13-year-old female with fever, diffuse swelling, and pain surrounding the left hip and buttock. (**a**) Coronal T2-FSE fs image revealed abnormal bright marrow signal centered in the acetabulum around the triradiate cartilage (*) with a large amount of bright signal abnormality within the surrounding soft tissues (*black arrows*). (**b**) Coronal T1-weighted image with fat suppression after intravenous contrast demonstrates abnormal enhancement of the bone marrow (*) consistent with pelvic osteomyelitis, with a large, rim enhancing abscess (*black arrows*) within the pelvis and perineum. This required urgent surgical drainage

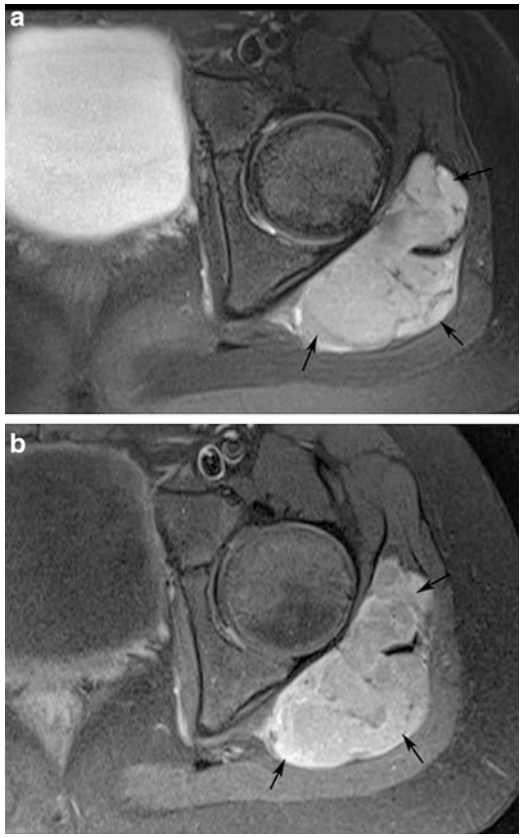

Fig. 10.10 (**a**) Axial T2-FSE fs image in a 9-year-old male with left hip pain demonstrated a well-marginated lesion within the gluteal muscles (*black arrows*) with internal septations and bright signal intensity, concerning for complex cystic lesion versus solid mass. (**b**) Axial T1-weighed image with fat suppression after the administration of intravenous contrast demonstrated relatively homogeneous enhancement of the solid mass, which was later confirmed to represent a synovial sarcoma

patients with avascular necrosis (AVN) may be related to prognosis [20].

Fluid-Sensitive Sequences

Most disease processes (infection, traumatic fractures, malignancy, etc.) are associated with an increase in water content. This increased fluid content will contrast sharply with adjacent bony and soft tissue structures on sequences optimized to be fluid-sensitive. T2-weighted images are defined by both high TR (>2,000 ms) and high TE (>80 ms), which allow fluid signal to appear bright. Fat also appears bright on T2-weighted images and may mask underlying pathology. Ideally, a sequence designed to look for "pathology" should allow for markedly bright fluid signal and relatively diminished signal from all adjacent tissue structures, including fat. For this reason, it is common in musculoskeletal imaging to employ fat saturation with T2-weighted images. This increases the contrast between fat and nonfat containing tissues and also affects the overall dynamic range of the image [22]. This can be exceptionally helpful when evaluating patients with sports injuries and increases detection of subtle osseous or soft tissue lesions such as stress reaction or mild muscle strain (Fig. 10.11). The most common types of fat-suppression techniques include chemical fat suppression as well as short inversion time inversion-recovery (STIR) technique. Chemical fat suppression selectively diminishes the signal from fat with a spoiler sequence, without diminishing signal from other frequencies [18]. STIR sequences are performed in areas of magnetic field inhomogeneities that limit chemical fat-suppression techniques, but with a decrease in overall SNR. In STIR sequences, a 180° inversion pulse prior to spin-echo techniques negates the signal from fat but may also diminish signal from nearby frequencies [18]. The end result of both sequences is that the high signal from fat is removed, and the signal from water appears hyperintense [18]. Generally, most hip MR protocols rely on at least one fluid-sensitive image through the hip, often in the axial plane, and usually with fat suppression (Fig. 10.12). MR examinations performed to evaluate sports- or activity-related trauma or injury may require several planes of fluid-sensitive sequences, or a 3D volume acquisition that may be reformatted into multiple planes. This allows for optimal assessment of the bones and soft tissues for subtle edematous changes that may be missed if only a single imaging plane is performed.

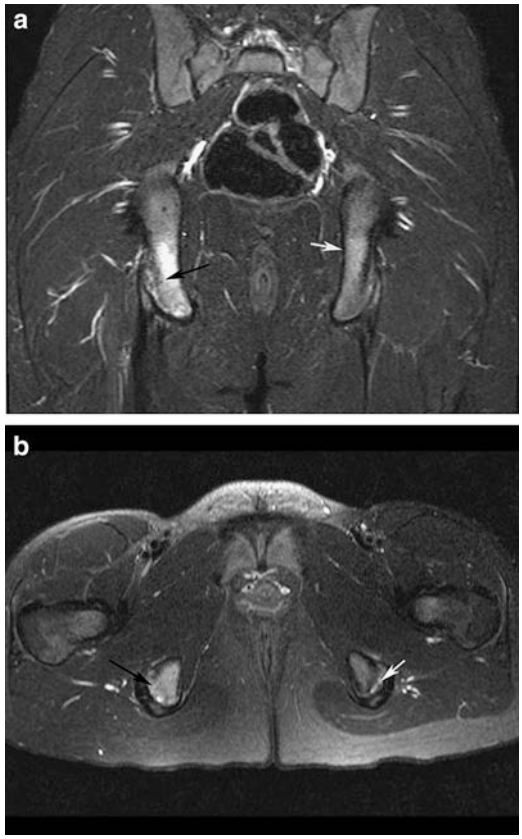

Fig. 10.11 Coronal STIR image (**a**) and axial T2-FSE with fs image (**b**) through the hips and pelvis in a 12-year-old female gymnast with hip pain reveals marrow edema within the right ischial tuberosity at the attachment site of the hamstring tendons (*black arrows*) consistent with avulsive stress injury. Subtle signal abnormality is also noted in the left ischial tuberosity (*white arrows*) on the left consistent with mild stress reaction

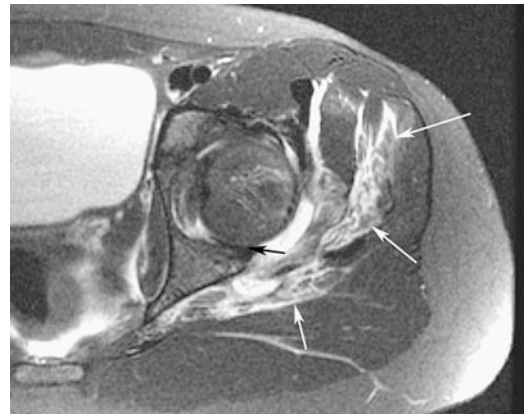

Fig. 10.12 Axial T2-FSE fs image through the left hip in an 11-year-old female with pain and inability to weight-bear after falling on her hip demonstrated a substantial amount of bright fluid in the surrounding musculature (*white arrows*) indicating edema and hemorrhage. There was a joint effusion which clearly demarcates the posterior labrum (*black arrow*) which had flipped between the femoral head and acetabulum

Cartilage Sequences

Assessment of the articular cartilage of the hip joint has become increasingly important, as advances in technology have enabled thin-section imaging through joints. Hip conditions such as developmental dysplasia of the hip (DDH) and FAI cause different patterns of cartilage damage within the hip joint [23]. Patients with cartilage damage related to DDH may be candidates for hip preserving procedures depending on the severity of the cartilage damage [24]. Patients with FAI may benefit from surgical intervention to relieve pain and return to activity [25]. Although cartilage contrasts with adjacent fluid on T2-weighted images, these sequences provide limited information about the cartilage other than its overall thickness. Likewise, the dark signal of fluid on T1-weighted image makes detection of cartilage lesions difficult given that there is little contrast between fluid and cartilage. For these reasons, other types of sequences are preferred for cartilage assessment.

Given the relatively thin cartilage surfaces in the hip, cartilage lesions are best appreciated at 3.0 T compared to 1.5 T in light of the increased SNR [26]. Patients with clinical concern for intra-articular pathology should be imaged at 3.0 T whenever feasible to optimally assess the cartilage integrity. Traditionally, non-contrast MRI with 2D fast spin-echo (FSE) sequences has been considered the workhorse sequences for cartilage imaging [27] in addition to 3D SPGR sequences [28] (Fig. 10.13). Intermediate-weighted (IM) FSE MRI sequences (TR 3,500–4,000, TE 30–35 ms) take advantage of the water content of the articular cartilage and demonstrate excellent contrast between articular cartilage and adjacent structures [29]

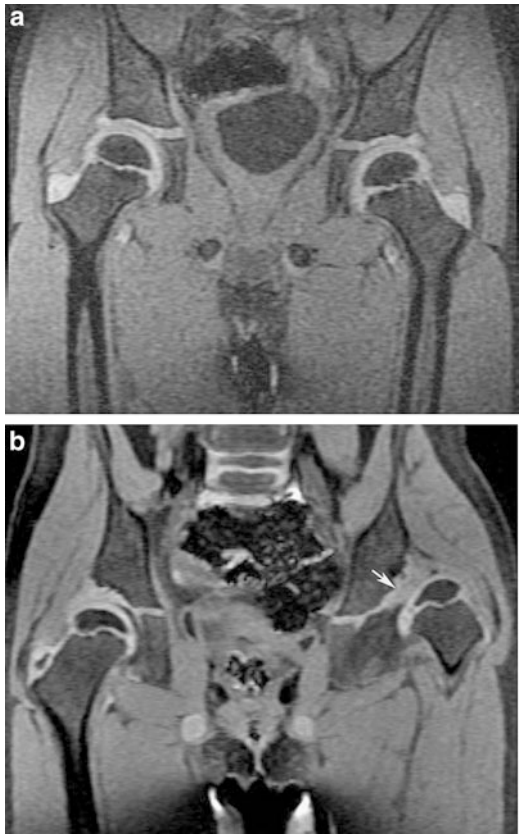

Fig. 10.13 (**a**) Coronal 3D SPGR image through the hips and pelvis of a 6-year-old male with hip pain revealed normal femoral head and acetabular cartilage. (**b**) Same sequence on a 5-year-old female with right-sided acetabular dysplasia revealed a shallow, irregular left acetabulum (*white arrow*) and aspherical left femoral head. Both studies were performed on a 1.5 T magnet with 1 mm slice thickness

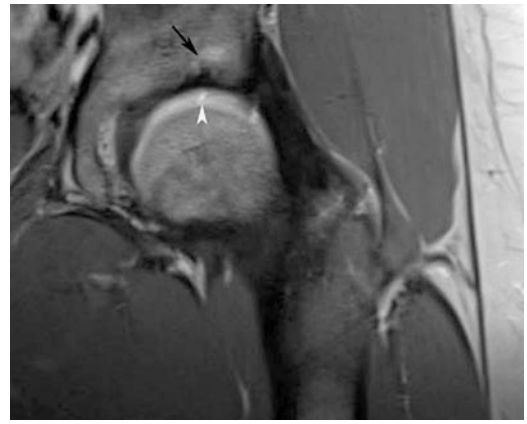

Fig. 10.14 Coronal IM-FSE (TR 3,500, TE 28) sequence through the left hip on a 3 T magnet with a small surface coil in a 24-year-old woman with left hip pain demonstrated marrow edema within the anterosuperior acetabulum (*black arrow*) and bright fluid insinuating into a focal acetabular cartilage defect (*white arrowhead*)

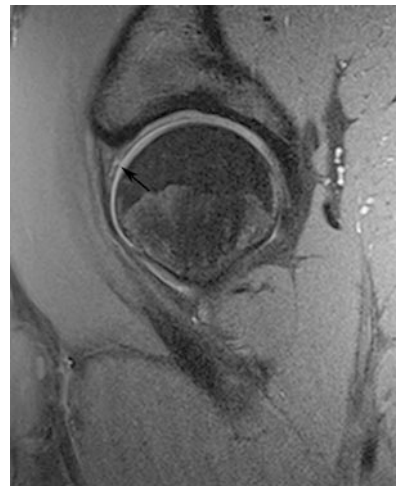

Fig. 10.15 Sagittal PD-FSE (TR 2,730, TE 11) image with fat suppression through the left hip in a 16-year-old male with hip pain was performed on a 3 T magnet with a small surface coil and a small, 16 cm FOV. Both the acetabular and femoral head cartilage are well visualized, and an anterosuperior labral tear (*black arrow*) can be easily appreciated despite the non-arthrographic technique

(Fig. 10.14). The TE is slightly higher in IM-FSE sequences (TE 30–60) compared to PD-FSE sequences (TE 10–30 ms) in order to achieve a more optimal contrast between labrum, cartilage, and fluid [9, 20], thereby achieving the benefits of both PD- and T2-weighted images in one sequence. Articular cartilage is intermediate in signal on IM-FSE sequences, fluid is bright, and fibrocartilage is dark [29]. PD-FSE sequences with lower TE values are useful for assessing fibrocartilagenous structures, but are not as fluid-sensitive as IM-FSE sequences [9] (Fig. 10.15). In some reports, non-contrast FSE sequences demonstrate up to 87 % sensitivity and 94 % specificity in the detection of cartilage lesions [30]. Disadvantages of 2D FSE sequences include anisotropic voxels, slice gaps, and partial volume effects [22].

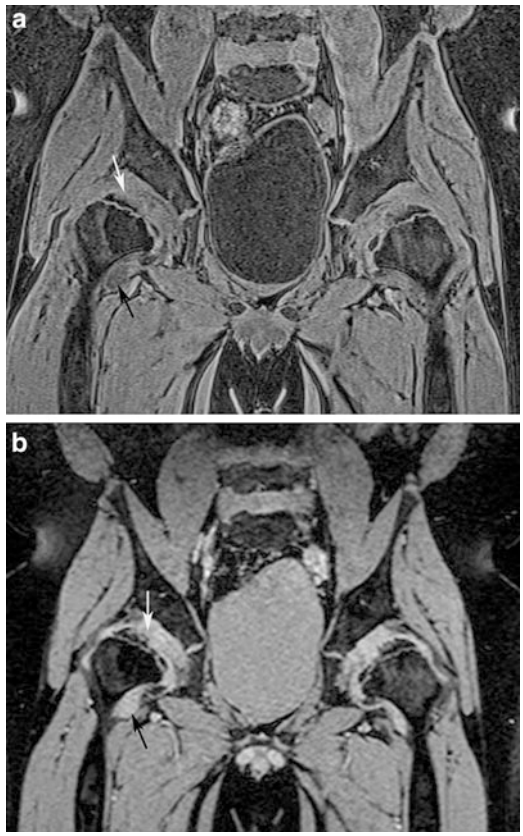

Fig. 10.16 MRI of the pelvis without contrast on a 1.5 T magnet for a 12-year-old boy with multiple epiphyseal dysplasia. (**a**) Coronal 3D SPGR sequence (TR 7.5, TE 2.9, FA 13) demonstrated excellent spatial resolution, though there is little contrast between the signal intensity of the femoral head cartilage (*white arrow*) and adjacent muscle. Joint fluid was dark (*black arrow*). (**b**) Coronal 3D MEDIC sequence (TR 32, TE 14, FA 8) demonstrates bright signal from cartilage (*white arrow*) and fluid (*black arrow*) which are now brighter than adjacent muscle

There are a variety of different gradient echo (GR) sequences that are commonly utilized for imaging cartilage. GR sequences utilize excitation pulses with flip angles less than 90°. Image contrast is determined by the TR, TE, and flip angle. Spoiled gradient echo (SPGR) with fat suppression is the standard for morphologic imaging of cartilage [22]. SPGR sequences eliminate the transverse magnetization from prior excitations with RF spoiling techniques, and produce relatively T1-weighted images. For this reason, fluid signal is dark on SPGR sequences, and the adjacent cartilage is relatively bright. The 2D multiple-echo data image combination (MEDIC) sequence is a different type of GR sequence, which utilizes a higher bandwidth and produces images with bright fluid signal [31] (Fig. 10.16). Both SPGR and MEDIC provide high spatial resolution, and are particularly useful for segmenting cartilage for assessment of cartilage volume and thickness [22]. Balanced SSFP (bSSFP) sequences are high-resolution, 3D GR images with bright fluid signal that have utility for imaging cartilage as well as other soft tissue structures [22]. Although conventional fat suppression may be applied to this sequence, other fat- and water-suppressive techniques such as IDEAL (iterative decomposition of water and fat with echo asymmetry and least-squares estimation) may best depict other soft tissue structures. This sequence is better recognized by its trade names: TrueFISP (Siemens Healthcare) and FIESTA (GE Healthcare) (refer to Fig. 10.6). The inherently bright cartilage signal of each of these GR sequences limits visualization of internal cartilage pathology, which may be better visualized with more IM-FSE sequences [32]. Susceptibility artifacts are also accentuated on GR sequences compared to FSE sequences, which may limit cartilage assessment in patients who have undergone prior surgery.

Three-dimensional double-echo steady state (DESS) is a different type of cartilage imaging technique with demonstrated utility in imaging knee cartilage [33, 34]. DESS sequences average the images resulting from two gradient echo signals in a 3D steady state sequence, one of which has mixed T1 and T2 weighting, the other of which is more heavily T2-weighted. The resulting averaged image demonstrates improved contrast between muscle and cartilage (which have a short T2) and joint fluid (which has a long T2). Adjusting the TR and TE alters the contrast between the soft tissues, and optimally both should be relatively low (TR = 30, TE1 = 7, TE2 = 53 ms) to maximize contrast between fluid and cartilage while maintaining high SNR [33]. Friedrich et al. compared qualitative and quantitative measures of image quality of several isotropic 3D MR-sequences in the knee and concluded that individually weighted DESS was the most promising candidate for

high-resolution isotropic cartilage imaging of the knee at 3 T [35]. The TrueFISP sequence was best able to distinguish between cartilage and surrounding tissues, but was also highly sensitive to artifacts [35]. Although most of the literature on cartilage imaging is focused in the knee (secondary to its thicker cartilage and less spherical articular surfaces) these techniques are also useful in the hip.

Isotropic Sequences

Three-dimensional FSE sequences are volumetric acquisitions with thin-section isotropic voxels, which allow images to be reformatted in any imaging plane. These sequences employ parallel imaging techniques to maintain acceptable imaging times. The advantages of 3D over 2D image acquisition include thinner imaging sections and decreased imaging time. Although the 3D sequences typically are longer to acquire than a corresponding 2D sequence, the 3D acquisition can replace multiple 2D acquisitions in several imaging planes. A further advantage of the 3D sequence is the ability to reformat the images in nontraditional imaging planes that would be challenging to acquire directly without multiple localizers. MRI assessment of cartilage requires a spatial resolution on the order of 0.4 mm in order to detect early morphologic degenerative changes [36]. This type of spatial resolution cannot be attained with conventional 2D sequences. Ristow et al. demonstrated that 3D FSE sequence (TR/TE: 2,500:38 ms) in the knee had promise in assessing lesions of cartilage and intra-articular loose bodies compared to 2D FSE sequences (TR/TE: 4,200/50 ms), but was limited in detection of meniscal, ligament, and bone marrow abnormalities [37]. Although 3D sequences were associated with overall decreased imaging quality compared to 2D sequences, there were only minor limitations in diagnostic performance. In 75 % of cases the radiologists felt that one 3D FSE sequence could replace three 2D FSE sequences in the knee, even despite the fact that the quality of the image reformats was lower than the direct 2D FSE acquisitions [37]. 3D FSE imaging with isotropic voxels in the knee [38] and ankle [39] has been reported in the literature, but there is limited data regarding the utility of these sequences in the hip. The thin cartilage in the hip and the spherical cartilage surfaces limits the diagnostic performance of cartilage-sensitive sequences in the hip [40]. The thickness of the femoral articular cartilage has been measured at 1.14 mm (laterally) and 2.84 mm (centrally) [41]. It is not difficult to understand why thin-section images are necessary to reliably detect cartilage lesions. Blankenbaker et al. compared a 3D iterative decomposition of water and fat with echo asymmetry and least-squares estimation (IDEAL)-spoiled gradient-recalled echo (SPGR) sequence (TR/TE 11.4/5.3 ms; flip angle 14°; 1 mm thickness, no gap) acquired during MRA to a standard 2D T1-weighted fat-suppressed sequences (4 mm thickness with 0.4 mm intersection gap). The thin-section IDEAL-SPGR sequence had significantly higher accuracy than standard 2D sequences for assigning precise grades to cartilage lesions likely by reducing partial volume artifact [42]. Similar studies with 3D FSE sequences in the hip, however, have yet to be performed. 3D-SPACE (Sampling Perfection with Application-optimized Contrast using different flip-angle Evolutions) is a non-gradient echo 3D technique, which accelerates 3D turbo-spin techniques and can be combined with water excitation to produce high-resolution proton-density-weighted images (Fig. 10.17). A possible limiting factor with 3D FSE sequences is the loss of SNR compared to 2D sequences [37]. This is not true of all 3D FSE sequences. Gold et al. demonstrated that a 3D XETA (eXtended Echo-Train Acquisition) sequence with half-Fourier acquisition and ARC parallel imaging provided isotropic data with higher SNR for both cartilage and muscle in the knee compared to both 2D FRFSE and 2D FSE sequences, though fluid signal was lower for the 3D sequence [38]. Further investigation into 3D FSE sequences in the hip is necessary in order for these sequences to become routinely employed in hip imaging. Many practices still perform 2D FSE sequences in the hip for cartilage assessment

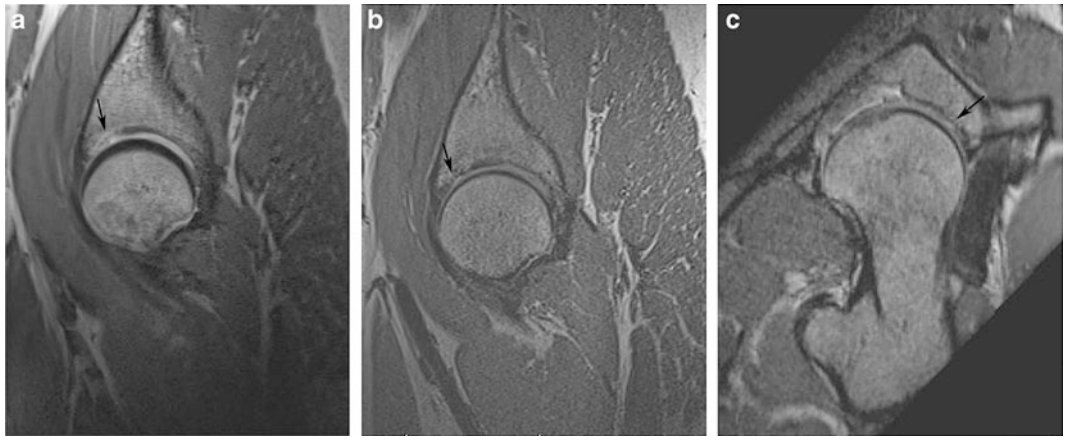

Fig. 10.17 Sagittal images of the left hip performed on a 3 T magnet in a 24-year-old woman using a small surface coil (same patient as in Fig. 10.14). (**a**) IM-FSE sequence acquired at 2.5 mm slice thickness (no gap) demonstrated acetabular cartilage damage in the anterosuperior joint (*black arrow*). (**b**) 3D SPACE sequence (TR 1,100, TE 36, ETL 40) with 0.74 mm slice thickness demonstrated same area (*black arrow*) but with relatively decreased SNR compared to the 2D acquisition. (**c**) Radially reformatted images created from the SPACE sequence reveals the same area of cartilage damage (*black arrow*)

and utilize a 3D GR sequence for volumetric thin-section imaging. The relatively long imaging times of 3D FSE sequences have made them rather impractical to perform routinely on 1.5 T scanners, particularly if the quality of the reformats is not superior to the 2D FSE images. As higher field strength magnets become more widespread and 3D FSE sequences continue to improve, these sequences may soon become standard in many hip protocols.

Quantitative Imaging Sequences

In addition to morphologic imaging of cartilage, quantitative imaging sequences are also increasingly useful. These techniques include T2 [43–45] and T2* mapping [46], T1 rho [47, 48], and delayed gadolinium-enhanced MRI of cartilage (dGEMRIC) [49]. Of these techniques, dGEMRIC and T2 mapping are the more commonly used biomechanical cartilage mapping sequences. T2 mapping detects zonal variations in cartilage based upon the interactions between water and collagen molecules in the cartilage matrix. T2 mapping does not require intravenous contrast administration and requires relatively short scan times (~6 min) [29]. dGEMRIC relies on the proteoglycan content of the cartilage to serve as an indicator of overall cartilage health. Early on in the development of osteoarthritis, there is a loss of negatively charged glycosaminoglycan (GAG) molecules in the cartilage without necessarily a reduction in the overall cartilage thickness (i.e., morphologic sequences will not be able to detect the cartilage damage at this early stage). dGEMRIC examinations require an intravenous injection of negatively charged contrast agent which, over time, will disperse into cartilage at a rate inversely related to the GAG content of the cartilage. In order for dGEMRIC to be an effective imaging technique, a sufficient dose of contrast is required (at our institution patients receive 0.4 mL/kg of gadopentetate meglumine, Magnevist; Berlex Laboratories, Wayne, NJ, USA). Patients are then asked to exercise (walk) for 15–20 min prior to imaging. The imaging examination begins 30–45 min after injection with mapping sequences occurring later in the sequence protocol such that 1 h has elapsed between injection and mapping. The potential use of dGEMRIC for assessment of early osteoarthritis in patients with DDH was demonstrated by Kim et al. [49]. T1 values of cartilage after intravenous gadolinium administration ($T1_{Gd}$) decreased as the grade of dysplasia increased,

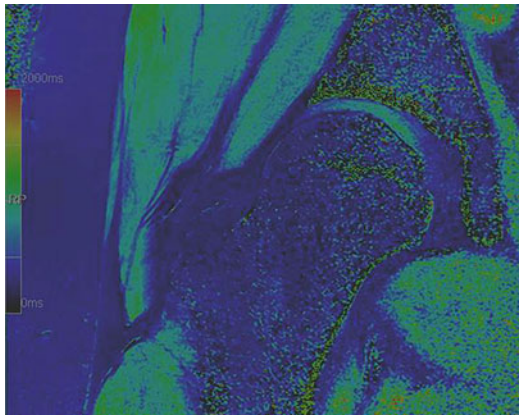

Fig. 10.18 Coronal T1 map from a dGEMRIC examination of the right hip in a 17-year-old male with clinical symptoms and exam consistent with FAI. The color scale on the left hand side of the image indicates the T1 values that correspond to the color map overlying the femoral head and acetabular cartilage

decreasing from 550 ms (mild DDH) to 500 ms (moderate DDH) to 420 (severe DDH). ($T1_{Gd}$) values in normal volunteers, in contrast, were approximately 570 ms [49]. This laid the foundation for the clinical use of dGEMRIC for identifying patients with DDH who may be poor candidates for a pelvic redirecting osteotomy [24]. More recently, dGEMRIC has been shown to be useful in revealing patterns of zonal T1 variation in cartilage in patients with different subgroups of FAI [50, 51] (Fig. 10.18). Quantitative cartilage imaging will be discussed in greater detail in a separate chapter.

MR Arthrography

MRA of the hip is a well-described technique [52–54] for detection and evaluation of labral tears and other intra-articular pathology. MRA involves direct injection of a dilute gadolinium solution (0.2 mmol/L of Magnevist; Berlex Laboratories, Wayne, NJ, USA) into the hip joint, usually under fluoroscopic guidance. A small amount of iodinated contrast material is included within the gadolinium solution to confirm position within the joint. The volume of contrast administered into the joint varies between 8 and 20 mL depending on patient size and tolerance [53]. Dedicated imaging of the injected hip is performed immediately after injection when the joint is maximally distended. Imaging sequences consist of either T1-weighted or PD-weighted images with fat suppression. Imaging planes vary by institution but usually include sequences in the coronal, axial, and sagittal planes. The sagittal images are often oblique along the axis of the femoral neck to better visualize the anterosuperior labrum, or an additional sagittal oblique sequence is performed. The sagittal (or axial) oblique plane has the highest individual rate of detecting labral tears compared to any other individual sequence [55] based on the obliquity of the labrum in the anterosuperior sector, where most tears occur (Fig. 10.19). Some centers include radial images, which rotate around the acetabulum [56, 57]. Radial imaging is ideally suited for imaging the acetabular labrum given the complicated, spherical shape of the acetabulum. Radial imaging allows for sections to be oriented perpendicular to the labrum in all planes. At least one T2-weighted sequence with fat suppression through the hip is also performed as part of an MRA protocol to evaluate for bone marrow edema.

The most common indication for MRA of the hip is labral tear. Overall, MRA is superior to conventional non-contrast MRI for detecting acetabular labral tears in adults [58]. The acetabular labrum consists of fibrocartilage and most commonly appears as a triangular-shaped, low-signal structure along the rim of the acetabulum from anteriorly to posteroinferiorly and which blends with the transverse ligament inferiorly. There are variants in labral shape with some labra appearing round, irregular, or even absent, with the round and irregular labral shapes increasing with age [57]. Tears in the labrum occur either within the substance of the labrum or as a detachment from the acetabular rim, and may be secondary to trauma, dysplasia, or degeneration [42]. Paralabral cysts are associated with labral tear or degeneration [59, 60] and may fill with contrast at MRA. Please refer to separate chapter on MRA for more discussion on this technique.

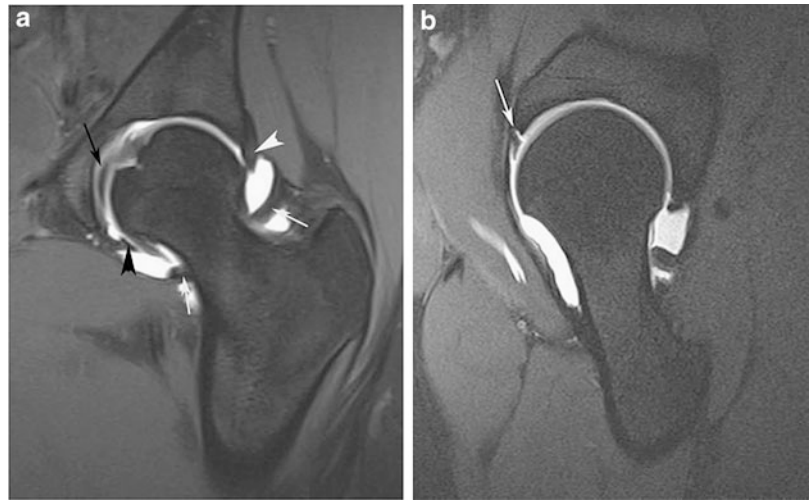

Fig. 10.19 Images from an MR arthrogram of the left hip in a 19-year-old gymnast with hip pain performed on a 3 T magnet. (**a**) Coronal T1-weighted image with fat suppression demonstrates the normal anatomy of the hip: ligamentum teres (*black arrow*), zona orbicularis (*white arrows*), acetabular labrum (*white arrowhead*), and transverse ligament (*black arrowhead*). (**b**) Sagittal oblique T1-weighted image with fat suppression through the left hip demonstrates a tear at the chondrolabral junction (*arrow*)

Diffusion-Weighted Imaging

Diffusion-weighted imaging (DWI) and apparent diffusion coefficient (ADC) measurements may detect ischemia within the femoral head in patients developing AVN. Piglet models of AVN have demonstrated reduced blood flow and restricted diffusion in the hips, suggesting this technique may be applicable to patients [61, 62]. Preliminary studies on a pediatric population of patients with LCP disease suggest that DWI may be helpful in differentiating favorable and unfavorable outcomes [63]. More recent studies show that ADC measurements may detect AVN in patients with SCD [64]. With continued investigation in this potentially valuable technique, DWI may have clinical utility in routine evaluation of patients at risk for AVN of the hip, including patients with SCD and DDH s/p reduction. DWI may also be useful in evaluating soft tissue masses around the hip joint. Although there is an overlap in the ADC values of benign and malignant soft tissue tumors, the change in ADC values of malignant tumors after therapy may be helpful in evaluating therapy response [65] (Fig. 10.20). Further investigation in this area is ongoing.

Conclusion

MRI scanners, coils, and sequences have become remarkably sophisticated over the past several decades. Morphologic imaging with spin-echo and gradient echo sequences has become faster and image quality has continued to improve. It is now considered routine to acquire submillimeter images through the joint in less than 10 min. Imaging parameters have been adjusted to allow for optimal evaluation of bone and soft tissue structure, often in the same sequence. Both fat and water signals may be suppressed to further increase contrast between anatomic structures. Quantitative imaging allows for biochemical assessment of cartilage integrity before morphologic changes are detectable. DWI and ADC mapping may become a valuable technique in evaluation of femoral head ischemia, as well as to follow treatment response in patients with soft tissue tumors. The indications for imaging will continue to increase as additional technology is developed and improved. With a basic understanding of imaging techniques, it is possible to develop and utilize imaging protocols for specific indications while acquiring fundamental morphologic, high-resolution imaging of the joint (Table 10.1).

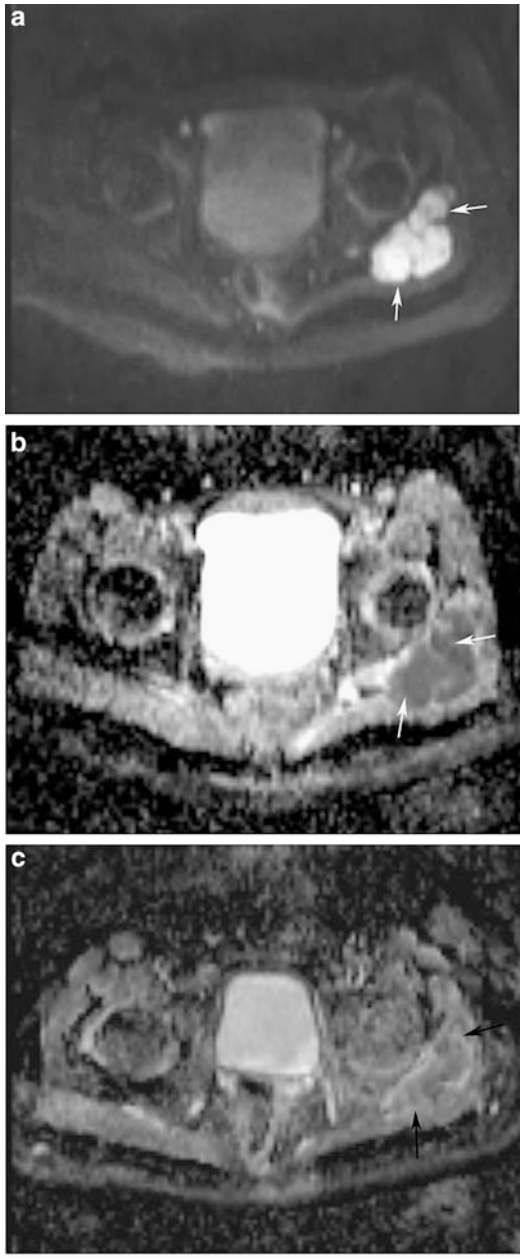

Fig. 10.20 Axial DWI (**a**) and corresponding ADC map (**b**) in a 9-year-old boy with confirmed synovial sarcoma of the gluteal muscles (same patient as in Fig. 10.10) revealed restricted diffusion in the lesion as evidenced by bright signal on the DWI images and corresponding low ADC values (*white arrows*). ADC map after three rounds of chemotherapy (**c**) demonstrates decreased size of the lesion (*arrows*) and slight increase in the ADC values

Table 10.1 Sample hip MRI protocols

Sequence	Plane
Protocol 1: acute hip pain (trauma)	
Field strength: 1.5 T or 3.0 T	
Coil: small surface coil	
FOV: single hip (and surrounding muscles)	
T1	Coronal
FSEIR	Coronal
T2-FSE fs	Axial
PD-FSE fs	Sagittal
T1 fs (*opt*) (*hematoma*)	Axial
Protocol 2: inflammatory arthropathy (hips/sacroiliac joints)	
Field strength: 1.5 T or 3.0 T	
Coil: body/torso/cardiac coil	
FOV: both hips and pelvis	
T1	Coronal
FSEIR	Coronal
T2-FSE fs	Axial
FSEIR	Coronal oblique (*sacroiliac joints*)
PD-FSE fs	Sagittal
C+ T1 with fs	Axial
	Coronal
Protocol 3: avascular necrosis	
Field strength: 1.5 T or 3.0 T	
Coil: body/torso/cardiac coil	
FOV: both hips and pelvis	
T1	Coronal
T2-FSE fs	Coronal
T2-FSE fs	Axial
PD-FSE fs	Sagittal
DWI/ADC	Axial
Dynamic C+	Axial
LAVA/VIBE fs	
C+ T1 fs	Coronal
Protocol 4: labral tear (MR arthrogram)	
Field strength: 3.0 T preferred	
Coil: small surface coil	
FOV: single hip	
T1/PD fs	Coronal
	Sagittal
	Oblique sagittal
T2-FSE fs	Coronal
3D SPGR/bSSFP/DESS	Sagittal
	Radial reformat (*femoral neck*)
PD fs	Radial (acetabulum)

(continued)

Table 10.1 (continued)

Sequence	Plane
Protocol 5: femoroacetabular impingement (FAI)/ developmental dysplasia of the hip (DDH)	
Field strength: 3.0 T preferred	
Coil: small surface coil and body coil	
FOV: (1) Single hip, small FOV (small surface coil)	
(2) Pelvis, femoral condyles (body coil)	
T1	Coronal—*both hips*
GRE (T1-weighted)	Axial—*femoral condyles*
For femoral version	Axial—*both hips* (*remaining sequences single hip only*)
IM*-FSE fs	Coronal
IM*-FSE fs	Sagittal
T2-FSE fs	Axial/coronal
PD-FSE fs	Sagittal
3D SPGR or bSSFP fs vs. 3D PD-weighted FSE (e.g., SPACE/ CUBE)	Sagittal
	Axial reformat
	Axial oblique reformat
	Radial reformat (femoral neck)
Optional: *T2/T2*/T1rho mapping versus dGEMRIC*	*Varies by institution*

Please note:
fs fat suppression (chemical suppression, though other techniques may be substituted), *PD* proton-density-weighted, *IM* intermediate-weighted, *C+* intravenous contrast-enhanced

References

1. Frayne R, Goodyear BG, Dickhoff P, Lauzon ML, Sevick RL. Magnetic resonance imaging at 3.0 Tesla: challenges and advantages in clinical neurologic imaging. Invest Radiol. 2003;38:385–402.
2. MacKenzie JD, Vasanawala SS. State-of-the-art in pediatric body and musculoskeletal magnetic resonance imaging. Semin Ultrasound CT MR. 2010;31:86–99.
3. Chavhan GB, Babyn PS, Singh M, Vidarsson L, Shroff M. MR imaging at 3.0T in children: technical differences, safety issues, and initial experience. Radiographics. 2009;29:1451–66.
4. Gold GE, Han E, Stainsby J, Wright G, Brittain J, Beaulieu C. Musculoskeletal MRI at 3.0T: relaxation times and image contrast. Am J Roentgenol. 2004;183:343–51.
5. Schindera ST, Merkle EM, Dale BM, Delong DM, Nelson RC. Abdominal magnetic resonance imaging at 3.0T: what is the ultimate gain in signal-to-noise ratio? Acad Radiol. 2006;13:1236–43.
6. Gold GE, Suh B, Sawyer-Flover A, Beaulieu C. Musculoskeletal MRI at 3.0 T: initial clinical experience. Am J Roentgenol. 2004;183(5):1479–86.
7. Rubin DA, Kneeland JB. MR imaging of the musculoskeletal system: technical considerations for enhancing image quality and diagnostic yield. Am J Roentgenol. 1994;163:1155–63.
8. Peh WC, Chan JH. Artifacts in musculoskeletal magnetic resonance imaging: identification and correction. Skeletal Radiol. 2001;30:179–91.
9. Link TM. MR imaging in osteoarthritis: hardware, coils, and sequences. Radiol Clin North Am. 2009;47(4):617–32.
10. Nishii T, Kuroda K, Matsuoka Y, Sahara T, Yoshikawa H. Change in knee cartilage T2 in response to mechanical loading. J Magn Reson Imaging. 2008;28:175–80.
11. Gabriel H, Fitzgerald SW, Myers MT, Donaldson JS, Poznanski AK. MR imaging of hip disorders. Radiographics. 1994;14:763–81.
12. Potter HG, Schachar J. High resolution noncontrast MRI of the hip. J Magn Reson Imaging. 2010;31:268–78.
13. Murray RO. The aetiology of primary osteoarthritis of the hip. Br J Radiol. 1965;38(455):810–24.
14. Nicholls AS, Kiran A, Pollard TC, et al. The association between hip morphology parameters and nineteen-year risk of end-stage osteoarthritis of the hip: a nested case-control study. Arthritis Rheum. 2011;63(11):3392–400.
15. Pollard TC, Villar RN, Norton MR, et al. Genetic influences in the aetiology of femoroacetabular impingement: a sibling study. J Bone Joint Surg Br. 2010;92:209–16.
16. Felson DT. Risk factors for osteoarthritis: understanding joint vulnerability. Clin Orthop Relat Res. 2004; (427 Suppl):S16–21.
17. Mettler FA Jr, Guiberteau MJ. Skeletal system. In: Essentials of nuclear medicine. 5th ed. Philadelphia, PA: Saunders; 2006. pp. 243–244.
18. Andrews CL. From the RSNA refresher course. Radiological society of North America. Evaluation of the marrow space in the adult hip. Radiographics. 2000;20:S27–42.
19. Meyers SP, Wiender SN. Magnetic resonance imaging features of fractures using the short tau inversion recovery (STIR) sequence: correlation with radiographic findings. Skeletal Radiol. 1991;20:499–507.
20. Sebag G, Ducou Le Pointe H, Klein I, et al. Dynamic gadolinium-enhanced subtraction MR imaging—a simple technique for the early diagnosis of Legg-Calve-Perthes disease: preliminary results. Pediatr Radiol. 1997;27:216–20.

21. Kim EY, Kwack KS, Cho JH, Lee DH, Yoon SH. Usefulness of dynamic contrast-enhanced MRI in differentiating between septic arthritis and transient synovitis in the hip joint. Am J Roentgenol. 2012;198:428–33.
22. Gold GE, Chen CA, Koo S, Hargreaves BA, Bangerter NK. Recent advances in MRI of articular cartilage. Am J Roentgenol. 2009;193:628–38.
23. Stelzeneder D, Mamisch TC, Kress I, et al. Patterns of joint damage seen on MRI in early hip osteoarthritis due to structural hip deformities. Osteoarthritis Cartilage. 2012;20(7):661–9.
24. Cunningham T, Jessel R, Zurakowski D, Millis MB, Kim YJ. Delayed gadolinium-enhanced magnetic resonance imaging of cartilage to predict early failure of Bernese periacetabular osteotomy for hip dysplasia. J Bone Joint Surg Am. 2006;88(7):1540–8.
25. Philippon MJ, Stubbs AJ, Schenker ML, Mazwell RB, Ganz R, Leunig M. Arthroscopic management of femoroacetabular impingement: osteoplasty technique and literature review. Am J Sports Med. 2007;35:1571–80.
26. Eckstein F, Charles HC, Buck RJ, et al. Accuracy and precision of quantitative assessment of cartilage morphology by magnetic resonance imaging at 3.0T. Arthritis Rheum. 2005;52:3132–6.
27. Mintz DN, Hooper T, Connell D, Buly R, Padgett DE, Potter HG. Magnetic resonance imaging of the hip: detection of labral and chondral abnormalities using noncontrast imaging. Arthroscopy. 2005;21:385–93.
28. Nishii T, Nakanishi K, Sugano N, Masuhara K, Ohzono K, Ochi T. Articular cartilage evaluation in osteoarthritis if the hip with MR imaging under continuous leg traction. Magn Reson Imaging. 1998;16:871–5.
29. Jazrawi LM, Alaia MJ, Chang G, FitzGerald EF, Recht MP. Advances in magnetic resonance imaging of articular cartilage. J Am Acad Orthop Surg. 2011;19:420–9.
30. Potter HG, Linklater JM, Allen AA, Hannafin JA, Haas SB. Magnetic resonance imaging of articular cartilage in the knee: an evaluation with use of fast spin-echo imaging. J Bone Joint Surg Am. 1998;80:1276–84.
31. Schmid MR, Pfirrmann CW, Koch P, Zanetti M, Kuehn B, Hodler J. Imaging of patellar cartilage with a 2D multiple-echo data image combination sequence. Am J Roentgenol. 2005;184:1744–8.
32. Bauer JS, Barr C, Henning TD, et al. Magnetic resonance imaging of the ankle at 3.0 Tesla and 1.5 Tesla in human cadaver specimens with artificially created lesions of cartilage and ligaments. Invest Radiol. 2008;43:604–11.
33. Hardy PA, Recht MP, Piraino D, Thomasson D. Optimization of a dual echo in the steady state (DESS) free-precession sequence for imaging cartilage. J Magn Reson Imaging. 1996;6:329–35.
34. Rheum S, Zanetti M, Romero J, Hodler J. MRI of patellar articular cartilage: evaluation of an optimized gradient-echo sequence (3D-DESS). J Magn Reson Imaging. 1998;8:1246–51.
35. Friedrich KM, Reiter G, Kaiser B, et al. High-resolution cartilage imaging of the knee at 3T: basic evaluation of modern isotropic 3D MR-sequences. Eur J Radiol. 2011;78:398–405.
36. Rubenstein JD, Li JG, Majumdar S, Henkelman RM. Image resolution and signal-to-noise ratio requirements for MR imaging of degenerative cartilage. Am J Roentgenol. 1997;169:1089–96.
37. Ristow O, Steinbach L, Sabo G, et al. Isotropic 3D fast spin-echo imaging versus standard 2D imaging at 3.0T of the knee-image quality and diagnostic performance. Eur Radiol. 2009;19:1263–72.
38. Gold GE, Busse RF, Beehler C, et al. Isotropic MRI of the knee with 3D fast spin-echo extended echo-train acquisition (XETA): initial experience. Am J Roentgenol. 2007;188:1287–93.
39. Stevens KJ, Busse RF, Han E, et al. Ankle: isotropic MR imaging with 3D-FSE-cube- initial experience in healthy volunteers. Radiology. 2008;249:1026–33.
40. Kijowski R, Gold GE. Routine 3D magnetic resonance imaging of joints. J Magn Reson Imaging. 2011;33:758–71.
41. Nakanishi K, Tanaka H, Sugano N, et al. MR-based three-dimensional presentation of cartilage thickness in the femoral head. Eur Radiol. 2001;11:2178–83.
42. Blankenbaker DG, Ullrick SR, Kijowski R, et al. MR arthrography of the hip: comparison of IDEAL-SPGR volume sequence to standard MR sequences in the detection and grading of cartilage lesions. Radiology. 2011;261:863–71.
43. Gold SL, Burge AJ, Potter HG. MRI of hip cartilage: joint morphology, structure, and composition. Clin Orthop Relat Res. 2012;470:3321–31.
44. Mosher TJ, Smith HE, Collins C, et al. Change in knee cartilage T2 at MR imaging after running: a feasibility study. Radiology. 2004;234:245–9.
45. Liess C, Lüsse S, Karger N, Heller M, Glüer CC. Detection of changes in cartilage water content using MRI T2-mapping in vivo. Osteoarthritis Cartilage. 2002;10:907–13.
46. Bittersohl B, Miese FR, Hosalker HS, et al. T2* mapping of hip joint cartilage in various histological grades of degeneration. Osteoarthritis Cartilage. 2012;20:653–60.
47. Wheaton AJ, Dodge GR, Elliott DM, Nicoll SB, Reddy R. Quantification of cartilage biomechanical and biochemical properties via T1rho magnetic resonance imaging. Magn Reson Med. 2005;54 (5):1087–93.
48. Regatte RR, Akella SV, Lonner JH, Kneeland JB, Reddy R. T1rho relaxation mapping in human osteoarthritis (OA) cartilage: comparison of T1rho with T2. J Magn Reson Imaging. 2006;23(4):547–53.
49. Kim YJ, Jaramillo D, Millis MB, Gray ML, Burstein D. Assessment of early osteoarthritis in hip dysplasia with delayed gadolinium enhanced magnetic resonance imaging of cartilage. J Bone Joint Surg Am. 2003;85:1987–92.
50. Bittersohl B, Steppacher S, Haamberg T, et al. Cartilage damage in femoroacetabular impingement (FAI): preliminary results on comparison of standard

diagnostic vs delayed gadolinium-enhanced magnetic resonance imaging of cartilage (dGEMRIC). Osteoarthritis Cartilage. 2009;17:1297–306.
51. Mamisch TC, Kain MS, Bittersohl B, et al. Delayed gadolinium-enhanced magnetic resonance imaging of cartilage (dGEMRIC) in femoroacetabular impingement. J Orthop Res. 2011;29:1305–11.
52. Petersilge CA. Current concepts of MR arthrography of the hip. Semin Ultrasound CT MR. 1997;18:291–301.
53. Petersilge CA, Haque MA, Petersilge WJ, Lewin JS, Lieberman JM, Buly R. Acetabular labral tears: evaluation with MR arthrography. Radiology. 1996;200:231–5.
54. Czerny C, Hofmann S, Neuhold A, et al. Lesions of the acetabular labrum.: accuracy of MR imaging and MR arthrography in detection and staging. Radiology. 1996;200:225–30.
55. Ziegert AJ, Blankenbaker DG, De Smet AA, Keene JS, Shinki K, Fine JP. Comparison of standard hip MR arthrographic imaging planes and sequences for detection of arthroscopically proven labral tear. Am J Roentgenol. 2009;192:1397–400.
56. Kubo T, Horii M, Yamaguchi J, et al. Radial magnetic resonance imaging and pathological findings of acetabular labrum in dysplastic hips. Pathophysiology. 2000;7(3):171–5.
57. Abe I, Harada Y, Oinuma K, et al. Acetabular labrum: abnormal findings at MR imaging in asymptomatic hips. Radiology. 2000;216:576–81.
58. Smith TO, Hilton G, Toms AP, Donell ST, Hing CB. The diagnostic accuracy of acetabular labral tears using magnetic resonance imaging and magnetic resonance arthrography: a meta-analysis. Eur Radiol. 2011;21:863–74.
59. Schnarkowski P, Steinbach LS, Tirman PFJ, Peterfy CG, Genant HK. Magnetic resonance imaging of labral cysts of the hip. Skeletal Radiol. 1996;25:733–7.
60. Magee T, Hinson G. Association of paralabral cysts with acetabular disorders. Am J Roentgenol. 2000;174:1381–4.
61. Menezes NM, Connolly SA, Shapiro F, et al. Early ischemia in growing piglet skeleton: MR diffusion and perfusion imaging. Radiology. 2007;242:129–36.
62. Jaramillo D, Connolly SA, Vajapeyam S, et al. Normal and ischemic epiphysis of the femur: diffusion MR imaging study in piglets. Radiology. 2003;227:825–32.
63. Merlini L, Combescure C, De Rosa V, Anooshiravani M, Hanquinet S. Diffusion-weighted imaging findings in Perthes disease with dynamic gadolinium-enhanced subtraceted (DGS) MR correlation: a preliminary study. Pediatr Radiol. 2010;40:318–25.
64. MacKenzie JD, Hernandez A, Pena A, et al. Magnetic resonance imaging in children with sickle cell disease-detecting alterations in the apparent diffusion coefficient in hips with avascular necrosis. Pediatr Radiol. 2012;42:706–13.
65. Einarsdottir H, Karlsson M, Wejde J, Bauer HC. Diffusion-weighted MRI of soft tissue tumors. Eur Radiol. 2004;14(6):959–63.

Labral Disease

11

Bernd Bittersohl and Christoph Zilkens

Introduction

The acetabular labrum is a continuous, usually triangular fibrocartilaginous structure outlining the rim of the acetabulum from anterior to superior and posterior [1]. Inferiorly, at the margins of the acetabular notch, it merges imperceptibly with the transverse ligament (Fig. 11.1). The labrum merges into the acetabular cartilage through a 1–2 mm transition zone. Further attachment zones are the bony rim of the acetabulum (non-articular side) and a zone of calcified subarticular cartilage [1].

The labrum provides stability against femoral head translation by increasing the depth of the acetabulum [2]. It also provides a seal, which aids in keeping synovial fluid in the intra-articular space, thus facilitating joint lubrication and load distribution [3, 4]. The hydrostatic fluid pressure within the intra-articular space enhances joint stability, whereas disruption of the fluid seal can make the joint unstable.

Lesions of the labrum typically present with groin pain and mechanical symptoms such as clicking or locking, although atypical symptoms for labral lesions are not uncommon [5]. Notably, labrum pathology is associated with early osteoarthritis (OA) of the hip joint, whereas disorders of the labrum have been reported to potentially precede articular cartilage damage [6, 7]. Therefore, early diagnosis and reliable determination of the location and severity of labrum pathology are important to allow for a timely surgical intervention, and thus obviate the risk for the development of advanced osteoarthritic damage. Furthermore, exclusion of differential diagnoses or recognition of potential etiologies such as trauma, femoroacetabular impingement (FAI) (Fig. 11.2), Legg Calvé Perthes disease, hip dysplasia, and degeneration is a clinical necessity [5].

Magnetic resonance imaging (MRI) and MR arthrography (MRA), with their superior soft tissue contrast and capability of multiplanar imaging, are the modalities of choice in noninvasively visualizing the hip joint. Nevertheless, the acetabular labrum may be difficult to image due to its small size, curved orientation, variable morphological appearance, redundancy of the joint capsule when not distended, and several technical limitations such as volume averaging and a decrease in signal intensity owing to the relatively large distance between the labrum and the coil.

This chapter reviews the technical aspects of MRI and MRA in the evaluation of labrum pathology. Approved imaging protocols at 1.5 and 3 T, including two-dimensional (2D) and three-dimensional (3D) sequences, are provided. It also illustrates the radiological appearance of commonly encountered conditions and seeks to raise awareness of potential pitfalls.

B. Bittersohl (✉)
Department of Orthopedics, Heinrich-Heine University Medical School, Düsseldorf, Moorenstr. 5, 40225 Düsseldorf, Germany
e-mail: bernd.bittersohl@med.uni-duesseldorf.de; bbittersohl@partners.org

Y.-J. Kim (eds.), *Hip Magnetic Resonance Imaging*,
DOI 10.1007/978-1-4614-1668-5_11,

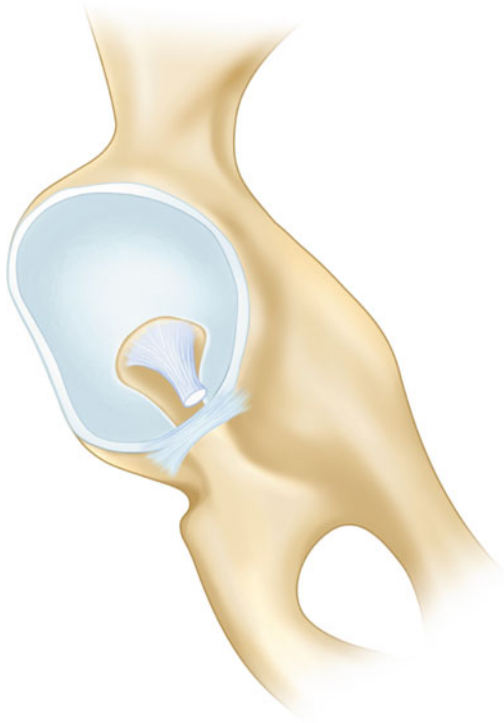

Fig. 11.1 The acetabular labrum outlines the rim of the acetabulum from anterior to superior and posterior. Inferiorly, at the margins of the acetabular notch, it merges imperceptibly with the transverse ligament

Fig. 11.2 PD-weighted radial MR arthrogram depicting a detached labrum and cartilage signal changes at the anterior-superior aspect of the hip joint of a symptomatic cam-FAI patient. Note the non-spherical shape of the femoral head along with insufficient femoral head–neck offset that causes mechanical impaction involving the proximal femur and acetabular rim, inducing labral failure and varying degrees of cartilage damage

Technique

Non-contrast Magnetic Resonance Imaging Versus Magnetic Resonance Arthrography

Numerous studies seeking the most appropriate method for imaging the hip joint and labrum have been performed. While most studies have revealed superior diagnostic accuracy for acetabular tears when using MRA (sensitivity values ranging from 66 % [8] to 100 % [9]), current reports also indicate high diagnostic accuracy without the instillation of contrast medium by using high-resolution, proton-density (PD)-weighted MRI (reported sensitivity values of 94 % [10] to 100 % [11]).

A recent meta-analysis indicated that both non-contrast MRI and MRA provide acceptable accuracy in evaluating the acetabular labrum [12]. However, in particular at 1.5 T, the sensitivity of MRA in detecting acetabular labral tears was to some extent greater when compared to conventional MRI, although considerable variations and/or limitations in methodology (i.e., inapplicable sequence setting when performing non-contrast MRI) have to be taken into account.

There are advantages and disadvantages with both non-contrast MRI and MRA. The intra-articular application of contrast medium in MRA facilitates the detection of labrum pathology by distending the hip capsule off the labrum, outlining the labrum with contrast, and by filling any clefts that are associated with labral tears and labrum detachment. Thereby, even distinct fissures within the labrum surface and at the transitional zone between the labrum and

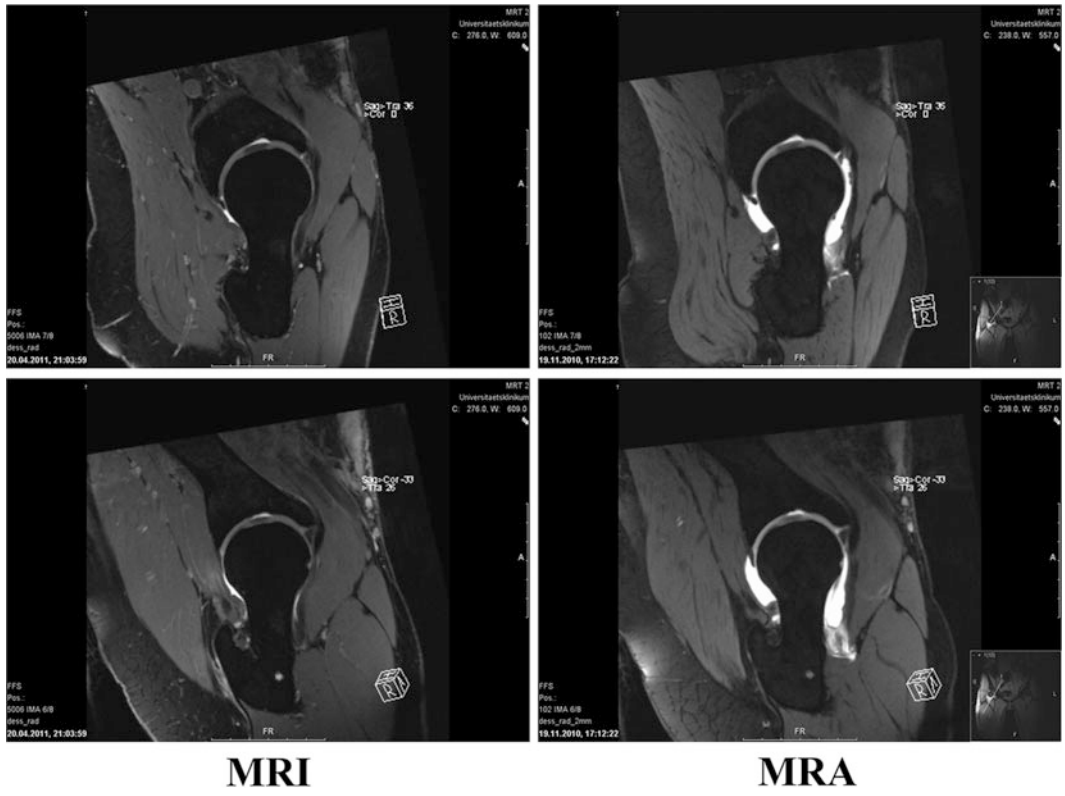

Fig. 11.3 Corresponding 3D DESS MRI (*left*) and MRA (*right*) reformat revealing minor, yet important, differences between both MR imaging techniques. The intra-articular application of contrast medium in MRA facilitates the detection of labrum pathology by distending the hip capsule off the labrum, outlining the labrum with contrast, and by filling any clefts that are associated with labral tears and labrum detachment. Thereby, fissures within the labrum surface and at the transitional zone between labrum and cartilage or subchondral bone may be better identified than with MRI

cartilage or subchondral bone can be identified (Fig. 11.3). The intra-articular technique, on the other hand, is certainly more invasive and uncomfortable for the patient, needs a more stringent sterile environment, and poses, although extremely rare, the risk of joint infection that could turn out to be disastrous. The non-contrast approach may be less sensitive for subtle labral surface changes but it is noninvasive and no extra time and expenses are required to process its application. Of note, the sensitivity in detecting intra-labral changes, which have no connection to the labrum surface, is similar for both non-contrast MRI and MRA (Fig. 11.4).

Indirect MRA after intravenous contrast medium application has been reported to be an effective means of hip evaluation for labral tears [13]. The motivation to perform indirect MRA is that it provides superior contrast resolution relative to non-contrast MRI, but it is less invasive compared to direct MRA. Furthermore, it does not require fluoroscopy or a physician to perform the injection, it is easy to schedule, and is able to depict synovitis and extra-articular enhancement.

Nevertheless, labrum evaluations based on indirect MRA (enhancement of joint fluid with intravenously administered contrast medium) [14] compare poorly with direct MRA due to

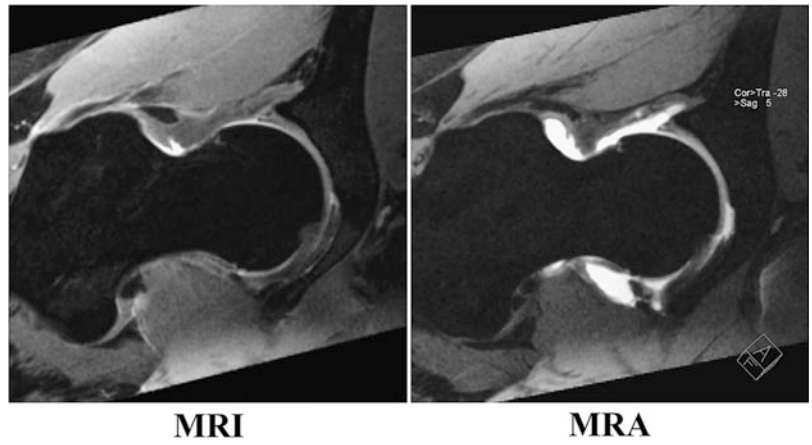

Fig. 11.4 Corresponding 3D DESS MRI (*left*) and MRA (*right*) reformat revealing no differences between both MR imaging techniques in detecting intra-labral changes, which have no connection to the labrum surface

lack of capsular distension which can help delineate intra-articular structure such as labrum. Furthermore, indirect MRA includes a higher contrast load compared to direct MRA and necessitates at least 15 min of exercise prior to MR imaging for contrast medium uptake, causing relevant lengthening of the total scan time.

The role of 3 T MRI or 3 T MRA on the hip joint and acetabular labrum imaging is still being investigated. However, primary studies and our own data suggest that the evaluation of the acetabular labrum and cartilage will be notably improved owing to the increased signal to noise ratio (SNR) and contrast to noise ratio (CNR) [15]. Notably, Sundberg et al. reported that all surgically confirmed labral tears diagnosed by 1.5 T MRA were detected on 3 T MRI, whereas 3 T MRI also detected an additional confirmed labral tear that was missed on MRA [16]. Furthermore, 3 T MRI was superior to 1.5 T MRA in differentiating chondral lesions. Both techniques (1.5 T MRA and 3 T MRI) were superior to 1.5 T MRI.

Imaging Protocol

MRA, if indicated, consists of two steps. First, using a 20-gauge spinal needle, 10–20 mL of a 2 mM solution of Gd-DTPA^{2-} (1.88 mg/mL, Magnevist, Schering AG, Berlin, Germany) diluted in sterile saline is injected into the hip joint by an experienced radiologist or an orthopedic surgeon under fluoroscopic guidance and strict sterile precautions. Alternatively, 10–20 mL of a 2 mM solution of Gd-DOTA^{-} (1.88 mg/mL, Artirem, Bayer AG, Leverkusen, Germany) may be used. Iodinated contrast material is utilized to document the intra-articular position of the needle. Subsequently, the patient is transferred to the MR scanner. No exercise is performed after intra-articular contrast medium application in order to avoid discharge of the contrast medium from the hip joint.

Bilateral hip examination combined with a large field of view (FOV) may be a good screening instrument for hip and pelvic abnormalities. However, it is not useful for diagnosing labral tears and cartilage damage given the small size and narrowness of these structures. Therefore, in cases where pathology is expected to be unilateral (such as a labral tear), unilateral hip imaging should be performed and a smaller FOV should be utilized by employing a dedicated surface coil (i.e., a flexible four-channel flex coil) to keep the SNR and CNR acceptable while increasing the spatial resolution.

The subject is examined in the supine position with the pelvis at the isocenter of the magnet and the coil accurately placed on top of the hip joint to be scanned. MRI and MRA protocols that have been successfully implemented for the diagnosis

Fig. 11.5 2D PD-weighted radial image depicting a partial labral tear at the transition zone between the fibrocartilaginous labrum and the articular hyaline cartilage. This type of tear is frequently perpendicular to the articular surface and, in some cases, extends to the subchondral bone. Note the saturation effect, appearing as a band of low signal in the center of acetabulum and femoral neck, which are constantly present in 2D radial MR imaging. As saturation does not involve the relevant capsular–labrum–cartilage complex, diagnostic imaging of the labrum and cartilage will be unaffected

Fig. 11.6 PD-weighted sagittal MRA image visualizing a partial labral tear at the base of the labrum at the anterior aspect of the hip joint

of hip anomalies and joint damage [17, 18] include (1) an axial 2D turbo spin echo (TSE) sequence with T1-weighting to evaluate the femoral head–neck offset, joint capsule, and peri-articular soft tissues; (2) a high-resolution, thin-sectioned axial 2D fast low angle shot (FLASH) sequence with T1-weighting for acetabular version assessment; (3) a coronal 2D TSE sequence with PD-weighting; (4) a sagittal 2D TSE sequence with PD-weighting; and (5) a radial 2D TSE sequence with PD-weighting that is planned around the femoral neck perpendicular to the acetabular rim. Fat suppression may be used in order to reduce the chemical shift and improve the visualization of contrast material uptake.

The radial sequence is created on two planes (a sagittal-oblique and a coronal-oblique localizer image) in order to reduce saturation effects. Saturation effects, appearing as a band of low signal in the center of the acetabulum and femoral neck, are always present in 2D radial MR imaging. However, saturation does not involve the relevant capsular–labrum–cartilage complex and thus diagnostic imaging of the labrum and cartilage will be unaffected (Figs. 11.2 and 11.5).

A TSE sequence with PD-weighting is selected due to its high spatial resolution and ability to outline cartilage and labrum tissue. The coronal and the sagittal sequences are used to visualize the labrum and the limbus. Coronal images are suitable to depict the suprafoveal articular cartilage over the femoral head, lateral dome, and superior labrum, whereas sagittal images are optimal for the assessment of the anterior labrum and cartilage (Fig. 11.6).

Radial imaging with (MRA) and without contrast-enhancement (MRI) is a standard approach to evaluate the hip as it minimizes volume averaging by displaying the joint in perpendicular sections around the entire circumference [19–22]. Anatomy and potential abnormalities of the femur, acetabulum, and labrum are, by this means, optimally visualized in one step. Furthermore, the risk of missing etiological factors and the

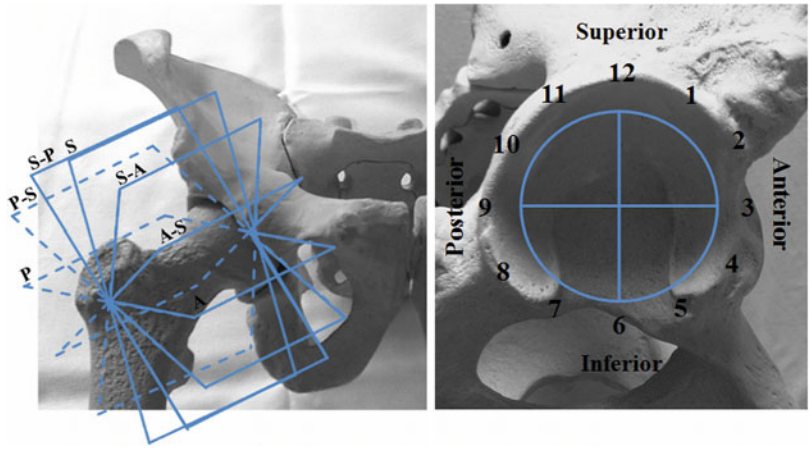

Fig. 11.7 2D or 3D radial imaging with (MRA) and without contrast-enhancement (MRI) is a standard approach to evaluate the hip because it minimizes volume averaging by displaying the joint in perpendicular sections around the entire circumference whereas anatomy and potential abnormalities of femur, acetabulum, and labrum are optimally visualized. Furthermore, it provides useful information on the localization and extent of labral tears from anterior to superior and posterior (*left*) that is critical if surgical treatment is intended. Alternatively, a clock-face localization (*right*), which is consistent with arthroscopic interpretation, may be implemented where the 6 o'clock position depicts the acetabular notch and 3 o'clock is anterior

patho-mechanism of a labral tear and cartilage aberration, which could eventually initiate early OA, such as circumscribed osseous bump formation, may be minimized. It also provides useful information on the localization and extent of labral tears (i.e., anterior to superior-anterior), which is critical if surgical treatment is intended. Alternatively, a clock-face localization, which is consistent with arthroscopic interpretation, may be implemented, in which the 6 o'clock position depicts the acetabular notch and 3 o'clock is anterior (Fig. 11.7).

High-resolution 3D sequences allowing for multiplanar and radial reconstructions are potential alternatives in the assessment of the hip joint. A 3D double-echo steady state (DESS) sequence with water excitation is an effective instrument in labrum and cartilage assessment, owing to its strong fluid signal that creates an arthrogram-like effect within the joint that may increase the conspicuity of the labrum and cartilage lesions, in particular if non-contrast imaging is being performed.

Further details on the imaging parameters are provided in Tables 11.1 and 11.2.

Labrum Evaluation

The normal capsule–labrum–cartilage complex reveals a triangular-shaped labrum with homogeneous low signal intensity and a perilabral recess between the labrum and joint capsule.

Labrum pathology is classified by location, morphology, and etiology (i.e., traumatic versus degenerative) [1, 23, 24]. Labral tears may occur at the transition zone between the fibrocartilaginous labrum and the articular hyaline cartilage (Figs. 11.5 and 11.8a). This type of tear is frequently perpendicular to the articular surface and, in some cases, extends to the subchondral bone. Tears of various lengths parallel to the base of the labrum are not uncommon (Figs. 11.8b and 11.9). Labral tears may also occur within the substance of the labrum itself, revealing variable planes (radial, longitudinal) and depth (partial or complete) (Figs. 11.8c, 11.10, and 11.11). As outlined above, using a clock-face method to describe the localization and extent of labrum pathology, in which the 6 o'clock position depicts the acetabular notch and 3 o'clock is anterior, can provide useful information to the

Table 11.1 MRI/MRA protocol at 1.5 T

	Axial 2D TSE	Coronal 2D TSE	Sagittal 2D TSE	Axial 2D FLASH	Radial 2D TSE
TR (repetition time, ms)	491	3,060	2,900	250	1,800
TE (echo time, ms)	13	9.1	9.1	12	13
FA (flip angle, degree)	150	150	150	90	180
NEX (number of excitation)	2	3	3	2	2
FOV (field of view, mm^2)	160	130	130	120	180
Slice thickness (mm)	3	2	2	2	4
Matrix	512 × 256	256 × 205	256 × 205	256 × 205	512 × 256
Number of slices	20	23	23	11	14
Slice gap (mm)	0.2	0.3	0.2	0.2	–
Bandwith (Hz/pixel)	130	130	130	130	130
TA (acquisition time, min)	4.14	5.35	5.35	3.52	4.25

TSE turbo spin echo, *FLASH* fast low angle shot

Table 11.2 Imaging parameters of a 3D DESS sequence at 3 T

	3D DESS Water excitation
TR (repetition time, ms)	14.75
TE (echo time, ms)	5.03
FA (flip angle, degree)	25
NEX (number of excitation)	1
FOV (field of view, mm^2)	192
Slice thickness (mm)	0.6
In-plane resolution (mm)	0.6 × 0.6
Slice gap (mm)	0.2
Bandwith (Hz/pixel)	260
TA (acquisition time, min)	13.17

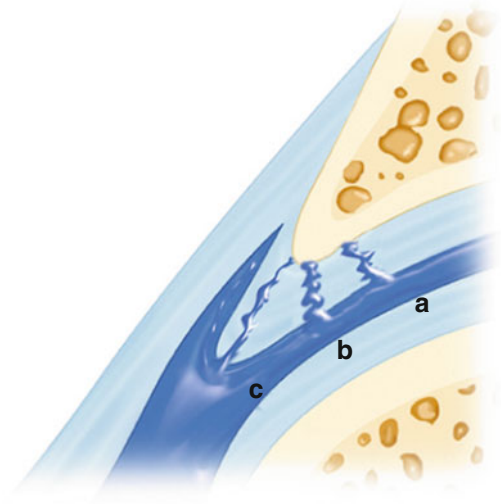

Fig. 11.8 Schematic drawing illustrating (*a*) a labral tear at the transition zone between fibrocartilaginous labrum and articular hyaline cartilage perpendicular to the articular surface, (*b*) a radially oriented partial tear at the base of the labrum, and (*c*) a longitudinal tear within the labrum

orthopedic surgeon to accurately localize a labral tear during surgery.

Czerny et al. have established a classification scheme for the MRA appearance of labral pathology that includes two types (A and B) and four stages (Fig. 11.12) [25]. Stage "0" corresponds to a normal labrum with a triangular shape, homogeneous low signal intensity, and a perilabral sulcus between the labrum and joint capsule. Stage "1" reveals an increased signal within the labrum that does not extend to the labral margin, reflecting intra-labral degeneration. Stage "2" is indicative of a partial tear, whereas stage "3" reveals detachment of the labrum from the acetabulum (complete tear). A type "A" labrum represents a triangular-shaped and normal-sized labrum, whereas a type "B" labrum typifies a hypertrophied and deformed labrum depleting the perilabral sulcus (Fig. 11.13).

Fig. 11.9 PD-weighted radial MRA image depicting a full-thickness labral tear at the anterior aspect of the hip joint

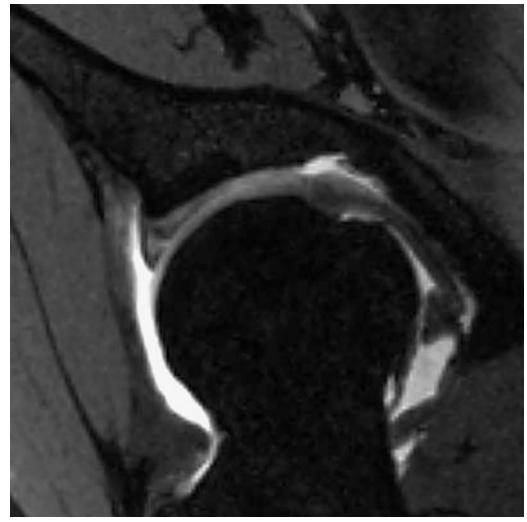

Fig. 11.10 3D DESS MRA reformat revealing a partial labral tear within the substance of the labrum

Pearls and Pitfalls

Because of the small size and narrowness of the capsule–labrum–cartilage complex, which is prone to volume averaging in particular in the setting of parallel sections, subtle labral tears may be difficult to visualize. However, with suitable MR sequence parameters (radial imaging, unilateral hip assessment and a reasonably small FOV, high SNR and spatial resolution) accurate labrum assessment is feasible. A dedicated surface coil to increase spatial resolution should be utilized, whereas the correct positioning of the coil is an important determinant of performance because surface coils rapidly reach their limits if the distance between the region of interest and the coil exceeds their available capacity (the SNR decreases with increasing distance). Notably, the SNR decreases substantially if the distance between the region of interest and the coil exceeds the diameter of the coil. This can be of considerable significance in obese patients due to signal attenuation and corresponding image quality impairment.

The presence of paralabral cysts (extravasation of synovial fluid arising from a torn labrum) is indicative of a labral tear or labrum detachment (Figs. 11.14 and 11.15) [26]. These paralabral cysts should not be confused with degenerative cysts in hip OA. Labral lesions, on the other hand, are frequently associated with cartilage damage. Labral tears commonly involve the anterior to superior quadrant [5], while tears of the posterior-superior labrum are typically seen in younger patients, i.e., after a posterior hip dislocation or in patients with hip dysplasia [23, 27, 28].

The evaluation of the labrum is simplified in the presence of an effusion as the increased signal intensity of joint fluid, similar to intra-articular contrast material, can be visualized clearly. By this means, an arthrogram-like effect is created, distinctly outlining the labral tissue and any surface irregularities if present. This benefit could be made available to the clinician if a scheduled diagnostic injection of anesthetic into the hip joint ordered to confirm intra-articular pathology (artificially creating an effusion) is combined with subsequent MRI.

Anatomical variants of the labrum have been reported that need, in light of further clinical information, to be considered when interpreting labral images. The size of the labrum varies whereas the labrum is found to be larger at the

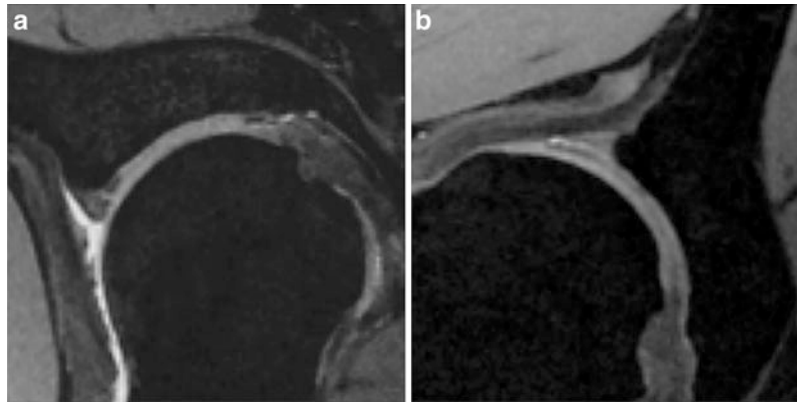

Fig. 11.11 3D DESS MRI reformats demonstrating a radial (**a**) and a longitudinal (**b**) labral tear

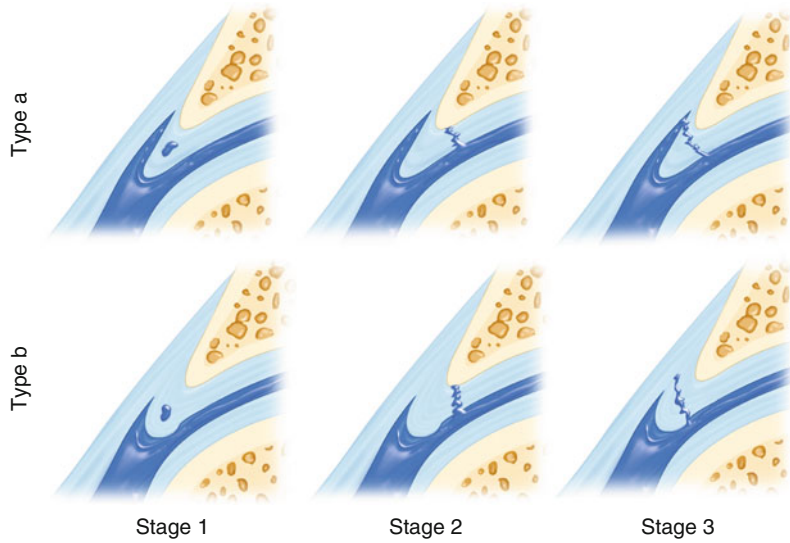

Fig. 11.12 Labrum classification according to Czerny. Stage "0" corresponds to a normal labrum with triangular shape, homogeneous low signal intensity, and a perilabral sulcus between labrum and joint capsule. Stage "1" reveals an increased signal within the center of the labrum that does not extend to the labral margin reflecting intra-labral degeneration. Stage "2" is indicative of a partial tear whereas stage "3" reveals detachment of the labrum from the acetabulum (complete tear). A type "A" labrum represents a triangular-shaped and normally sized labrum whereas a type "B" labrum typifies a hypertrophied and deformed labrum depleting the perilabral sulcus

posterior aspect [29]. Furthermore, although the labrum is typically triangular in shape and of homogeneous low signal intensity on all MR sequences, rounded or flatted labra revealing increased intra-labral signals on both T1- and T2-weighted sequences have been noted in asymptomatic patients [30–33]. The existence of a sublabral recess at the posteroinferior [34] and at the anterior aspect of the joint [35, 36], defined as distinct linear interposition of contrast medium partially separating the base of the labrum without any perilabral anomalies, has been reported as an anatomical variant. However, the characterization of such a sulcus as normvariant is controversial [37], and, notably, in previously published studies involving

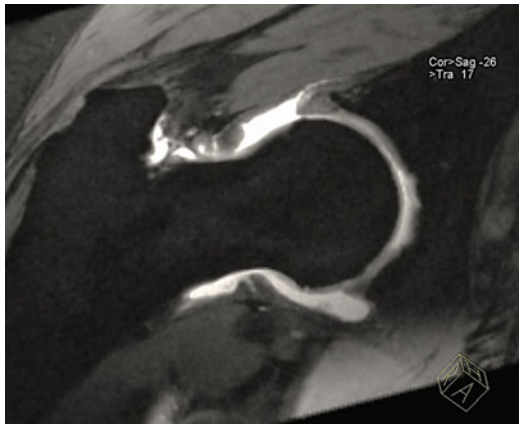

Fig. 11.13 3D DESS MRA reformat demonstrating a hypertrophied and deformed labrum depleting the perilabral sulcus which corresponds to a type B labrum according to the Czerny classification scheme

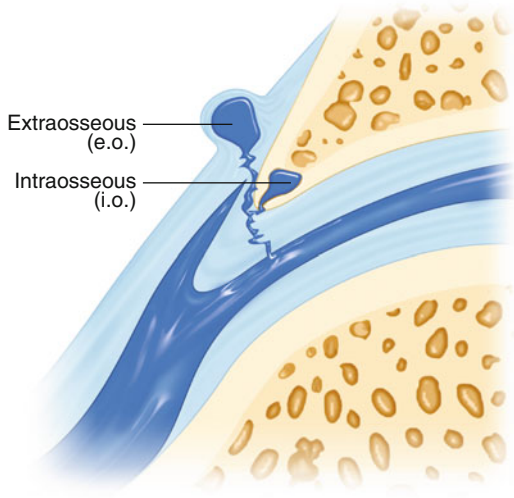

Fig. 11.14 Schematic drawing illustrating intraosseous (i.o.) and extraosseous (e.o.) extravasation of synovial fluid arising from a torn labrum

cadavers for macroscopic and histological evaluation, sublabral sulci could not be identified [38, 39].

Further pitfalls should be considered. An irregularity of the junctional zone between the labrum and transverse ligament is normal and should not be confused with a labral tear [37]. Similarly, the iliopsoas tendon can mimic a labral abnormality as it crosses over the anterior labrum. The merging zone of the labrum and acetabular cartilage may appear as a focal area of high signal intensity potentially representing volume averaging and should not be mistaken for a labral tear [38]. In this case, the diagnosis of a labral tear may be excluded if there is no contrast material filling in this region on MRA images [25, 38].

Summary

The small size and narrowness of the capsule–labrum–cartilage complex, which is prone to volume averaging, in particular in the setting of parallel imaging, pose challenges for an accurate assessment of the acetabular labrum. In addition, normal variations of the labrum in shape and signal intensity in correlation with labral portion and age have been described and they must not be confused with symptomatic labrum pathology. MRA combines the advantages of an arthrography including capsule distention and delineation of intra-articular structures with the superior spatial resolution of MRI and remains, despite its potential substitutes and alleged limitations, the imaging modality of choice in patients in whom a labral lesion is suspected. However, MRA by itself does not guarantee an accurate hip joint assessment. Instead, image quality, and thus reliable labrum evaluation, is equally affected by pulse sequence parameter and coil selection. If MRA is not applicable, reliable labrum evaluation without contrast medium administration is feasible, provided that appropriate pulse sequences (i.e., PD-weighted imaging) are being used. High-resolution 3D sequences, which allow for multiplanar and radial reconstructions, are further potential imaging alternatives in the assessment of the hip joint. Today, radial imaging (2D or 3D) is considered a diagnostic standard of MR hip joint assessment because it facilitates the visualization of the entire acetabular circumference, which is of high value in identifying the exact localization and extent of any existing labrum and cartilage pathology. Future studies that involve 3 T MR imaging for acetabular

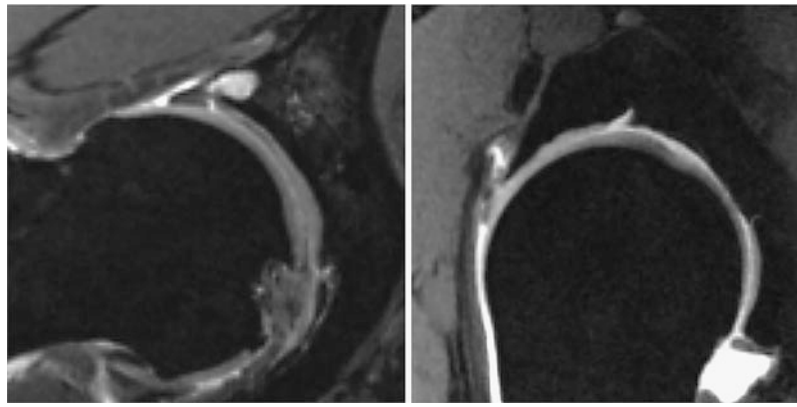

Fig. 11.15 The presence of paralabral cysts (intraosseous [*left*] or extraosseous [*right*] extravasation of synovial fluid arising from a torn labrum) is indicative of a labral tear or labrum detachment. Of note, these paralabral cysts should not be confused with degenerative cysts in hip OA

labrum imaging will likely show improvements due to increased SNR and CNR, potentially relativizing the traditional concept of hip joint evaluation and MRA.

References

1. Seldes RM, Tan V, Hunt J, Katz M, Winiarsky R, Fitzgerald RH Jr. Anatomy, histologic features, and vascularity of the adult acetabular labrum. Clin Orthop Relat Res. 2001;382:232–40.
2. Tschauner C, Hofmann S, Czerny C. Hip dysplasia. Morphology, biomechanics and therapeutic principles with reference to the acetabular labrum. Orthopade. 1997;26:89–108.
3. Ferguson SJ, Bryant JT, Ganz R, Ito K. The acetabular labrum seal: a poroelastic finite element model. Clin Biomech (Bristol, Avon). 2000;15:463–8.
4. Hlavacek M. The influence of the acetabular labrum seal, intact articular superficial zone and synovial fluid thixotropy on squeeze-film lubrication of a spherical synovial joint. J Biomech. 2002;35:1325–35.
5. Fitzgerald RH Jr. Acetabular labrum tears. Diagnosis and treatment. Clin Orthop Relat Res. 1995;311:60–8.
6. Dorrell JH, Catterall A. The torn acetabular labrum. J Bone Joint Surg Br. 1986;68:400–3.
7. McCarthy JC, Noble PC, Schuck MR, Wright J, Lee J. The Otto E. Aufranc Award: the role of labral lesions to development of early degenerative hip disease. Clin Orthop Relat Res. 2001;393:25–37.
8. Byrd JW, Jones KS. Diagnostic accuracy of clinical assessment, magnetic resonance imaging, magnetic resonance arthrography, and intra-articular injection in hip arthroscopy patients. Am J Sports Med. 2004;32:1668–74.
9. Chan YS, Lien LC, Hsu HL, Wan YL, Lee MS, Hsu KY, et al. Evaluating hip labral tears using magnetic resonance arthrography: a prospective study comparing hip arthroscopy and magnetic resonance arthrography diagnosis. Arthroscopy. 2005;21:1250.
10. Mintz DN, Hooper T, Connell D, Buly R, Padgett DE, Potter HG. Magnetic resonance imaging of the hip: detection of labral and chondral abnormalities using noncontrast imaging. Arthroscopy. 2005;21:385–93.
11. James SL, Ali K, Malara F, Young D, O'Donnell J, Connell DA. MRI findings of femoroacetabular impingement. AJR Am J Roentgenol. 2006;187:1412–9.
12. Smith TO, Hilton G, Toms AP, Donell ST, Hing CB. The diagnostic accuracy of acetabular labral tears using magnetic resonance imaging and magnetic resonance arthrography: a meta-analysis. Eur Radiol. 2011;21:863–74.
13. Zlatkin MB, Pevsner D, Sanders TG, Hancock CR, Ceballos CE, Herrera MF. Acetabular labral tears and cartilage lesions of the hip: indirect MR arthrographic correlation with arthroscopy—a preliminary study. AJR Am J Roentgenol. 2010;194:709–14.
14. Winalski CS, Aliabadi P, Wright RJ, Shortkroff S, Sledge CB, Weissman BN. Enhancement of joint fluid with intravenously administered gadopentetate dimeglumine: technique, rationale, and implications. Radiology. 1993;187:179–85.
15. Ramnath RR. 3T MR imaging of the musculoskeletal system (Part II): clinical applications. Magn Reson Imaging Clin N Am. 2006;14:41–62.
16. Sundberg TP, Toomayan GA, Major NM. Evaluation of the acetabular labrum at 3.0-T MR imaging compared with 1.5-T MR arthrography: preliminary experience. Radiology. 2006;238:706–11.
17. Bittersohl B, Steppacher S, Haamberg T, Kim YJ, Werlen S, Beck M, et al. Cartilage damage in femoroacetabular impingement (FAI): preliminary

results on comparison of standard diagnostic vs delayed gadolinium-enhanced magnetic resonance imaging of cartilage (dGEMRIC). Osteoarthritis Cartilage. 2009;17:1297–306.
18. Werlen S. MR-Arthrographietechnik. In: Wirth CJ, Zichner J, editors. Orthopädie und Orthopädische Chirurgie. Stuttgart: Georg Thieme Verlag; 2004. p. 75–8.
19. Horii M, Kubo T, Hirasawa Y. Radial MRI of the hip with moderate osteoarthritis. J Bone Joint Surg Br. 2000;82:364–8.
20. Kubo T, Horii M, Harada Y, Noguchi Y, Yutani Y, Ohashi H, et al. Radial-sequence magnetic resonance imaging in evaluation of acetabular labrum. J Orthop Sci. 1999;4:328–32.
21. Kubo T, Horii M, Yamaguchi J, Terauchi R, Wu Y, Hasegawa Y, et al. Radial magnetic resonance imaging and pathological findings of acetabular labrum in dysplastic hips. Pathophysiology. 2000;7:171–5.
22. Plotz GM, Brossmann J, von Knoch M, Muhle C, Heller M, Hassenpflug J. Magnetic resonance arthrography of the acetabular labrum: value of radial reconstructions. Arch Orthop Trauma Surg. 2001; 121:450–7.
23. McCarthy J, Noble P, Aluisio FV, Schuck M, Wright J, Lee JA. Anatomy, pathologic features, and treatment of acetabular labral tears. Clin Orthop Relat Res. 2003;406:38–47.
24. Schmerl M, Pollard H, Hoskins W. Labral injuries of the hip: a review of diagnosis and management. J Manipulative Physiol Ther. 2005;28:632.
25. Czerny C, Hofmann S, Neuhold A, Tschauner C, Engel A, Recht MP, et al. Lesions of the acetabular labrum: accuracy of MR imaging and MR arthrography in detection and staging. Radiology. 1996;200:225–30.
26. Magee T, Hinson G. Association of paralabral cysts with acetabular disorders. AJR Am J Roentgenol. 2000;174:1381–4.
27. Dameron Jr TB. Bucket-handle tear of acetabular labrum accompanying posterior dislocation of the hip. J Bone Joint Surg Am. 1959;41-A:131–4.
28. Groh MM, Herrera J. A comprehensive review of hip labral tears. Curr Rev Musculoskelet Med. 2009;2: 105–17.
29. Uhthoff HK. The embryology of the human locomotor system. Berlin: Springer; 1990.
30. Abe I, Harada Y, Oinuma K, Kamikawa K, Kitahara H, Morita F, et al. Acetabular labrum: abnormal findings at MR imaging in asymptomatic hips. Radiology. 2000;216:576–81.
31. Aydingoz U, Ozturk MH. MR imaging of the acetabular labrum: a comparative study of both hips in 180 asymptomatic volunteers. Eur Radiol. 2001;11: 567–74.
32. Lecouvet FE, Vande Berg BC, Malghem J, Lebon CJ, Moysan P, Jamart J, et al. MR imaging of the acetabular labrum: variations in 200 asymptomatic hips. AJR Am J Roentgenol. 1996;167:1025–8.
33. Petersilge C. Imaging of the acetabular labrum. Magn Reson Imaging Clin N Am. 2005;13:641–52. vi.
34. Dinauer PA, Murphy KP, Carroll JF. Sublabral sulcus at the posteroinferior acetabulum: a potential pitfall in MR arthrography diagnosis of acetabular labral tears. AJR Am J Roentgenol. 2004;183:1745–53.
35. Petersilge CA, Haque MA, Petersilge WJ, Lewin JS, Lieberman JM, Buly R. Acetabular labral tears: evaluation with MR arthrography. Radiology. 1996;200: 231–5.
36. Studler U, Kalberer F, Leunig M, Zanetti M, Hodler J, Dora C, et al. MR arthrography of the hip: differentiation between an anterior sublabral recess as a normal variant and a labral tear. Radiology. 2008; 249:947–54.
37. Czerny C, Hofmann S, Urban M, Tschauner C, Neuhold A, Pretterklieber M, et al. MR arthrography of the adult acetabular capsular-labral complex: correlation with surgery and anatomy. AJR Am J Roentgenol. 1999;173:345–9.
38. Hodler J, Yu JS, Goodwin D, Haghighi P, Trudell D, Resnick D. MR arthrography of the hip: improved imaging of the acetabular labrum with histologic correlation in cadavers. AJR Am J Roentgenol. 1995; 165:887–91.
39. Plotz GM, Brossmann J, Schunke M, Heller M, Kurz B, Hassenpflug J. Magnetic resonance arthrography of the acetabular labrum. Macroscopic and histological correlation in 20 cadavers. J Bone Joint Surg Br. 2000;82:426–32.

Osteonecrosis

12

Nancy A. Chauvin and Diego Jaramillo

MRI Techniques to Detect Osteonecrosis

General Considerations

Osteonecrosis of the femoral head is a common final pathway in which traumatic and nontraumatic insults decrease the blood flow to the femoral head, resulting in cellular death. More than 20,000 new patients are affected each year in the United States with most cases occurring in patients between 20 and 50 years of age [1, 2]. Ischemia of the femoral head accounts for nearly 10 % of the 500,000 total hip replacements performed in the US each year [3]. Approximately 10–20 % of cases have no clear, identifiable risk factor and are classified as idiopathic osteonecrosis [4]. The goal of imaging is to diagnose the disease at its earliest stages so that optimal treatment can be instituted.

Bone ischemia of the femoral head results when a vascular insult results in decreased blood supply to the marrow cells. Reduced epiphyseal perfusion can be primarily arterial [5], venous [6], or due to increased tissue pressure [7]. It is important to consider these mechanisms as they have implications for imaging. The arterial supply is provided by the circumflex arteries particularly the medial circumflex artery (MCA). Multiple branches of the MCA course along the femoral neck and its posterosuperior branch of the MCA becomes the lateral epiphyseal artery. Disruption of arterial perfusion can occur when the MCA is stretched [5] or when its intracapsular branches are disrupted during a femoral neck fracture or blocked by increased intrasynovial pressure. Disruption of the arterial microvascularity can occur with vasculitides (such as systemic lupus erythematosus) [8] or radiation therapy [9, 10] or by diseases that cause intravascular thrombosis such as sickle cell disease. Intraepiphyseal pressure related to venous hypertension appears to contribute to osteonecrosis in closed reduction for hip dysplasia [6], Legg–Calvé–Perthes (LCP) disease [11], sickle cell anemia, septic arthritis [12], synovitis, therapy for steroids, and storage diseases such as Gaucher disease. Proliferation of adipocytes in patients being treated with steroids, or of histiocytes in patients with Gaucher disease [13], appear to produce increased pressure within a tight marrow space and may alter epiphyseal perfusion. If ischemia persists, the marrow cells become edematous and eventually die. Typically hematopoietic cells are most sensitive to hypoxia, followed by bone cells and finally by fat cells [14]. Cell death elicits an inflammatory response with increased fluid in the extracellular space. Dead bone is removed and the existing bone weakens leading to collapse of the subchondral bone. Eventually there is

N.A. Chauvin (✉)
Department of Radiology, The Children's Hospital of Philadelphia, Perelman School of Medicine at the University of Pennsylvania, 34th Street, Civic Center Boulevard, Philadelphia, PA 19104, USA
e-mail: chauvinn@email.chop.edu

Y.-J. Kim (eds.), *Hip Magnetic Resonance Imaging*,
DOI 10.1007/978-1-4614-1668-5_12,

reperfusion with a zone of repair surrounding the ischemic region. In the growing epiphysis the repair is usually through the peri-epiphyseal vessels primarily along the lateral column of the femoral head. In some cases there is reperfusion through neovasculature which develops across the physis. Although the reperfusion leads to reconstitution of bone structure, when it occurs through the physis it can lead to growth disturbance.

Normal Imaging Characteristics

In the child, the marrow of the epiphysis is fatty and therefore of high signal intensity (SI) on T1-weighted images and of low SI on fat-suppressed T1-weighted images [15]. On fat-suppressed water-sensitive sequences, epiphyseal marrow is of low SI. In the metaphysis there is hematopoietic marrow, which is of intermediate to low SI on T1-weighted images and intermediate to high SI on water-sensitive sequences. On water-sensitive sequences, the proximal femoral physeal region is of high SI, and the zone of provisional calcification is of low SI. Following contrast administration, there is very modest enhancement of the proximal femoral epiphyseal ossification center, with significant enhancement of the metaphyseal marrow [16]. Subtraction images (postcontrast minus precontrast) demonstrate a clear but modest enhancement of the epiphyseal marrow and a more abundant enhancement in the metaphyseal marrow.

MR Imaging Characteristics of Osteonecrosis

Conventional Sequences

T1-Weighted and Water-Sensitive Sequences

In the early phases of osteonecrosis the SI of the marrow fat is high on T1-weighted images. Although initially this was believed to most closely resemble fat [17, 18], it appears that high SI represents stagnant blood as described below. In the weeks beyond the very early phase of osteonecrosis, epiphyseal ischemia results in marrow edema, with the epiphysis showing decreasing SI on T1-weighted images and increasing SI on water-sensitive sequences [19]. This may initially reflect blood, but usually it represents edema of the marrow. Early weakening of the bony epiphysis decreases the height of the epiphyseal subchondral bone leading to a rim of high SI in the anterior femoral head on water-sensitive sequences. Subsequently, collapse and fibrosis further decrease marrow SI and a fragmented ossified femoral epiphysis can be of very low SI. A region of infarct has an area of high T1 signal intensity surrounded by a serpiginous rim of low SI which can appear as a double line on water-sensitive images. In cases where there is no femoral head collapse, this band-like region of low SI on T1-weighted images can persist on long-term follow-up images for more than 10 years [20].

Sagittal Imaging

The anterior half of the femoral head is more affected by osteonecrosis and the imaging findings such as marrow edema, subchondral fluid, or collapse are more prominent anteriorly [21]. In LCP, the metaphyseal changes are also mostly anterior [22]. When the abnormalities are very anterior, it is difficult to appreciate the full extent of epiphyseal and metaphyseal involvement on coronal sections and for this reason sagittal imaging can better depict the extent of epiphyseal and metaphyseal abnormalities in osteonecrosis (Fig. 12.1).

Fat-Suppressed T1-Weighted Imaging

In the early stages of osteonecrosis, the marrow is of high SI, following the signal characteristics of fat and blood. Since the high SI most likely reflects stagnant blood, fat-suppressed T1-weighted images are valuable in detecting bone ischemia [23]. With ischemia, the SI will continue to be elevated even after fat suppression.

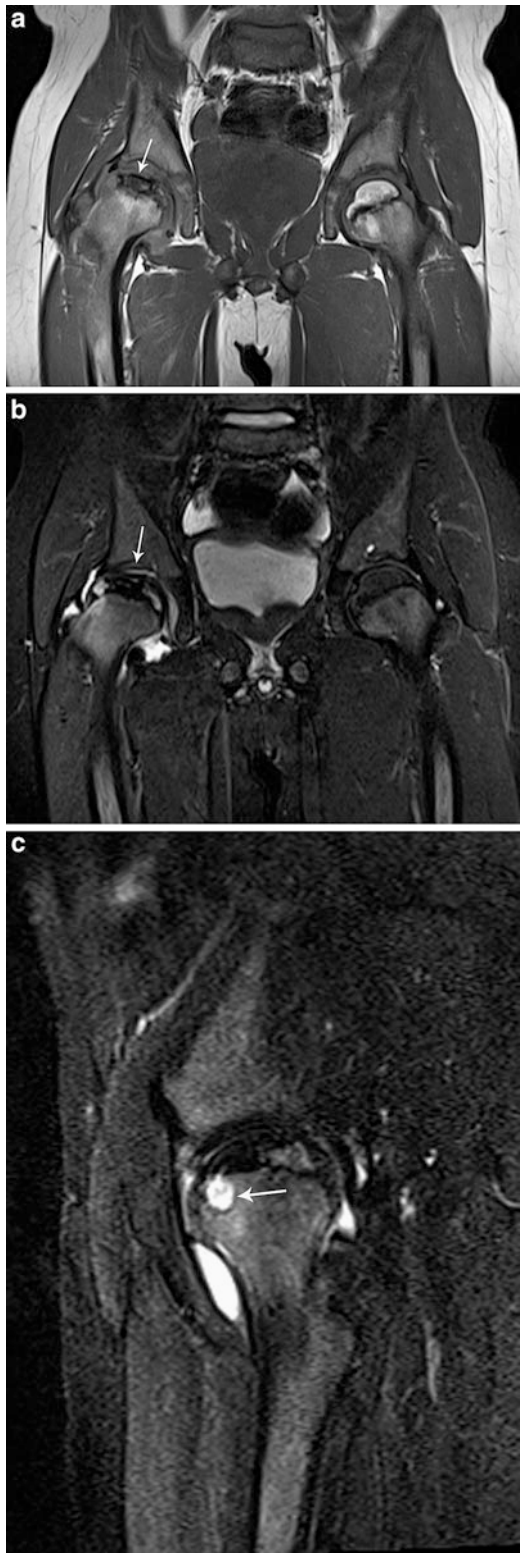

Perfusion Imaging

Static

Gadolinium-enhanced imaging is important in the diagnosis of ischemia at several stages of disease. In patients with unexplained hip pain, normal radiographs and normal or unclear unenhanced MR images, gadolinium-enhanced imaging can demonstrate lack of enhancement. The significance of this absent perfusion in a child is unclear, as it may indicate early LCP or an effusion with increased intrasynovial pressure interfering with epiphyseal perfusion (Fig. 12.2). In children with established osteonecrosis, gadolinium-enhanced imaging can demonstrate the pattern of epiphyseal reperfusion. When the femoral head is revascularized through the physis, the physeal neovascularity induces ossification and thus physeal bony bridging. Thus, transphyseal revascularization is related to a poor outcome [24, 25].

In adults, decreased bone marrow perfusion can be associated with increasing age and greater content of fatty marrow. Most of the gadolinium enhancement is attributed to the accumulation of focal inflammatory infiltrates, fibrocystic repair, and viable granulation tissue surrounding the necrotic areas [26, 27].

Dynamic

Dynamic contrast-enhanced MRI (DCE-MRI), although not routinely performed, may be useful to demonstrate the blood flow in bone marrow. In the initial phase of femoral head ischemia, there is constriction of arteries and decrease of blood flow. This is followed by reactive hyperemia and vasodilation that is associated with increased blood flow, which leads to increased intramedullary pressure, resulting in hip pain.

Fig. 12.1 Eight-year-old boy with right hip Legg–Calvé–Perthes (LCP). Coronal T1-weighted (**a**) and coronal water-sensitive (**b**) images of the hips demonstrate collapse of the right capital epiphysis with decreased SI centrally (*arrows*) compatible with necrosis. The proximal metaphysis demonstrates mild bone marrow edema. (**c**) Sagittal water-sensitive image clearly demonstrates a large cyst within the anterior aspect of the metaphysis (*arrow*)

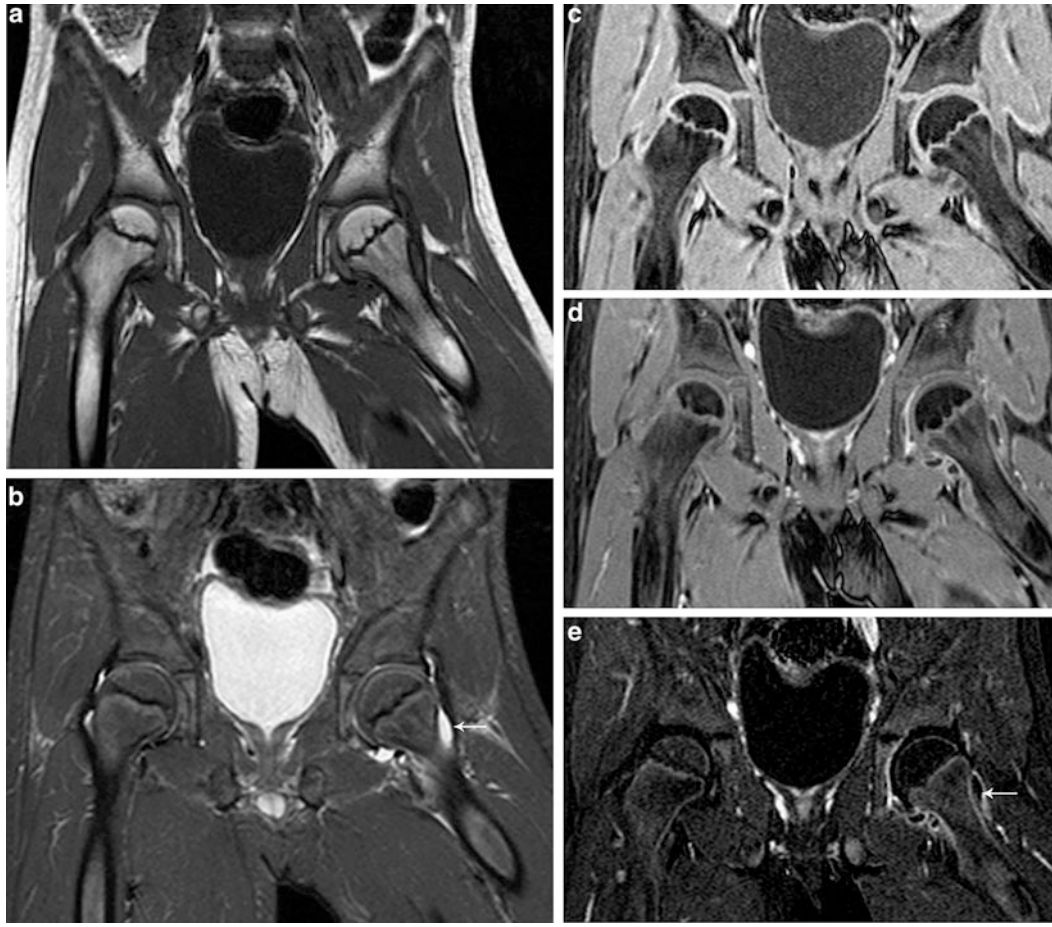

Fig. 12.2 Seven-year-old boy with left hip pain. (**a**) Coronal T1-weighted image of the pelvis shows normal bone marrow signal with fatty SI of the capital epiphyses which are rounded. (**b**) Coronal water-sensitive image shows a small left hip effusion (*arrow*) with normal bone marrow SI. Coronal T1-weighted fat saturated (**c**), T1-weighted contrast-enhanced (**d**), and subtraction views (**e**) show decreased perfusion of the left capital epiphysis with synovitis (*arrow*)

Recent work by Chan et al. [28] has demonstrated that there is delayed perfusion of the femoral head with an increase in peak enhancement that correlates with the progression of the severity of osteonecrosis. This increase in peak enhancement with delayed perfusion of the proximal femur is attributed to an increase in the exchange rate between the extracellular space and the intertrochanteric plasma due to vascular stasis [29]. In symptomatic hips without abnormal SI on conventional T1-weighted and T2-weighted sequences, dynamic contrast is useful as it can demonstrate a delayed time-to-peak enhancement pattern, which can progress to early osteonecrotic changes evident on routine MRI sequencing on follow-up studies.

Diffusion-Weighted Imaging

Although very early epiphyseal ischemia briefly restricts diffusion, most patients with proximal femoral osteonecrosis present at a stage where there is cellular wall breakdown and increased diffusion. Therefore, the findings of epiphyseal osteonecrosis are better appreciated on apparent diffusion coefficient (ADC) mapping. Perfusion and diffusion convey a different degree of

information over time regarding osteonecrosis. Whereas perfusion is initially decreased and later abnormally increased, diffusion increases rapidly and remains elevated throughout the disease [30]. There has also been interest in the metaphyseal changes that accompany LCP. In this disease, increased metaphyseal diffusion is associated with transphyseal reperfusion and increased risk of growth arrest [25, 31].

Staging of Osteonecrosis by MRI

It is imperative to accurately stage early lesions so that appropriate therapy can preserve the integrity of the hip joint [2]. The size of the osteonecrotic lesion inconsistently correlates with the patient's severity of pain. There are many classification systems for staging femoral head osteonecrosis based on the conventional radiography/or MR appearance [32]. With conventional radiography, the most critical point in detecting osteonecrosis is the loss of the spherical surface of the femoral head. Other significant features are the size of the osteonecrotic region and the location of the lesion [4]. MRI is an extremely valuable modality in the evaluation of the early, pre-collapse stages and has many advantages over conventional radiography including its multiplanar imaging capability, ability to directly image the bone marrow, effectively evaluate the articular cartilage, and accurately assess the osteonecrotic head in relation to the acetabulum [4].

While Ficat and Arlet developed one of the first classification systems for femoral head osteonecrosis based on the conventional radiographic appearance [29], one of the earliest MR imaging classifications, developed by Mitchell et al., classified osteonecrosis based on the type of tissue that the ischemic bone resembles [17, 18]. In the earliest stage (class A), the signal resembles fat with hyperintensity on T1-weighted and intermediate signal on T2-weighted images. Class B demonstrates changes of hemorrhage with increased SI on T1 and T2-weighted images. The next stage (class C) shows fluid signal with hypointensity on T1-weighted and hyperintensity on T2-weighted sequences (Fig. 12.3). The most advanced stage (class D) exhibits signal characteristics of fibrous tissue with hypointensity on all sequences. This system was adapted into the University of Pennsylvania staging system [33], one of the most widely used classification systems [32]. The University of Pennsylvania classification system defines seven precise stages utilizing both conventional radiographs and/or MRI to characterize lesion size (Table 12.1). Using this system, a group of investigators from the Association Research Circulation Osseous (ARCO) developed subsequent classification models; however, there is no widely accepted osteonecrosis classification system at this time.

Considerations Related to Specific Pathologies

Osteonecrosis During Treatment of Developmental Dysplasia of the Hip

The treatment of severe developmental dysplasia of the hip is based on immobilizing the hip in abduction. A reduced, stable femoral head continues to remodel the acetabulum. Unfortunately, maintaining the head in significant permanent abduction results in avascular necrosis in more than 20 % of cases. Since treatment in spica casts is often done before the appearance of the proximal femoral ossification center, MR imaging focuses on detecting abnormal blood flow to the cartilaginous femoral epiphysis. Immediately after placement of the spica cast, gadolinium-enhanced MR imaging can determine whether the femoral head is perfused. A normal pattern reveals enhancement of the vascular canals of the epiphyseal cartilage and of the primary spongiosa of the metaphysis [34, 35] (Fig. 12.4). A patchy pattern of enhancement appears not to have a predictive value for subsequent osteonecrosis. A global significant decrease or total absence of enhancement of the femoral epiphysis, however, is associated with a tenfold increase in the odds of developing avascular necrosis [36] (Fig. 12.5). The signal characteristics of the epiphyseal cartilage on

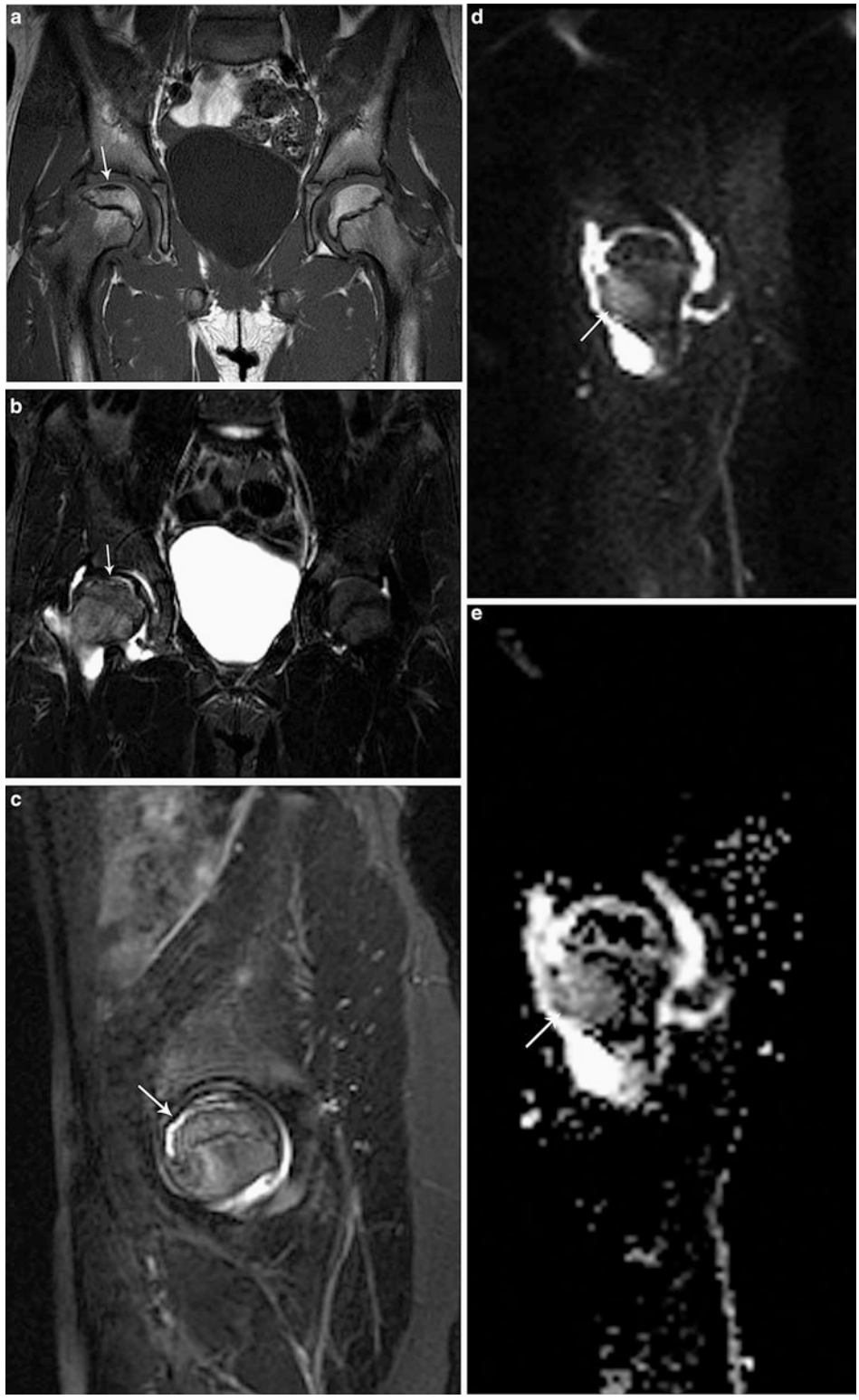
a
b
c
d
e

Table 12.1 Classification system of the University of Pennsylvania (Steinberg) [33]

Stage	Criteria
0	Normal radiograph, bone scan, and magnetic resonance images
I	Normal radiograph. Abnormal bone scan and/or magnetic resonance images
	A: Mild (<15 % of femoral head affected)
	B: Moderate (15–30 % of femoral head affected)
	C: Severe (>30 % of femoral head affected)
II	Cystic and sclerotic changes in femoral head
	A: Mild (<15 % of femoral head affected)
	B: Moderate (15–30 % of femoral head affected)
	C: Severe (>30 % of femoral head affected)
III	Subchondral collapse without flattening (crescent sign)
	A: Mild (<15 % of femoral head affected)
	B: Moderate (15–30 % of femoral head affected)
	C: Severe (>30 % of femoral head affected)
IV	Flattening of femoral head
	A: Mild (<15 % of surface and <2 mm of depression)
	B: Moderate (15–30 % of surface and 2–4 mm of depression)
	C: Severe (>30 % of surface and >4 mm of depression)
V	Joint narrowing or acetabular changes
	A: Mild
	B: Moderate
	C: Severe
VI	Advanced degenerative changes

T1-weighted and water-sensitive sequences do not change appreciably with early ischemia, and therefore contrast enhancement is necessary for early detection of ischemia.

MRI is performed in the supine position with a large multichannel flex coil placed over the spica cast. A complete perfusion protocol after closed hip reduction and SPICA cast placement includes coronal T2-weighted fat-suppressed images, axial T1-weighted fat-suppressed before administration of contrast, and axial and coronal postcontrast T1-weighted fat-suppressed images. Subtraction views are constructed in the axial plane. Images should be acquired as soon as possible after closed reduction (optimally within a 6 h period) to allow for manipulation or removal of the cast, if necessary. If the study is performed relatively soon after administration of general anesthesia, most infants are usually still sedated enough to comply with the MRI study. In addition, immobilization from SPICA cast placement further reduces the potential for motion artifact. No additional sedatives are needed to perform the study. Acquisition of the images requires approximately 20–25 min.

For open reductions, coronal T2-weighted fat-suppressed and axial T1-weighted fat-suppressed images are sufficient. We do not routinely evaluate perfusion with gadolinium-enhancement in these cases as it is expected that the surgical manipulation of the hip will alter the enhancement pattern of the femoral head.

Fig. 12.3 Ten-year-old gymnast with right hip pain. (**a**) Coronal T1-weighted image of the pelvis demonstrates flattening of the right femoral head with linear subchondral SI. The left hip is normal. (**b**, **c**) Coronal and sagittal water-sensitive images show diffuse bone marrow edema with focal linear subchondral SI compatible with Class C changes. There is a moderate, reactive joint effusion. (**d**, **e**) Sagittal diffusion-weighted and ADC images demonstrate a region of increased diffusion within the anterior aspect of the proximal femoral metaphysis (*arrows*) which is associated with transphyseal reperfusion and increased risk of growth arrest in a child

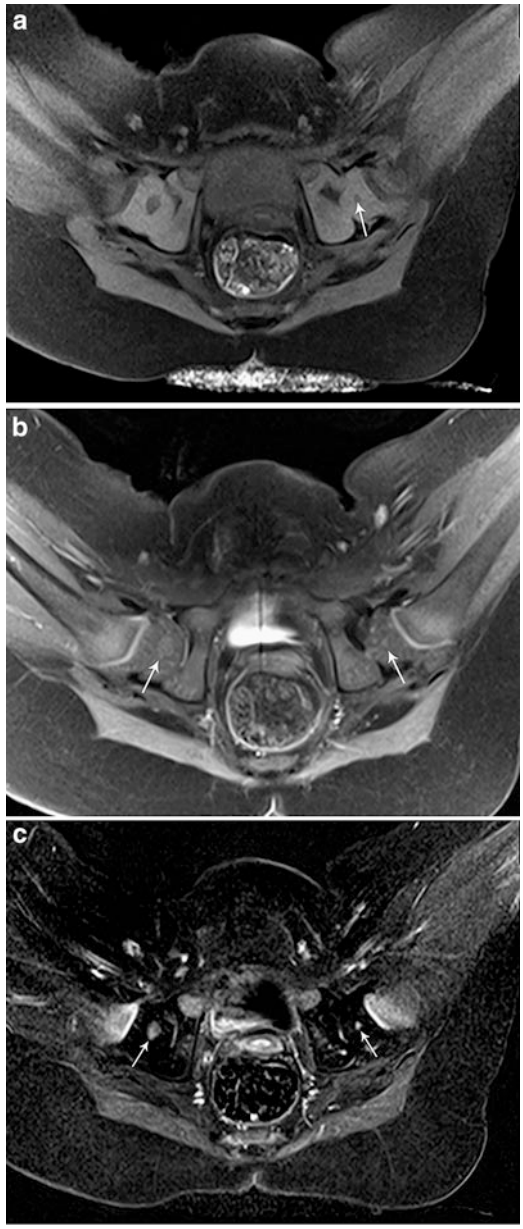

Fig. 12.4 Six-month-old girl with developmental dysplasia of the left hip status post closed reduction and SPICA cast placement with immediate MR imaging. (**a**) Axial T1 fat-saturated image shows a small left femoral head with shallow acetabulum. The left femoral ossification center (*arrow*) is smaller than the right. The right hip is normal. (**b**) Axial T1 fat-saturated post-gadolinium image shows symmetric enhancement of both ossification centers (*arrows*). (**c**) Axial subtraction images demonstrate symmetric enhancement of both femoral head ossification centers (*arrows*). Epiphyseal vessels can be seen as linear regions of enhancement within the cartilage of both femoral epiphyses

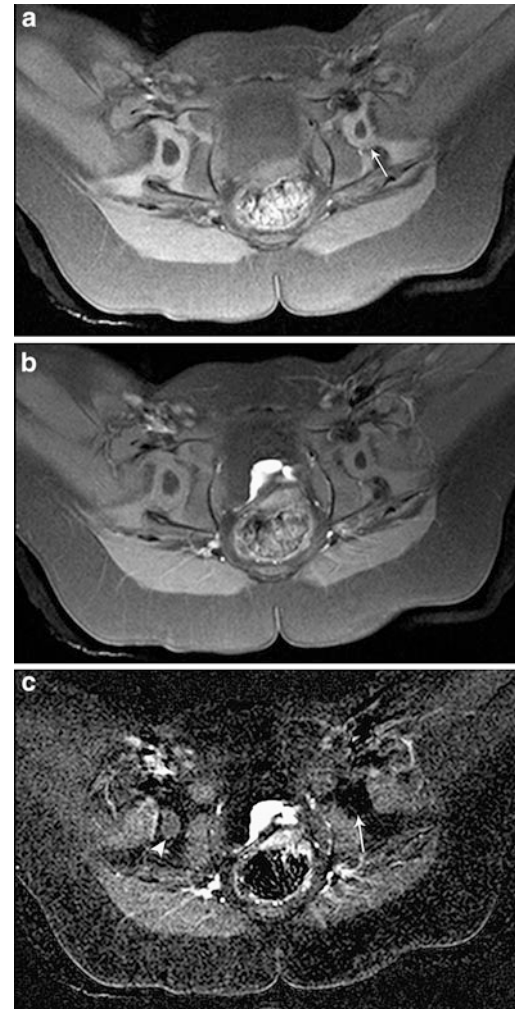

Fig. 12.5 Thirteen-month-old girl with developmental dysplasia of the left hip status post closed reduction and SPICA cast placement with immediate post-reduction MR imaging. (**a**) Axial T1 fat-saturated image shows a small left femoral head within a shallow acetabulum (*arrow*). The right hip is normal. (**b**) Axial T1 fat-saturated post-gadolinium image shows asymmetric appearance of the ossification centers with decreased SI on the left. (**c**) Axial subtraction images demonstrate non-enhancement of the left femoral head ossification center (*arrow*). No epiphyseal vessels are seen within the cartilage of the left femoral epiphysis. Normal enhancement of the right femoral head ossification center is present (*arrowhead*). The patient was subsequently recasted

Legg–Calvé–Perthes Disease

Most children presenting with LCP have abnormalities on MR imaging at presentation, even if the radiographs are normal. Four prognostic indicators in LCP include extent of osteonecrosis, lateral extrusion, physeal

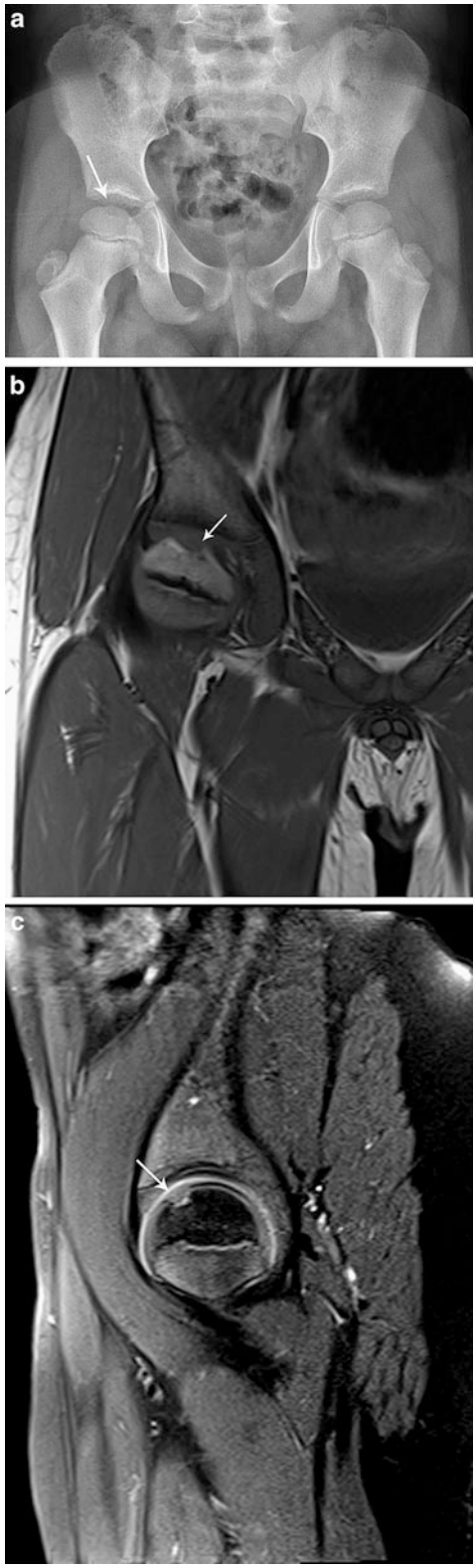

involvement, and metaphyseal abnormalities [37, 38]. Physeal abnormalities and metaphyseal cysts are believed to indicate subsequent growth disturbances and are predictors of poor outcome. In a study using multivariate analysis, the probability of subsequent growth arrest was 100 % when both epiphyseal and metaphyseal abnormalities were present, 75 % when only physeal interruption was present and 50 % when only metaphyseal cystic changes were detected [39]. Changes of LCP should not be confused with a femoral epiphyseal notch, a normal variant seen within the developing ossific femoral epiphysis [15]. The femoral epiphyseal notch is located along the vertex of the epiphysis and contains normal-thickness epiphyseal and articular cartilage with normal epiphyseal marrow SI (Fig. 12.6).

An MRI protocol to evaluate for LCP should include images of both hips in order for the asymptomatic hip to serve as a control. MR imaging of the pelvis is best performed with the patient in a supine position. Children less than 7 years of age generally require sedation while older patients are much more likely to tolerate the MRI examination without medication. A body array coil or a cardiac coil is recommended and 3.0 T imaging is optimal. Precontrast and postcontrast images in several planes with contrast subtraction views in both the coronal and sagittal planes allows for evaluation of perfusion defects [24]. Coronal T1-weighted, and coronal fat-suppressed T1-weighted and T2-weighted images enable evaluation of the SI and morphology of the proximal femoral epiphysis as well as allowing for depiction of the relationship of the femoral head with respect to the acetabulum. Labral abnormalities, acetabular deformities,

Fig. 12.6 Seven-year-old boy with right hip pain. (**a**) AP radiograph of the pelvis shows subtle lucency along the vertex of the right femoral head. (**b**) Coronal T1-weighted images show normal signal within the epiphysis with a notch at the vertex with intermediate SI compatible with cartilage (*arrow*). (**c**) Sagittal intermediate-weighted image shows normal bone marrow SI within the epiphysis and demonstrates normal thickness cartilage along the femoral head (*arrow*). No abnormality was seen within the right hip

and joint fluid also can be assessed on coronal sequences. Sagittal T1-weighted fat-suppressed images are obtained to evaluate for the full extent of epiphyseal and metaphyseal involvement, particularly since abnormalities may be located very anteriorly within the epiphysis and metaphysis and therefore poorly evaluated on coronal images. In addition, sagittal precontrast T1-weighted images allow for creation of subtraction views postcontrast administration. Axial T2-weighted fat-suppressed imaging may be added to allow for more detailed evaluation of the hip musculature and pelvic anatomy. We acquire diffusion imaging in the sagittal oblique plane, which allows differentiation between epiphyseal and metaphyseal abnormalities while decreasing the susceptibility artifacts encountered during coronal and sagittal DWI (Fig. 12.7). Imaging acquisition should take approximately 35 min.

Slipped Capital Femoral Epiphysis and Acute Trauma

Osteonecrosis is a serious complication of slipped capital femoral epiphysis (SCFE) and the incidence of osteonecrosis varies depending on the stability and severity of the slip as well as the intervention employed [40]. The unstable slips, in which the patient is unable to bear weight, demonstrate the highest incidence of subsequent osteonecrosis. Radiographs and MR images demonstrate increasing collapse and loss of height of the epiphysis. MR imaging after pinning is limited by metallic artifact.

An acute Salter–Harris type 1 fracture of the proximal femoral epiphysis almost always results in avascular necrosis. Unlike SCFE, there is no time for the vessels along the femoral neck to adapt to the displacement of the head, and the femoral epiphyseal blood supply is usually interrupted acutely.

Septic Arthritis

Septic Arthritis occurs more often in infants, with most cases presenting in the first 5 years of life. The accumulation of joint fluid results in a rapid increase in intra-articular pressure. This leads to decreased epiphyseal perfusion (Fig. 12.8). In two series of children with septic arthritis [12, 41], gadolinium-enhanced MR imaging demonstrated decreased perfusion to the proximal femoral epiphysis; this did not happen in children with toxic synovitis. To what extent hips with decreased epiphyseal perfusion will become osteonecrotic is presently unknown.

Sickle Cell Disease

Osteonecrosis occurs in about 15–30 % of patients with sickle cell anemia [42], affecting both patients with sickle cell disease and sickle cell trait. Vascular ischemia is due to hyperviscosity syndrome produced by high hemoglobin concentrations leading to intravascular sickling within sinusoids. Sickling may be enhanced in hematopoietic marrow as the large sinusoids may create a favorable environment due to stasis. This phenomenon leads to the short, temporary occlusion of vascular channels within the femoral head resulting in ischemia [1, 3]. Often, children with sickle cell disease have deformity of the hip in the absence of symptoms [43]. In adults with sickle cell disease and symptomatic osteonecrosis of the hip, there is a high likelihood of femoral head collapse, with more than 85 % of patients exhibiting degrees of femoral head collapse within 5 years of the onset of symptoms [44].

In patients with sickle cell anemia, MR images show expansion of the hematopoietic bone marrow due to enhanced demand resulting from chronic hemolysis [3]. Hyperplastic marrow can extend into the femoral epiphyses, either partially or completely replacing fatty marrow and osteonecrosis can occur in both regions of fatty and hematopoietic marrow changes. The most consistent MRI manifestation is the development of areas of low SI within the femoral heads on T1-weighted images with variable shapes. However, due to the low SI of hyperplastic marrow in anemia, subchondral T1-weighted changes in early AVN may be missed [3]. Areas of acute necrosis will demonstrate focal increased SI on T2-weighted images consistent with increased free water [45] (Fig. 12.9). Diffusion-weighted imaging of the hips in children with sickle cell disease shows that ADC values are elevated in patients with

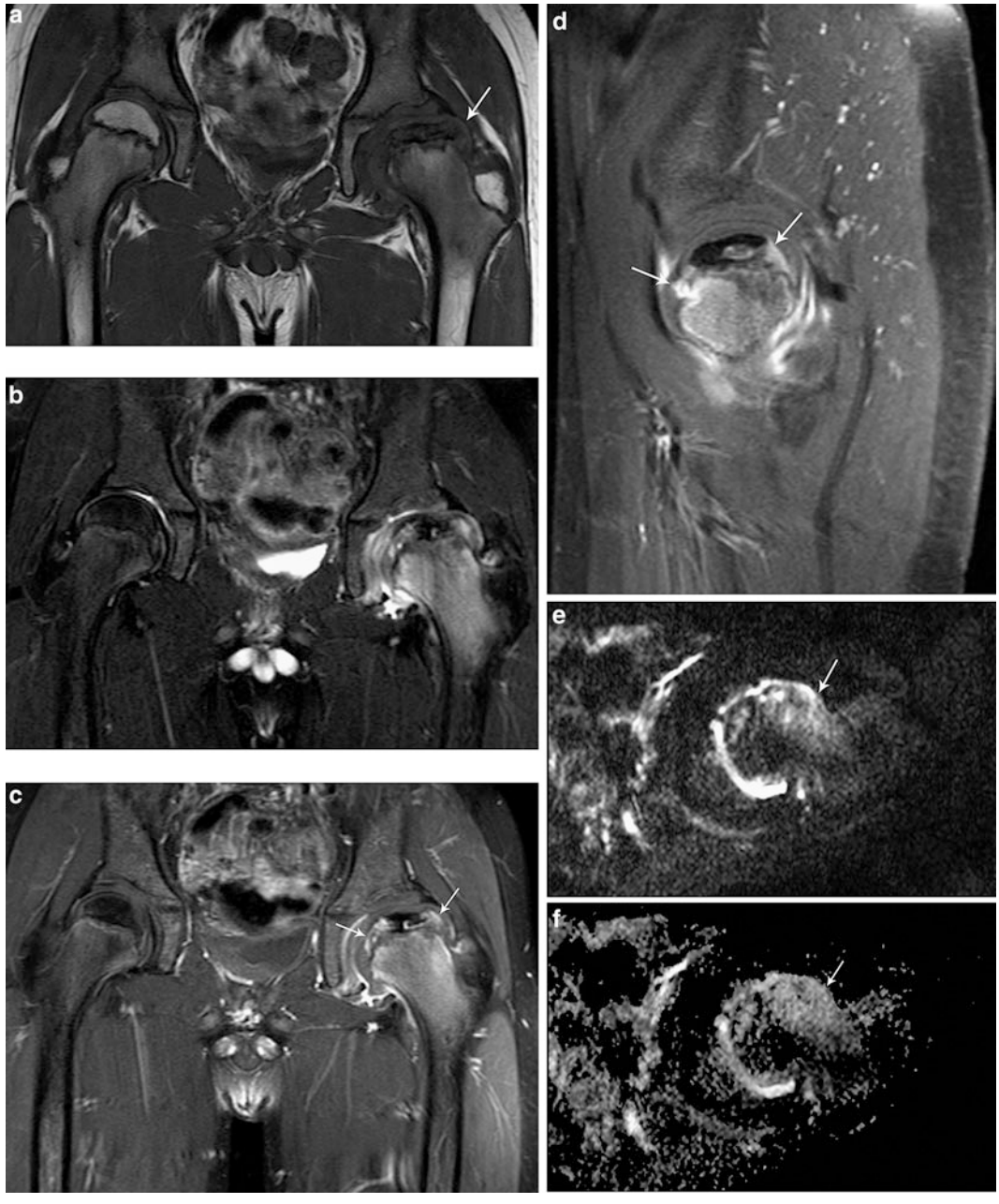

Fig. 12.7 Ten-year-old boy with left LCP disease. (**a**) Coronal T1-weighted image of the pelvis shows collapse of the capital epiphysis with central necrosis and lateral extrusion of the femoral head (*arrow*). The right hip is normal. (**b**) Coronal water-sensitive image demonstrates bone marrow edema within the proximal left femur with central necrosis and joint effusion. (**c**, **d**) Coronal and sagittal T1-weighted fat-suppressed postcontrast images demonstrate the full extent of metaphyseal changes with increased perfusion surrounding the region of the epiphyseal necrosis (*arrows*) and enhancement within the proximal metaphysis. Sagittal oblique diffusion (**e**) and ADC (**f**) images show increased diffusion within the anterior aspect of the proximal left femoral metaphysis (*arrows*) inferring a poor prognostic outcome

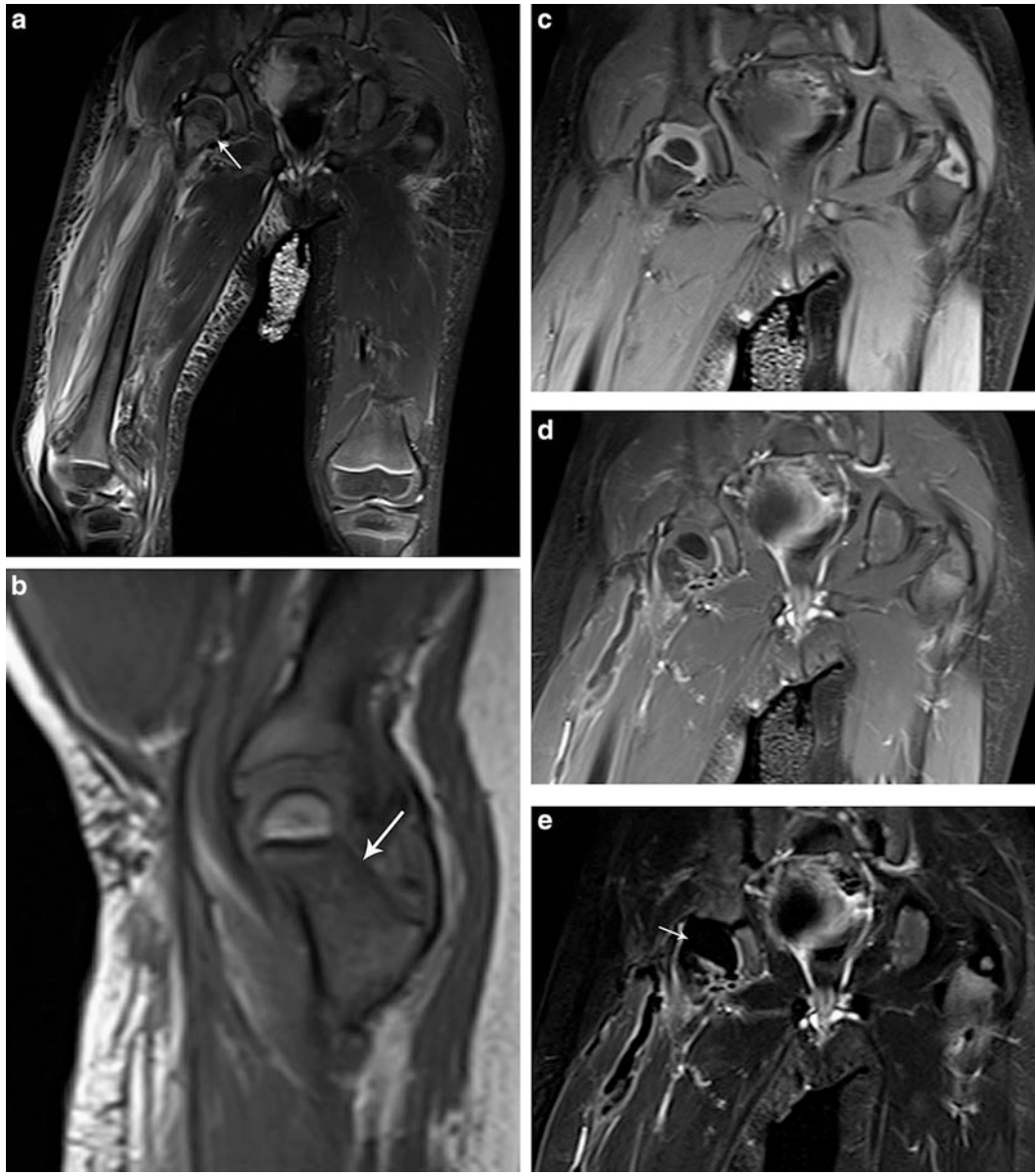

Fig. 12.8 Three-year-old febrile girl with methicillin-resistant *Staphylococcus aureus* (MRSA) septic arthritis of the right hip with osteomyelitis and pyomyositis. (**a**) Coronal water-sensitive image of the pelvis and thighs shows a small right hip effusion with bone marrow edema within the proximal right femoral metaphysis. There is extensive edema seen within the soft tissues of the right thigh extending to the knee with fluid tracking along the fascial planes. (**b**) Sagittal T1-weighted image of the right hip demonstrates corresponding decreased SI within the proximal femoral metaphysis consistent with osteomyelitis. Coronal T1-weighted fat-saturated (**c**), T1-weighted contrast-enhanced (**d**), and subtraction views (**e**) show right hip synovitis with non-perfusion of the right femoral head (*arrow*) consistent with ischemia due to increased intra-articular pressure

osteonecrosis, and differ significantly from the ADC values of normal children, asymptomatic children with sickle cell disease, and children with the disease who had symptoms referable to their hips but did not show osteonecrosis on other imaging studies [46] (Fig. 12.10).

Steroids

Steroid-associated osteonecrosis accounts for more than 50 % of the cases of non-traumatic osteonecrosis [47]. Studies have demonstrated that high doses of steroids (>30 mg/day) and longer durations of treatment were most predictive of osteonecrotic change [48, 49]. Patient age at the time of initial administration of corticosteroids has also been shown to be an independent risk factor for the development of osteonecrosis [50, 51]. In a study evaluating patients with Systemic Lupus Erythematosus, there was a higher incidence of hip osteonecrosis in adolescent and adult patients compared with pediatric patients (<15 years old) [52]. No patient younger than 14 years developed hip osteonecrosis, which was thought to be related to the abundant vascularity within the physis and red marrow.

There have been many hypotheses behind the pathogenesis of steroid-associated osteonecrosis, including enhanced adipogenesis, endothelial cell injury, and fat embolism formation [1, 47]. A proposed mechanism includes a combination of interactions including early apoptosis of osteocytes, concurrent increases in intramedullary adipocytosis as well as down-regulation of vascular endothelial growth factors [2]. In patients receiving corticosteroids, increased marrow fat appears to increase intramedullary pressure and predispose to osteonecrosis. A study showed a greater percentage of fat marrow in the femoral neck, a greater index of conversion to fatty marrow in the proximal femur, and a shorter T1 value (also correlated inversely with the amount of marrow

Fig. 12.9 Eighteen-year-old man with sickle cell anemia and left hip pain. (**a**) Coronal T1-weighted image of the pelvis demonstrates low SI within the bone marrow of the lumbar spine, iliac bones, and femoral metaphyses compatible with hematopoietic marrow. There is subchondral collapse of the left femoral head of more than 4 mm with serpiginous decreased SI involving more than 30 % of the femoral head. (**b**, **c**) Coronal and sagittal fluid-sensitive sequence shows a small left hip effusion with marrow edema within the femoral neck. Findings are consistent with Stage IVc according to the Classification System of the University of Pennsylvania

fat) in patients with osteonecrosis who had received corticosteroids [53]. Recent work by Sheng et al. [47] has demonstrated that changes in perfusion MRI in a corticosteroid-induced osteonecrosis rabbit model of the proximal femur, preceded changes on conventional T1-weighted and T2-weighted images. Histopathological evaluation demonstrated that marrow space was occupied by adipose cells, compressing the marrow sinusoids, resulting in ischemia. In this model, specimens with more than 50 % decrease of marrow enhancement ultimately demonstrated necrosis, indicating a threshold of ischemia with regard to the development of osteonecrotic change.

Survivors of Malignancy

Corticosteroid therapy, alone or in combination with other chemotherapy, is considered the most important predisposing factor in the development of osteonecrosis in the treatment of malignancy. Osteonecrosis caused by chemotherapy without corticosteroids is rare [54]. Corticosteroids are administered for the treatment of the underlying malignancy; to control for graft-versus-host disease, nausea, and vomiting; and for immunosuppression in patients who have undergone hematopoietic stem-cell transplant [55].

The risk of osteonecrosis is particularly severe for survivors of pediatric leukemia and lymphoma, with osteonecrosis of the weight-bearing joints affecting as many as one-third of patients with acute lymphoblastic leukemia [56]

Fig. 12.10 Sixteen-year-old boy with sickle cell anemia and bilateral hip pain. Coronal T1-weighted (**a**) and coronal water-sensitive (**b**) images of the pelvis show low T1 SI within the bone marrow of the iliac bones and femoral metaphyses compatible with hematopoietic marrow. There is moderate subchondral collapse of the right femoral head with decreased SI on both T1 and water-sensitive sequences along the vertex consistent with fibrotic tissue (*arrowheads*). *White arrows* denote regions of bone marrow edema on water-sensitive image within both femoral heads and both proximal femurs. There is increased diffusion in these regions on diffusion-weighted (**c**) and ADC (**d**) images (*arrows*) consistent with acute infarcts. Increased T1 SI (*black arrows*) within the proximal femurs is compatible with stagnant blood in infarcted areas

Fig. 12.11 Asymptomatic 17-year-old boy with large B-cell lymphoma, treated with high-dose corticosteroids. (**a**) Coronal T1-weighted image of the right hip demonstrates serpiginous low SI within the proximal right femur without evidence of femoral head collapse. (**b**) Coronal water-sensitive image of the right hip shows minimal associated bone marrow edema consistent with predominately chronic changes. There is moderate involvement of the femoral head (15–30 %) compatible with Stage 1B according to the Classification System of the University of Pennsylvania. Three-year follow-up imaging (not shown) did not demonstrate progression of changes

(Fig. 12.11). Osteonecrosis involving at least 30 % of the articular surface of the hip is associated with a worse outcome and can be predictive of articular surface collapse in 80 % of cancer patients within 2 years of presentation, with approximately 50 % of requiring arthroplasty [2]. In children with leukemia and lymphoma, symptoms of osteonecrosis are correlated with the extent of subchondral involvement and the size of the lesion [57, 58].

Imaging with Metallic Artifacts

Degradation of image quality due to metallic artifact in the postoperative patient is due to a combination of signal voids, image distortion and signal inhomogeneity. Strategies that can be employed to reduce the size and degree of artifacts include selection of metal hardware material, patient positioning, and MRI sequence adjustments and techniques. Bulk metal and metallic alloy hardware are the most susceptible to MRI artifact production while titanium and ceramic-surfaced zirconium create significantly less image distortion. Metal produces MRI artifact by the ferromagnetic properties of the hardware which result in intra-voxel dephasing, diffusion-related signal loss, slice thickness variation, misregistration artifacts, and inhomogeneous or paradoxical tissue-selective signal suppression with fat saturation techniques [59]. The magnetic field immediately adjacent to the implant becomes inhomogeneous and unpredictable in strength, giving rise to susceptibility artifact.

Imaging at a higher field strength is generally advantageous in musculoskeletal imaging due to improved soft tissue contrast, better spatial resolution, and optimal image quality in shorter acquisition times; however, hardware-related artifacts increase with increasing magnetic field strength. Imaging at 1.5 T over 3.0 T is generally recommended. Patient positioning within the scanner should be considered prior to imaging. Optimally, the orientation of the long axis of the

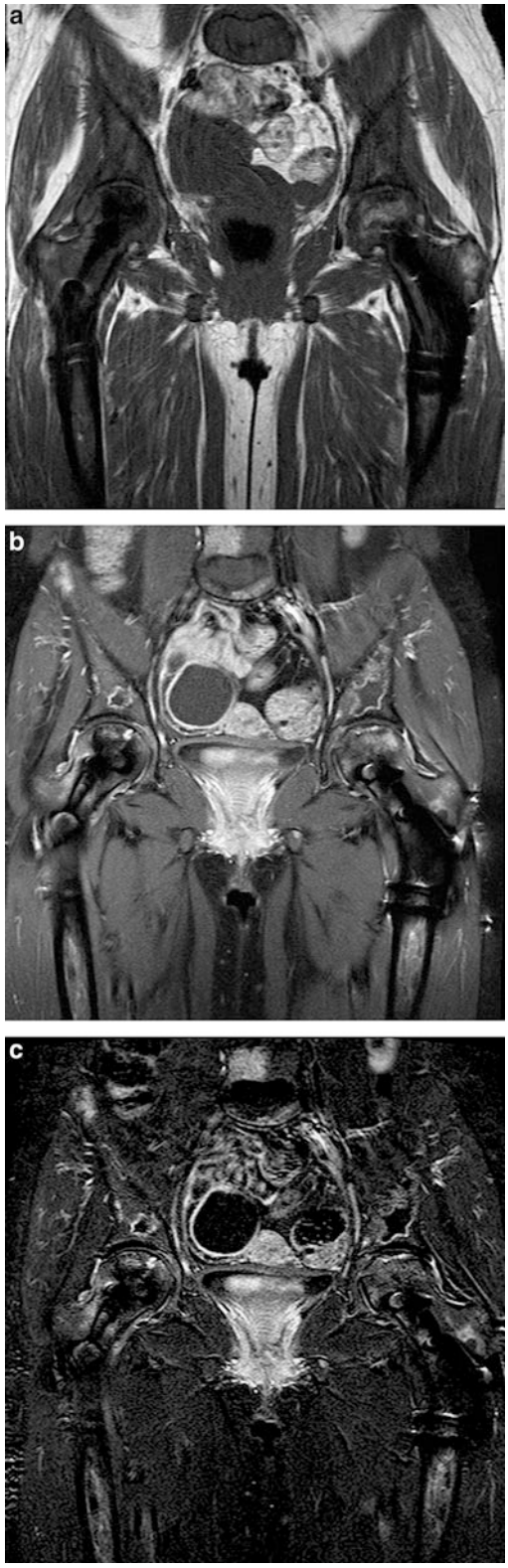

hardware should be parallel with the direction of the main magnetic field (z axis) [59].

Certain MRI sequences are more susceptible to image artifact. Gradient recalled echo (GRE) sequences are extremely vulnerable to hardware-related image distortion, resulting in signal loss around the metal, and limiting their usefulness in the postoperative patient. Pulse sequences that are less susceptible to artifact include spin-echo (SE) and fast spin-echo (FSE) sequences which use a 180° refocusing pulse that corrects for field inhomogeneities and result in a dramatic improvement in image quality [59, 60]. An increased echo train length resulting in more refocusing pulses helps reduce artifacts. Other important strategies for metallic artifact reduction include increasing the receiver bandwidth, increasing the matrix in the frequency-encoding direction, and reducing the field of view. The slice thickness should also be minimized because small voxel size in MRI in the vicinity of metal increases image quality by improving spatial resolution and reducing the apparent size of the signal void. Since metallic artifacts are produced along the frequency-encoding direction, the frequency-encoding gradient should be aligned along the axis of the metallic prosthesis. Misregistration artifacts occur in the vicinity of metal result in signal loss or dark bands around the implant. Misregistration artifacts occur in the frequency-encoding direction and can be overcome by swapping the frequency and phase-encoding gradients. Fat suppression, frequently utilized in hip imaging, is commonly performed by two different methods: fat saturation or short tau inversion recovery (STIR) pulse sequences. Fat saturation is performed by employing a

Fig. 12.12 Twenty-year-old man with sickle cell anemia and extensive osteonecrosis, status post-bilateral femoral head core decompressions with hardware placement. (**a**) Coronal T1-weighted image shows femoral neck screws with lateral plate and screw fixation devices. There is mild susceptibility artifact seen along the devices. (**b**) Coronal T1-weighted fat-saturated postcontrast image shows increased metallic artifact. (**c**) Subtraction T1-weighted postcontrast image depicts the areas of abnormal enhancement more accurately, as there are no artifacts related to deficient fat suppression

saturation pulse to nullify signal related to lipid and fat tissue, which optimally performs best in a uniform imaging field. This is impeded in regions of metal, resulting in poor or no local fat suppression. A better strategy is to perform subtraction of non-fat-saturated T1-weighted images obtained before and after the administration of contrast, thus more accurately depicting the areas of abnormal enhancement (Fig. 12.12). STIR imaging is less sensitive to field inhomogeneities and is the primary alternative to fat saturation imaging. The major drawback in STIR imaging is decreased signal to noise, resulting in decreased tissue resolution [59]. Newer techniques incorporating metal artifact reduction sequences (MARS) have been shown to reduce susceptibility artifact in postoperative patients without increasing imaging time. MARS have been effective in imaging postoperative patients with femoral neck fractures, thereby enabling evaluation of the femoral head marrow and periprosthetic soft tissues, allowing for depiction of early osteonecrotic change [61]. Other techniques such as multiacquisition variable-resonance imaging combination (MAVRIC) have been shown to substantially reduce susceptibility artifacts near metallic hip implants [62].

Acknowledgment Conflict of Interest: The authors have no financial disclosures.

References

1. Lavernia CJ, Sierra RJ, Grieco FR. Osteonecrosis of the femoral head. J Am Acad Orthop Surg. 1999;7 (4):250–61.
2. Kaste SC, Karimova EJ, Neel MD. Osteonecrosis in children after therapy for malignancy. AJR Am J Roentgenol. 2011;196(5):1011–8.
3. Rao VM, et al. Femoral head avascular necrosis in sickle cell anemia: MR characteristics. Magn Reson Imaging. 1988;6(6):661–7.
4. Zibis AH, et al. The role of MR imaging in staging femoral head osteonecrosis. Eur J Radiol. 2007;63 (1):3–9.
5. Ogden JA. Treatment positions for congenital dysplasia of the hip. J Pediatr. 1975;86(5):732–4.
6. Yousefzadeh DK, et al. Biphasic threat to femoral head perfusion in abduction: arterial hypoperfusion and venous congestion. Pediatr Radiol. 2010;40 (9):1517–25.
7. Watson RM, Roach NA, Dalinka MK. Avascular necrosis and bone marrow edema syndrome. Radiol Clin North Am. 2004;42(1):207–19.
8. Malizos KN, et al. Osteonecrosis of the femoral head: etiology, imaging and treatment. Eur J Radiol. 2007;63(1):16–28.
9. Chang CC, Greenspan A, Gershwin ME. Osteonecrosis: current perspectives on pathogenesis and treatment. Semin Arthritis Rheum. 1993;23 (1):47–69.
10. Petrigliano FA, Lieberman JR. Osteonecrosis of the hip: novel approaches to evaluation and treatment. Clin Orthop Relat Res. 2007;465:53–62.
11. Roy DR. Current concepts in Legg-Calvé-Perthes disease. Pediatr Ann. 1999;28(12):748–52.
12. Kwack KS, et al. Septic arthritis versus transient synovitis of the hip: gadolinium-enhanced MRI finding of decreased perfusion at the femoral epiphysis. AJR Am J Roentgenol. 2007;189(2):437–45.
13. Lafforgue P. Pathophysiology and natural history of avascular necrosis of bone. Joint Bone Spine. 2006;73 (5):500–7.
14. Shapiro F, et al. Femoral head deformation and repair following induction of ischemic necrosis: a histologic and magnetic resonance imaging study in the piglet. J Bone Joint Surg Am. 2009;91(12):2903–14.
15. Laor T, Jaramillo D. MR imaging insights into skeletal maturation: what is normal? Radiology. 2009;250 (1):28–38.
16. Dwek JR, et al. Normal gadolinium-enhanced MR images of the developing appendicular skeleton: part 2. Epiphyseal and metaphyseal marrow. AJR Am J Roentgenol. 1997;169(1):191–6.
17. Mitchell DG, et al. Avascular necrosis of the femoral head: morphologic assessment by MR imaging, with CT correlation. Radiology. 1986;161(3):739–42.
18. Mitchell DG, et al. Femoral head avascular necrosis: correlation of MR imaging, radiographic staging, radionuclide imaging, and clinical findings. Radiology. 1987;162(3):709–15.
19. Saini A, Saifuddin A. MRI of osteonecrosis. Clin Radiol. 2004;59(12):1079–93.
20. Takao M, et al. Repair in osteonecrosis of the femoral head: MR imaging features at long-term follow-up. Clin Rheumatol. 2010;29(8):841–8.
21. Ha AS, Wells L, Jaramillo D. Importance of sagittal MR imaging in nontraumatic femoral head osteonecrosis in children. Pediatr Radiol. 2008;38 (11):1195–200.
22. Song HR, et al. Classification of metaphyseal change with magnetic resonance imaging in Legg-Calvé-Perthes disease. J Pediatr Orthop. 2000;20(5):557–61.
23. Jain R, Sawhney S, Rizvi SG. Acute bone crises in sickle cell disease: the T1 fat-saturated sequence in differentiation of acute bone infarcts from acute osteomyelitis. Clin Radiol. 2008;63(1):59–70.

24. Lamer S, et al. Femoral head vascularisation in Legg-Calvé-Perthes disease: comparison of dynamic gadolinium-enhanced subtraction MRI with bone scintigraphy. Pediatr Radiol. 2002;32(8):580–5.
25. Merlini L, et al. Diffusion-weighted imaging findings in Perthes disease with dynamic gadolinium-enhanced subtracted (DGS) MR correlation: a preliminary study. Pediatr Radiol. 2010;40(3):318–25.
26. Cova M, et al. Bone marrow perfusion evaluated with gadolinium-enhanced dynamic fast MR imaging in a dog model. Radiology. 1991;179(2):535–9.
27. Sakai T, et al. MR findings of necrotic lesions and the extralesional area of osteonecrosis of the femoral head. Skeletal Radiol. 2000;29(3):133–41.
28. Chan WP, et al. Relationship of idiopathic osteonecrosis of the femoral head to perfusion changes in the proximal femur by dynamic contrast-enhanced MRI. AJR Am J Roentgenol. 2011;196 (3):637–43.
29. Ficat RP. Idiopathic bone necrosis of the femoral head. Early diagnosis and treatment. J Bone Joint Surg Br. 1985;67(1):3–9.
30. Menezes NM, et al. Early ischemia in growing piglet skeleton: MR diffusion and perfusion imaging. Radiology. 2007;242(1):129–36.
31. Yoo WJ, et al. Diffusion-weighted MRI reveals epiphyseal and metaphyseal abnormalities in Legg-Calvé-Perthes disease: a pilot study. Clin Orthop Relat Res. 2011;469(10):2881–8.
32. Mont MA, et al. Systematic analysis of classification systems for osteonecrosis of the femoral head. J Bone Joint Surg Am. 2006;88 Suppl 3:16–26.
33. Steinberg ME, Hayken GD, Steinberg DR. A quantitative system for staging avascular necrosis. J Bone Joint Surg Br. 1995;77(1):34–41.
34. Barnewolt CE, Shapiro F, Jaramillo D. Normal gadolinium-enhanced MR images of the developing appendicular skeleton: part I. Cartilaginous epiphysis and physis. AJR Am J Roentgenol. 1997;169 (1):183–9.
35. Jaramillo D, et al. Age-related vascular changes in the epiphysis, physis, and metaphysis: normal findings on gadolinium-enhanced MRI of piglets. AJR Am J Roentgenol. 2004;182(2):353–60.
36. Tiderius C, et al. Post-closed reduction perfusion magnetic resonance imaging as a predictor of avascular necrosis in developmental hip dysplasia: a preliminary report. J Pediatr Orthop. 2009;29 (1):14–20.
37. de Sanctis N, Rega AN, Rondinella F. Prognostic evaluation of Legg-Calvé-Perthes disease by MRI. Part I: the role of physeal involvement. J Pediatr Orthop. 2000;20(4):455–62.
38. de Sanctis N, Rondinella F. Prognostic evaluation of Legg-Calvé-Perthes disease by MRI. Part II: pathomorphogenesis and new classification. J Pediatr Orthop. 2000;20(4):463–70.
39. Jaramillo D, et al. Cartilaginous abnormalities and growth disturbances in Legg-Calvé-Perthes disease: evaluation with MR imaging. Radiology. 1995;197 (3):767–73.
40. Mullins MM, et al. The management of avascular necrosis after slipped capital femoral epiphysis. J Bone Joint Surg Br. 2005;87(12):1669–74.
41. Kim EY, et al. Usefulness of dynamic contrast-enhanced MRI in differentiating between septic arthritis and transient synovitis in the hip joint. AJR Am J Roentgenol. 2012;198(2):428–33.
42. Bohrer SP. Bone changes in the extremities in sickle cell anemia. Semin Roentgenol. 1987;22(3):176–85.
43. Hernigou P, et al. Deformities of the hip in adults who have sickle-cell disease and had avascular necrosis in childhood. A natural history of fifty-two patients. J Bone Joint Surg Am. 1991;73(1):81–92.
44. Hernigou P, Bachir D, Galacteros F. The natural history of symptomatic osteonecrosis in adults with sickle-cell disease. J Bone Joint Surg Am. 2003;85-A(3):500–4.
45. Rao VM, et al. Marrow infarction in sickle cell anemia: correlation with marrow type and distribution by MRI. Magn Reson Imaging. 1989;7(1):39–44.
46. Mackenzie JD, et al. Magnetic resonance imaging in children with sickle cell disease-detecting alterations in the apparent diffusion coefficient in hips with avascular necrosis. Pediatr Radiol. 2012;42(6):706–13.
47. Sheng H, et al. Functional perfusion MRI predicts later occurrence of steroid-associated osteonecrosis: an experimental study in rabbits. J Orthop Res. 2009;27(6):742–7.
48. Colwell Jr CW, et al. Osteonecrosis of the femoral head in patients with inflammatory arthritis or asthma receiving corticosteroid therapy. Orthopedics. 1996;19(11):941–6.
49. Hungerford DS. Treatment of avascular necrosis in the young patient. Orthopedics. 1995;18(9):822–3.
50. Stern PJ, Watts HG. Osteonecrosis after renal transplantation in children. J Bone Joint Surg Am. 1979;61 (6A):851–6.
51. Gregg PJ, et al. Avascular necrosis of bone in children receiving high-dose steroid treatment. Br Med J. 1980;281:116.
52. Nakamura J, et al. Age at time of corticosteroid administration is a risk factor for osteonecrosis in pediatric patients with systemic lupus erythematosus: a prospective magnetic resonance imaging study. Arthritis Rheum. 2010;62(2):609–15.
53. Vande Berg BC, et al. Correlation between baseline femoral neck marrow status and the development of femoral head osteonecrosis in corticosteroid-treated patients: a longitudinal study by MR imaging. Eur J Radiol. 2006;58(3):444–9.
54. Marymont JV, Kaufman EE. Osteonecrosis of bone associated with combination chemotherapy without corticosteroids. Clin Orthop Relat Res. 1986;204:150–3.
55. Talamo G, et al. Avascular necrosis of femoral and/or humeral heads in multiple myeloma: results of a prospective study of patients treated with

dexamethasone-based regimens and high-dose chemotherapy. J Clin Oncol. 2005;23(22):5217–23.
56. Karimova EJ, et al. Femoral head osteonecrosis in pediatric and young adult patients with leukemia or lymphoma. J Clin Oncol. 2007;25(12):1525–31.
57. Karimova EJ, et al. MRI of knee osteonecrosis in children with leukemia and lymphoma: part 1, observer agreement. AJR Am J Roentgenol. 2006;186(2):470–6.
58. Karimova EJ, et al. MRI of knee osteonecrosis in children with leukemia and lymphoma: part 2, clinical and imaging patterns. AJR Am J Roentgenol. 2006;186(2):477–82.
59. Harris CA, White LM. Metal artifact reduction in musculoskeletal magnetic resonance imaging. Orthop Clin North Am. 2006;37(3):349–59.
60. Venook RD, et al. Prepolarized magnetic resonance imaging around metal orthopedic implants. Magn Reson Med. 2006;56(1):177–86.
61. Olsen RV, et al. Metal artifact reduction sequence: early clinical applications. Radiographics. 2000;20 (3):699–712.
62. Hayter CL, et al. MRI after arthroplasty: comparison of MAVRIC and conventional fast spin-echo techniques. AJR Am J Roentgenol. 2011;197 (3):405–11.

Extra-articular Conditions

13

Nadja Mamisch-Saupe

Abductor Tendon Pathologies

Lateral hip pain causes differential diagnostic problems because pain can arise from the hip joint itself or the periarticular soft tissues. Greater trochanteric pain is commonly caused by bursitis, tendinopathy, or tears of the gluteal tendons. Such tears of the abductor tendons of the hip, are also known as "rotator cuff tears of the hip" [1, 2]. Their etiology is degenerative or traumatic, similar to rotator cuff tears of the shoulder [3, 4]. Tears of the gluteus medius and minimus muscles appear to be associated with lateral hip or groin pain [5].

The gluteus medius and minimus tendons have a common attachment at the greater trochanter (Figs. 13.1 and 13.2) in the form of a broad musculotendinous sheet [6]. The gluteus medius attachment can be divided into three parts. The main tendon arises from the central posterior portion of the muscle and has a strong insertion covering the superoposterior facet. The lateral part of the gluteus medius tendon arises from the undersurface of the muscle, is usually thin, and is purely muscular in nature. It continues anteriorly to comprise the third attachment of the gluteus medius, covering the gluteus minimus tendon insertion to the anterior facet. The gluteus minimus attachment can be divided into two distinct components. The main tendon arises from the superficial part of the muscle fascia and demonstrates a consistent insertion to the anterior facet of the trochanter, its morphology in the transverse plane being flat and biconcave. The second component of the distal insertion is a muscular and tendinous attachment to the ventral and superior capsule of the hip joint [7, 8].

Gordon et al. [9] suggested that tears of the gluteal tendons are likely to be responsible for calcifications seen radiographically in some patients. In patients with tears of the gluteus medius and/or minimus tendons reactive sclerosis and bone proliferation can be observed particularly at the anterior edge of the sclerotic area [10]. In a study of Steinert et al. [11] including 150 patients, 90 % of patients with trochanteric surface irregularities larger than 2 mm on conventional radiographs have a lesion of the abductor tendons on MR images (positive likelihood ratio of 5.8). 98 % of patients with trochanteric surface irregularities larger than 2 mm on conventional radiographs have peritendinous fluid changes around the gluteus medius and minimus tendon insertions (positive likelihood ratio of 17.5). These findings are of importance to orthopedic surgeons and rheumatologists. In many institutions, a preoperative MR before arthroplasty of the hip is performed when an abductor tendon lesion is suspected clinically. If abductor tendon pathologies are detected on MR

N. Mamisch-Saupe (✉)
Department of Radiology, Center for Musculoskeletal Radiology, Hirslanden Clinic, Witelliker Street 40, Zurich 8032, Switzerland
e-mail: nadja.mamisch-saupe@hirslander.ch

Y.-J. Kim (eds.), *Hip Magnetic Resonance Imaging*,
DOI 10.1007/978-1-4614-1668-5_13,

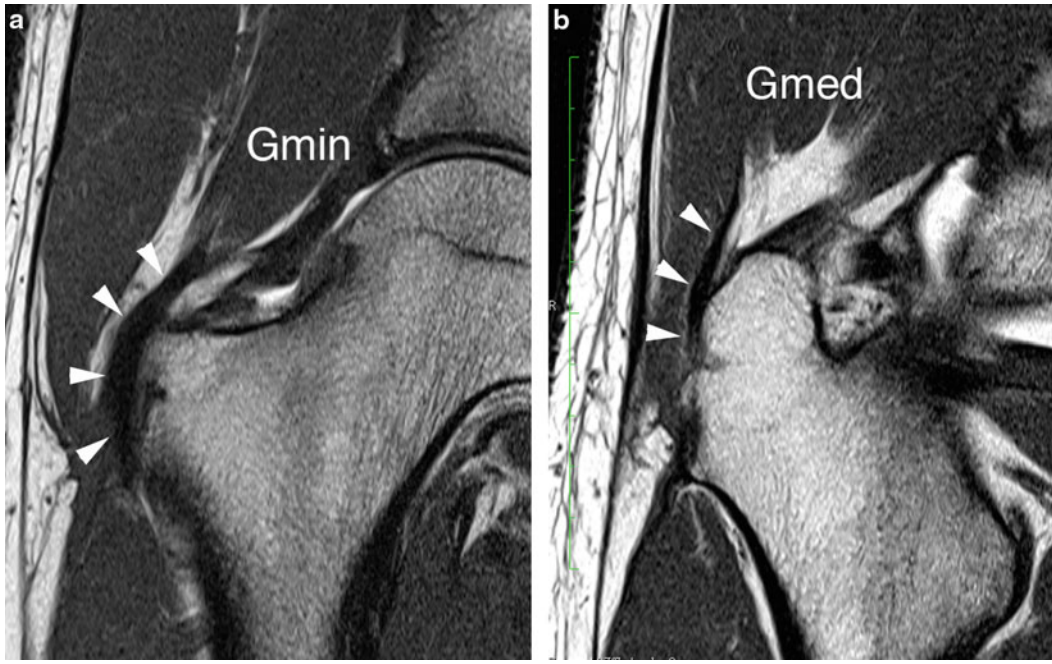

Fig. 13.1 (**a**, **b**) Normal abductor tendons. Intermediate-weighted fast spin-echo images coronal plane in a 25-year-old male (TR/TE 2,590 ms/15 ms, FOV180 × 143 mm, NEX 1; matrix 512 × 256, ETL factor 7, section thickness 3 mm). MR images show a normal insertion of gluteus minimus tendon in (**a**) (*white arrowheads*) at the anterior facet of the greater trochanter and a normal insertion of gluteus medius tendon at the lateral facet (**b**) (*white arrowheads*). Both tendons show a homogeneous hypointense signal (*Gmin* gluteus minimus muscle, *Gmed* gluteus medius muscle)

images (Figs. 13.3, 13.4, 13.5, and 13.6), the orthopedic surgeon may change the surgical approach. In the presence of an abductor tendon tear, a possible posterior approach is chosen and the abductor tendons are reattached during the implantation of the hip arthroplasty. In case of no tendon pathology, a minimal invasive anterior approach without touching the abductor tendons is performed [12]. Many clinicians, even orthopadic surgeons, seem to underestimate tears of the abductor tendons as a cause of hip pain and treatment option for hip pain. Cormier et al. [13] showed that almost half (45 %) out of 459 French orthopedic surgeons, who were contacted by mail, were not aware of the possibility that tendon tears can occur in the rotator cuff of the hip. Only 13 % (60/459) had performed surgical repair of a gluteal tendon which had been correctly diagnosed preoperatively. However, surgical treatment of gluteal tendon tears has been shown to be very effective [14]. Lequesne and colleagues [14] showed a complete or total remission of symptoms in 90 % after the surgical treatment of abductor tendon tears. Kagan [15] reported seven patients treated with success by gluteus medius tendon repair. Moreover, Miozzari et al. [16] demonstrated that 75 % of all patients with late repair of abductor dehiscence after transgluteal approach for hip arthroplasty were satisfied.

There are also a relationship between gluteal tendon abnormalities at the insertion onto the greater trochanter and bursitis as previously been reported [17, 18]. Bird et al. [18] described 24 patients with trochanteric pain of which 8 % showed a bursitis comparable to the cases in this present study where increased bursal fluid was seen in 9 % of all patients (14/150). Kingzett-Taylor et al. [5] demonstrated that 14 of 35 patients (40 %) with a tendinopathy or an abductor tendon tear also had increased amounts of bursal fluid. However, this does not necessarily

Fig. 13.2 STIR sequence (turbo-inversion-recovery-magnitude) (TR/TE/TI, 4,890 ms/45 ms/150 ms, FOV 180 × 180 mm, NEX 1, matrix 256 × 179, ETL 9, section thickness 7 mm) of a 48-year-old female patient shows a partial tear of the gluteus minimus tendon attachment with increased signal within the tendon (*white arrows*) and severe peritendinous fluid adjacent to the partial tear

Fig. 13.3 T2-weighted coronal image of an 82-year-old female patient (TR 4,000 ms, TE 70 ms, slice thickness 6 mm) shows a full thickness tear of the gluteus minimus tendon. No tendon attachment (*white arrowheads*) onto the anterior facet of the greater trochanter is shown

Fig. 13.4 T2-weighted coronal image of an 82-year-old female patient (TR 4,000 ms, TE 70 ms, slice thickness 6 mm) shows a full thickness tear of the gluteus medius tendon. No tendon attachment (*white arrowheads*) onto the lateral facet of the greater trochanter is shown

mean that there is a symptomatic bursitis because bursal fluid is a nonspecific reaction to a number of different abnormalities. Blankenbaker et al. [19] commonly found bursal fluid and peritrochanteric edema in asymptomatic hips (88 %).

Iliopsoas Musculotendinous Unit: Iliopsoas Tendinitis

The iliopsoas muscle can be followed inferiorly on transverse images because it proceeds from a medial and anterior location to a lateral and posterior location. MRI can depict the psoas tendon attachment onto the lesser trochanter of the femur, whereas most of the iliacus attaches onto the proximal femoral shaft without a tendon. T1-weighted transverse images will delineate the psoas tendon and intramuscular portions of iliacus tendon separated by a thin cleft of increased signal on T1-weighted images [20, 21]. The increased

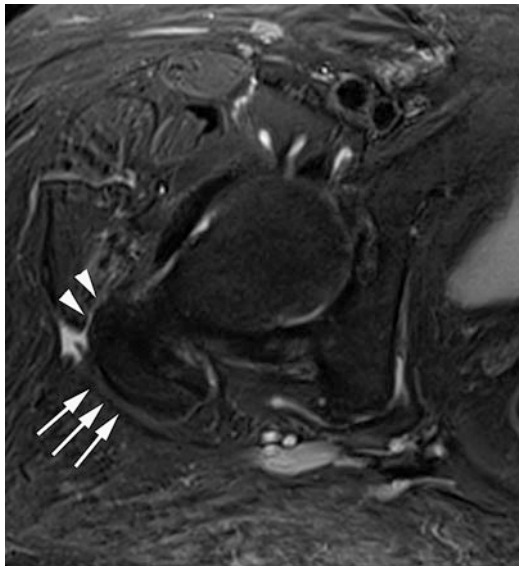

Fig. 13.5 Corresponding transverse STIR image in the same patient as in Figs. 13.3 and 13.4 (TR 4,300 ms, TE 37 ms, TR 150 ms, slice thickness 6 mm). MR image shows a full thickness tear of gluteus minimus and medius tendon. The image demonstrates the missing tendon attachments. Additionally, slight peritendinous fluid is present (*white arrows* missing gluteus medius tendon attachment and *white arrowheads* missing gluteus minimus tendon attachment)

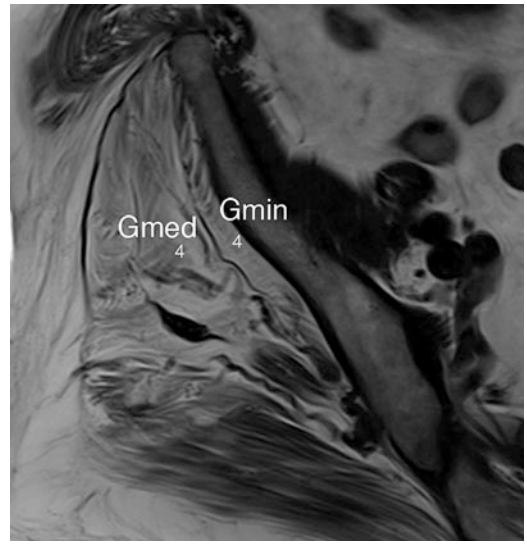

Fig. 13.6 T1-weighted transverse image (TR 500 ms, TE 13 ms, slice thickness 5 mm) illustrates fatty muscle infiltration of gluteus minimus muscle (Gmin) grade 4 according to Goutallier classification and also fatty infiltration of the gluteus medius muscle (grade 4). *Gmin* M.gluteus minimus, *Gmed* M.gluteus medius

signal is produced by the fatty fascia from the iliacus tendon.

The normal iliopsoas tendon extends anterior to the anterior superior labrum at the level of the hip joint. The anterior hip images best in transverse and sagittal planes while the patient is lying in a supine position.

Iliopsoas tendinopathy has been reported as groin or trochanteric pain getting worse during active flexion and adduction of the hip. Patients who participate kicking related sports as well as soccer or hockey are involved [22]. Daily activities such as walking or getting up or down from a chair can also produce typical pain [23]. Treatment suggestions are resting, anti-inflammatory medication and stretching [24]. MR shows in patients with a present tendinopathy a thickening of the tendon or an increased intrasubstance signal intensity of the tendon along its course or at the insertion. Additionally peritendinous fluid seen as high signal intensity on T2-weighted images and distension of the iliopsoas bursa can also be seen [21]. Partial tendon tears appear with focal fluid within the tendon or as focal discontinuity of the tendon fibers. The localization of the tear often involves the iliopsoas tendinous attachment close or at the lesser tuberosity attachment. The most severe tendon injury, a complete tear, appears to be more function of age, gender, and possible underlying comorbid nonneoplastic conditions, rather than a consequence of athletic injury [25] (Figs. 13.7 and 13.8).

Hip Bursae

The hip is surrounded by 15–20 bursae [26]. Most of the cases can be diagnosed clinically and the treatment is conservative; MR imaging is very helpful in detection and localizing of fluid collections around the hip. Characteristic sites

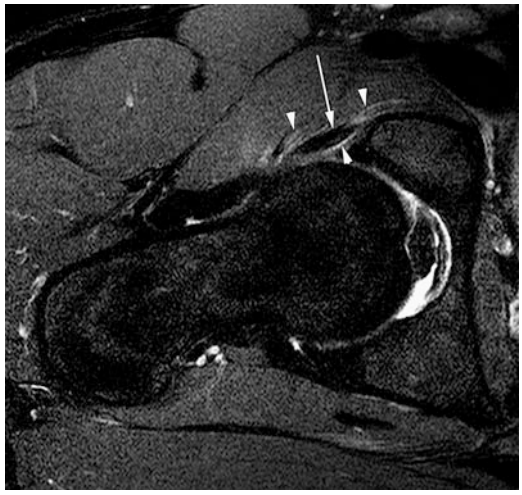

Fig. 13.7 T2-weighted fat-saturated axial TSE sequence of a 22-year-old male patient (TR 3,641 ms/TE 62 ms, slice thickness 3 mm) shows an iliopsoas tendinitis with increased peritendinous signal (*white arrowheads*) around the iliopsoas tendon (*white arrow*). The iliopsoas tendon shows an increased signal within the tendon structure

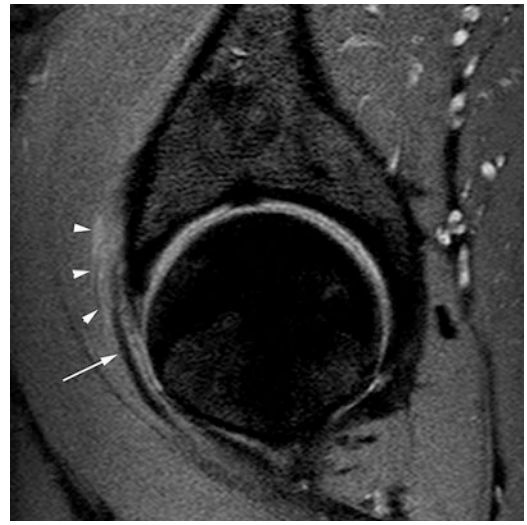

Fig. 13.8 Intermediate-weighted sagital TSE sequence of a 22-year-old male patient (TR 5,777 ms/TE 30 ms, slice thickness 3 mm) shows also the iliopsoas tendinitis with increased peritendinous signal (*white arrowheads*) around the tendinopathic iliopsoas tendon (*white arrow*)

for bursae are the iliopsoas bursae and trochanteric bursae.

Trochanteric Bursae and Bursitis

A complex of three bursae has been described over the facets of the greater trochanter. The trochanteric bursa is located between the gluteus medius muscle and the posterior facet of the trochanter. On axial T1-weighted images, the nondistended trochanteric bursa may be seen as a thin band posterior to the trochanter with intermediate signal.

The subgluteus medius bursa lies between the gluteus medius tendon and the lateral facet of the greater trochanter. The subgluteus minimus bursa has its location between the gluteus minimus tendon and the anterior facet of the greater trochanter. There is a relationship between contour or surface irregularities of the greater trochanter and increased bursal fluid in the bursae complex. If surface irregularities are larger than 2 mm appear, 15 % of the patients will show increased bursal fluid [11].

Fig. 13.9 Axial STIR (short tau inversion recovery) image (TR 4,890 ms/TE 245/TI 150 ms, slice thickness 6 mm) demonstrates a bursitis trochanterica (*arrow*) in a 52-year-old female patient. Also note the peritendinous fluid adjacent to the abductor tendons

Patients with a bursitis commonly presenting lateral hip pain. Trochanteric bursitis is a well known injury in athletes such as ballet dancers or secondary to blunt trauma occurring during playing football or hockey.

On MR imaging the bursitis is shown as an increased fluid within the bursa as hyperintense signal on T2-weighted images. Often increased peritendinous signal adjacent to the bursa and the

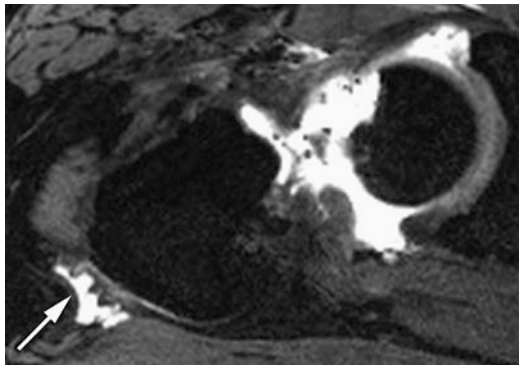

Fig. 13.10 T2-weighted axial 3D sequence at saturated axial TSE sequence of a 47-year-old male patient (TR 11.3 ms/TE 4.9 ms, slice thickness 0.7 mm) demonstrates also a bursitis trochanterica (*arrow*) in a 47-year-old female patient

abductor tendons are shown (Figs. 13.9 and 13.10).

Iliopsoas/Iliopectineal Bursa and Bursitis

It is the largest bursa in the body and can extend from the region of the lesser trochanter upward into the iliac fossa. The iliopectineal bursa around the hip joint might communicate with the hip joint in 15 % of the people because there is a hiatus between the pubofemoral and iliofemoral ligaments. That is why in MR-arthrograms contrast agent might extend into the iliopsoas [27].

A bursitis is believed to be caused by irritation of the iliopsoas as moves over the iliopectineal eminence of the femoral head. Patients present anterior hip or groin pain. This pain tends to exacerbate during hip extension and relieved during hip flexion and external rotation.

Associated sports are running, soccer, gymnastics, or resistance training.

On MR imaging the bursitis is displayed as a well-defined cystic mass along the iliopsoas tendon and has a thin wall. After contrast media

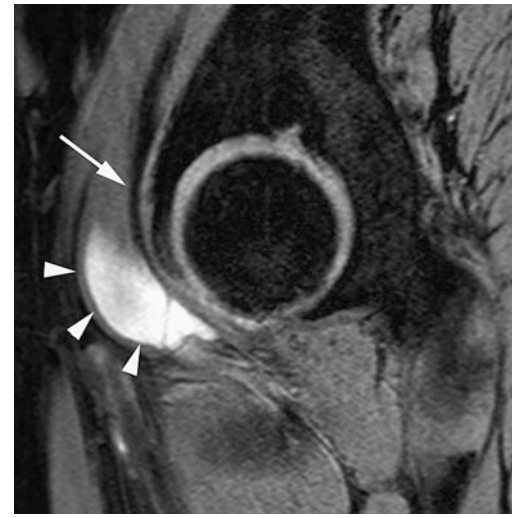

Fig. 13.11 T2-weighted sagittal 3D sequence of a 57-year-old woman (TR 25.2 ms/TE 8.6 ms, slice thickness 1.7 mm) shows an iliopsoas/iliopectinea bursitis as a thin-walled cystic lesion (*white arrowheads*) directly adjacent to the iliopsoas tendon (*white arrow*), which shows a normal hypointense signal on T2-weighted image

Fig. 13.12 T2-weighted axial TSE sequence of a 57-year-old woman (TR 2,870 ms/TE 57 ms, slice thickness 2 mm) shows also the iliopsoas/iliopectinea bursitis (*white arrowheads*) and small incomplete septations

Table 13.1 Different types of ML lesions

	Type 1	Type 2	Type 3	Type 4	Type 5	Type 6
	Seroma	Subcutaneous hematoma	Chronic organizing hematoma	Closed lazeration	Pseudo-nodular	Infected
Morphology	Laminar	Oval	Oval	Linear	Round	Variable sinus tract
Capsule	Occasional	Thin	Thick	Absent	Thin/ thick	Thick
T1-signal	Hypointense	Hyperintense	Intermediate	Hypointense	Variable	Variable
T2-signal	Hyperintense	Hyperintense	Heterogeneous	Hyperintense	Varible	Variable
Contrast enhancement	Absent	Variable	Internal/peripheral	Variable	Internal/ peripheral	Internal/ peripheral

application, the wall enhances peripherally [28] (Figs. 13.11 and 13.12).

Posttraumatic Lesions: Morel Lavallée Lesion

The exposed nature of the trochanteric and hip region as well as the proximal thigh, the great extension and firm attachment of the anterolateral fascia and iliotibial band, the mobility of skin and the rich pattern of local dermic vascularization may account for the high frequency of lesions in this area [29, 30]. Posttraumatic fluid collections dissecting subcutaneous fatty tissue were first described by Victor Auguste François Morel-Lavallée [31]. The classic description of ML lesion refers to fluctuant subcutaneous cystic structures lined by a fibrous capsule and filled with a sterile hemolymphatic or serohematic content.

ML effusions are well known to the orthopedic surgeons resulting from tangential trauma, most commonly in the setting of high speed motorcycle accidents usually in association with pelvic and acetabular fractures [29, 32]. They also can be occurred after plastic surgery such as liposuction and combined abdominoplasty [33].

ML lesions may be detected after trauma with swelling, contour deformity, or palpable bulge but may be missed in up to one third of cases and may be detected after a month or even years when the acute lesions are already resolved [29, 32, 34]. In the acute phase ML lesions require surgical intervention and debridement of necritic tissue to avoid the risk of any infection. Conservative therapy also may be attempted.

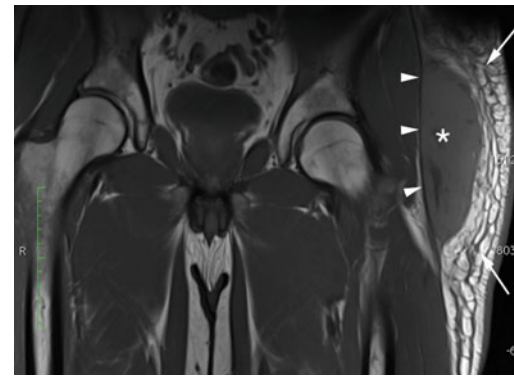

Fig. 13.13 T1-weighted coronal image (TR 731 ms/TE 20 ms, slice thickness 6 mm) of a 47-year-old male patient after trauma (bicycle accident) showing a Type 1 ML lesion. The left thigh demonstrates an oval hypointense lesion (*asterisk*) which disects the virtual space between the subcutaneous fatty tissue (*arrows*) and the iliotibial band (*arrowheads*)

MR imaging features are very variable and show different signal intensity, partial or complete separations, and fluid–fluid levels. There is a partial or complete peripheral rim possible which represents a fibrous capsule. Different types of ML lesions (Type 1–5) showing different imaging parameters described in Table 13.1 [35].

Differential diagnosis including other subcutaneous lesions with posttraumatic background such as fat necrosis, coagulopathy-related hematoma, pseudolipoma, or soft tissue tumors (Figs. 13.13, 13.14, and 13.15).

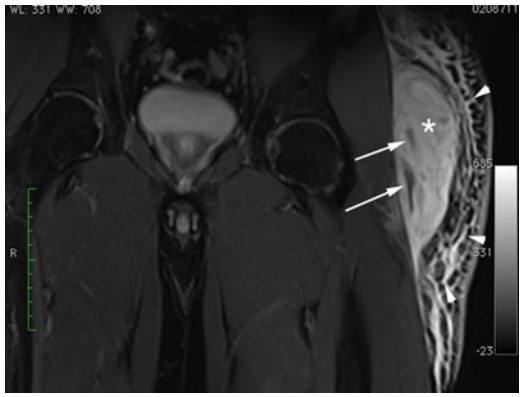

Fig. 13.14 Coronal STIR (short tau inversion recovery) image (TR 5,930 ms/TE 29 ms/TI 150 ms slice thickness 6 mm) of a 47-year-old male patient showing a Type 1 ML lesion (*asterisk*) with hypointense signal within the lesion as small areas of hemorrhage (*arrows*). Also note the fluid imbibition (*arrowheads*) and severe swelling of the subcutaneous fatty tissue

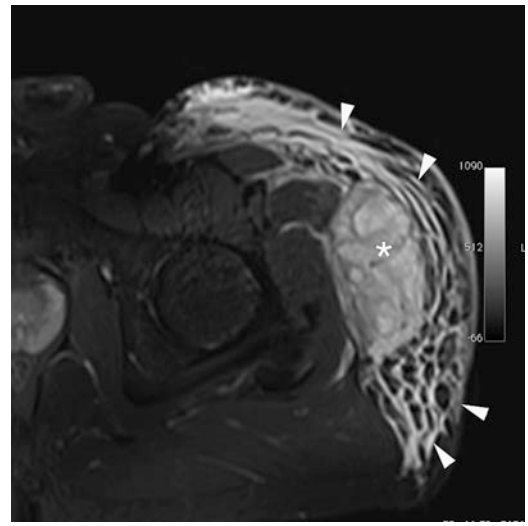

Fig. 13.15 Axial STIR (short tau inversion recovery) image (TR 3,500 ms/TE 29/TI 150 ms, slice thickness 5 mm) of the same patient as in Figs. 13.13 and 13.14 with a Type 1 ML lesion (*asterisk*) and the fluid imbibition as well as the swelling of the subcutaneous fatty tissue (*arrowheads*)

Liposclerosing Myxofibrous Tumor

Liposclerosing myxofibrous tumor (LSMFT) is a benign fibro-osseous lesion characterized by a complex mixture of histologic elements, which may include lipoma, fibroxanthoma, myxoma, myxofibroma, fibrous dysplasia–like features, cyst formation, fat necrosis, ischemic ossification, and, rarely, cartilage [36–38]. The designation of "sclerosing" refers to the intralesional bone formed or mineralized within altered fat. The term "myxofibrous" refers to the fibrous or myxofibrous areas that may demonstrate metaplastic curvilinear or circular woven bone ossicles and/or dystrophic mineralization in necrotic fat.

The lesion shows a histologic complexity but with a characteristic radiologic appearance and skeletal distribution and is associated with an increased prevalence of malignant transformation compared to fibrous dysplasia and other benign fibro-osseous lesions [39].

The origin of LSMFT is not clear, but it is suspected a combination of changes in the altered fat of a partially involuted lipoma or lipogenic lesion of bone with superimposed proliferative change [39].

The prevalence of a malignant transformation is described in the literature between 10 and 16 % in most of the cases to an osteosarcoma or a malignant fibrous histiocytoma [36, 37, 39].

LSMFT of bone is found in most of the cases in femur (85 %). Approximately 91 % are located proximally in the intertrochanteric region. Pain is the most common presenting clinical symptom and the duration of pain varies from a few weeks to 10 years. The lesion is an incidental finding in about 41 % of patients [39].

The radiographs show a well-defined, geographic lytic lesion with a sclerotic margin. Marginal sclerosis is always present but the amount is variable.

On MR images the lesion is well-defined with a variable-thickness peripheral rim of low signal intensity that corresponds to the sclerosis is seen on the radiographs. On the T1-weighted images, the lesion is normally homogeneous with a signal similar to that of skeletal muscle. On T2-weighted images, it is mildly to moderately heterogeneous, with a signal intensity equal to or greater than that of fat. The inversion recovery

Fig. 13.16 Intermediate-weighted fat-saturated coronal MR image of a 25-year-old male patient presenting with hip pain (TR 2,300 ms, TE 10 ms, slice thickness 3 mm) shows a well-defined intertrochanteric lesion (*arrow*) with isointense signal compared to muscle tissue

Fig. 13.17 Presents the corresponding T1-weighted coronal image (TR 700 ms, TE 12 ms, slice thickness 3 mm) shows the lesion (*arrow*) also with a signal similar to that of skeletal muscle

MR images (STIR) show markedly increased signal intensity. There is normally no lesion to demonstrate a signal intensity of fat [39] (Figs. 13.16, 13.17, and 13.18).

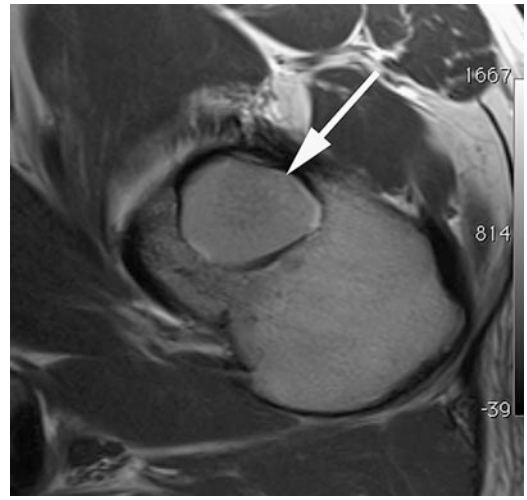

Fig. 13.18 Corresponding T1-weighted transverse image (TR 600 ms, TE 23 ms, slice thickness 4 mm) shows the lesion (*arrow*) with the hypointense sclerotic rind

References

1. Armfield DR, Towers JD, Robertson DD. Radiographic and MR imaging of the athletic hip. Clin Sports Med. 2006;25(2):211–39.
2. Newberg AH, Newman JS. Imaging the painful hip. Clin Orthop Relat Res. 2003;406:19–28.
3. Hong RJ, Hughes TH, Gentili A, Chung CB. Magnetic resonance imaging of the hip. J Magn Reson Imaging. 2008;27(3):435–45.
4. Jeanneret L, Kurmann PT, van Linthoudt D. Rotator cuff tear of the hip [in French]. Rev Med Suisse. 2008;4(157):1226–9.
5. Kingzett-Taylor A, Tirman PF, Feller J, et al. Tendinosis and tears of gluteus medius and minimus muscles as a cause of hip pain: MR imaging findings. AJR Am J Roentgenol. 1999;173(4):1123–6.
6. Nazarian S, Tisserand P, Brunet C, Müller ME. Anatomic basis of the transgluteal approach to the hip. Surg Radiol Anat. 1987;9(1):27–35.
7. Dwek J, Pfirrmann C, Stanley A, Pathria M, Chung CB. MR imaging of the hip abductors: normal anatomy and commonly encountered pathology at the greater trochanter. Magn Reson Imaging Clin N Am. 2005;13(4):691–704.
8. Resnick D, Niwayama G. Entheses and enthesopathy: anatomical, pathological, and radiological correlation. Radiology. 1983;146(1):1–9.
9. Gordon EJ. Trochanteric bursitis and tendinitis. Clin Orthop Relat Res. 1961;20:193–202.
10. Bunker TD, Esler CN, Leach WJ. Rotator-cuff tear of the hip. J Bone Joint Surg Br. 1997;79(4):618–20.

11. Steinert L, Zanetti M, Hodler J, Pfirrmann CW, Dora C, Saupe N. Are radiographic trochanteric surface irregularities associated with abductor tendon abnormalities? Radiology. 2010;257(3):754–63.
12. Chung CB, Robertson JE, Cho GJ, Vaughan LM, Copp SN, Resnick D. Gluteus medius tendon tears and avulsive injuries in elderly women: imaging findings in six patients. AJR Am J Roentgenol. 1999;173(2):351–3.
13. Cormier G, Berthelot JM, Maugars Y, SRO (Société de Rhumatologie de l'Ouest). Gluteus tendon rupture is underrecognized by French orthopedic surgeons: results of a mail survey. Joint Bone Spine. 2006;73(4):411–3.
14. Lequesne M, Djian P, Vuillemin V, Mathieu P. Prospective study of refractory greater trochanter pain syndrome: MRI findings of gluteal tendon tears seen at surgery—clinical and MRI results of tendon repair. Joint Bone Spine. 2008;75(4):458–64.
15. Kagan A 2nd. Rotator cuff tears of the hip. Clin Orthop Relat Res. 1999;(368):135–40.
16. Miozzari HH, Dora C, Clark JM, Nötzli HP. Late repair of abductor avulsion after the transgluteal approach for hip arthroplasty. J Arthroplasty. 2010;25(3):450–7.
17. Segal NA, Felson DT, Torner JC, et al. Greater trochanteric pain syndrome: epidemiology and associated factors. Arch Phys Med Rehabil. 2007;88(8):988–92.
18. Bird PA, Oakley SP, Shnier R, Kirkham BW. Prospective evaluation of magnetic resonance imaging and physical examination findings in patients with greater trochanteric pain syndrome. Arthritis Rheum. 2001;44(9):2138–45.
19. Blankenbaker DG, Ullrick SR, Davis KW, De Smet AA, Haaland B, Fine JP. Correlation of MRI findings with clinical findings of trochanteric pain syndrome. Skeletal Radiol. 2008;37(10):903–9.
20. Polster JM, Elgabaly M, Lee H, Klika A, Drake R, Barsoum W. MRI and gross anatomy of the iliopsoas tendon complex. Skeletal Radiol. 2008;37(1):55–8.
21. Blankenbaker DG, Tuite MJ. Iliopsoas musculotendinous unit. Semin Musculoskelet Radiol. 2008;12(1):13–27.
22. Fredberg U, Hansen LB, Kissmeyer-Nielsen P, Torntoft EB. Iliopsoas tendinitis in athletes. Diagnosis and treatment. Ugeskr Laeger. 1995;157(28):4031–3.
23. Shabshin N, Rosenberg ZS, Cavalcanti CF. MR imaging of iliopsoas musculotendinous injuries. Magn Reson Imaging Clin N Am. 2005;13(4):705–16.
24. Johnston CA, Wiley JP, Lindsay DM, Wiseman DA. Iliopsoas bursitis and tendinitis. Sports Med. 1998;25(4):271–83.
25. Bui KL, Ilaslan H, Recht M, Sundaram M. Iliopsoas injury: an MRI study of patterns and prevalence correlated with clinical findings. Skeletal Radiol. 2008;37(3):245–9.
26. Pfirrmann CW, Chung CB, Theumann NH, Trudell DJ, Resnick D. Greater trochanter of the hip: attachment of the abductor mechanism and a complex of three bursae–MR imaging and MR bursography in cadavers and MR imaging in asymptomatic volunteers. Radiology. 2001;221(2):469–77.
27. Armstrong P, Saxton H. Ilio-psoas bursa. Br J Radiol. 1972;45(535):493–5.
28. Wunderbaldinger P, Bremer C, Schellenberger E, Cejna M, Turetschek K, Kainberger F. Imaging features of iliopsoas bursitis. Eur Radiol. 2002;12(2):409–15.
29. Collinge C, Tornetta 3rd P. Soft tissue injuries associated with pelvic fractures. Orthop Clin North Am. 2004;35(4):451–6.
30. Hak DJ, Olson SA, Matta JM. Diagnosis and management of closed internal degloving injuries associated with pelvic and acetabular fractures: the Morel-Lavallee lesion. J Trauma. 1997;42:1046–105.
31. Morel-Lavallee VAF. Decollements traumatiques de la peau et des couches sous-jacentes. Arch Gen Med. 1863;1:20–38. 172–200, 300–32.
32. Letournel E. The treatment of acetabular fractures through the ilioinguinal approach. Clin Orthop Relat Res. 1993;292:62–76.
33. Zecha PJ, Missotten FE. Pseudocyst formation after abdominoplasty:extravasations of Morel-Lavallee. Br J Plast Surg. 1999;52(6):500–2.
34. Hudson DA, Knottenbelt JD, Krige JE. Closed degloving injuries: results following conservative surgery. Plast Reconstr Surg. 1992;89:853–5.
35. Mellado JM, Bencardino JT. Morel-Lavallee lesion: review with emphasis on MR imaging. Magn Reson Imaging Clin N Am. 2005;13:775–82.
36. Ragsdale BD, Sweet DE. Bone. In: Henson DE, Albores-Saavedra J, editors. The pathology of incipient neoplasia. Philadelphia, PA: Saunders; 1986. p. 381–423.
37. Ragsdale BD. Polymorphic fibro-osseous lesions of bone: an almost site-specific diagnostic problem in the proximal femur. Hum Pathol. 1993;24:505–12.
38. Gilkey FW. Liposclerosing myxofibrous tumor of bone (letter). Hum Pathol. 1993;24:1264.
39. Kransdorf MJ, Murphey MD, Sweet DE. Liposclerosing myxofibrous tumor: a radiologic-pathologic-distinct fibro-osseous lesion of bone with a marked predilection for the intertrochanteric region of the femur. Radiology. 1999;212:693–8.

Cartilage Damage

14

T. Charles Mamisch

MR is the only "almost" noninvasive method, to assess the extent and pattern of cartilage damage [1, 2] in the hip joint, whether the examination is performed on a 1.5 or 3 T [3] system, direct or indirect arthrography is used, or biochemical imaging, like dGeMRIC, is added.

To assess the extent of cartilage damage in early stages of osteoarthritis, MRI is necessary due to the fact that conventional roentgen images are inadequate [4] in detecting the extent of early cartilage damage. Clinically, detection of early cartilage degeneration is important given the fact that current surgical treatment to preserve the joint is ineffective in advance stages of osteoarthritis (OA). Having objective prognosticating information is very important in facilitating the discussion between the surgeon and patient regarding the choice of optimal treatment and setting the appropriate expectation regarding treatment outcome. In the late stages of OA, MRI only provides information on the loss of the cartilage, hence MR imaging should focus on detecting early disease (Fig. 14.1).

There are different imaging protocols and approaches in detecting cartilage lesions of the hip using MRI; however, there is one common element for all protocols—high resolution. It is difficult to separate the femoral cartilage from the acetabular cartilage layer because of the thin cartilages of the femoroacetabular joint and the circumferential geometry, hence high image resolution is the key!

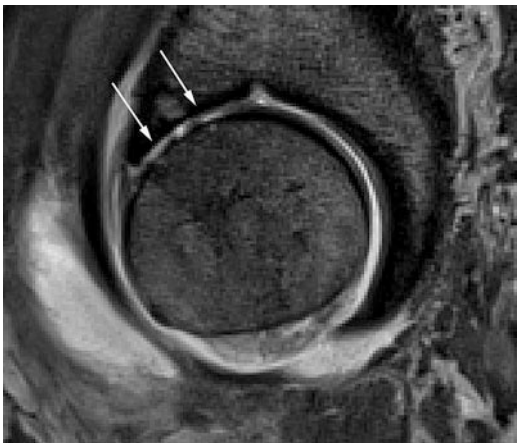

Fig. 14.1 Cartilage degeneration in late stage of OA disease with complete loss of femoral and acetabular cartilage (*white arrows*)

Current Status MR Imaging of Hip Joint Cartilage Damage

Compared with the well-established techniques for detecting osteonecrosis and for evaluating the acetabular labrum, techniques for assessing cartilage lesions in the hip have been disappointing. As in the detection of acetabular labrum lesions, both non-contrast techniques and MR arthrography are used.

T.C. Mamisch (✉)
Department of Radiology, Brigham & Women's Hospital, 75 Francis Street, Boston, MA, USA
e-mail: charles.mamisch@mdh-ag.de

Y.-J. Kim (eds.), *Hip Magnetic Resonance Imaging*,
DOI 10.1007/978-1-4614-1668-5_14,

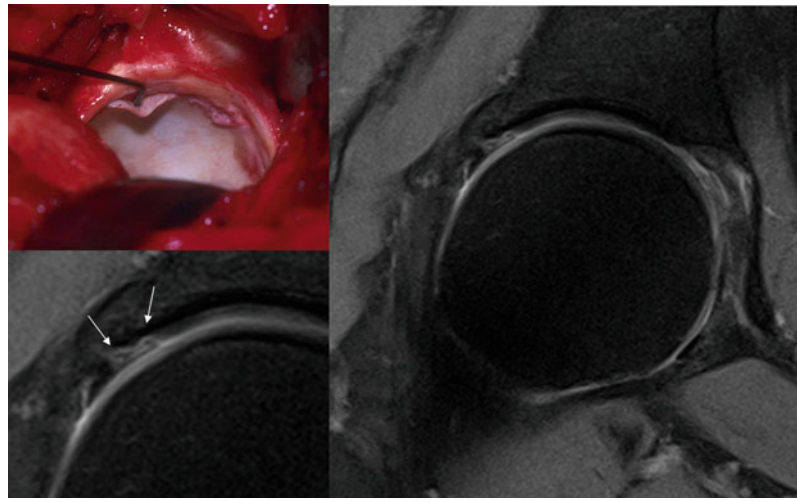

Fig. 14.2 Cartilage delemination in patient with femoroacetabular impingement. Diagnosis by high-resolution non-contrast PD TSE sequence (0.3 × 0.3 × 3 mm) at 3 T using fat saturation

Non-contrast techniques, using two- and three-dimensional sequences, analyze mainly thickness patterns to detect osteoarthritic changes [5]. The sensitivity for these measurements is reported to be 47 % for grade 1 lesions and 49 % for grade 2 lesions. The low diagnostic sensitivities suggest that these measurements are more useful in follow-up studies. Mintz et al. [6] also tried to classify cartilage based on cartilage thickness and signal intensity changes according to the Outerbridge score, but the results were unreliable. Therefore, they compared only grades 1 through 3 lesions to no lesion (grade 0) for sensitivity and accuracy. Thus, the results are comparable to thickness measurement studies with the same limitations.

With the use of MR arthrography, the detection of cartilage lesions can be improved. Schmidt et al. [1] assessed improvement in cartilage diagnosis using MR arthrography, but the classification within this study was done without staging or grading, and the sensitivity was only moderate (47 %). Additionally, the analysis was limited by low spatial resolution, restriction to two-dimensional imaging, and low signal-to-noise ratio due to field strength of only 1.0 or 1.5 T; hence, it was not possible to separate the femoral and acetabular cartilages. High interobserver variability was reported.

Beaule et al. [7] investigated cartilage delamination using MR arthrography and its correlation with intraoperative findings in four patients. They classified surgically observed cartilage delamination using the Beck classification. Beaule et al. found that MR arthrography was only able to detect a cleavage lesion (with a frayed edge). MR arthrography did not detect debonding, which is where the cartilage appears macroscopically sound but is detached from bone (carpet phenomenon). This carpet lesion is an early phase of chondral damage seen in patients with FAI. Therefore, early detection of cartilage degeneration appears limited using MR arthrography in FAI.

Pfirrmann et al. [8] showed high specificity for detecting cartilage lesion in patients with FAI by detection fluid under the cartilage delamination; however, sensitivity is low. Hypointense areas in the acetabular cartilage seen on intermediate-weighted fat-saturated or T1-weighted images appear to be helpful diagnostic criteria.

Overall, the cartilage diagnosis in the hip is limited so far and no reliable staging and grading system has been established. However, using dedicated coils and high-resolution imaging, the delamination of the cartilage as described by Beaule and Pfirrmann can be detected with high specificity (Fig. 14.2).

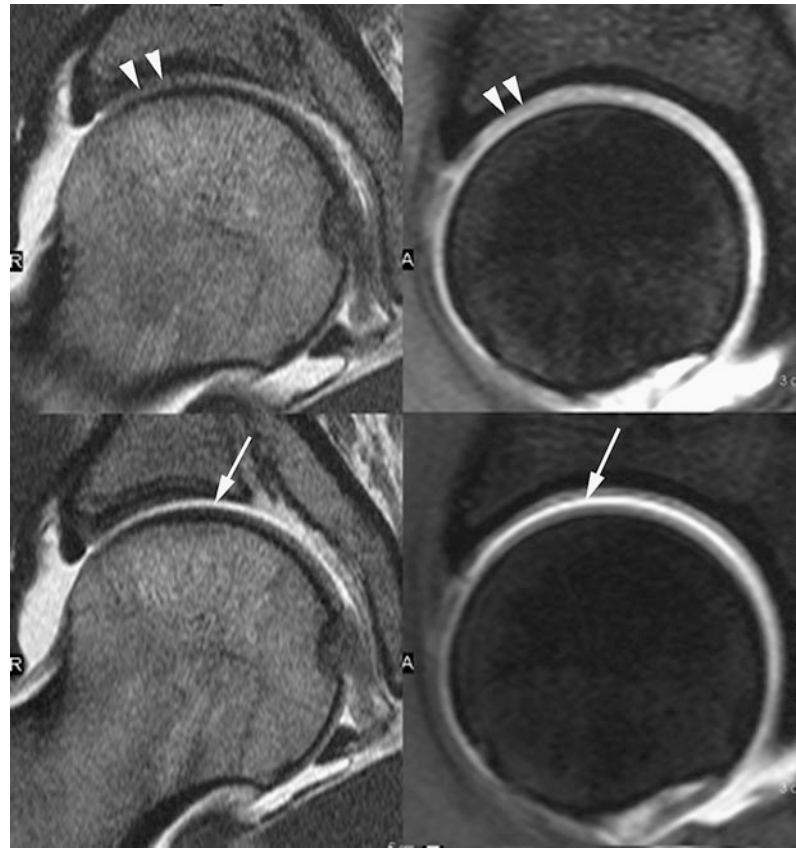

Fig. 14.3 1.5 T MR images of an 28-year-old male patient show in the *upper row* a coronal intermediate-weighted sequence (TR/TE 3,540/39 ms, matrix 256 × 256, FOV 160 × 100 mm) and a sagittal T2 weighted 3D DESS sequence (TR/TE 25.16/8.56 ms, matrix 256 × 192, FOV 150 × 100 mm) without traction and with traction in the *lower row*. The *lower row* shows very well the cartilage surfaces, femoral and acetabular, and even the cartilage interface with contrast media (*white arrows*) between them. In the *upper row* both cartilage interfaces are not distinguishable from each other (*white arrowheads*)

Cartilage Damage Detection Using Leg Traction

One method to overcome the limitation of assessment of cartilage damage in the hip is to separate the femoral and acetabular cartilages with the use of traction as described by Llopis et al. [9]. They showed the potential advantage of applying manual traction followed by gentle leg traction during MR arthrography of the hip. Such traction produces enough space for the intra-articular contrast agent to enter the tight central compartment. This combination of contrast agent and additional space allows visualization of the cartilage surfaces as distinct entities. The limited traction is well tolerated and can be applied in a short time without specialized equipment. The arbitrarily chosen 6 kg of traction is well within the traction force used during arthroscopy, and no adverse effects such as transient neuropraxia occurred.

MR Imaging at 3 T

Recent developments in high-resolution and cartilage-specific imaging, including the introduction of novel sequences, local gradient and radio frequency coils, and high field strength, have improved the diagnostic potential of MRI to depict different structural and compositional characteristics of articular cartilage and are therefore focused on improving characterization of morphological and structural changes. Besides novel MR sequences, imaging quality can mainly improved by using higher field strengths because they provide a higher intrinsic SNR—critical for high-resolution imaging. There are preliminary studies published on the use of 3 T imaging in the hip revealing the capability of improvement in cartilage diagnosis due to high-resolution imaging and, in addition, the possibility of accurate hip imaging without the need for contrast agent.

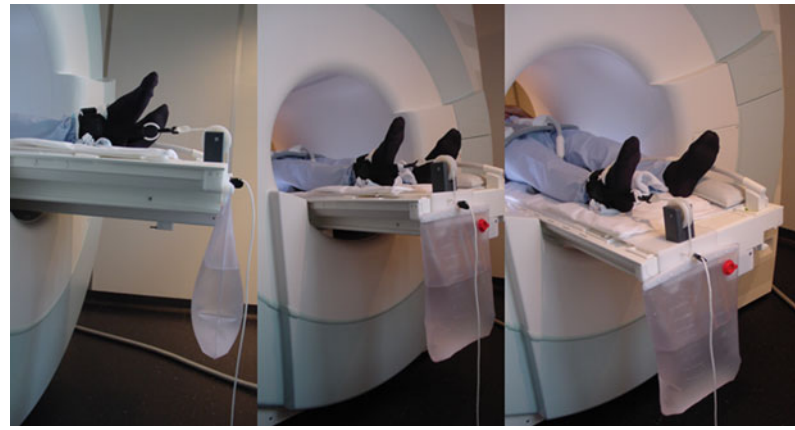

Fig. 14.4 Traction device. Photographs show a lifting block loaded with a 6 kg water bag in male patients (Balgrist University Hospital Zurich, Switzerland)

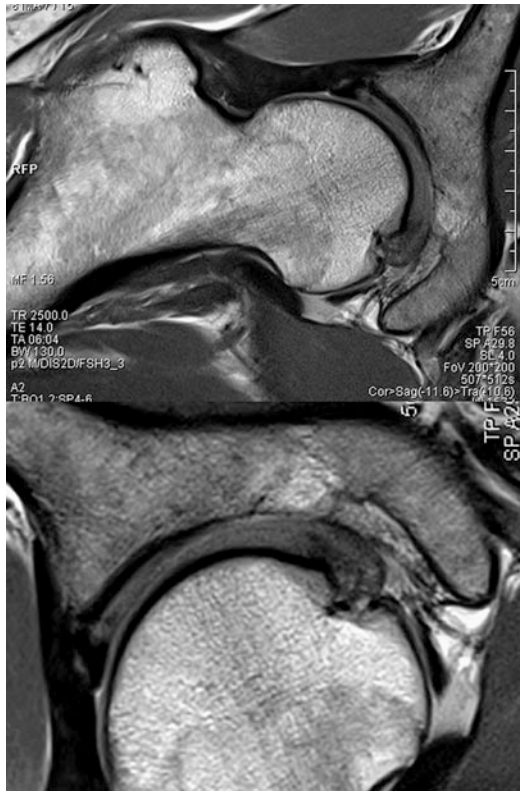

Fig. 14.5 PD TSE oblique coronal view. Note the separation of femoral and acetabular cartilage (non-contrast) and the clear assessment of acetabular labrum and adjacent cartilage

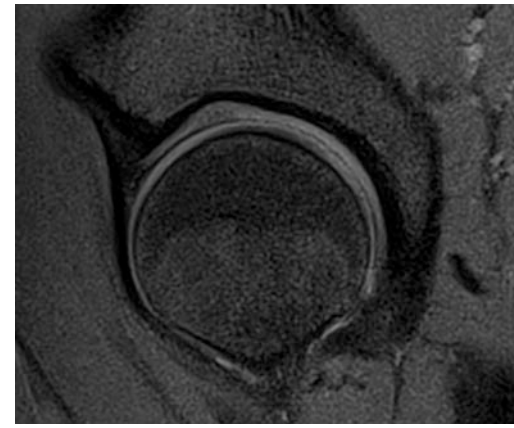

Fig. 14.6 Oblique sagittal PD TSE sequence (with fat saturation). Note the separation of femoral and acetabular cartilage (non-contrast) and the clear assessment of acetabular labrum and adjacent cartilage

Figures 14.3 and 14.4 show examples of high-resolution proton density (PD) weighted TSE (with and without fat saturation) imaging at 3 T without the use of contrast agents. Visualization of acetabular and femoral cartilage separation as well as assessment of the acetabular labrum and adjacent cartilage, essential for precise diagnosis of FAI, can be improved by using high-resolution techniques (Figs. 14.5 and 14.6).

The use of 3.0-T imaging, in combination with MR arthrography, in the future can overcome these limitations and improve cartilage diagnosis significantly. Nevertheless, distinguishing the femoral cartilage layer from the acetabular cartilage layer will remain challenging because the cartilage of the femoroacetabular joint is thin and the cavity is circumferential.

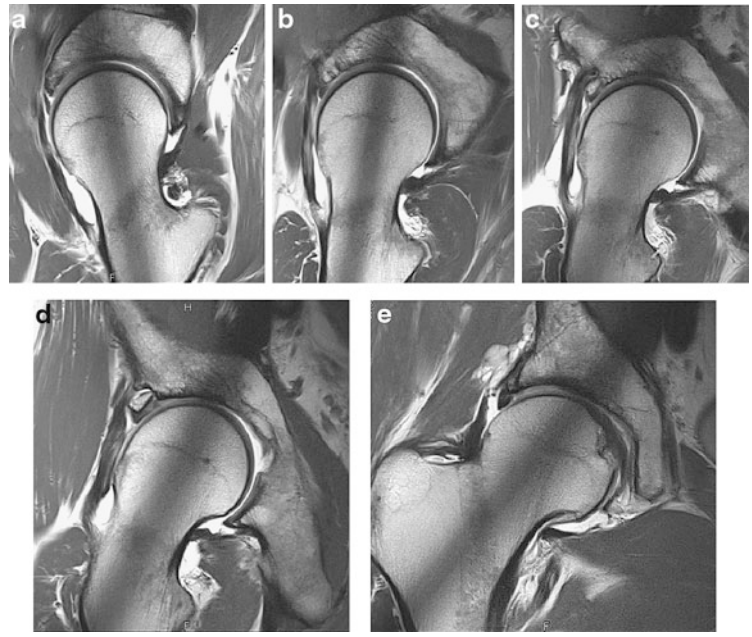

Fig. 14.7 (**a**–**e**) Radial PD TSE sequence around the femoral neck in patient with CAM type impingement. (**a**) Anterior Labral damage (tear). (**b–d**) Anterior-Superior acetabular cartilage degeneration with brighter signal. (**e**) Posterior normal labrum and no cartilage pathologies

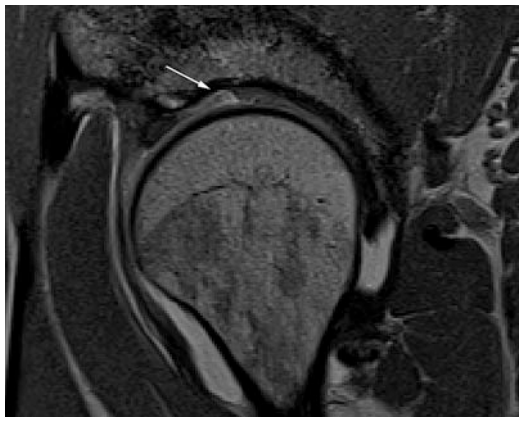

Fig. 14.8 Oblique sagittal PD TSE sequence perpendicular to the acetabular rim. Delamination of the acetabular cartilage with increased signal between cartilage flap and bone

Fig. 14.9 Radial PD TSE sequence around the femoral neck. Malacia of the acetabular cartilage with increased signal (*white arrows*)

Assessment of Cartilage Damage in Femoroacetabular Impingement

The goal of assessing cartilage damage in FAI is a combination of assessing the morphology and the spatial pattern of the cartilage lesion. Therefore, radial imaging (Fig. 14.7) is often used in addition to oblique coronal and sagittal sequences to diagnose cartilage lesion in all locations around the joint with minimal partial voluming.

The cartilage damage in the acetabulum mainly begins at the anterosuperior rim and usually this is where the labral-chondral separation

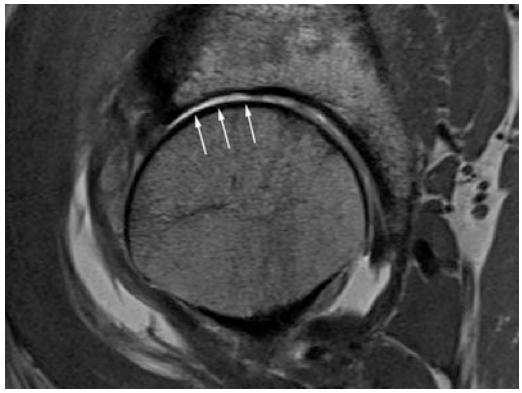

Fig. 14.10 Advanced cartilage degeneration in patient with CAM impingement with loss of acetabular and femoral cartilage in anterior-superior area and extension towards central area (*white arrows*). Femoral head starts to migrate into the defect

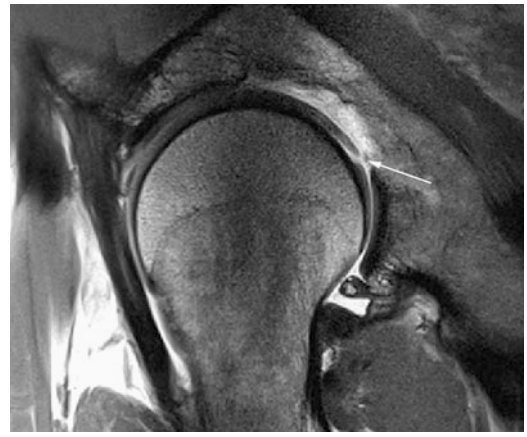

Fig. 14.12 MR arthrography in patient with CAM type impingement. Cartilage tear of the femoral cartilage (*white arrow*)

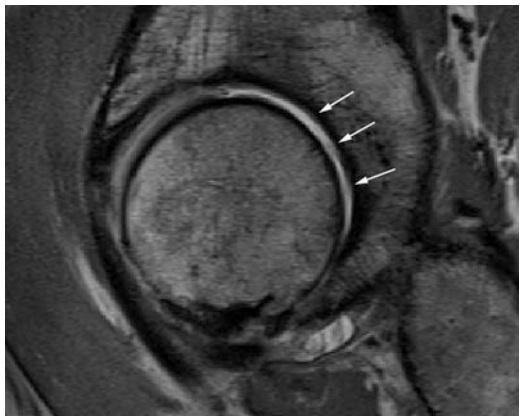

Fig. 14.11 Advanced cartilage degeneration in typical posterior location in patient with PINCER impingement (*white arrows*)

Fig. 14.13 MR arthrography in patient with PINCER type impingement and advanced cartilage degeneration. Central lesion of femoral and acetabular cartilage

is located. In most cases of cam FAI there is a small band of cartilage abrasion along the outer rim of acetabulum. This damage is best seen when the contrast material gets within the gap between femoral cartilage and the thinned acetabular cartilage. The flap is seen as a sheet of cartilage loosened from the bone with contrast medium between bone and flap (Fig. 14.8).

The cartilage separated from his bony base will undergo further malacia and therefore change intensity to a brighter signal (Fig. 14.8). More fresh flaps may be hardly visible when the flap is reduced and pressed against the subchondral bone.

In advanced cases the cartilage thinning or even deficiencies extend towards the center of the acetabulum (Fig. 14.9). In some cases, focal cartilage ulceration becomes visible (Fig. 14.10).

In pincer FAI, there is also a cartilage abrasion postero-inferiorly; it is explained as "contrecoup lesion" of the leverage (Fig. 14.11).

With further progression of chondral damage, cartilage thinning of the femoral head takes place at the site of impingement and the head migrates into the defect. Later it extends to the center, around the fovea, and even showing tears (Fig. 14.12) or further degeneration (Fig. 14.13) of the femoral cartilage.

References

1. Schmid MR, Notzli HP, Zanetti M, Wyss TF, Hodler J. Cartilage lesions in the hip: diagnostic effectiveness of MR arthrography. Radiology. 2003;226(2):382–6.
2. Locher S, Werlen S, Leunig M, Ganz R. [MR-arthrography with radial sequences for visualization of early hip pathology not visible on plain radiographs]. Z Orthop Ihre Grenzgeb. 2002;140(1):52–7.
3. Sundberg TP, Toomayan GA, Major NM. Evaluation of the acetabular labrum at 3.0-T MR imaging compared with 1.5-T MR arthrography: preliminary experience. Radiology. 2006;238(2):706–11.
4. Locher S, Werlen S, Leunig M, Ganz R. [Inadequate detectability of early stages of coxarthrosis with conventional roentgen images]. Z Orthop Ihre Grenzgeb. 2001;139(1):70–4.
5. Nishii T, Nakanishi K, Sugano N, et al. Articular cartilage evaluation in osteoarthritis of the hip with MR imaging under continuous leg traction. Magn Reson Imaging. 1998;16(8):871–5.
6. Mintz DN, Hooper T, Connell D, Potter H. Magnetic resonance imaging of the hip: detection of labral and chondral abnormalities using noncontrast imaging. Arthroscopy. 2005;21(4):385–93.
7. Beaulé PE, Zaragoza E, Copelan N. Magnetic resonance imaging with gadolinium arthrography to assess acetabular cartilage delamination. A report of four cases. J Bone Joint Surg Am. 2004;86-A (10):2294–8.
8. Pfirrmann CW, Mengiardi B, Dora C, Kalberer F, Zanetti M, Hodler J. Cam and pincer femoroacetabular impingement: characteristic MR arthrographic findings in 50 patients. Radiology. 2006;240(3):778–85.
9. Llopis E, Cerezal L, Kassarjian A, Higueras V, Fernandez E. Direct MR arthrography of the hip with leg traction: feasibility for assessing articular cartilage. AJR Am J Roentgenol. 2008;190 (4):1124–8.

Structural Assessment

15

Christoph Zilkens and Bernd Bittersohl

Introduction

Despite its high intrinsic stability due to its ball-and-socket configuration, the hip joint maintains a wide range of motion. However, structural deviations of the hip joint anatomy may produce abnormal forces throughout the joint, putting the hip at risk of developing early osteoarthritis (OA). Such variations in the acetabulum or proximal femur may be classified, in accordance with Tschauner's classification scheme [1], as follows:

1. Variations in acetabular size/femoral head coverage:
   (a) Acetabular dysplasia
   (b) Acetabular protrusio
2. Variations in acetabular version:
   (a) Abnormal anteversion
   (b) Insufficient anteversion, relative retroversion, retroversion
3. Variations in femoral version (=torsion):
   (a) Abnormal antetorsion (coxa antetorta)
   (b) Insufficient antetorsion, relative retrotorsion, retrotorsion (coxa retrotorta)
4. Variations in femoral head/neck offset (femoral offset)
5. Variations in acetabular/femoral head/neck offset (femoroacetabular offset).

C. Zilkens (✉)
Department of Orthopedics, Heinrich-Heine University, Medical School, Düsseldorf, Moorenstr. 5, 40225 Düsseldorf, Germany
e-mail: christoph.zilkens@med.uni-duesseldorf.de

The aim of this chapter is to illustrate the magnetic resonance imaging (MRI) techniques used to assess hip joint structure, including the standard acetabular and femoral metrics that are used in the standard hip joint approach, and other recently described novel MRI techniques.

Magnetic Resonance Imaging

Previous sections of this book have described potential MRI techniques and sequences in great detail. In brief, in order to assess the hip joint structure, 1.5 or 3 T MRI scanners must be used in order to achieve the necessary signal-to-noise ratio (SNR) and resolution in a reasonable amount of time. The imaging protocol must include T1-, T2-, and proton-density [PD]-weighted sequences to reliably demonstrate anatomy, joint alignment, and marrow abnormality. A short tau inversion recovery (STIR) sequence may be utilized in order to detect bone marrow edema or cysts [2].

The patient is imaged in the supine position with a surface coil around the hip joint and the feet fixed in neutral hip rotation in order to ensure reproducibility. Axial, sagittal, and coronal planes are required for detailed hip joint assessment. In addition, radial images through the center of the femoral head and perpendicular to the acetabular rim are required in order to assess femoral and femoroacetabular offset throughout the hip joint (Fig. 15.1). Three-dimensional (3D) isotropic sequences are potential alternatives that

Y.-J. Kim (eds.), *Hip Magnetic Resonance Imaging*,
DOI 10.1007/978-1-4614-1668-5_15,

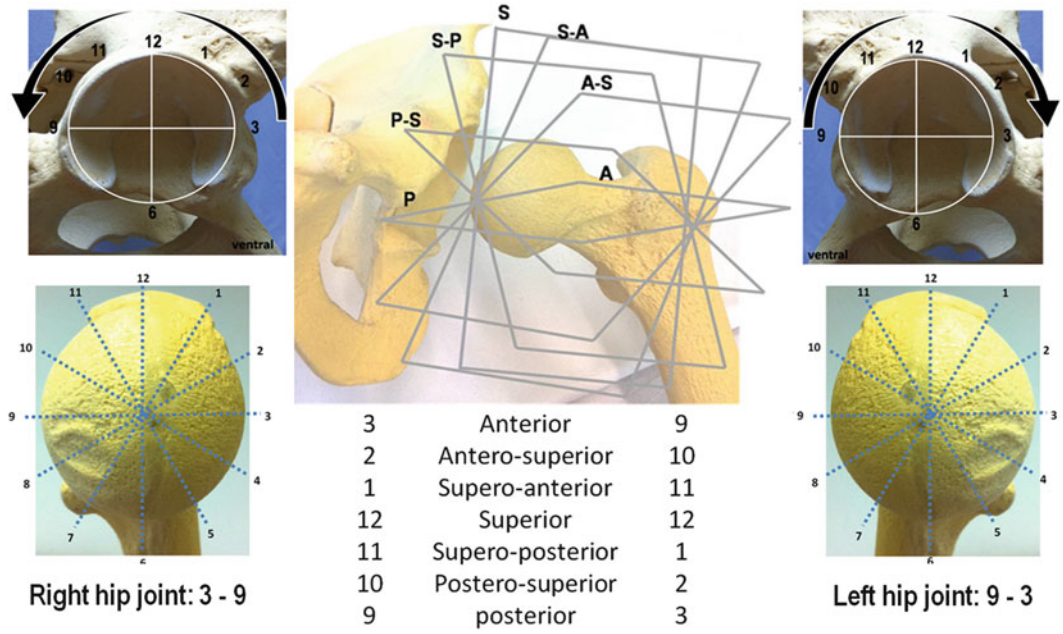

Fig. 15.1 Radial images through the center of the femoral head and perpendicular to the acetabular rim are created

offer high SNR, high resolution, lower partial volume-effects, and the advantage of 3D hip joint assessment.

Structural Assessment

Variations in Acetabular Size/Femoral Head Coverage

The size and configuration of the acetabulum can be measured utilizing radiographically established parameters, although baseline MRI values for the assessment of acetabular size/femoral head coverage are not currently available.

The lateral center–edge angle (LCA) and the ventral center–edge angle (VCA) may be measured in order to quantify the lateral and anterior femoral head coverage in accordance with the radiographic descriptions of Wiberg [3] and Lequesne and de Seze [4].

In MRI, the LCA is assessed on coronal images by measuring the angle between (1) a line perpendicular to the transverse axis of the pelvis through the center of the femoral head and (2) a line connecting the center of the femoral head with the most superolateral point of the acetabulum. The VCA is measured on sagittal images by measuring the angle between (1) a vertical line passing through the center of the femoral head and (2) a line connecting the center of the femoral head and the most anterior part of the acetabulum (Fig. 15.2).

According to Pfirrmann et al. [5], the acetabular depth can be quantified on transverse oblique images wherein the depth of the acetabulum is quantified as the distance between the center of the femoral head and a line connecting the anterior and posterior acetabular rim (Fig. 15.3). The value is classified as "positive" if the center of the femoral head is lateral to the line that connects the anterior and the posterior acetabular rim. In their study on patients with femoroacetabular impingement (FAI), Pfirrmann et al. noted that the acetabulum was significantly deeper in patients with pincer impingement arising by general or local femoral head overcoverage (coxa profunda, mean depth: 4.8 mm)

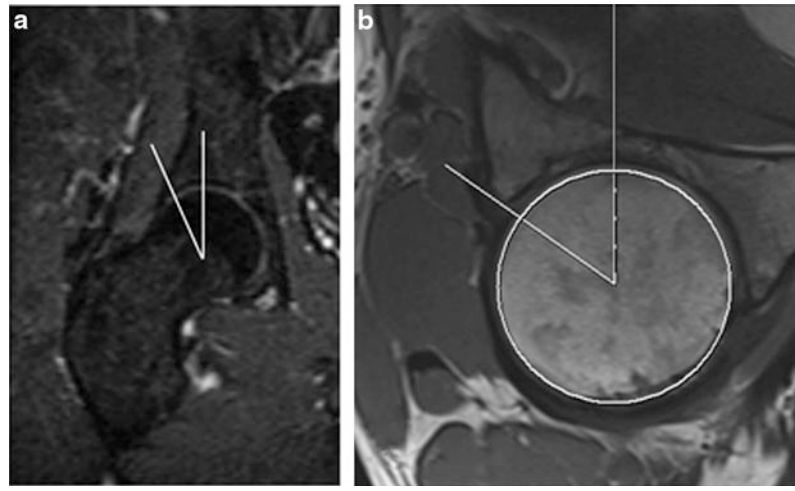

Fig. 15.2 Lateral center–edge angle (LCA) (**a**) and ventral center–edge angle (VCA) (**b**) assessment

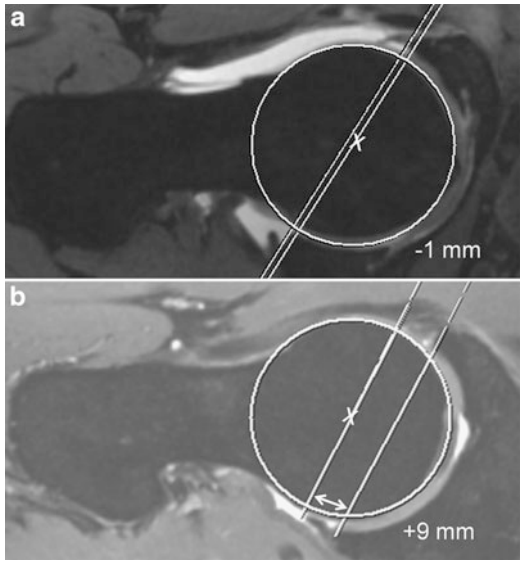

Fig. 15.3 Acetabular depth assessment according to Pfirrmann et al. [5]. The depth of the acetabulum is quantified as the distance between the center of the femoral head and a line connecting the anterior and posterior acetabular rim. The value is classed as positive if the center of the femoral head is lateral to the line that connects both the anterior and the posterior acetabular rim

compared to those with a cam impingement (mean depth: 0.7 mm) with an insufficient femoral offset but normal acetabulum configuration. However, as with the LCA and VCA measures, normative MRI values for the acetabular depth have yet to be determined.

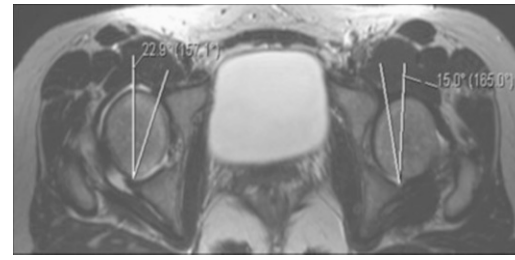

Fig. 15.4 Measurement of acetabular version. The acetabular version is obtained in the axial plane by measuring the angle between a *line* connecting the anterior and posterior rim, and a *line* extending anteriorly from the posterior wall. Of note, measurements of the acetabular version should be performed in multiple planes, i.e., cranially and centrally

Variations in Acetabular Version

The acetabular version, defined as the angle between (1) a line connecting the anterior and posterior rim of the acetabulum and (2) a line extending anteriorly from the posterior wall, is measured on axial images (Fig. 15.4). The acetabulum is normally anteverted by 15–25°. However, given the normal decrease in anteversion from superior to inferior [6], it is important to measure the acetabular version in various planes, i.e., cranially and centrally [7]. As noted earlier, baseline values, which originate from 3D imaging techniques such as MRI or CT, are not currently available.

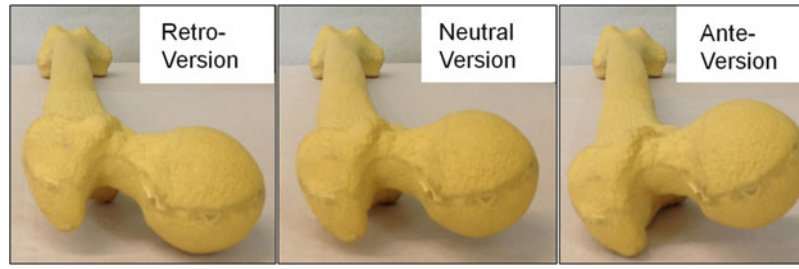

Fig. 15.5 Femoral retroversion (*left*), neutral version (*middle*), and anteversion (*right*)

Variations in Femoral Version

The femoral anteversion decreases from approximately 40° in childhood to 15° in adulthood. Clinically, patients with a pathological increase or decrease in femoral torsion may present with an in-toeing or out-toeing gait pattern. Notably, an abnormal femoral neck version has been associated with OA of the hip and knee, slipped capital femoral epiphysis (SCFE), and patella instability [6, 8, 9] (Fig. 15.5).

Several techniques have been described for the assessment of femoral version. According to Tomczak [10] and Koenig [11], the patient is placed on the MR table in the supine position with the hips and knees in neutral rotation. Transverse images are obtained through the hips and knees from the coronal localizer sequence. First, an image is chosen that illustrates both the femoral head and neck and an angle is drawn between a line along the length of the femoral neck and a horizontal line (femoral neck angle). Subsequently, an image of the knee joint that demonstrates the convexities of the posterior aspects of the femoral condyles is chosen and the angle between a line along the posterior aspect of the femoral condyles and a horizontal line is measured. The degree of femoral version is then determined by subtracting the angle measured at the femoral condyles from the femoral neck angle, if the distal femur is externally rotated relative to the femoral neck. Otherwise, if the distal femur is internally rotated relative to the femoral neck, the angle measured at the femoral condyles is added to the femoral neck angle. Figure 15.6 illustrates the measurement of the femoral version.

Variations in Femoral Head/Neck Offset (Femoral Offset)

The alpha angle reported by Nötzli et al. [12] is commonly used to assess the femoral offset. The alpha angle is the angle between (1) the axis along the femoral neck passing through the narrowest portion of the femoral neck and the center of the femoral head and (2) the axis connecting the center of the femoral head with the point at which the head contour extends beyond the best-fit circle around the perimeter of the femoral head (Fig. 15.7).

Dudda et al. [13] compared alpha-angle values measured on plain radiographs with values derived from radial MR images and noted higher alpha angles at the anterosuperior aspect of the head–neck junction. Notably, even when conventional radiographs appeared to be normal, an abnormally increased alpha angle was present anterosuperiorly, indicating that, without the use of radial imaging, asphericity is potentially underestimated.

Variations in Acetabular/Femoral Head/Neck Offset (Femoroacetabular Offset)

In contrast to the alpha angle, which exclusively involves the femoral site, the beta angle takes both joint partners (femur and acetabulum) and their potential deformities into consideration. The beta angle is drawn between (1) the axis connecting the center of the femoral head with the point at which the head contour extends beyond a best-fit circle around the perimeter of the femoral head and (2) a line

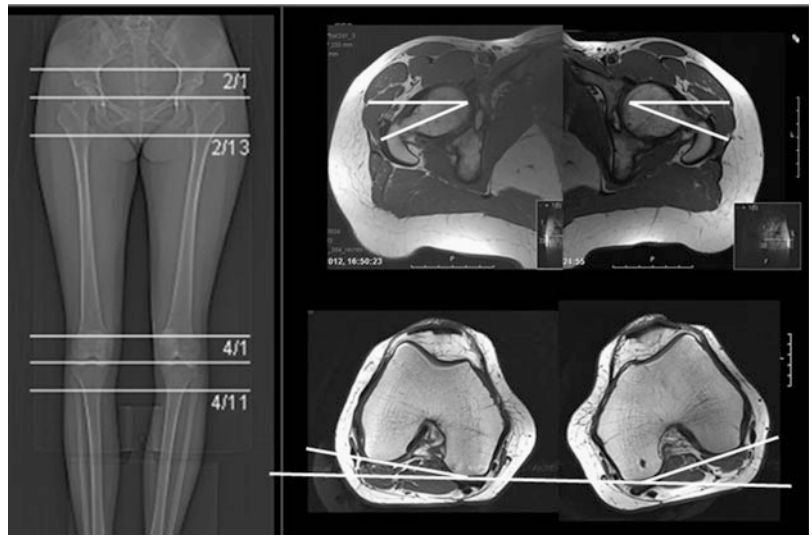

Fig. 15.6 Technique for the measurement of femoral version

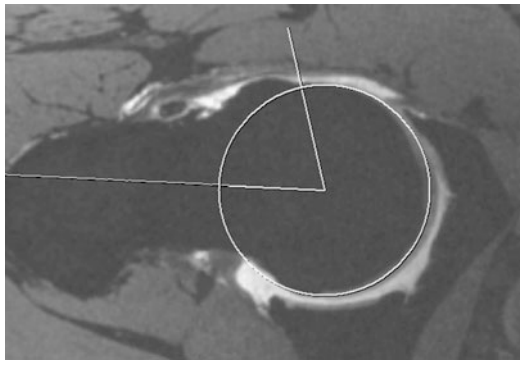

Fig. 15.7 Alpha angle measurement

that connects the femoral head with the acetabular rim [14, 15]. Three-dimensional, circumferential assessment of the femoroacetabular offset is feasible when performing beta angle measurements in radial images around the hip. Both alpha- and beta-angle measurements are illustrated in Fig. 15.8.

Summary

Structural deviations of the hip joint anatomy put the hip at risk of developing premature OA. Therefore, valid and reliable methods of assessment of hip joint structure are essential to provide the most favorable treatment at the right time. MRI is a standard modality for hip joint evaluation offering advantages such as 3D assessment and high soft-tissue contrast without the potential side effects of radiation. However, existing data lack baseline values, which are essential to differentiate between "normal" and "abnormal." Furthermore, unlike plain radiographic evaluation, MRI constantly bears the risk of measuring one parameter in somewhat different images/planes, thus compromising data reproducibility and validity. Therefore, it is essential to have reliable standards to minimize measurement errors and misinterpretations. It should also be emphasized that the metrics for the evaluation of acetabulum and femur illustrated above are parameters that originate from plain radiography and were adopted for hip evaluation with MRI. Therefore, the current data on MRI of the hip joint lack normative values, and inter- and intra-observer reliability for most of the described parameters have not yet been thoroughly investigated. Further studies that clearly define the various assessment methodologies by means of MRI that involve a sufficient number of healthy hip joints are needed in order to overcome these limitations and to obtain normal values for 3D hip joint assessment. This will improve comparability and reliability, both of which are essential for a valid diagnosis and proper treatment approach.

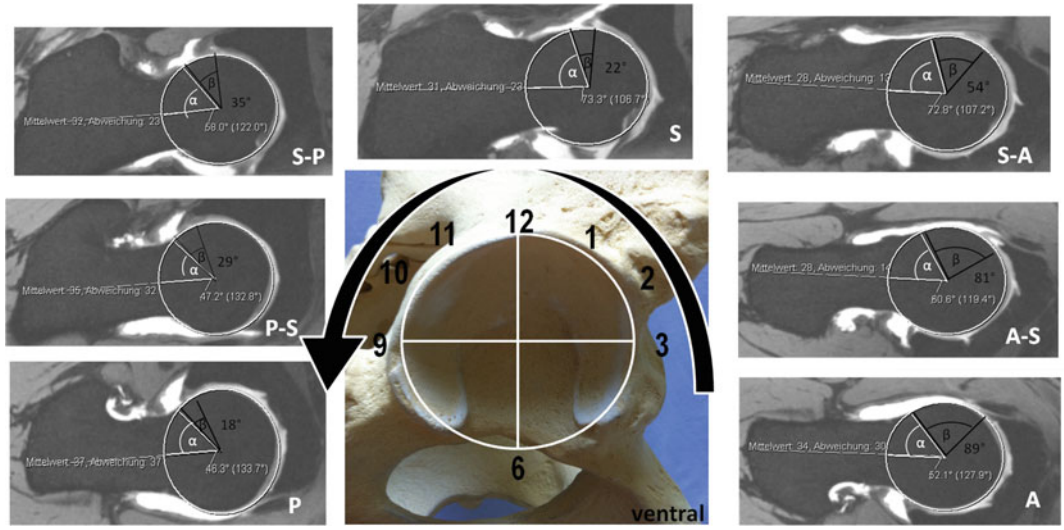

Fig. 15.8 Alpha- and beta-angle assessment on radial images. *Note*: *a* anterior, *a-s* anterosuperior, *s-a* supero-anterior, *s* superior, *s-p* superoposterior, *p-s* postero-superior, *p* posterior

References

1. Tschauner C, Fock CM, Hofmann S, Raith J. Rotational abnormalities of the hip joint. Radiologe. 2002;42(6):457–66.
2. Kassarjian A, Brisson M, Palmer WE. Femoroacetabular impingement. Eur J Radiol. 2007;63(1):29–35.
3. Wiberg G. Studies on dysplastic acetabula and congenital sublaxation of the hip joint. Acta Chir Scand. 1939;83 Suppl 58:5–135.
4. Lequesne M, de Seze. False profile of the pelvis. A new radiographic incidence for the study of the hip. Its use in dysplasias and different coxopathies. Rev Rhum Mal Osteoartic. 1961;28:643–52.
5. Pfirrmann CW, Mengiardi B, Dora C, Kalberer F, Zanetti M, Hodler J. Cam and pincer femoroacetabular impingement: characteristic MR arthrographic findings in 50 patients. Radiology. 2006;240(3):778–85.
6. Tonnis D, Heinecke A. Acetabular and femoral anteversion: relationship with osteoarthritis of the hip. J Bone Joint Surg Am. 1999;81(12):1747–70.
7. Dolan MM, Heyworth BE, Bedi A, Duke G, Kelly BT. CT reveals a high incidence of osseous abnormalities in hips with labral tears. Clin Orthop Relat Res. 2011;469(3):831–8.
8. Gelberman RH, Cohen MS, Shaw BA, Kasser JR, Griffin PP, Wilkinson RH. The association of femoral retroversion with slipped capital femoral epiphysis. J Bone Joint Surg Am. 1986;68(7):1000–7.
9. Crane L. Femoral torsion and its relation to toeing-in and toeing-out. J Bone Joint Surg Am. 1959;41-A (3):421–8.
10. Tomczak RJ, Guenther KP, Rieber A, Mergo P, Ros PR, Brambs HJ. MR imaging measurement of the femoral antetorsional angle as a new technique: comparison with CT in children and adults. AJR Am J Roentgenol. 1997;168(3):791–4.
11. Koenig JK, Pring ME, Dwek JR. MR evaluation of femoral neck version and tibial torsion. Pediatr Radiol. 2012;42(1):113–5.
12. Notzli HP, Wyss TF, Stoecklin CH, Schmid MR, Treiber K, Hodler J. The contour of the femoral head–neck junction as a predictor for the risk of anterior impingement. J Bone Joint Surg Br. 2002;84 (4):556–60.
13. Dudda M, Albers C, Mamisch TC, Werlen S, Beck M. Do normal radiographs exclude asphericity of the femoral head–neck junction? Clin Orthop Relat Res. 2009;467(3):651–9.
14. Wyss TF, Clark JM, Weishaupt D, Notzli HP. Correlation between internal rotation and bony anatomy in the hip. Clin Orthop Relat Res. 2007;460:152–8.
15. Brunner A, Hamers AT, Fitze M, Herzog RF. The plain beta-angle measured on radiographs in the assessment of femoroacetabular impingement. J Bone Joint Surg Br. 2010;92(9):1203–8.

Section IV

Utilization of Biochemical Imaging Biomarkers in Treatment of Hip Disorders

Application of dGEMRIC to the Study of Hip Disorders

16

Andreas Hingsammer and Young-Jo Kim

Introduction

Magnetic resonance imaging (MRI) is an excellent diagnostic imaging tool to assess degenerative changes in cartilage, labrum, and bone [1]. It is reliable and reproducible in most of the diarthrodial joints, especially the knee. However, due to technical limitations related to the deep position within the body and thin articular cartilage, MR imaging of the hip joint has always been more challenging. Most MRI studies of cartilage imaging are performed in the knee. Unfortunately it has been difficult to reproduce the relatively good accuracy, sensitivity, and specificity to detect cartilage lesions in the knee in other joints with thinner cartilage, such as the hip joint [2, 3]. With MR arthrography (MRA) using intra-articular gadolinium, labral tears, and cartilage clefts may be better identified through the contrast medium filling into the tears and clefts [4, 5]. However, even with MRA the ability to detect varying grades of cartilage damage has proven to be limited [2, 6]. The hip joint is of special interest for MRI studies because of the advances in surgical therapies for conditions such as acetabular dysplasia and femoroacetabular impingement (FAI) that leads to early OA. The results of these surgical treatments is a direct function of the presurgical cartilage damage, hence, MR imaging will have a direct impact in clinical decision making [7].

Delayed gadolinium-enhanced MRI of Cartilage (dGEMRIC) is a contrast-based MR imaging technique that allows quantification of the charge density in articular cartilage, which precedes macroscopic tissue loss. This imaging technique may improve diagnostic imaging of cartilage damage by providing a quantitative assessment of the cartilage lesion detected by traditional morphologic assessment. Furthermore, this technique has the potential to detect lesions before morphologic changes, which may be irreversible, are detected (Fig. 16.1). The clinical value of biochemical imaging is in more accurate staging of hip OA for improved patient selection for joint preservation surgery and understanding of the progression of hip OA in various hip conditions. Furthermore, unlike plain radiography, biochemical imaging technique allows detection of cartilage recovery, potentially demonstrating a disease modifying effect of either surgical or medical therapies. For these reasons, the dGEMRIC technique has been applied extensively in the hip.

Contrast Administration and Timing of Imaging in Clinical Studies

Technical issues regarding optimization of the dGEMRIC technique for human clinical application have been investigated and reviewed [8, 9].

Y.-J. Kim (✉)
Department of Orthopedic Surgery, Boston Children's Hospital, 300 Longwood Avenue, Boston, MA 02115, USA
e-mail: Young-jo.kim@childrens.harvard.edu

Y.-J. Kim (eds.), *Hip Magnetic Resonance Imaging*,
DOI 10.1007/978-1-4614-1668-5_16,

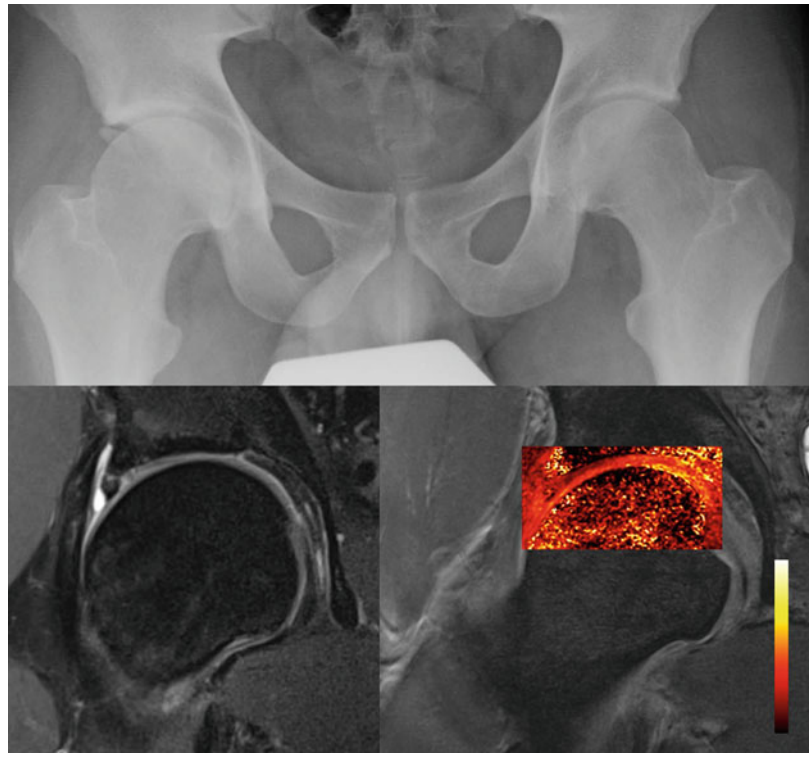

Fig. 16.1 Radiographs (*top panel*), MRI with indirect arthrography (*bottom left panel*), and dGEMRIC scan (*bottom right panel*) of hip with mixed impingement. No evidence of joint space narrowing seen on radiograph but a rim fracture is noted. On the morphologic MRI scan, there is labral chondral degeneration. The dGEMRIC scan shows fairly extensive acetabular cartilage damage as indicated by *dark red and black* regions in the acetabular cartilage. The femoral head cartilage is intact (color code: *white*—T1 1,200 ms, *black*—T1 200 ms)

The dGEMRIC effect depends on the use of a charged gadolinium contrast agent. A non-ionic contrast agent will not be able differentiate between disease and normal tissue. Additionally, the relaxivity of the contrast agent will influence the change in T1, hence, when the dGEMRIC scans are quantitated the amount and type of contrast agent used will be critical. The most commonly used contrast agent for the dGEMRIC technique is Magnevist (Bayer Heathcare). Even though the contrast agent Magnevist has been approved for clinical use as an MRI contrast agent, the dGEMRIC technique itself is an off-label application. The recommended dose for dGEMRIC studies is 0.2 mM/kg or twice the recommended clinical dose but this should be corrected for body mass index [10] due to the fact that plasma levels of Gd-DTPA(2-) was 1.4 times higher in subjects with BMI of 45 compared to subjects with BMI of 20. Some authors have advocated using a triple dose to improve sensitivity to small changes in GAG [11]. However, due to the risk of contrast reaction [12], most clinical studies are performed using double dose contrast injection.

The "delay" refers to the time that is required for the contrast agent to diffuse into the cartilage after an intravenous (IV) injection. In femoral knee cartilage, $T1_{Gd}$ was found to be relatively stable at 90–120 min postinjection, which has been the recommended window for dGEMRIC imaging of the knee [8, 11]. In the hip joint, early data indicated no difference in signal intensity in T1-weighted images between 30 and 90 min postinjection [8], and a time point of 30 min postinjection has been used for some hip dGEMRIC studies [13, 14]. Most recent study evaluating the optimal window for hip dGEMRIC imaging in asymptomatic individuals and patients with early hip osteoarthritis (OA) due to dysplasia shows that the wash-in of Gd-DTPA(2-) into healthy hip cartilage is similar to previously determined kinetics in femoral knee cartilage, with a maximum concentration at approximately 90–120 min [11, 15]. However, diseased cartilage had faster wash-in kinetics (Fig. 16.2). The results indicate that imaging at

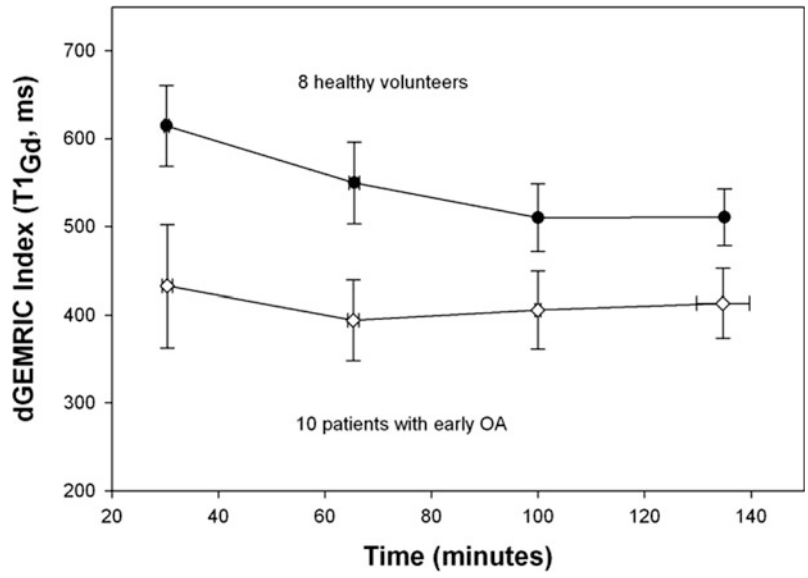

Fig. 16.2 The dGEMRIC index (mean ± sd) at four times (min ± sd) after intravenous injection of double dose Magnevist. The dGEMRIC index was 20–30 % lower in the patients with early OA compared to healthy volunteers ($P < 0.003$) at all time points, with largest difference at the earlier time points due to faster wash-in of the contrast in the OA cartilage. However, earlier time point in the OA subjects showed a higher SD, possibly due to variability of contrast penetration slope during this wash-in period (Magn Reson Med. 2007 Apr;57 (4):803–5)

earlier time points (30–65 min) increases the sensitivity to disease, but may decrease the reproducibility due to imaging during the slope of wash-in.

Exercise of the joint after contrast administration has been shown to increase convective transport of the contrast agent into the joint and cartilage [15]. The reproducibility of hip dGEMRIC measured at 30 min post-contrast shows CV% on the order of 15 % [13]. However, with standardization of timing of image acquisition and exercise routine and with the use of more rapid T1 acquisition, the reproducibility can be improved to 5–8 % in the hip [16] and 4–7 % in the knee [17]. For cross-sectional studies, the ease of early imaging may motivate early imaging time points. For longitudinal studies in which reproducibility is a concern, the later, more stable time points may be beneficial.

Fast T1-Mapping

Traditionally dGEMRIC has been performed using a two-dimensional T1-weighted inversion recovery (2D-IR) sequence to acquire data for quantitative T1 mapping [18, 19]. The major advantage of this method is the widespread availability of the sequence and desirable contrast properties (cartilage versus fluid). However, the 2D technique suffers from obvious limitations such as limited coverage (single slice) and susceptibility to motion effects between acquisitions with different inversion times (TI) [20]. Therefore, it has not been possible to perform a full-joint assessment of the GAG distribution in a single imaging session. Furthermore, in single-slice 2D imaging, difficulties associated with obtaining the same section in subsequent imaging sessions makes interpretation of follow-up scans unclear. Given the spatial variations observed with cartilage diseases, and the importance of following the progression of disease over time, it is important to be able to obtain information about the biochemical status of cartilage across the joint [10].

Recently, several methods for performing dGEMRIC in a three-dimensional (3D) volume of interest have emerged. In the long-term, there are many advantages of using 3D sequences for dGEMRIC. With 3D, it will be possible to evaluate the whole joint cartilage, instead of just a selected cross-section as with 2D. This will make it possible both to study local changes and lesions over larger portions of the cartilage, including improved possibilities for giving diagnoses regarding specific locations on the cartilage as well as improved possibilities for performing

measurements that can more easily be reproduced [21].

As of today, the usage of 3D techniques in dGEMRIC is at an early stage; however, validation studies comparing 3D to 2D techniques [20, 22] appear promising. To obtain full-joint coverage, a 3D inversion recovery spoiled gradient echo (IR-SPGR) sequence has been shown to be effective. However, to sample the T1 recovery curve comparable to the 2D approach, the total acquisition time is considerably long, approximately 18 min for 5 TIs [10]. Alternate 3D methods for fast and efficient T1 mapping have been introduced. The two main 3D techniques that are considered for T1 quantification in dGEMRIC today are 3D-Look-Locker (3D-LL) [11, 20] and 3D-variable flip angle (3D-VFA) [22, 23].

The 3D Look-Locker technique has been validated against the traditional inversion recovery technique. With this approach, volume imaging can be obtained within an acquisition time comparable to single slice 2D acquisition with IR-FSE (with 5 TIs), while sampling the T1 recovery curve better (typically using 10–12 TI values). Preliminary feasibility and accuracy studies, comparing the 3D-LL technique with traditional 2D IR-FSE technique, indicated a potential limitation of the technique in terms of segmentation of the cartilage for analysis. Because of the short echo times (TE) used for the acquisition, the contrast between the cartilage and synovial fluid was minimal [20, 24]. These limitations can be overcome by acquiring a set of additional position-matched anatomical images immediately before or after 3D-LL acquisitions. These anatomical images provide sufficient contrast between cartilage and fluid, and much better signal to noise ratio (SNR) and, hence, serve as a visual guide to define anatomy [20].

The dual flip angle technique has been validated against the traditional inversion recovery technique. It can decrease the imaging time significantly compared to IR techniques while still allowing 3-D acquisition. It must be noted that the choice of flip angle is optimized for a range of T1 values. Outside, this window, the T1 measurement will be inaccurate (Fig. 16.3). Furthermore, with this gradient echo-based technique, it is important to center the hip in the middle of the imaging matrix since the T1 mapping data is inaccurate at the periphery of the imaging matrix [22].

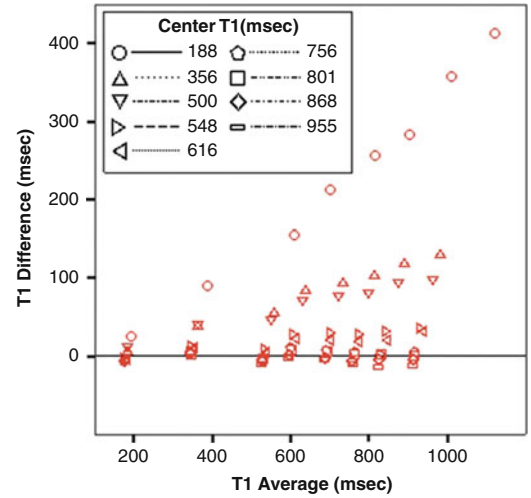

Fig. 16.3 T1 was measured using dual flip angle fast T1 mapping technique vs. inversion recovery in gadolinium phantoms. Bland-Altman plots of T1 values measured are shown. For center T1 of 756 ms, the Pearson regression constant was −1.65 ms and the slope was 0.01 with R^2 of 0.17. When the center T1 deviates from the measured range, the dual flip angle technique becomes inaccurate (Magn Reson Med. 2008 Oct;60(4):768–73)

Both Look-Locker [20] and dual flip angle [23] techniques of fast T1 mapping is dependent on accurate knowledge of the flip angle, hence, any type of B1 inhomogeneity will cause an error in the T1 measurement. B1 field inhomogeneity correction methods are available and recommended when using these fast T1 mapping techniques [25].

1.5 T Versus 3 T

The current literature suggests that musculoskeletal imaging at 3 T MRI offers multiple benefits compared to 1.5 T [26, 27]. Firstly, 3 T MRI results in an increase in SNR compared with 1.5 T MRI. The use of 3 T imaging results in an SNR that is roughly twice that of a 1.5 T scanner.

This gain in SNR can be used to either improve image quality or decrease the scan time in contrast to 1.5 T imaging. Higher spatial resolution in a joint with thin cartilage such as the hip can result in improved diagnostic accuracy. Decreased scan times possible at 3 T MRI will help reduce artifacts related to patient motion in individuals who are unable to or who have difficulty holding still during the MRI process. This results in a preservation of image quality and resolution even at reduced imaging times [28].

However, in practice, altered relaxation times of tissue together with the need for changing the imaging parameters results in SNR gains that are inferior to what has been predicted by theory [29]. For example, since the chemical shift increases linearly with the field strength, an adjustment of the receiver bandwidth is necessary to maintain the fat-water shift used at lower field strengths. This further reduces the possible increase of the SNR while the larger frequency dispersion at 3.0 T facilitates an improved frequency-selective fat suppression that might be beneficial for knee and hip imaging. Some authors even reported a reduced contrast between suppressed fat and surrounding hypointense tissues [29]. Imaging at higher field strength is also prone to pronounced susceptibility gradients, in particular for gradient echo and steady-state free precession (SSFP) sequences. Nonetheless, a number of in vitro studies have shown improved visualization of cartilage and ligament pathology at the knee and ankle using 3.0 T in comparison with 1.5 T MRI [30, 31]. Studies have also demonstrated 3.0 T MRI to have high sensitivity and specificity in diagnosing knee meniscus, cartilage, and ligamentous pathology when compared with subsequent arthroscopy [32]. Wong et al. performed a study comparing visualization of cartilage, ligaments, and menisci at 1.5 and 3.0 T in the same subjects. They showed that 3.0 T MRI was superior for detecting and grading cartilage lesions compared to 1.5 T. Though a higher diagnostic confidence was found at 3.0 T, the false-positive rate was not decreased. Overall image quality at 3.0 T was rated superior to 1.5 T [28].

When performing dGEMRIC at 3 T, the change in relaxivity at the higher field strength will alter the T1 value obtained. In general, the T1 value of the same cartilage will be higher at 3 T. Additionally, the effects of B1 inhomogenity will be higher and hence B1 correction algorithm should be used when performing fast T1 mapping at 3 T.

dGEMRIC in Dysplasia

By some estimates, 20–40 % of hips requiring arthroplasties may be due to secondary OA from DDH [33–35]. The smaller area of anterolateral acetabular coverage in DDH increases mechanical stress in the cartilage, which results in cartilage damage [36]. The risk of developing OA in dysplastic hips appears to be a function of severity of dysplasia and age [37]. Cooperman at al. [38] have shown that hips with severe dysplasia with joint subluxation degenerated quickly, while Murphy et al. [39] demonstrated that hips with center–edge angle less than 16° all developed eventual osteoarthritis. Fuji et al. reported in their arthroscopic study that cartilage lesions in DDH are commonly seen in the anterosuperior aspect of the acetabulum. They found cartilage lesions in 14 of 18 hips in pre-arthritic cases with 11 located in the anterosuperior part of the acetabulum in patients younger than 20 years [40]. McCarthy and Lee confirmed this pattern of early cartilage damage. They reported that 100 (59 %) of 170 hips with DDH had chondral defects situated in the anterior quadrant and concomitant anterior labral lesions were as frequent as 66 % [41].

Kim et al. investigated the applicability of dGEMRIC in hip dysplasia [13]. In 68 hips (43 patients), the dGEMRIC index and joint space width were compared to radiographically and clinically relevant factors such as pain, severity of dysplasia, and age. The dGEMRIC index correlated significantly with pain and lateral center–edge angle as measure of severity of dysplasia. In contrast, joint space width did not correlate with pain or severity of dysplasia as

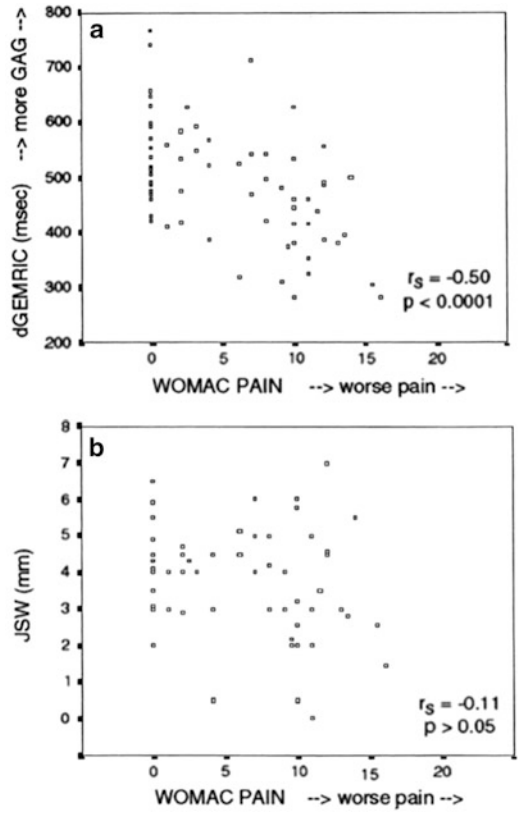

Fig. 16.4 Scatter plots of the dGEMRIC index and joint space width (JSW) versus the WOMAC pain score. The Spearman rank correlation showed a significant negative correlation between the dGEMRIC index and pain but no significant correlation between joint space width and pain. *GAG* glycosaminoglycan content (J Bone Joint Surg Am. 2003 Oct;85-A(10):1987–92)

shown in Fig. 16.4. A statistically significant difference of the dGEMRIC index among mild, moderate, and severe dysplasia could be observed. The average dGEMRIC index ranged from 570 ms (no dysplasia), to 550 ms (mild dysplasia), to 500 ms (moderate dysplasia), to 420 ms (severe dyplasia). This study demonstrates that biochemical MRI (i.e., dGEMRIC scans) correlates better with clinical important parameters in hip dysplasia than do traditional radiographic measures of OA, thus suggesting that this is a valid metric to be used in clinical studies of OA.

In an attempt to better understand the anatomic and demographic factors that may predispose a hip to early OA, a study involving 96 hips with acetabular dysplasia was performed to look at risk factors of early OA as defined using dGEMRIC [42]. Hips with a dGEMRIC index <390 ms were used as the definition of hips with early OA; by this metric, cases <390 ms were older, had smaller lateral and anterior center–edge angles, and had an increased incidence of radiographic joint subluxation and labral tears. Using these data, the probability of significant OA (T1 < 390 ms) as a function of age, severity of dysplasia, and with and without labral tears could be plotted (Fig. 16.5). This type of paradigm shift may improve our understanding of other conditions that lead to OA. The results of the study are consistent with the conclusion by Murphy et al. [39] that osteoarthritis will eventually develop in hips with a lateral center–edge angle of less than approximately 15°.

Bernese periacetabular osteotomy (PAO) is effective for mild to severe hip dysplasia in relieving hip pain and improving joint biomechanics. The goal of surgery to treat AHD is to realign the acetabulum into its optimal mechanical position. The PAO does not produce a normal acetabulum. This surgery reorients the position of an abnormally shallow acetabulum to optimize stress transfer across the joint by increasing the contact area [43]. This osteotomy may slow the progression of secondary OA and delay the need for salvage surgery, arthrodesis, or arthroplasty [44]. In general, early reconstructive osteotomies performed on younger patients who have little radiographic evidence of OA by Tönnis grades are regarded the best candidates for this procedure. Hips that fail prematurely after osteotomy are expected to have more evidence of OA on radiographs [45].

In order to assess the clinical value of dGEMRIC in predicting surgical outcome after pelvic osteotomy, a cohort of 47 patients who underwent PAO for hip dysplasia was investigated prospectively [14]. In addition to patient age, radiographic severity of OA, severity of dysplasia, and the dGEMRIC index was evaluated. This study showed that PAO is an expedient tool to reduce pain and ameliorate joint function. When clinical and radiographic failure groups were compared with satisfactory

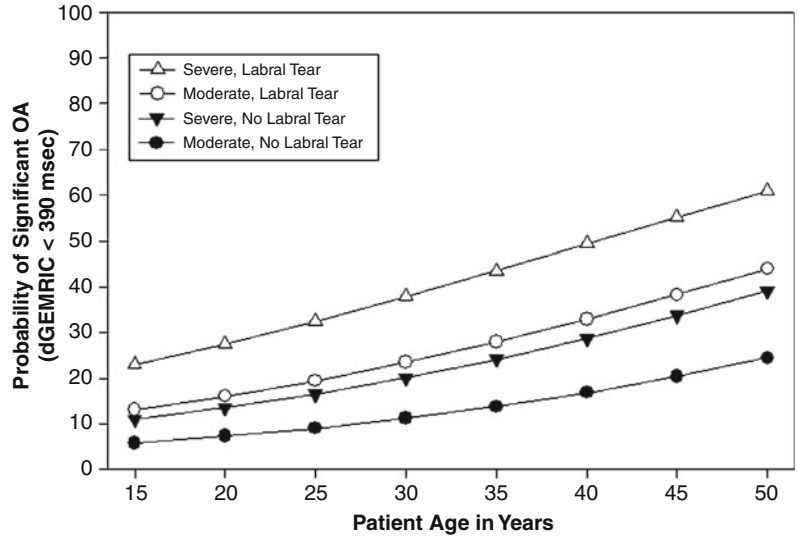

Fig. 16.5 Probability of osteoarthritis developing as a function of age in moderately (lateral center–edge angle 5–15°) and severely (LCE < 5°) dysplastic hips with and without labral tear (J Bone Joint Surg Am. 2009 May;91(5):1120–9)

groups, identified predictors included radiographic joint subluxation, Tönnis grade, joint space width, and the dGEMRIC index (498 ± 105 ms [satisfactory] versus 370 ± 88 ms [failed]; $P < 0.01$). A multiple logistic regression model that included joint space width, joint subluxation, Tönnis grade, and dGEMRIC index as independent variables showed the preoperative dGEMRIC value and joint subluxation to be the best independent predictors of early postoperative failure of the PAO. The probability of total hip arthroplasty increased dramatically when the dGEMRIC index was <390 ms (Fig. 16.6).

These studies demonstrate the validity of dGEMRIC as a metric of OA in dysplastic hips. By extension, these studies demonstrate the validity of using dGEMRIC in the clinical setting and support the use of this metric as the primary radiographic tool to assess osteoarthritis rather than plan radiographs.

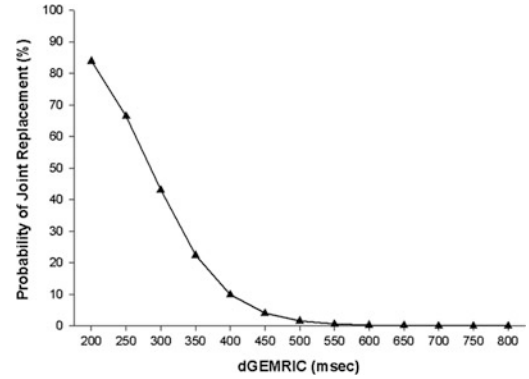

Fig. 16.6 Calculated probability of the patient needing an arthroplasty after periacetabular osteotomy for hip dysplasia as a function of the preoperative dGEMRIC index (J Bone Joint Surg Am. 2006 Jul;88(7):1540–8)

dGEMRIC in FAI

The most frequent location for FAI is the anterosuperior rim area and the most critical motion is internal rotation of the hip in 90° flexion. Two types of FAI have been identified. Cam-type FAI, more prevalent in young male patients, is caused by an offset pathomorphology between head and neck and produces an outside-in delamination of the acetabulum. This carpet phenomenon is located mostly in the anterosuperior region of the acetabulum and results in permanent intraarticular cartilage damage [46]. Pincer-type FAI, more prevalent in middle-aged women, is produced by a more linear impact between a local (retroversion of the acetabulum) or general overcoverage (coxa profunda/protrusio) of the acetabulum. The damage pattern is more restricted to the rim and the

process of joint degeneration is slower, so that the labrum might be damaged prior to cartilage damage. Most hips, however, show a mixed FAI pattern with cam predominance [47, 48].

The abnormal contact between the acetabular rim and femoral head neck junction can progress over time and result in osteoarthritis (OA) of the hip joint if the underlying cause of impingement is not addressed. Untreated symptomatic FAI is a risk factor for the development of premature osteoarthritis (OA) in the hip [47]. Multiple reports have shown good outcomes following early surgical intervention in patients with preexisting mild changes of OA, but poor results in patients with advanced degenerative changes [49]. Therefore, it is understandably critical for the treating clinician to be able to detect cartilage changes of damage and degeneration not only in detail, but also at an early stage to maximize patient benefit and to identify the appropriate patient for surgical treatment. Corrective surgical procedures, aimed at removing the bony abnormalities of FAI and treating the associated labral and cartilage lesions, have been proposed in order to delay or prevent OA [50].

Pollard et al. investigated the potential of dGEMRIC to detect cartilage disease in asymptomatic hips with cam deformities compared with morphologically normal hips to establish whether dGEMRIC could identify advanced disease in hips with positive clinical findings and establish whether cartilage damage correlated with the severity of the cam deformity [51]. Subjects were recruited from a prospective study of individuals with a family history of osteoarthritis and their spouses who served as control subjects. dGEMRIC was performed on a 3 T system, studying two regions of interest: the anterosuperior aspect of the acetabular cartilage ($T1_{acetabular}$) and the total femoral and acetabular cartilage ($T1_{total}$). The cohort was placed in subgroups by joint morphology, impingement test status, and genetic predisposition. The mean T1 scores were compared, and the alpha angle and T1 were correlated. Hips with a cam deformity had reduced acetabular glycosaminoglycan content compared with normal hips. Hips with a positive impingement test result had global depletion of glycosaminoglycan compared with hips with a negative result (mean $T1_{total} = 625$ versus 710 ms; $P = 0.0152$). $T1_{acet}$ inversely correlated with the magnitude of the alpha angle, suggesting that the severity of cartilage damage correlates with the magnitude of the cam deformity.

Bittersohl et al. characterized the zonal distribution of 3D $T1_{Gd}$ mapping in the hip joint of ten asymptomatic adult volunteers at 1.5 T [52]. MRI protocol included standard sequences for hip imaging and a dual-flip-angle 3D gradient echo (GRE) sequence with volumetric interpolated breath-hold examination (VIBE) post-contrast administration. Analysis of the radial distribution revealed an increase of $T1_{Gd}$ values toward the superior regions. $T1_{Gd}$ values differed between the peripheral and central portions. The standard deviation (SD) ranged from 76.2 to 124.1 ms in the peripheral zone and from 69.1 to 112.9 ms in the central zone. In both zones, SD was low in the superior regions compared with the anterior and posterior regions of the joint. Based on the high intra- and interobserver agreement, normative data obtained from this study are preparing the foundation for further studies of dGEMRIC and T1 measurement in the hip.

Recently, Lattazi et al. performed, in a preliminary validation study, a retrospective review of ten hips on ten patients who underwent hip arthroscopy and had an MRI scan of the symptomatic hip less than 4 months before surgery [53]. FAI cartilage lesions are believed to invariably originate near the chondrolabral junction, and then progress over time to involve the adjacent acetabular cartilage and the rest of the joint. They assumed that the central portion of the femoral cartilage is healthy in early stages of FAI and may provide an effective and reliable reference for dGEMRIC measurements. By using a fixed threshold of 500 ms, they tried to validate their hypothesis by using intraoperative findings as the reference. They were able to show that the proposed standardized dGEMRIC could predict cartilage abnormalities with high sensitivity and accuracy in FAI patients.

Mamisch et al. compared the dGEMRIC indices in a group of six cam and seven pincer patients to a control group ($n = 12$) of asymptomatic controls that had no plain MRI findings of osteoarthritis [54]. The superior portion of the

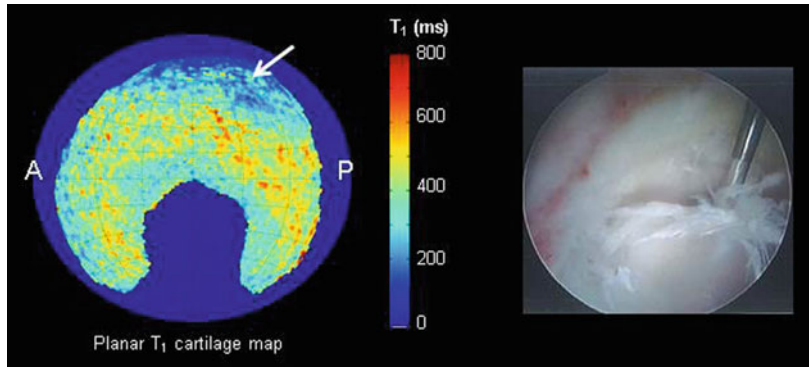

Fig. 16.7 A two dimensional rendering of the acetabular cartilage dGEMRIC T1 values after automatic segmentation of the cartilages (*left panel*). The *blue* areas indicate areas of low T1 suggesting extensive cartilage damage. At time of arthoscopy (*right panel*) extensive cartilage delamination is seen in the superior portion of the joint

hip joint was divided into seven regions from 9 to 3 o'clock. These regions were then subdivided into peripheral and central regions. The cam and pincer groups both had statistically lower dGEMRIC values compared to the control group. The cam group demonstrated not only peripheral but also central involvement of the joint and this was concentrated in the anterior portion of the joint. The pincer group exhibited more global hip involvement with all areas of the hip averaging a dGEMRIC index 28 % less than controls. The authors concluded that the use of dGEMRIC can elicit more specific patterns of cartilage wear in patients with impingement, which may improve patient selection and help better understand the progression of osteoarthritis throughout the hip joint (Fig. 16.7).

dGEMRIC in Other Developmental Hip Deformities

The complex femoral morphologies of Legg–Calvé–Perthes disease (LCPD) and slipped capital femoral epiphysis (SCFE) are developmental hip conditions that lead to premature osteoarthritis.

Legg–Calvé–Perthes Disease

In LCPD, idiopathic osteonecrosis occurs due to disruption of blood supply to, and growth arrest of, the femoral head growth plate. LCPD results in altered proximal femur morphology with a misshapen femoral head, a short and wide neck, and, in severe cases, overgrowth of the greater trochanter [55].

The deformities can be quite complex and may cause hip instability, FAI, or combinations of both and may ultimately lead to degenerative joint disease and early osteoarthritis (OA) of the hip. In the long-term follow-up of LCPD, OA is reported to be a direct function of time, femoral head sphericity, and congruency of the joint [56].

Holstein et al. compared quantitative cartilage imaging (dGEMRIC) with morphologic MRI in the long-term follow-up after LCPD [57]. dGEMRIC values within the weight-bearing zone of hip cartilage were significantly lower in hips after LCPD than in unaffected contralateral hips, with mean dGEMRIC values of 513 $\pm$ 100 ms in hips after LCPD and 579 $\pm$ 103 ms in the control group. In the active stage of LCPD, the GAG content of cartilage is not reduced. In the long-term course, the necrosis of the femoral head often leads to deformation and to secondary dysplastic changes of the acetabulum that may cause progressive degeneration [57].

Zilkens et al. also investigated the GAG content of the hip joint cartilage after LCPD using dGEMRIC. Therefore, hips from adults with LCPD in childhood were analyzed to investigate the regional variation in the dGEMRIC values in comparison to morphologically normal appearing and asymptomatic contralateral hips [58]. The morphologically normal hips had similar mean $T1_{Gd}$ of approximately 580 ms, whereas the hips with LCPD had $T1_{Gd}$ of

approximately 530 ms. This is equivalent to the findings in FAI [59].

They were able to show that in LCPD the decrease of GAG is statistically significant at the medial compartment whereas there was no statistically significant difference at the central and lateral compartment. They found only a moderate correlation between dGEMRIC and Tönnis grade but high correlation between OA due to LCPD and age of the patient and congruency of the joint [58].

Slipped Capital Femoral Epiphysis

SCFE, the displacement of the epiphysis over the metaphysis, is among the most common disorders of the young and adolescent hip. The etiology of SCFE is unknown; however, the prototypical patient is an obese, pubertal boy of approximately 12 years. The incidence of SCFE is reported to be about 4–5/100,000 for all patients in prepuberty and puberty. There seems to be an obvious correlation between the severity of residual hip joint deformity and the long-term outcome in affected patients with less favorable outcome for more severe slips [60].

The reduced offset of the femoral head–neck junction and resulting pistol-grip deformity, as residuum of SCFE has been described as prototype of cam FAI causing premature cartilage damage and early osteoarthritis (OA) through repetitive micro trauma during hip flexion and rotation [61]. There seems to be compelling evidence that a decreased head–neck offset as a sequel of SCFE leads to OA of the hip joint [47].

Zilkens et al. investigated the potential of dGEMRIC in the diagnosis of hip joint cartilage damage on 28 young-adult subjects with SCFE in childhood and without radiographic signs of OA. They were able to depict the potential of dGEMRIC to reveal degenerative changes in the mid-term follow-up of SCFE in the absence of radiographic signs or clinical symptoms of OA [58].

These results are similar to previously reported T1Gd values depicting cartilage changes in hip dysplasia or patients with early OA of the hip joint [13]. The dGEMRIC technique may provide additional information concerning the joint status in the follow-up of SCFE before radiographic changes take place.

Summary

Currently, progress in clinical research in OA is slow, partly because of the lack of a reliable biomarker that shows early changes. As illustrated here, biochemical MRI can improve present therapies for joint preservation. More importantly, by allowing rapid assessment of new therapies, additional and novel therapeutic options for joint preservation may become possible.

References

1. Pfirrmann CW, Mengiardi B, Dora C, Kalberer F, Zanetti M, Hodler J. Cam and pincer femoroacetabular impingement: characteristic MR arthrographic findings in 50 patients. Radiology. 2006;240(3):778–85. Epub 2006/07/22.
2. Schmid MR, Notzli HP, Zanetti M, Wyss TF, Hodler J. Cartilage lesions in the hip: diagnostic effectiveness of MR arthrography. Radiology. 2003;226(2):382–6. Epub 2003/02/04.
3. Shepherd DE, Seedhom BB. Thickness of human articular cartilage in joints of the lower limb. Ann Rheum Dis. 1999;58(1):27–34. Epub 1999/05/27.
4. Locher S, Werlen S, Leunig M, Ganz R. MR-arthrography with radial sequences for visualization of early hip pathology not visible on plain radiographs. Z Orthop Ihre Grenzgeb. 2002;140(1):52–7. Epub 2002/03/19. Arthro-MRI mit radiarer Schnittsequenz zur Darstellung der praradiologischen Huftpathologie.
5. Petersilge CA. MR arthrography for evaluation of the acetabular labrum. Skeletal Radiol. 2001;30(8):423–30. Epub 2001/08/02.
6. Knuesel PR, Pfirrmann CW, Noetzli HP, Dora C, Zanetti M, Hodler J, et al. MR arthrography of the hip: diagnostic performance of a dedicated water-excitation 3D double-echo steady-state sequence to detect cartilage lesions. AJR Am J Roentgenol. 2004;183(6):1729–35. Epub 2004/11/18.
7. Wenger DR, Bomar JD. Human hip dysplasia: evolution of current treatment concepts. J Orthop Sci. 2003;8(2):264–71. Epub 2003/04/01.
8. Burstein D, Velyvis J, Scott KT, Stock KW, Kim YJ, Jaramillo D, et al. Protocol issues for delayed

Gd(DTPA)(2-)-enhanced MRI (dGEMRIC) for clinical evaluation of articular cartilage. Magn Reson Med. 2001;45(1):36–41. Epub 2001/01/09.
9. Siversson C, Tiderius CJ, Neuman P, Dahlberg L, Svensson J. Repeatability of T1-quantification in dGEMRIC for three different acquisition techniques: two-dimensional inversion recovery, three-dimensional look locker, and three-dimensional variable flip angle. J Magn Reson Imaging. 2010;31(5):1203–9. Epub 2010/05/01.
10. McKenzie CA, Williams A, Prasad PV, Burstein D. Three-dimensional delayed gadolinium-enhanced MRI of cartilage (dGEMRIC) at 1.5T and 3.0T. J Magn Reson Imaging. 2006;24(4):928–33.
11. Tiderius CJ, Olsson LE, de Verdier H, Leander P, Ekberg O, Dahlberg L. Gd-DTPA2)-enhanced MRI of femoral knee cartilage: a dose-response study in healthy volunteers. Magn Reson Med. 2001;46(6):1067–71. Epub 2001/12/18.
12. Tiderius CJ, Jessel R, Kim YJ, Burstein D. Hip dGEMRIC in asymptomatic volunteers and patients with early osteoarthritis: the influence of timing after contrast injection. Magn Reson Med. 2007;57(4):803–5. Epub 2007/03/29.
13. Kim YJ, Jaramillo D, Millis MB, Gray ML, Burstein D. Assessment of early osteoarthritis in hip dysplasia with delayed gadolinium-enhanced magnetic resonance imaging of cartilage. J Bone Joint Surg Am. 2003;85-A(10):1987–92. Epub 2003/10/18.
14. Cunningham T, Jessel R, Zurakowski D, Millis MB, Kim YJ. Delayed gadolinium-enhanced magnetic resonance imaging of cartilage to predict early failure of Bernese periacetabular osteotomy for hip dysplasia. J Bone Joint Surg Am. 2006;88(7):1540–8. Epub 2006/07/05.
15. Trattnig S, Mlynarik V, Breitenseher M, Huber M, Zembsch A, Rand T, et al. MRI visualization of proteoglycan depletion in articular cartilage via intravenous administration of Gd-DTPA. Magn Reson Imaging. 1999;17(4):577–83. Epub 1999/05/07.
16. Bittersohl B, Hosalkar HS, Haamberg T, Kim YJ, Werlen S, Siebenrock KA, et al. Reproducibility of dGEMRIC in assessment of hip joint cartilage: a prospective study. J Magn Reson Imaging. 2009;30(1):224–8. Epub 2009/06/27.
17. Multanen J, Rauvala E, Lammentausta E, Ojala R, Kiviranta I, Hakkinen A, et al. Reproducibility of imaging human knee cartilage by delayed gadolinium-enhanced MRI of cartilage (dGEMRIC) at 1.5 Tesla. Osteoarthritis Cartilage. 2009;17(5):559–64.
18. Bashir A, Gray ML, Hartke J, Burstein D. Nondestructive imaging of human cartilage glycosaminoglycan concentration by MRI. Magn Reson Med. 1999;41(5):857–65. Epub 1999/05/20.
19. Tiderius CJ, Olsson LE, Leander P, Ekberg O, Dahlberg L. Delayed gadolinium-enhanced MRI of cartilage (dGEMRIC) in early knee osteoarthritis. Magn Reson Med. 2003;49(3):488–92. Epub 2003/02/21.
20. Li W, Scheidegger R, Wu Y, Vu A, Prasad PV. Accuracy of T1 measurement with 3-D Look-Locker technique for dGEMRIC. J Magn Reson Imaging. 2008;27(3):678–82. Epub 2008/01/10.
21. Siversson C, Tiderius CJ, Dahlberg L, Svensson J. Local flip angle correction for improved volume T1-quantification in three-dimensional dGEMRIC using the Look-Locker technique. J Magn Reson Imaging. 2009;30(4):834–41. Epub 2009/09/30.
22. Mamisch TC, Dudda M, Hughes T, Burstein D, Kim YJ. Comparison of delayed gadolinium enhanced MRI of cartilage (dGEMRIC) using inversion recovery and fast T1 mapping sequences. Magn Reson Med. 2008;60(4):768–73. Epub 2008/09/26.
23. Trattnig S, Marlovits S, Gebetsroither S, Szomolanyi P, Welsch GH, Salomonowitz E, et al. Three-dimensional delayed gadolinium-enhanced MRI of cartilage (dGEMRIC) for in vivo evaluation of reparative cartilage after matrix-associated autologous chondrocyte transplantation at 3.0T: preliminary results. J Magn Reson Imaging. 2007;26(4):974–82.
24. Kimelman T, Vu A, Storey P, McKenzie C, Burstein D, Prasad P. Three-dimensional T1 mapping for dGEMRIC at 3.0 T using the Look Locker method. Invest Radiol. 2006;41(2):198–203.
25. Siversson C, Chan J, Tiderius CJ, Mamisch TC, Jellus V, Svensson J, et al. Effects of B1 inhomogeneity correction for three-dimensional variable flip angle T1 measurements in hip dGEMRIC at 3 T and 1.5 T. Magn Reson Med. 2012;67(6):1776–81.
26. Craig JG, Go L, Blechinger J, Hearshen D, Bouffard JA, Diamond M, et al. Three-tesla imaging of the knee: initial experience. Skeletal Radiol. 2005;34(8):453–61. Epub 2005/06/22.
27. Shapiro MD, Magee T, Williams D, Ramnath R, Ross JS. The time for 3T clinical imaging is now. AJNR Am J Neuroradiol. 2004;25(9):1628–9. author reply 9. Epub 2004/10/27.
28. Wong S, Steinbach L, Zhao J, Stehling C, Ma CB, Link TM. Comparative study of imaging at 3.0 T versus 1.5 T of the knee. Skeletal Radiol. 2009;38(8):761–9.
29. Mosher TJ. Musculoskeletal imaging at 3T: current techniques and future applications. Magn Reson Imaging Clin N Am. 2006;14(1):63–76. Epub 2006/03/15.
30. Bauer JS, Barr C, Henning TD, Malfair D, Ma CB, Steinbach L, et al. Magnetic resonance imaging of the ankle at 3.0 Tesla and 1.5 Tesla in human cadaver specimens with artificially created lesions of cartilage and ligaments. Invest Radiol. 2008;43(9):604–11.
31. Masi JN, Sell CA, Phan C, Han E, Newitt D, Steinbach L, et al. Cartilage MR imaging at 3.0 versus that at 1.5 T: preliminary results in a porcine model. Radiology. 2005;236(1):140–50.
32. Kijowski R, Blankenbaker DG, Davis KW, Shinki K, Kaplan LD, De Smet AA. Comparison of 1.5- and 3.0-T MR imaging for evaluating the articular cartilage of the knee joint. Radiology. 2009;250(3):839–48.

33. Aronson J. Osteoarthritis of the young adult hip: etiology and treatment. Instr Course Lect. 1986;35:119–28. Epub 1986/01/01.
34. Harris WH. Etiology of osteoarthritis of the hip. Clin Orthop Relat Res. 1986;213:20–33. Epub 1986/12/01.
35. Solomon L. Patterns of osteoarthritis of the hip. J Bone Joint Surg Br. 1976;58(2):176–83. Epub 1976/05/01.
36. Hipp JA, Sugano N, Millis MB, Murphy SB. Planning acetabular redirection osteotomies based on joint contact pressures. Clin Orthop Relat Res. 1999;364:134–43. Epub 1999/07/23.
37. Jacobsen S, Sonne-Holm S. Hip dysplasia: a significant risk factor for the development of hip osteoarthritis. A cross-sectional survey. Rheumatology (Oxford). 2005;44(2):211–8.
38. Cooperman DR, Wallensten R, Stulberg SD. Post-reduction avascular necrosis in congenital dislocation of the hip. J Bone Joint Surg Am. 1980;62(2):247–58. Epub 1980/03/01.
39. Murphy SB, Ganz R, Muller ME. The prognosis in untreated dysplasia of the hip. A study of radiographic factors that predict the outcome. J Bone Joint Surg Am. 1995;77(7):985–9. Epub 1995/07/01.
40. Fuji M, Nakashima Y, Jingushi S, Yamamoto T, Noguchi Y, Suenaga E, et al. Intraarticular findings in symptomatic developmental dysplasia of the hip. J Pediatr Orthop. 2009;29(1):9–13. Epub 2008/12/23.
41. McCarthy JC, Lee JA. Acetabular dysplasia: a paradigm of arthroscopic examination of chondral injuries. Clin Orthop Relat Res. 2002;405:122–8. Epub 2002/12/04.
42. Jessel RH, Zurakowski D, Zilkens C, Burstein D, Gray ML, Kim YJ. Radiographic and patient factors associated with pre-radiographic osteoarthritis in hip dysplasia. J Bone Joint Surg Am. 2009;91(5):1120–9. Epub 2009/05/05.
43. McKinley TO. The Bernese periacetabular osteotomy for treatment of adult hip dysplasia. Skeletal Radiol. 2010;39(11):1057–9. Epub 2010/07/21.
44. Clohisy JC, Barrett SE, Gordon JE, Delgado ED, Schoenecker PL. Periacetabular osteotomy in the treatment of severe acetabular dysplasia. Surgical technique. J Bone Joint Surg Am. 2006;88(Suppl 1 Pt 1):65–83. Epub 2006/03/03.
45. Matheney T, Kim YJ, Zurakowski D, Matero C, Millis M. Intermediate to long-term results following the Bernese periacetabular osteotomy and predictors of clinical outcome. J Bone Joint Surg Am. 2009;91(9):2113–23. Epub 2009/09/03.
46. Anderson LA, Peters CL, Park BB, Stoddard GJ, Erickson JA, Crim JR. Acetabular cartilage delamination in femoroacetabular impingement. Risk factors and magnetic resonance imaging diagnosis. J Bone Joint Surg Am. 2009;91(2):305–13. Epub 2009/02/03.
47. Ganz R, Parvizi J, Beck M, Leunig M, Notzli H, Siebenrock KA. Femoroacetabular impingement: a cause for osteoarthritis of the hip. Clin Orthop Relat Res. 2003;417:112–20. Epub 2003/12/04.
48. Siebenrock KA, Schoeniger R, Ganz R. Anterior femoro-acetabular impingement due to acetabular retroversion. Treatment with periacetabular osteotomy. J Bone Joint Surg Am. 2003;85-A(2):278–86. Epub 2003/02/07.
49. Murphy S, Tannast M, Kim YJ, Buly R, Millis MB. Debridement of the adult hip for femoroacetabular impingement: indications and preliminary clinical results. Clin Orthop Relat Res. 2004;429:178–81. Epub 2004/12/04.
50. Botser IB, Smith Jr TW, Nasser R, Domb BG. Open surgical dislocation versus arthroscopy for femoroacetabular impingement: a comparison of clinical outcomes. Arthroscopy. 2011;27(2):270–8. Epub 2011/01/27.
51. Pollard TC, McNally EG, Wilson DC, Wilson DR, Madler B, Watson M, et al. Localized cartilage assessment with three-dimensional dGEMRIC in asymptomatic hips with normal morphology and cam deformity. J Bone Joint Surg Am. 2010;92(15):2557–69. Epub 2010/11/05.
52. Bittersohl B, Hosalkar HS, Werlen S, Trattnig S, Siebenrock KA, Mamisch TC. DGEMRIC and subsequent T1 mapping of the hip at 1.5 Tesla: normative data on zonal and radial distribution in asymptomatic volunteers. J Magn Reson Imaging. 2011;34(1):101–6.
53. Lattanzi R, Petchprapa C, Glaser C, Dunham K, Mikheev AV, Krigel A, et al. A new method to analyze dGEMRIC measurements in femoroacetabular impingement: preliminary validation against arthroscopic findings. Osteoarthritis Cartilage. 2012;20(10):1127–33. Epub 2012/07/10.
54. Mamisch TC, Kain MS, Bittersohl B, Apprich S, Werlen S, Beck M, et al. Delayed gadolinium-enhanced magnetic resonance imaging of cartilage (dGEMRIC) in Femoacetabular impingement. J Orthop Res. 2011;29(9):1305–11. Epub 2011/03/26.
55. Kim YJ, Novais EN. Diagnosis and treatment of femoroacetabular impingement in Legg-Calve-Perthes disease. J Pediatr Orthop. 2011;31(2 Suppl):S235–40. Epub 2011/09/01.
56. Weinstein SL. Legg-Calve-Perthes disease: results of long-term follow-up. Hip. 1985;28-37. Epub 1985/01/01.
57. Holstein A, Zilkens C, Bittersohl B, Jager M, Haamberg T, Mamisch TC, et al. Delayed gadolinium-enhanced MRI of cartilage (dGEMRIC) and morphologic MRI of cartilage in the long-term follow-up after Legg-Calve-Perthes disease (LCPD). J Med Imaging Radiat Oncol. 2011;55(3):259–65. Epub 2011/06/24.
58. Zilkens C, Holstein A, Bittersohl B, Jager M, Haamberg T, Miese F, et al. Delayed gadolinium-enhanced magnetic resonance imaging of cartilage in the long-term follow-up after Perthes disease. J Pediatr Orthop. 2010;30(2):147–53. Epub 2010/02/25.

59. Bittersohl B, Hosalkar HS, Hughes T, Kim YJ, Werlen S, Siebenrock KA, et al. Feasibility of T2* mapping for the evaluation of hip joint cartilage at 1.5T using a three-dimensional (3D), gradient-echo (GRE) sequence: a prospective study. Magn Reson Med. 2009;62(4):896–901.
60. Carney BT, Weinstein SL, Noble J. Long-term follow-up of slipped capital femoral epiphysis. J Bone Joint Surg Am. 1991;73(5):667–74. Epub 1991/06/01.
61. Leunig M, Casillas MM, Hamlet M, Hersche O, Notzli H, Slongo T, et al. Slipped capital femoral epiphysis: early mechanical damage to the acetabular cartilage by a prominent femoral metaphysis. Acta Orthop Scand. 2000;71(4):370–5. Epub 2000/10/12.

Application of T1rho to the Hip

17

Kawan S. Rakhra

Introduction

Osteoarthritis (OA) is a major cause of physical disability in society—a social, economic, and medical burden that will only increase with an increasingly physically active and aging population [1, 2]. Primarily a disease of articular cartilage, the end result of OA is degradation of cartilage, with subsequent joint instability and failure [3].

OA is initiated by changes within hyaline cartilage at the molecular level [4]. The earliest biochemical change within cartilage in the pathway of OA is proteoglycan (PG) depletion from the extracellular matrix (ECM). This leads to weakening of the collagen framework of the ECM, resulting in microscopic and eventually gross macroscopic structural changes to the cartilage [5, 6].

Role of MRI

Magnetic resonance imaging (MRI) is a powerful, noninvasive tool for evaluating joint hyaline cartilage [7–9]. Traditional MRI sequences have been effective in identifying qualitative, macroscopic changes of cartilage such as thickness and volume. Specifically, both routine MRI [10, 11] and magnetic resonance arthrography [12–16] have been used to detect chondral abnormality in the hip. However, these gross structural alterations often manifest late in the OA pathway, at a point where treatment options may be limited to invasive, surgical reconstructive procedures. Consequently, advanced MRI techniques are being explored in hope of detecting biochemical changes in the macromolecular matrix of cartilage before gross, morphologic damage occurs [17]. Recent advances in MRI technology, research, and sequence development have given rise to relatively noninvasive techniques that allow for detection of quantitative, biochemical, microscopic alterations to cartilage [18]. MRI can now provide relative quantification and spatial mapping of the molecular components of hyaline cartilage, such as PG [19].

T1ρ MRI Cartilage Mapping

T1-rho (T1ρ) MRI is a technique for evaluating hyaline cartilage, sensitive to PG content. Correlation between PG depletion and T1ρ relaxation time changes has been previously established [20–25]. T1ρ MRI has been shown to detect alterations in the cartilage profile of the osteoarthritic knee, manifest by increased T1ρ relaxation times [26–32].

The vast majority of cartilage mapping studies in the normal, symptomatic, and arthritic hip

K.S. Rakhra (✉)
Department of Medical Imaging, The Ottawa Hospital, General Campus, 501 Smyth Road, Room, Ottawa, ON, Canada K1H 8L6,
e-mail: krakhra@ottawahospital.on.ca

Y.-J. Kim (eds.), *Hip Magnetic Resonance Imaging*,
DOI 10.1007/978-1-4614-1668-5_17,

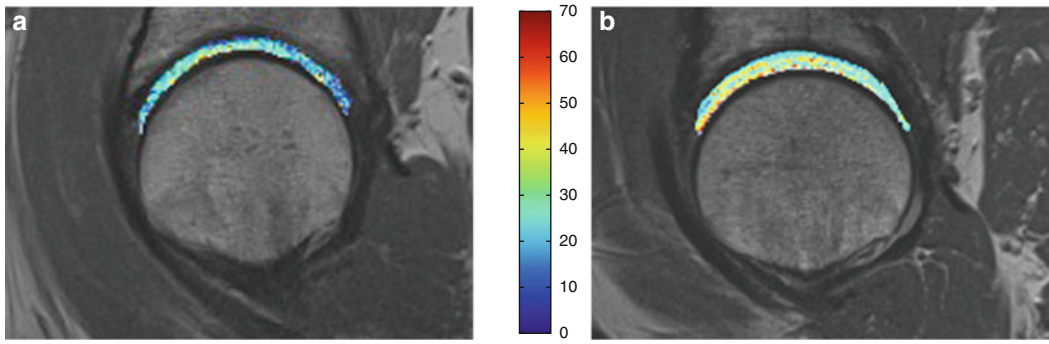

Fig. 17.1 T1-rho color map of hip hyaline cartilage superimposed over oblique sagittal anatomical image in normal (*left*) and arthritic hip (*right*). Mean T1-rho relaxation values: 32.37 ms in Control subject on the left; 36.18 ms, cam-FAI patient on right. Note the elevation of T1-rho relaxation values in the FAI subject, reflecting proteoglycan depletion, diffusely in the weight-bearing cartilage of the joint and most pronounced in the more anterior aspect

have employed the delayed gadolinium-enhanced magnetic resonance imaging of cartilage (dGEMRIC) technique [33–36]. Only limited studies have been conducted using T1ρ MRI in the normal and arthritic hip demonstrating the feasibility of the technique [37, 38]. T1ρ MRI has demonstrated differences between the cartilage profile of the normal and arthritic hip in femoroacetabular impingement. Specifically, T1ρ relaxation values have been shown to be increased in the known target zones of impingement reflecting proteoglycan depletion [37, 39] (Fig 17.1a–c).

T1ρ MRI Technique

T1ρ MRI can be carried out on both 1.5 and 3.0 T systems. However, it should be noted that the T1ρ pulse sequence is not commercially available. The study is performed on a single hip at a time. A flexible coil is wrapped around the hip, with the patient supine and the leg fixed in neutral rotation. The T1ρ pulse sequence employs a spin-lock technique making it sensitive to low frequency chemical exchange processes between water molecules and the ECM [22, 40]. Typically the protocol is based on a gradient recalled echo sequence with a water excitation technique of fat suppression, with the sequence repeated several times at variable spin locking times. High spatial resolution imaging is required to allow for accurate cartilage segmentation, given how thin the hyaline cartilage may be. Offline image processing is required and hyaline cartilage is segmented manually, possibly semiautomated. Continuous, quantitative T1ρ relaxation times (continuous, quantitative values expressed in milliseconds (ms)) are generated based on the signal intensity of the pixels and mathematical algorithms [37, 38]. A T1ρ color map can be produced and is often registered to anatomic MRI images spatially matched to the T1ρ sequence to allow visual representation of the distribution of the T1ρ values, which are inversely related to the proteoglycan concentration.

One of the major limitations of the T1ρ sequence is that it imparts a relatively large amount of radiofrequency energy (quantified by specific absorption rate—SAR) into the soft tissues, which can lead to heating. All MRI scanners have inherent limiters that prevent SAR thresholds from being exceeded, although this may limit the robustness of the T1ρ protocol and thus image quality. T1ρ MRI would be best on high field strength MRI scanners as the higher signal-to-noise ratio can generate higher spatial resolution images in shorter times. However, higher field strength also results in higher SAR values.

Comparison to Other Cartilage Mapping Techniques

In addition to T1ρ, other more established MRI techniques for evaluating the biochemical composition and structure of hyaline cartilage have been studied, at both the basic science and clinical levels. Delayed gadolinium-enhanced MRI of cartilage (dGEMRIC) is another PG-sensitive, proton MRI-based technique. However, it requires the intravenous injection of a gadolinium contrast agent followed by a regimented exercise protocol prior to imaging [6, 41]. T2 [42] and T2* [43, 44] relaxation time mapping has also been investigated as a non-contrast technique. However, they are predominantly sensitive to changes in collagen content and organization [45]. Recent studies have recognized that T1ρ and T2 may provide complimentary information, predominantly but not necessarily exclusively about, PG and collagen, respectively [28, 46]. T1ρ may be preferred over T2 mapping for several reasons. PG depletion from hyaline cartilage is believed to be one of earliest steps in the evolution of OA, preceding collagen structure alteration [47]. T1ρ is less susceptible to artifacts such as background inhomogeneity, susceptibility variations, diffusion-induced signal losses, and magic angle artifact [27, 32]. T1ρ has also been found to have greater reproducibility [32, 38] and larger dynamic range within cartilage [27, 48] and it shows larger differences between normal and OA subjects [28, 48] than does T2. Although the non-contrast T1ρ MRI cartilage mapping is promising, further studies are required before confirming it as an equally efficacious alternative to the more established dGEMRIC.

Challenges of Cartilage Mapping in the Hip

There are inherent challenges to biochemical imaging of hip cartilage compared to other joints such as the knee, upon which much of the initial research on cartilage mapping was based. Hip hyaline cartilage is much thinner, especially in the periphery of the joint [16]. As well, the hip joint is grossly spherical with resultant curvature of the joint space and articular surfaces, such that planar acquisition slices can be susceptible to volume averaging artifacts. The articular surfaces of the acetabulum and femoral head are very closely opposed to one another, making spatial separation of the two surfaces challenging. For this reason several previous studies on cartilage mapping in the hip performed the analysis on a combined bilayer, including both the acetabular and femoral surfaces together [38]. However, more recently, studies have attempted to resolve the two cartilage surfaces [35, 37]. The advent of high field scanners (3.0 T and higher), 3D volume acquisitions, and continual advances in scanner hardware and surface coil technology will allow for higher resolution scanning with higher signal-to-noise ratios and shorter scan times facilitating this cartilage layer separation [18].

Conclusion

T1ρ MRI is a promising noninvasive and non-contrast-based MRI cartilage mapping technique. Along with other imaging techniques including dGEMRIC, T2, and T2* mapping, it may be able to fulfill the rapidly growing medical demand for a reliable, objective, non-invasive, and quantitative investigation of cartilage status. At present, most medical and surgical therapies for OA are only palliative and concentrate on the treatment of symptoms. However, advanced biochemical imaging techniques will detect changes much earlier, possibly before any symptoms or significant joint damage occurs. This may lead to a shift in the management of OA, from palliative, to more preventative and disease modifying. Furthermore, these novel protocols may serve as a future tool in monitoring the progression of cartilage changes and the responses to therapy, in both the clinical and research environments [18].

References

1. Felson DT. Clinical practice. Osteoarthritis of the knee. N Engl J Med. 2006;354(8):841–8.
2. Felson DT, Nevitt MC. Epidemiologic studies for osteoarthritis: new versus conventional study design

approaches. Rheum Dis Clin North Am. 2004;30 (4):783–97, vii.
3. van den Berg WB. Pathophysiology of osteoarthritis. Joint Bone Spine. 2000;67(6):555–6.
4. Poole AR. An introduction to the pathophysiology of osteoarthritis. Front Biosci. 1999;4:D662–70.
5. Buckwalter JA, Martin J. Degenerative joint disease. Clin Symp. 1995;47(2):1–32.
6. Burstein D, Bashir A, Gray ML. MRI techniques in early stages of cartilage disease. Invest Radiol. 2000;35(10):622–38.
7. Recht MP, et al. MRI of articular cartilage: revisiting current status and future directions. AJR Am J Roentgenol. 2005;185(4):899–914.
8. Gold GE, et al. MRI of articular cartilage in OA: novel pulse sequences and compositional/functional markers. Osteoarthritis Cartilage. 2006;14(Suppl A): A76–86.
9. Burstein D, Gray ML. Is MRI fulfilling its promise for molecular imaging of cartilage in arthritis? Osteoarthritis Cartilage. 2006;14(11):1087–90.
10. Mintz DN, et al. Magnetic resonance imaging of the hip: detection of labral and chondral abnormalities using noncontrast imaging. Arthroscopy. 2005;21 (4):385–93.
11. James SL, et al. MRI findings of femoroacetabular impingement. AJR Am J Roentgenol. 2006;187 (6):1412–9.
12. Schmid MR, et al. Cartilage lesions in the hip: diagnostic effectiveness of MR arthrography. Radiology. 2003;226(2):382–6.
13. Kassarjian A, et al. Triad of MR arthrographic findings in patients with cam-type femoroacetabular impingement. Radiology. 2005;236(2):588–92.
14. Werlen S. Magnetic resonance arthrography of the hip in femoroacetabular impingement. Oper Tech Orthop. 2005;15:191–203.
15. Beaule PE, Zaragoza E, Copelan N. Magnetic resonance imaging with gadolinium arthrography to assess acetabular cartilage delamination. A report of four cases. J Bone Joint Surg Am. 2004;86-A (10):2294–8.
16. Wyler A, et al. Comparison of MR-arthrography and CT-arthrography in hyaline cartilage-thickness measurement in radiographically normal cadaver hips with anatomy as gold standard. Osteoarthritis Cartilage. 2009;17(1):19–25.
17. Mamisch TC, et al. Magnetic resonance imaging of the hip at 3 Tesla: clinical value in femoroacetabular impingement of the hip and current concepts. Semin Musculoskelet Radiol. 2008;12(3):212–22.
18. Beaule PE, et al. New frontiers in cartilage imaging of the hip. Instr Course Lect. 2012;61:253–62.
19. Gray ML, et al. 2007 Elizabeth winston lanier award winner. Magnetic resonance imaging of cartilage glycosaminoglycan: basic principles, imaging technique, and clinical applications. J Orthop Res. 2008;26 (3):281–91.
20. Duvvuri U, et al. T1rho-relaxation in articular cartilage: effects of enzymatic degradation. Magn Reson Med. 1997;38(6):863–7.
21. Wheaton AJ, et al. Quantification of cartilage biomechanical and biochemical properties via T1rho magnetic resonance imaging. Magn Reson Med. 2005;54(5):1087–93.
22. Akella SV, et al. Proteoglycan-induced changes in T1rho-relaxation of articular cartilage at 4T. Magn Reson Med. 2001;46(3):419–23.
23. Regatte RR, et al. Proteoglycan depletion-induced changes in transverse relaxation maps of cartilage: comparison of T2 and T1rho. Acad Radiol. 2002;9 (12):1388–94.
24. Regatte RR, et al. Proton spin-lock ratio imaging for quantitation of glycosaminoglycans in articular cartilage. J Magn Reson Imaging. 2003;17(1):114–21.
25. Duvvuri U, et al. T(1rho) relaxation can assess longitudinal proteoglycan loss from articular cartilage in vitro. Osteoarthritis Cartilage. 2002;10(11):838–44.
26. Li X, et al. In vivo 3T spiral imaging based multi-slice T(1rho) mapping of knee cartilage in osteoarthritis. Magn Reson Med. 2005;54(4):929–36.
27. Regatte RR, et al. T1rho relaxation mapping in human osteoarthritis (OA) cartilage: comparison of T1rho with T2. J Magn Reson Imaging. 2006;23(4):547–53.
28. Li X, et al. Spatial distribution and relationship of T1rho and T2 relaxation times in knee cartilage with osteoarthritis. Magn Reson Med. 2009;61(6):1310–8.
29. Taylor C, et al. Comparison of quantitative imaging of cartilage for osteoarthritis: T2, T1rho, dGEMRIC and contrast-enhanced computed tomography. Magn Reson Imaging. 2009;27(6):779–84.
30. Stahl R, et al. T1rho, T2 and focal knee cartilage abnormalities in physically active and sedentary healthy subjects versus early OA patients–a 3.0-tesla MRI study. Eur Radiol. 2009;19(1):132–43.
31. Regatte RR, et al. In vivo proton MR three-dimensional T1rho mapping of human articular cartilage: initial experience. Radiology. 2003;229 (1):269–74.
32. Regatte RR, et al. T 1 rho-relaxation mapping of human femoral-tibial cartilage in vivo. J Magn Reson Imaging. 2003;18(3):336–41.
33. Kim YJ, et al. Assessment of early osteoarthritis in hip dysplasia with delayed gadolinium-enhanced magnetic resonance imaging of cartilage. J Bone Joint Surg Am. 2003;85-A(10):1987–92.
34. Bittersohl B, et al. Cartilage damage in femoroacetabular impingement (FAI): preliminary results on comparison of standard diagnostic vs delayed gadolinium-enhanced magnetic resonance imaging of cartilage (dGEMRIC). Osteoarthritis Cartilage. 2009;17(10):1297–306.
35. Pollard TC, et al. Localized cartilage assessment with three-dimensional dGEMRIC in asymptomatic hips with normal morphology and cam deformity. J Bone Joint Surg Am. 2010;92(15):2557–69.

36. Zilkens C, et al. Delayed gadolinium enhanced MRI of cartilage (dGEMRIC): molecular MRI of hip joint cartilage. Orthopade. 2009;38(7):591–9.
37. Rakhra KS, et al. Can T1-rho MRI detect acetabular cartilage degeneration in femoroacetabular impingement?: a pilot study. J Bone Joint Surg Br. 2012;94(9):1187–92.
38. Carballido-Gamio J, et al. Feasibility and reproducibility of relaxometry, morphometric, and geometrical measurements of the hip joint with magnetic resonance imaging at 3T. J Magn Reson Imaging. 2008;28(1):227–35.
39. Cardenas-Blanco A. et al. Non-contrast cartilage assessment (T1-Rho) of the hip in femoracetabular impingement: can we predict early change? In: International Society for Magnetic Resonance in Medicine, Melbourne. 2012
40. Duvvuri U, et al. Water magnetic relaxation dispersion in biological systems: the contribution of proton exchange and implications for the noninvasive detection of cartilage degradation. Proc Natl Acad Sci U S A. 2001;98(22):12479–84.
41. Williams A, et al. Glycosaminoglycan distribution in cartilage as determined by delayed gadolinium-enhanced MRI of cartilage (dGEMRIC): potential clinical applications. AJR Am J Roentgenol. 2004;182(1):167–72.
42. Watanabe A, et al. T2 mapping of hip articular cartilage in healthy volunteers at 3T: a study of topographic variation. J Magn Reson Imaging. 2007;26 (1):165–71.
43. Bittersohl B, et al. Feasibility of T2* mapping for the evaluation of hip joint cartilage at 1.5T using a three-dimensional (3D), gradient-echo (GRE) sequence: a prospective study. Magn Reson Med. 2009;62 (4):896–901.
44. Apprich S, et al. Evaluation of articular cartilage in patients with femoroacetabular impingement (FAI) using T2* mapping at different time points at 3.0 tesla MRI: a feasibility study. Skeletal Radiol. 2012;41(8):987–95.
45. Mosher TJ, Dardzinski BJ. Cartilage MRI T2 relaxation time mapping: overview and applications. Semin Musculoskelet Radiol. 2004;8(4):355–68.
46. Blumenkrantz G, Majumdar S. Quantitative magnetic resonance imaging of articular cartilage in osteoarthritis. Eur Cell Mater. 2007;13:76–86.
47. Dijkgraaf LC, et al. The structure, biochemistry, and metabolism of osteoarthritic cartilage: a review of the literature. J Oral Maxillofac Surg. 1995;53 (10):1182–92.
48. Akella SV, et al. Reduction of residual dipolar interaction in cartilage by spin-lock technique. Magn Reson Med. 2004;52(5):1103–9.

Index

Y.-J. Kim (eds.), *Hip Magnetic Resonance Imaging*,
DOI 10.1007/978-1-4614-1668-5,